Investigation of Metal Oxides/Sulfides as Negative Electrode Materials for Li-ion and Beyond-Li Batteries

Zur Erlangung des akademischen Grades eines
DOKTORS DER NATURWISSENSCHAFTEN
(Dr. rer. nat.)

von der KIT-Fakultät für Chemie und Biowissenschaften
des Karlsruher Instituts für Technologie (KIT)
genehmigte

DISSERTATION

von

M. Sc. Chengping Li

1. Referent: Prof. Helmut Ehrenberg
2. Korreferent: Prof. Rolf Schuster

Tag der mündlichen Prüfung: 07. 12. 2020

Selbstständigkeitserklärung

Hiermit versichere ich, die vorliegende Arbeit selbstständig verfasst und keine anderen als die angegebenen Quellen und Hilfsmittel verwendet sowie Zitate kenntlich gemacht zu haben. Die Dissertation wurde bisher an keiner anderen Hochschule oder Universität eingereicht.

Karlsruhe， den 07. 12. 2020

Chengping Li

Acknowledgements

First of all, I would like to acknowledge my supervisor and referee Prof. Dr. Helmut Ehrenberg, who gave me the opportunity to do research work in the Institute of Applied Materials-Energy Storage Systems (IAM-ESS), Karlsruhe Institute of Technology (KIT), for his great support, fruitful discussion, valuable guidance, and thoughtful comments. Next, I would like to express my sincere gratitude to my co-supervisor Dr. Sonia Dsoke for her support and encouragement, understanding, brilliant suggestion. I would like to thank Prof. Dr. Rolf Schuster as the second Referent for his valuable comments and suggestions. I would like to thank Ms. Kristina Pfeifer for PhD thesis correction, SEM/EDS measurement, German correction, and fruitful discussions. In addition, I would express my deep appreciation to Dr. Angelina Sarapulova for her kind support and valuable discussion on *in operando* synchrotron radiation diffraction and X-ray absorption spectroscopy (XAS).

It is a great pleasure to thank the financial supports by the China Scholarship Council (CSC, No.: 201707030004).

I would like to express my great appreciation and gratitude to all the people for their helpful scientific support and fruitful discussions with my colleagues at IAM-ESS. In particular, Dr. Michael Knapp (XRD Rietveld refinement course), Ms. Marina Bauer (German correction), Mrs. Almut Kriese (administrative support), Dr. Qiang Fu (*in operando* XRD, XAS), Mrs. Liuda Mereacre (TGA, FT-IR, Raman), Mr. Udo Geckle and Mrs. Bettina Hunzinger (SEM/EDS), Mrs. Vanessa Trouillet, Mr. Xinlin Luo, Ms. Lydia Gehrlein and Dr. Julia Maibach (XPS), Dr. Anna-Lena Hansen and Dr. Björn Schwarz (*in operando* XRD), Mr. Georg Bosch, Mr. Marcus Mayer and Mr. Julian Hansen (equipment support), Heinz-Robert Goebel (equipment support), and Richard Hans Schneider (IT support). Additionally, the kind help from Chinese colleagues at IAM-ESS, Dr. Guiying Tian, Dr. Zijian Zhao, Dr. Weibo Hua, Dr. Jiangong Zhu, Dr. Lihua Zhu, Dr. Jiarong He, Xinyang Liu, Jiaqi Wang, etc., are highly appreciated.

I am also grateful to Dr. Georgian Melinte from the Institute of Nanotechnology (INT, KIT) for the TEM measurements. I would also acknowledge Prof. Dr. Andrea Balducci (from Friedrich-Schiller-University Jena) for the preparation of different kinds of electrolytes and valuable discussion.

I am grateful to beamline scientists for the technical support from Dr. Martin Etter (*in operando* synchrotron radiation diffraction, beamline P02.1) and Dr. Edmund Welter (*in operando* XAS, beamline P65) at PETRA III, DESY, Hamburg. I would like to thank Dr. Aleksandr Missiul (*in operando* synchrotron radiation diffraction, beamline BL04-MSPD, ALBA.) and Dr. Nicola Pietro Maria Casati (*in operando* synchrotron radiation diffraction, Paul Scherrer Institute, Forschungsstrasse PSI, Switzerland).

Finally, I would like to express deep gratitude to my parents, my sisters, and my girlfriend Zemei He for their endless love, confidence, encouragement, and support during my life. Thank you all again.

Table of Contents

Abbreviations, Constants, and Symbols

CE	Coulombic efficiency
CMC	Carboxymethyl cellulose
CV	Cyclic Voltammetry
CNTs	Carbon nanotubes
DMC	Dimethyl carbonate
EC	Ethylene carbonate
EDS	Energy dispersive X-ray spectroscopy
et al.	*et alii / et aliae / et alia*
EXAFS	Extended X-ray absorption fine structure
FEC	Fluoroethylene carbonate
GCPL	Galvanostatic cycling with potential limitation
H_2bdc	Terephthalic acid
ICSD	Inorganic crystal structure database
KIBs	Potassium-ion batteries
LIBs	Lithium-ion batteries
NIBs	Sodium-ion batteries
OCV	Open-circuit voltage
OEA	Organic Elemental Analysis
PTFE	Polytetrafluoroethylene
PVdF	Polyvinylidene fluoride
R_p	Profile residual (reliability factor)
R_{wp}	Weighted profile residual
rGO	Reduced graphene oxide
SEI	Solid electrolyte interphase
SEM	Scanning electron microscopy
SHE	Standard hydrogen electrode
STEM	Scanning transmission electron microscopy
TEM	Transmission electron microscopy
XPS	X-ray photoelectron spectroscopy
XRD	X-ray diffraction
XAS	X-ray absorption spectroscopy
XANES	X-ray near-edge structure spectroscopy

[C]	C-rate
ΔG	Non-standard Gibbs free energy / J
ΔG^0	Standard Gibbs free energy / J
n	Number of electrons transferred in an electrode reaction
F	Farady constant (96485.3 C/mol)
E	Cell voltage under non-standard conditions / V
E^0	Standard battery potential (at room temperature and 1 bar pressure) / V
R	Universal gas constant (8.314 J mol^{-1} K^{-1})
T	Absolute temperature K or °C
T^0	Standard ambient temperature (298.15 K)
$U(t)$	Voltage as a function of time
$I(t)$	Current as a function of time
ε	The specific energy / Wh kg^{-1}
P	The specific power / W kg^{-1}
Q_{in}	The total discharge capacity
Q_{out}	The total charge capacity
η	Energetic efficiency
E_{in}	The total discharge energy
E_{out}	The total charge energy
σ	Conductivity
φ	The phase shift
θ	Bragg angle
v	Scan rate
f	Frequency of microwave radiation
j	The imaginary unit
Z	The impedance
Z'	The real part of the impedance
Z''	The imaginary part of the impedance

List of Figures

List of Tables

Zusammenfassung

Die Notwendigkeit zur Reduzierung des Verbrauchs traditioneller fossiler Brennstoffe und die Bewahrung der natürlichen Umwelt hat viel Aufmerksamkeit auf Energiespeichertechnologien gelenkt. Alkali-Ionen-Batterien sind eine der Energiespeichertechnologien. Die Entwicklung alternativer Anodenmaterialien mit langer Lebensdauer, hoher reversibler Kapazität und gesteigerter Ratenfähigkeit ist für Alkali-Ionen-Batterien von entscheidender Bedeutung. In dieser Arbeit werden Strukturdesign und Materialien auf Kohlenstoffbasis gleichzeitig verwendet, um die spezifische Kapazität und Stabilität zu verbessern. Darüber hinaus ist ein eingehendes Verständnis der Beziehung zwischen den Mechanismen zum Einlagern/Extrahieren von $Li^+/Na^+/K^+$-Ionen und dem elektrochemischen Verhalten wichtig, um die Leistung von wiederaufladbaren Batterien zu verbessern.

Diese Arbeit eröffnet erschließt mechanistische Merkmale von Materialien mit hoher Kapazität, sowie das Zusammenspiel mehrerer Komponenten in Alkali-Ionen-Batterien. Die Wirkung verschiedener Li-Salz Elektrolyte auf Fe-basierte Elektroden, sowie der Einfluss von Kohlenstoffadditiven (Super P und C65) und dem Elektrolytadditiv Fluorethylencarbonat (FEC) auf Sn-basierte Elektroden werden aufgedeckt. Diese Ergebnisse erlauben einen tiefen Einblick in das Verständnis des Alkali-Ionen-Speichermechanismus von Materialien des Umwandlungs-bzw. Legierungstyps.

Im ersten Teil dieser Arbeit wird eine Kern-Schale-Struktur von hohlen Fe_2O_3@C Nanokugeln aus metallorganischen Gerüsten als Anodenmaterial für LIBs verwendet. *In operandooperando*-Beugung von synchrotrons strahlung zeigte, dass sich die Zwischenphasen $Li_xFe_2O_3$ ($R\bar{3}m$, rhombohedral, $0 < x < 1$) und $Li_xFe_2O_3$ ($Fd\bar{3}m$, Li-arm, $0 < x < 4$) bilden, welche sich in $Li_xFe_2O_3$ ($Fd\bar{3}m$, Li-reich, $1 < x < 5$) und anschließend weiter zu metallischem Fe^0, Li_2O und $Li_xFe_2O_3$ ($Fd\bar{3}m$, X-Phase, $0 < x < 2$) umwandeln. Während des Delithiierungsprozesses kehrt das Material nicht zur ursprünglichen Fe_2O_3-Struktur zurück. Stattdessen verbleibt teilweise delithiiertes $Li_{x-1}Fe_2O_3$ ($Fd\bar{3}m$, X-Phase, $1 < x < 2.5$) und eine amorphe metallische Fe^0-Phase. Der Fe K-Kanten-XAS-Übergang und die Bildung von metallischem Fe^0 werden durch *in-operando*-Röntgenabsorptionsspektroskopie bestätigt. Darüber hinaus wird der Widerstandsbeitrag dieses Materials in zwei verschiedenen Li-Salzen durch elektrochemische Impedanzspektroskopie bewertet, welche abhängig vom Li-Salz unterschiedliche Zusammensetzungen der Festelektrolyt-Interphase zeigen.

In der Literatur wurde bereits berichtet, dass $Fe_{1-x}S$/C-Nanokomposite eine vielversprechende Leistung als Anodenmaterial für LIBs zeigen. Der zugrunde liegende Lithiumspeicherungsmechanismus im ersten Zyklus ist jedoch noch nicht vollständig verstanden. In dieser Arbeit ermöglicht die Kombination verschiedener *in operando* Techniken das Aufdecken ausgeprägter elektronischer und struktureller Änderungen auf verschiedenen Längenskalen. Zusätzlich werden kinetische Prozesse, morphologische Veränderungen und die Entwicklung des spezifischen spezifischen Widerstands untersucht. Diese Ergebnisse zeigen, dass die Phasenabfolge von $2Fe_{1-x}S + 2Li^+ + 2e^- \rightarrow Li_2Fe_{1-x}S_2 + (1-x)Fe^0$ und $Li_2Fe_{1-x}S_2 + 2Li^+ + 2e^- \rightarrow 2Li_2S + (1-x)\,Fe^0$ während des ersten Lithiierungsprozesses auftritt. Die Redoxreaktion von $Fe^{2+} + 2e^- \rightleftharpoons Fe^0$ wird durch *in operando* XAS bestätigt. Während des ersten Delithierungsprozesses wandeln sich Fe^0 wird durch *in operando* XAS bestätigt. Während des ersten Delithierungsprozesses wandeln sich Fe^0 und Li_2S in $Li_{2-y}Fe_{1-x}S_2$ um und Li^+ und e^- werden aus Li_2S extrahiert, um $Li_{2-y}S$ zu bilden ($0 < y < 2$). Die Umwandlung von Li_2S zu $Li_{2-y}S$ wurde in früheren Berichten nicht erkannt. Nach dem ersten Delithiierungsprozess werden sind amorphe lithiierte FeS-Nanopartikel in der verbleibenden Li_2S-Matrix eingebettet.

Schließlich werden wenige *in situ* erzeugte Schichten poröser SnS_2-Nanoblätter auf reduziertem Graphenoxid (SnS_2-rGO) als Anodenmaterial für NIBs und KIBs untersucht. Diese Arbeit untersucht den Einfluss verschiedener leitfähiger Kohlenstoffe (Super P und C65) auf SnS_2-rGO-Elektroden für NIBs und KIBs. Außerdem werden die Auswirkungen des Elektrolytadditivs Fluorethylencarbonat (FEC) auf die elektrochemische Leistung von Natrium-Ionen-Batterien und Kalium-Ionen-Batterien untersucht. Darüber hinaus werden der kinetische Prozess und der elektrochemische Widerstand mit elektrochemischer Impedanzspektroskopie untersucht. Die Kombination der ultradünnen SnS_2-Nanokristalle und dem hochleitenden rGO-Netzwerk fördert die Diffusion von Na^+/K^+-Ionen, stellt mehr Reaktionsstellen bereit, hemmt die Aggregation und toleriert die großvolumige Änderung bei längerem Zyklieren.

Abstract

The reduction of the consumption of traditional fossil fuels and maintaining an intact environment have drawn much attention on sustainable energy storage technologies. Alkali-ion batteries are one of the energy storage technologies. Developing an alternative negative electrode (further called the anode) with a stable cycling performance, high reversible capacity, and superior rate capability is crucial for alkali-ion batteries. In this thesis, structural design and carbon-based materials are utilized simultaneously to improve specific capacity and stability. Additionally, an in-depth understanding of the relation between Li^+/Na^+/K^+-ions insertion/extraction underlying mechanisms and electrochemical behavior is important to improve the performance of rechargeable batteries.

This thesis elucidates mechanistic features of high capacity materials as well as the interplay of several components in alkali-ion batteries. The effect of different Li-salt electrolytes on Fe-based electrodes, and the influence of carbon additives (Super P and C65) and electrolyte additive fluoroethylene carbonate (FEC) on Sn-based electrodes are uncovered. These results provide a deep insight into understanding the alkali-ion storage mechanism in conversion/alloying-type materials.

In the first part of this thesis, a core-shell structure Fe_2O_3@C of hollow nanospheres derived from metal-organic frameworks is used as anode material for lithium-ion batteries. *In operando* diffraction using synchrotron radiation diffraction revealed that the intermediate phases $Li_xFe_2O_3$ ($R\bar{3}m$, rhombohedral, $0 < x < 1$) and $Li_xFe_2O_3$ ($Fd\bar{3}m$, Li-lean, $0 < x < 4$) form and subsequently convert to $Li_xFe_2O_3$ ($Fd\bar{3}m$, Li-rich, $1 < x < 5$), which finally transforms into metallic Fe^0, Li_2O, and $Li_xFe_2O_3$ ($Fd\bar{3}m$, X phase, $0 < x < 2$). During the de-lithiation process, the material does not return to the initial Fe_2O_3 structure. Instead, the partially de-lithiated $Li_{x-1}Fe_2O_3$ ($Fd\bar{3}m$, X phase, $1 < x < 2.5$) and an amorphous metallic Fe^0 phase remain. The Fe K-edge XAS transition and the formation of metallic Fe^0 are confirmed by *in operando* XAS measurements. Furthermore, the resistive contribution of this material in two types of Li-salt is evaluated by electrochemical impedance spectroscopy, which highlights a different type of solid electrolyte interphase induced by the salt.

Furthermore, in literature was previously reported that the $Fe_{1-x}S$/C nanocomposite shows a promising performance as anode material for lithium-ion batteries. However, the underlying lithium storage mechanism was not entirely understood during the 1st cycle. In this thesis, the

combination of *in operando* techniques enables the uncovering of the pronounced electronic changes and structural alterations on different length-scales. Additionally, the investigation of kinetics processes, morphological changes, and internal resistance evolution are discussed. These results reveal that the phase transition of $2Fe_{1-x}S + 2Li^{+} + 2e^{-} \rightarrow Li_2Fe_{1-x}S_2 + (1-x)Fe^{0}$ and $Li_2Fe_{1-x}S_2 + 2Li^{+} + 2e^{-} \rightarrow 2Li_2S + (1-x)\ Fe^{0}$ occurs during the 1st lithiation process. The redox reaction of $Fe^{2+} + 2e^{-} \rightleftharpoons Fe^{0}$ is confirmed by *in operando* XAS. During the 1st de-lithiation process, Fe^0 and Li_2S convert to $Li_{2-y}Fe_{1-x}S_2$ and Li^+ and e^- are extracted from Li_2S to form $Li_{2-y}S$ ($0 < y < 2$). The phase transition from Li_2S to $Li_{2-y}S$ was not detected in previous reports. After the 1st de-lithiation process, amorphous lithiated FeS nanoparticles are embedded within the remaining Li_2S matrix.

Finally, porous few-layer SnS_2 nanosheets *in situ* grown on reduced graphene oxide (SnS_2-rGO) are investigated as anode material for sodium-ion batteries and potassium-ion batteries. This work explores the influence of different conductive carbon (Super P and C65) on SnS_2-rGO electrodes for sodium-ion batteries and potassium-ion batteries. Besides, the effects of the electrolyte additive fluoroethylene carbonate (FEC) on the electrochemical performance of sodium-ion batteries and potassium-ion batteries are investigated. Furthermore, the kinetic process and electrochemical impedance are examined by electrochemical impedance spectroscopy. By combining the ultrathin SnS_2 nanocrystals and the highly conductive reduced graphene oxide network, the unique structure can promote Na^+/K^+-ions diffusion, provide more reaction sites, inhibit aggregation, and tolerate the large volume change during prolonged cycling.

1 Introduction

1.1 Background

Nowadays, transform other forms of energy into electrical energy and storage have attracted great attention due to global warming. To cope with the ever-growing energy needs and consumption of fossil-fuel resources, researchers try to develop advanced renewable energy technologies, such as renewable energy sources and sustainable storage technologies.[1] Renewable energy sources like wind, tide, sunlight, geothermal heat, biomass, and nuclear power are exploited for the generation of electricity.[2] However, the drawback of renewable energy sources is generally dispersed, which does not meet the requirements for large-scale energy storage systems.[3] In order to make the best use of renewable energy sources, the design of new electrochemical storage techniques is required, which is aimed at the appropriate utilization of different energy sources. The desirable and high-performance energy storage techniques should be featured with efficiency, versatility, environmentally friendliness, and low-cost. Energy storage technologies available for large-scale applications can be categorized into four types: mechanical, electrical, chemical, and electrochemical.[4] Batteries stand for excellent energy storage technology with the highest energy efficiency. Among them, lithium-ion batteries (LIBs) technology is the outstanding representative. LIBs, which were first commercially introduced by Sony in 1990, are based on a lithium intercalation mechanism. LIBs have been widely used in portable electronic devices including computers, video, and digital cameras, mobile phones, electric vehicles, and stationary energy storage systems due to their high energy density and long-term cycling capability.[5–9] LIBs were considered as one of the most promising power sources for the next-generation hybrid electric vehicles (HEVs) and plug-in hybrids (PHEVs).[7] In addition, another three rechargeable batteries like lead-acid batteries, nickel-cadmium (Ni-Cd), and nickel-metal hydride batteries (Ni-MH) were also found in practical applications in daily life. However, the inherent limitations such as limited energy density, corrosion and poisoning of the Ni-based anode materials, limited high-rate capability, and poor Coulombic efficiency of the latter three systems impede their applications in large-scale energy storage.[10–13]

Sodium-ion batteries (NIBs) technology are an attractive and promising candidate to replace LIBs, because of the natural abundance, low-cost, and the similar electrochemical properties of sodium when compared to lithium.[14,15] Potassium-ion battery (KIB) technology is considered as another possible energy system, due to the abundance of K resources in the earth's crust and oceans, lower reduction potential compared to sodium, a high operating voltage, and a better conductivity of potassium electrolytes.[16–19]

1.2 Overview of alkali-ion batteries

1.2.1 Components and working principle

LIBs are composed of a positive electrode (further called "cathode" with respect to the discharge process) and a negative electrode ("anode") electronically separated by separator and electrolyte. The separator is a microporous film, which kept apart direct electronic contact between the cathode and the anode. The electrolyte can be a liquid or a solid electronic insulator with solely ionic conductivity. **Figure 1.1** demonstrates the basic LIB system consisting of a graphite anode and a $LiCoO_2$ cathode. Both electrodes enable reversible insertion and extraction of Li^+-ions from their respective structures. During charging, Li^+-ions migrate from the $LiCoO_2$ cathode and intercalate into the graphite anode (**Equation 1.1**). This process is driven by an external electron flow in the same direction. Conversely, during discharging, Li^+-ions spontaneously move back from the graphite anode to the $LiCoO_2$ cathode, resulting in an electron flow with the same direction to power the external device (**Equation 1.2**). The redox reaction is described below:

Charge process: $LiCoO_2 + C \rightarrow Li_{1-x}CoO_2 + CLi_x$ (1.1)

Discharge process: $Li_{1-x}CoO_2 + CLi_x \rightarrow LiCoO_2 + C$ (1.2)

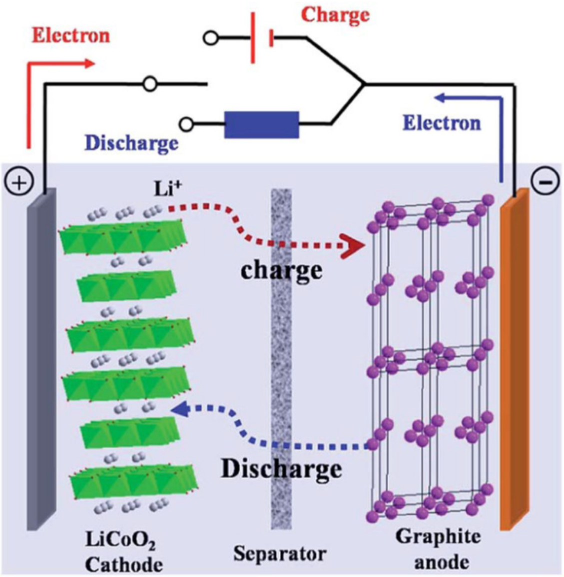

Figure 1.1 Scheme of the LIBs.[20] Copyright of The Royal Society of Chemistry 2014.

1.3 Overview of post lithium-ion batteries: sodium-ion batteries and potassium-ion batteries

The battery components and the working principles of NIBs and KIBs are the same as for LIBs except for their charge carriers. The similar electrochemical storage mechanism of LIBs, and NIBs/KIBs can promote the development of NIBs/KIBs by employing outcomes accumulated in LIB research. In contrast to the limited abundance (0.0017 wt %) and uneven distribution of lithium, sodium and potassium have a much higher crustal abundance of 2.36 and 2.09 wt % respectively, evenly distributed in the world.[21,22] In addition, aluminium foil can be used as a current collector for both, cathode and anode in NIBs and KIBs. Different from that, alloying reactions appear between Al and Li at the low potential in LIBs.[23] Furthermore, lower materials cost is expected for NIBs and KIBs. However, there are some differences between these systems. Desolvated Na^+-ions (1.02 Å) and K^+-ions (1.38 Å) are larger compared to Li^+-ions (0.76 Å), and the molecular weights of Na (23 g mol^{-1}) and K (39.1 g mol^{-1}) higher than of Li (6.9 g mol^{-1}), which affects the transport properties, phase stability, and storage capability of NIBs/KIBs. Additionally, the standard redox potential of sodium (-2.74 V for Na^+/Na *vs.* the standard hydrogen electrode [SHE]) and potassium (-2.96 V for K^+/K *vs.* SHE) are higher than Li (-3.04 V for Li^+/Li *vs.* SHE), thus limiting the energy density.[9] Despite the compromised energy density, NIBs/KIBs are promising alternative energy storage devices for future large-scale stationary applications.

1.4 Basic concepts and characteristics of batteries

1.4.1 Thermodynamics

The basic thermodynamic equations for a reversible redox reaction are given by:

$$\Delta G = -nFE \text{ or } \Delta G^0 = -nFE^0 \tag{1.3}$$

where ΔG^0 is the standard Gibbs free energy (the standard state at 25 °C and unit activity), n is the number of electrons transferred per mole of reactants, F is Faraday constant (96485.3 C mol^{-1} or 26.801 Ah mol^{-1}), E is the cell voltage with the specific chemical reaction, and E^0 is standard battery potential (at 25 °C temperature and 1 bar pressure). The non-standard Gibbs free energy, ΔG, for bulk chemical reactions can be expressed by Van't Hoff isotherm as:

$$\Delta G = \Delta G^0 + RTln(A_P/A_R) \tag{1.4}$$

where R is the universal gas constant (8.314 J mol^{-1} K^{-1}), T is the absolute temperature and A_P is the activity product of the products and A_R the activity product of the reactants. Combining **Equation 1.3** and **1.4** with the Van't Hoff isotherm, the Nernst equation for electrochemical reactions can be derived as:

$$E = E^0 + \frac{RT}{nF} ln \frac{A_P}{A_R} \tag{1.5}$$

1.4.2 Kinetics

The kinetics of the cell is determined by the electrode reactions (e.g. physical, chemical, charge-transfer, and charge transport reactions). In general, three different kinetics limitations affect the polarization, which have to be taken into account: (a) activation polarization, which happens due to the kinetics of the electrochemical redox reactions and takes place at the interfaces between the electrode and electrolyte; (b) ohmic polarization, which is related to the resistance of individual cell components; (c) concentration polarization, which is attributed to mass transport limitations during cell operation. The polarization, E_p, is given by:

$$E_p = E_{OCV} - E_T \tag{1.6}$$

where E_{OCV} stands for the voltage of the cell at open circuit and E_T presents the terminal cell voltage with a flowing current I.

1.4.3 Specific energy and energy density

The terms specific energy (gravimetric energy density in watthours per kilogram, Wh kg^{-1} and volumetric energy density in watthours per liter, Wh L^{-1}) are used to compare the energy contents of a system, which can be calculated by the following equation:[24,25]

$$\varepsilon = \frac{1}{3600 \cdot m} \int_{t_i}^{t_f} I(t) \cdot U(t) dt \tag{1.7}$$

where ε is the specific energy, *U(t)* the time-varying voltage, *I(t)* the current as a function of time (t), m is the mass of the energy storage device and t_i and t_f in s as initial time and final time of charge/discharge.

1.4.4 Specific power and power density

The specific power (P, W kg^{-1}) is characterized by the performance of a battery in terms of specific power. The power density of a cell is the available power per unit volume, W L^{-1}.

$$P = \frac{1}{(t_f - t_i) \cdot m} \int_{t_i}^{t_f} I(t) \cdot U(t) dt \tag{1.8}$$

1.4.5 Energetic efficiency

The Coulombic efficiency (CE), also called faradaic efficiency or current efficiency, monitors the magnitude of side reactions. For the anode, the CE is the ratio of the total charge capacity (Q_{out}) of the battery to the total discharge capacity (Q_{in}) of the cell in the same cycle. CE is defined as:

$$CE = \frac{Q_{out}}{Q_{in}} \times 100\ \% \tag{1.9}$$

where Q_{out} is the charge capacity of a cell, and Q_{in} is the discharge capacity of the cell in the same cycle.

The energetic efficiency (η) is based on energy output and input.

$$\eta = \frac{E_{out}}{E_{in}} \times 100\ \% \tag{1.10}$$

where E_{out} is the total energy during charging, and E_{in} is the total energy during discharging.

1.4.6 Electrochemical characterization

Galvanostatic cycling with potential limitation (GCPL) and cyclic voltammetry (CV) are the most commonly applied techniques to characterize batteries. GCPL measurements are performed in a constant current mode (A g^{-1} or A cm^{-2}) to investigate the charge/discharge long-cycling performance or to evaluate rate performances by applying different specific currents. CV is a potentiodynamic electrochemical measurement to study the reduction and oxidation processes of molecular species. Furthermore, CV is also employed to distinguish between surface-capacitive-controlled and diffusion-controlled reactions of the electrode. CV measurements can be performed at various scan rates. It's assumed that the current obeys a power-law in dependence on the scan rate (**Equation 1.11**).[26–28] Where a and b are two adjustable parameters, v is the sweep rate and i is the peak current response. The value of b ranges from 0.5 to 1.0, where b=0.5 indicates a diffusion (bulk)-controlled process, while b=1.0 implies a surface-controlled process. One cathodic peak and one anodic peak are chosen to determine the relationship of log (i) and log (v) (**Equation 1.12**).[29–31] Furthermore, to quantify the surface-capacitive contribution in the electrode, it is assumed that the current response obeys an exponential relationship with the scan rate equation (**Equation 1.13**).[32–34] The current response (i) at a specific potential (V) can be divided into surface-capacitive contribution (k_1v, named as Q_p) and diffusion (bulk)-controlled contribution ($k_2v^{0.5}$, named as Q_d). Where k_1 and k_2 are the coefficients denoted to the percentage of the surface-controlled process and the diffusion (bulk)-controlled process, respectively. After linearly fitting the relationship of $|i(v)|v^{-1/2}$ and $v^{1/2}$ (**Equation 1.14**)[32,35], k_1 can be obtained and k_2 is the intercept.

$$i = av^b \tag{1.11}$$

$$\log|(i)| = blog(v) + \log(a) \tag{1.12}$$

$$|i| = k_1v + k_2v^{0.5} \tag{1.13}$$

$$|i|v^{-0.5} = k_1v^{0.5} + k_2 \tag{1.14}$$

1.4.7 Electrochemical impedance spectroscopy

Electrochemical impedance spectroscopy (EIS) is another vital technique to investigate the dynamics of an electrochemical process. Electrochemical impedance is the response of an electrochemical system to an applied potential. EIS can separate the influences of different components like the contribution of the electron transfer resistance, double layer capacitance, etc. Additionally, EIS is very surface sensitive, which makes many changes visible that other techniques don't have access to. EIS is usually performed by applying a modulated sinusoidal alternating current (AC) potential excitation over a wide range of frequencies (i.e., 10^{6}~10^{-2} Hz) to an electrochemical cell with a static potential. The response current and its phase are measured.

Ohm's law (**Equation 1.15**) defines resistance in terms of the ratio between voltage E, and current, I. This is a well-known relationship, and its use is limited only one circuit element-the ideal resistor. An ideal resistor has several simplifying properties.

Electrochemical impedance is normally measured using a small excitation signal. The excitation signal, expressed as a function of time, has the form (**Equation 1.16**). Where $E(t)$ is the potential at the time, $|E|$ is the amplitude of the signal, and ω is the radial frequency. The relationship between radial frequency ω and frequency *f* is described as **Equation 1.17**.

$$\mathrm{R} = \frac{E}{I} \tag{1.15}$$

$$E(t) = |E|\sin(\omega t) \tag{1.16}$$

$$\omega = 2\pi f \tag{1.17}$$

In a linear system, the response signal, $\mathrm{I(t)}$, is shifted in phase (φ) and has a different amplitude than $|I|$. Therefore, the expression of the response signal is described as **Equation 1.18**. An expression analogous to Ohm's law allows researchers to calculate the impedance of the system as **Equation 1.19**. The impedance is therefore expressed in terms of magnitude, $|Z|$, and a phase shift, φ.

$$\mathrm{I(t)} = |I|\sin(\omega t + \varphi) \tag{1.18}$$

$$\mathrm{Z} = \frac{E(t)}{\mathrm{I(t)}} = \frac{|E|\sin(\omega t)}{|I|\sin(\omega t+\varphi)} = |Z|\frac{\sin(\omega t)}{\sin(\omega t+\varphi)} \tag{1.19}$$

By using Euler's formula (**Equation 1.20**), the impedance can therefore be expressed in complex numbers (**Equation 1.21**). *i* is the imaginary unit, $i = \sqrt{-1}$, the total impedance is the ratio of the potential's amplitude and the current amplitude. EIS can be expressed as the real part of the impedance Z', which is the resistance, and imaginary part Z'' (**Equation 1.22**).

$$e^{ix} = \cos(x) + isin(x) \tag{1.20}$$

$$Z = |Z|e^{i\varphi} = \frac{|Z|e^{iwt}}{|Z|e^{iwt+\varphi}} \tag{1.21}$$

$$Z = Z' + iZ'' \tag{1.22}$$

Resistance is the ratio of voltage or potential and current for a DC (direct current) system; the impedance is the ratio of voltage or potential and current for alternating current (AC) systems. The two notations are the origin of the two most popular plots for impedance spectra: the Bode plot (the absolute value of the impedance and the phase shift vs log frequency) and Nyquist plots (negative imaginary part impedance vs. real part impedance). **Figure 1.2** shows the EIS of a parallel resistor and capacitor in a schematic Bode and Nyquist plot.

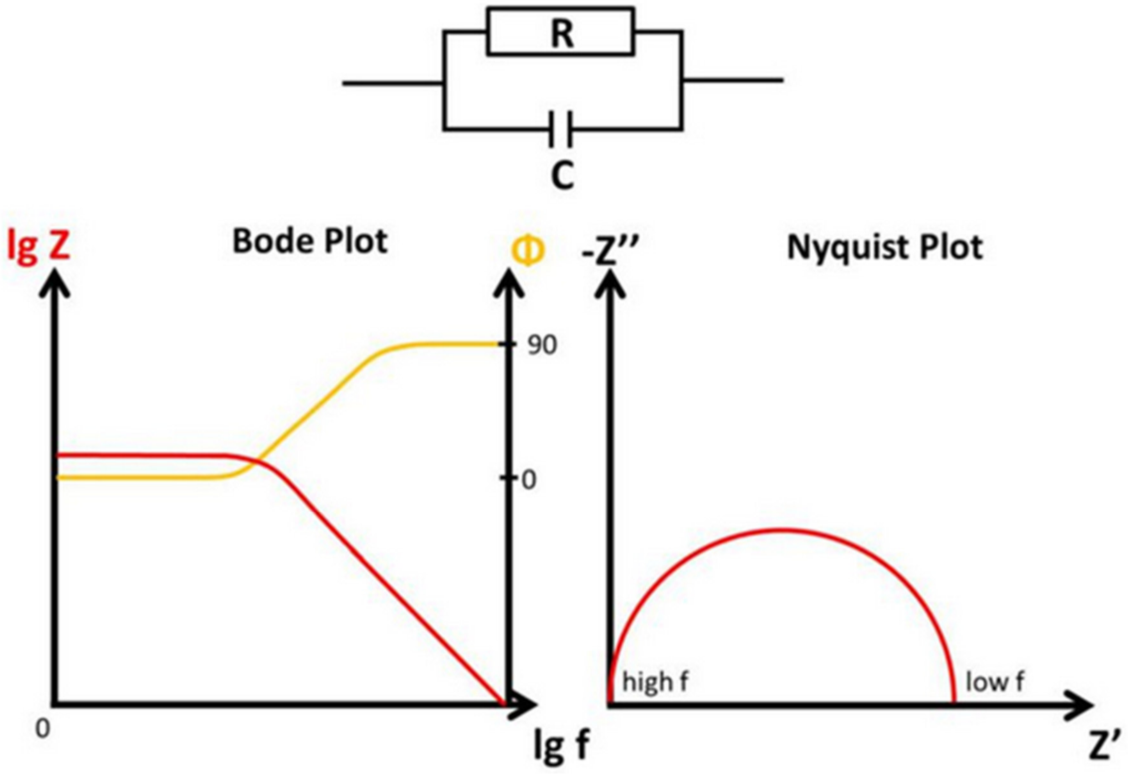

Figure 1.2 EIS of a parallel resistor and capacitor in a schematic Bode and Nyquist plot.

The Nyquist plots of electrodes were fitted using an equivalent circuit described as R_{el} ($R_{SEI}C_{SEI}$) ($R_{CT}C_{CT}$) W in Boukamp's notation,[36] which is expressed in **section 4.3, 5.3**, and **6.3.** R_{el} represents the electrolyte resistance (including separator and internal connections), R_{SEI} and C_{SEI} are assigned to SEI resistance and capacitance, R_{CT} and C_{CT} are related to the charge-transfer resistance and double-layer capacitance, R_e is the electronic features of active material. W is attributed to Warburg impedance in the low-frequency region.

1.5 Overview anode materials of alkali-ion batteries

Significant research has been performed to improve the cell properties to fulfill the requirements of rechargeable secondary batteries (LIBs, NIBs, and KIBs) for future energy storage applications. An ideal anode for energy storage devices should meet the demands of a high specific capacity and a most negative redox potential (if tolerated by the electrolyte), long-term cycling performance, low-cost, and environmental compatibility.

Based on their electrochemical reaction mechanism with lithium, sodium, and potassium, anode materials can be classified into three main groups: intercalation/de-intercalation; alloy/de-alloy, and conversion materials. In detail:[37,38]

a) Intercalation/de-intercalation materials are, for example, graphite and TiO_2, In general, the electrochemical reaction can be defined as: $MX_2 + xG^+ + xe^- \rightleftharpoons G_xMX_2$, where G stands for guest ions: Li^+, Na^+ or K^+; MX_2 stands for the host structure.

b) Alloy/de-alloy materials, e.g. Silicon, Germanium, Tin, Antimony, Aluminum, Bismuth, and tin oxide, etc. exhibit an electrochemical process, which can be described as: $H + xG^+ + xe^- \rightleftharpoons G_xH$, where G is a guest ion (Li^+, Na^+, or K^+), and H is the host structure.

c) Conversion materials are compounds like transition metal oxides (Fe_2O_3, Fe_3O_4, Mn_xO_y, NiO, Fe_xO_y, Cu_2O/CuO, Cr_2O_3, RuO_2, and MoO_2/MoO_3, etc.), metal sulfides, metal phosphides, and metal nitrides (M_xX_y; here X=S, P, N). Theoretically, the related electrochemical process can be described as: $M_aX_b + xG^+ + xe^- \rightleftharpoons \mathrm{b}\, G_{x/b}Y + \mathrm{a}\, M$, where M represents transition metal, X represents O, S, F, N, and P, etc.

1.5.1 Intercalation/de-intercalation materials

1.5.1.1 Carbonaceous materials

Carbonaceous materials with various morphologies were investigated as potential anode materials owing to abundant resources, impressive electrical (~10^{-4} S/cm), and thermal (~3000 W/mK) conductivity, renewability, and cost-effectiveness.

Graphite is used as anode material for commercial LIBs, where lithium reversibly inserts into graphite with the formation of LiC_6 (the final state for maximum Li intercalation, heoretical capacity of 372 mAh g^{-1}).[39] However, graphite is not suitable anode material for NIBs as sodium ions cannot be intercalated into graphite because of the lack of stable Na-C compounds due to energetical reasons.[14] The promising candidate anode material for NIBs is nongraphitic carbon, such as hard carbon and soft carbon.[40,41] Additionally, potassium intercalation into graphite formes KC_x.

1.5.1.2 Titanium-based oxides

Titanium-based oxides are considered as another important type of intercalation/de-intercalation anode materials for LIBs, NIBs, and KIBs. This kind of material shows interesting features such as reasonable operating voltage, inexpensiveness, low volume change (2-3 %), and environmental friendliness. TiO_2 was widely used as intercalation anode materials for LIBs and NIBs.[42] In addition, layered sodium-titanate ($Na_2Ti_3O_7$) compounds are also investigated as intercalation anode materials for NIBs. Potassium tetratitanate ($K_2Ti_4O_9$) as an analogue of the previously mentioned compounds was successfully examined as an intercalation anode materials for KIBs by Kishore *et al.*[22,43]

1.5.2 Alloy/de-alloy materials

Materials based on alloying reactions of alkali metals (Li^+, Na^+, or K^+) with other elements deliver high-capacities when applied as anodes in LIBs, NIBs, and KIBs. **Figure 1.3a** shows which elements alloy with lithium, sodium, or potassium. Similar to Li and Na, K can alloy with some elements like Si, P, Sn, Sb, Ge, and Pb. In this thesis, “alloys” and “intermetallic compounds” are not distinguished, although they are essentially different classes of compounds. Among them, Sb is attractive due to its low-cost and its ability to alloy up to compositions of Li_3Sb (or Na_3Sb) with a high specific capacity of 660 mAh g^{-1}. Similar alloy reactions with K result in the K-Sb system, meaning that Sb can be applied as a potential anode material in KIBs. Furthermore, Sn is promising due to its ability to alloy with Li forming $Li_{4.4}Sn$ (theoretical capacities of 991 mAh g^{-1}) and with Na forming $Na_{15}Sn_4$ (theoretical capacities of 845 mAh g^{-1}), respectively. Based on density functional theory (DFT) calculations, Kim *et al.*[17] observed two general trends for alloying reactions of K and Na with Si, P, Ge, Sn, Sb, and Pb (**Figure 1.3b**). Firstly, the amount of sodium that can be alloyed is higher than or equal to that of potassium; therefore, the capacities of the Na-alloying anodes are generally expected to be higher than those of their potassium counterparts. Secondly, the average voltage for sodium is lower than that for potassium for almost all of the alloying reactions, except for the reactions of P and Sb. Additionally, The volume expansion for the potassium system is substantially larger than that for the sodium system due to the larger ionic size of K (**Figure 1.3c**).

The major drawbacks of anode materials based on alloy reactions are the poor cycle life due to immense volume changes during ion-insertion/extraction. Another issue is the large irreversible capacity of the initial cycles. Several strategies have been developed: 1) the downsizing from micro to nanoscale particle size, like nanoparticles, nanowires, and nanosheets, etc.; 2) binary alloy materials such as NiSb, Sn_5SbP_3, CoP, FeP, and Sn_4P_3, etc; 3) carbon materials are introduced to enhance the electronic conductivity; 4) porous or hollow structures; 5) core-shell or yolk-shell structures; 6) optimized electrolytes, additives, and binders.[14]

1.5.3 Conversion materials

Conversion materials were regarded as promising anode materials for alkali-ion batteries due to their high theoretical capacities and redox reversibility. In general, conversion type materials are based on the transition metal compounds like oxides, phosphides, sulphides, and nitrides (M_xN_y; M=Fe, Co, Cu, Mn, and Ni; N=O, P, S, and N).[37] In contrast to intercalation materials, in which metal atoms are reversibly inserted/extracted into/from a host lattice, conversion reactions involve the chemical transformation process and the formation of new compounds.[22] Similar to alloying materials, conversion anodes also suffer from material pulverization, the formation of unstable SEI layers, and morphological changes and volume expansion. The main disadvantage of conversion type materials is the large volume expansion during electrochemical cycling, leading to structural damage of the electrode, a large voltage hysteresis, and fast capacity fading. Additionally, it is found that the theoretical capacity of conversion materials is higher than the practical one, which is due to the sluggish mobility of large Na^+ and K^+-ions.[44] To cope with the abovementioned limits, several studies have been focused on developing new methods such as nanostructured materials;[14] carbon coatings or carbon-based composites; designing mesoporous structures; fabrication of core-shell and yolk-shell structures.

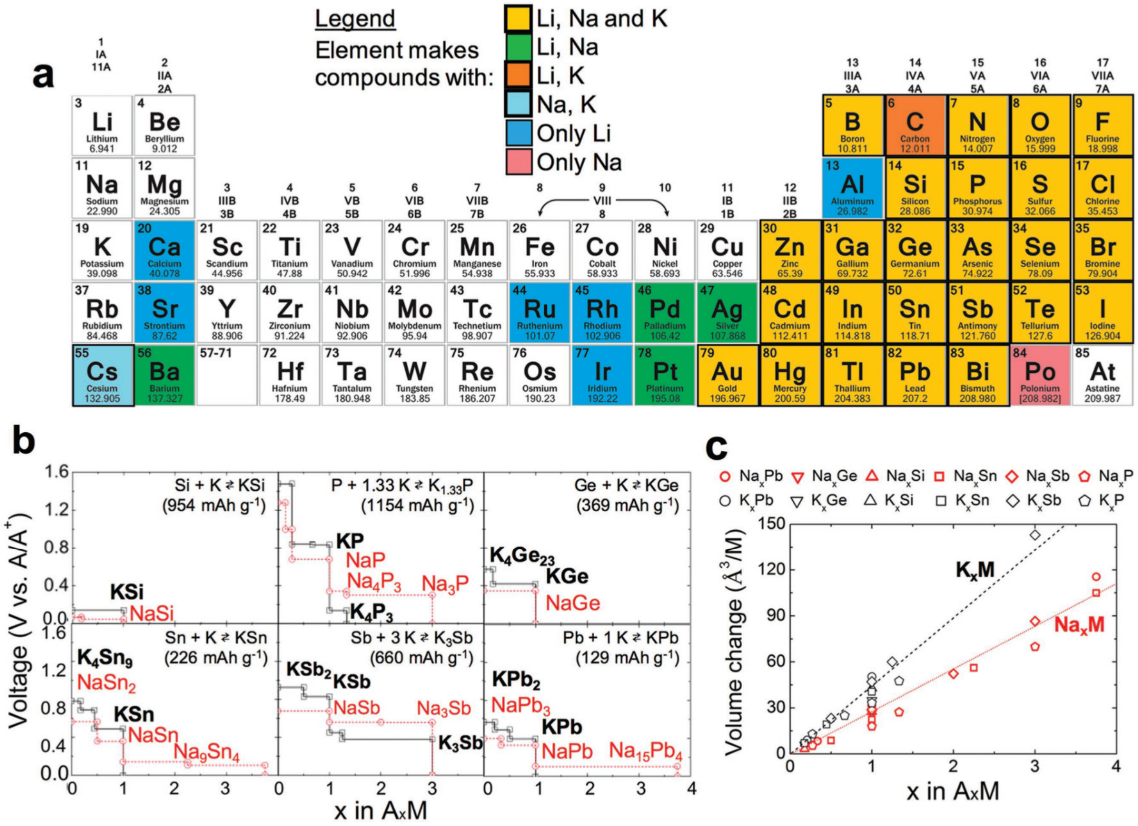

Figure 1.3 (a) Periodic table displaying the elements that alloy with Li, Na, and K; (b) Voltage-composition curves calculated for alloying reactions; (c) Volume changes upon alloying alkali metals with different metals as a function of x in A_xM.[17]

2 *In operando* Synchrotron Radiation Diffraction and *in operando* X-ray Absorption Spectroscopy

2.1 Introduction

Further development of the rechargeable alkali-metal-ion batteries (LIBs and beyond-LIBs) requires a better understanding of the electrodes electrochemistry in various battery technologies. The synchrotron X-ray technique is one of the most effective methods, which is capable of probing materials characteristics like electronic and geometric structures nearly non-destructive with different depth sensitivities via scattering, spectroscopy, and imaging capabilities.[45] Synchrotron sources are featured with high power and flux, which are ideally suited for rapid *in operando* studies. Materials can be investigated in the real environment and crystal structural information can be gained in a few seconds.[46,47] The combination of X-ray based analytical technique tools (imaging, spectroscopy, and scattering) and their applications such as *in situ*, *ex-situ*, and *in operando* is crucial to gain fundamental insights into battery materials. In this thesis, *in situ* stands for in position, while *in operando* means that the battery is in operation.

X-ray sources can be divided into hard and soft X-ray sources according to the different photon energy ranges. The photon energy of hard X-rays is 5 keV for the lower limit and no upper limit, while that of soft X-rays ranges 0.09-2.5 keV. Hard X-ray techniques have a deep penetration depth of microns and millimeters ranges (depends on the specific materials) and are applied for *in operando* experiments to characterize the bulk lattice and electronic structures. Soft X-rays are widely employed for chemical analysis at surfaces.[45]

Synchrotron X-ray absorption spectroscopy (XAS) is a powerful tool for studying the local structure of materials and the oxidation state of specific elements in a given material. The full XAS spectra are featured with two main regions: the X-ray near-edge structure spectroscopy (XANES) and the extended X-ray absorption fine structure (EXAFS). Both regions provide very specific information. The XANES region contains information about the oxidation state and the local geometric and electronic structure information, whereas EXAFS can offer further local structure information around the central atom. While XRD is used in a long-range ordering of the material and short-range order of the materials (pair-distribution functions), which leads to difficulties when characterizing different elements with similar X-ray scattering cross-sections. XAS techniques can differentiate those elements and deliver useful information like coordination numbers, bond length, and oxidation states for materials in gas, liquid, or solid states.[48] XAS is considered as the complementary nature of the XRD, and it is widely applied in structural studies for rechargeable battery materials.[49,50] Brookhaven National Laboratory first performed *in situ* XAS studies to probe the nickel oxidation state for nickel-metal hydride batteries in a plate-like cell.[51] In general, *in operando* XAS experiments were carried out at synchrotron light sources by using transmission or fluorescence detection modes. In transmission mode, the cell is put between the I_0 and I_t detection chambers. The absorption coefficient μ of the material can be examined by Bouguer-Lambert-Beer law:

$$I_t = I_0 \exp(-\mu x) \qquad (2.1)$$

Where I_0 and I_t present the intensity of the incoming and outgoing X-ray beam, μ is the absorption coefficient, and x is the thickness of the material. In the fluorescence mode, the sample is placed by ∼45 ° corresponding to the incident X-ray beam, and the detector is located at the right angle to the incident beam to collect the fluorescence X-rays.

2.2 *In operando* setup device

2.2.1 *In operando* coin cell holder

In operando characterization of complex electrochemical phenomena that can occur during charge and discharge of a battery requires cell housings with a well-defined electrolyte volume, chemically inert materials, airtightness, and low background contributions to the scattered intensity. *In operando* synchrotron powder diffraction is considered as one of the most powerful methods for the characterization of battery materials as several structural parameters can be investigated with respect to the state of charge.[52] Herein, we present a new compact *in operando* coin cell holder, which allows a facile and a fast coin cell mounting and reliable *in operando* experiments with up to eight simultaneously or individually measured samples. The setup operates in transmission mode for *in operando* measurements.[52]

Figure 2.1 shows the *in operando* coin cell holder design developed by our team.[52] The holder is composed of two main parts: a coin cell holder and a printed circuit board (PCB). The coin cell holder is made of an insulating rigid material like polyoxymethylene (POM). The coin cells are installed in concentrically arranged slots with a diameter of 20.6 mm and a depth of 5.0 mm. A helical spring (diameter of 9.5 mm) is positioned within a hole, which keeps the

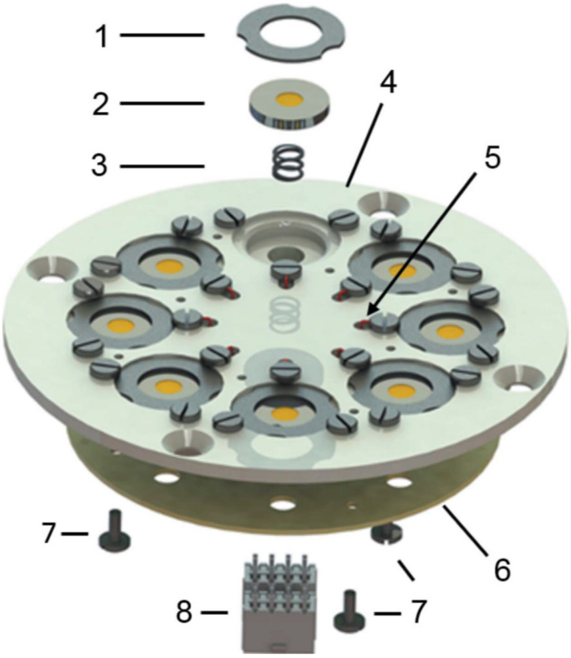

Figure 2.1 *In operando* coin cells holder: (1) metallic cap; (2) *in operando* coin cell with Kapton windows; (3) metallic helical spring; (4) nonconductive sample holder, e.g. made of POM; (5) wire to connect metallic cap with PCB; (6) PCB; (7) screws to fix PCB to sample holder; (8) 2 x MOLEX eight-pole connector.[52]

electrical contact of coin cells with certain positioning. This device is available for the investigation of common coin cells with different thicknesses like CR 2032 (thickness: 3.2 mm), CR 2025 (thickness: 2.5 mm), and CR 2016 (thickness: 1.6 mm). The metallic caps, which are connected to a rearward mounted PCB by a screw and a wire are used for electrical contact. The detailed conducting paths of the PCB are displayed in **Figure 2.2.** The detailed schematic drawing of the *in operando* coin cell and a cross-section of the coin cell holder are shown in **Figure 2.3**. All 16 poles conduct their electrical signals to the center. The potentiostat is connected with a flexible 16-wire cord attached to the center of the holder and two MOLEX eight-pole connectors. A concentric rotation of the holder is controlled by a stepper motor. With this design, disturbance of the beam path by the wiring is avoided.[52]

2.2.2 Setup at MSPD beamline of ALBA-CELLS and P65 beamline of DESY

In operando synchrotron diffraction with the transmission mode was carried out at the material science power diffraction (MSPD) beamline of ALBA in Barcelona, Spain. The detailed photographs of the setup adjusted to the beamline are shown in **Figure 2.4**. The holder

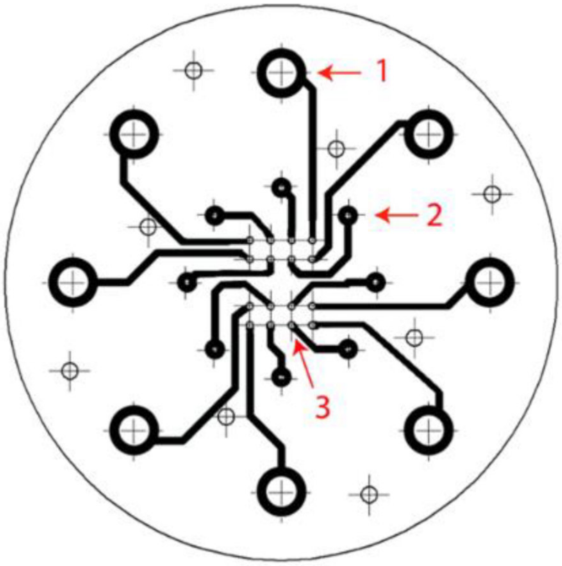

Figure 2.2 Detailed observation of the printed circuit board (PCB): 1: conducting pads for the helical spring (Figure 2.1, item 3); 2: conducting pads for the wire from metallic cap (Figure 2.1, item 1 and 5); 3: conducting pads for the MOLEX-connector (Figure 2.1, item 8).[52]

was installed onto a rotatable frame, which was realized by a stepper motor allowing a serial positioning and a successive measurement of each cell. A Mythen 6K detector is utilized to collect the diffraction data. The whole setup can concentric rock ±15 ° within the Eulerian cradle for reducing the effect of the preferred orientation of crystallites. In general, exposure times of 40 s per pattern leads to sufficient statistics in intensity. One whole round of measurement time is about 360 s, including the time for the sample change. In the case of a measurement with a high current/low current, the exposure time and the number of samples should be adjusted.

2.3 Overview of synchrotron light sources

Synchrotron radiation is based on classical electrodynamics. In a typical synchrotron facility, electrons are accelerated to a final energy of around 1.5-8 GeV and filled into a storage ring, close to the speed of light, and maintain a fixed energy in the storage ring. Electromagnetic radiation is produced when the electron bunches are accelerated by a magnetic field. Modern synchrotron facilities work with several types of magnetic structures to keep the focus of the electron orbits and to acquire X-ray radiation with different properties.

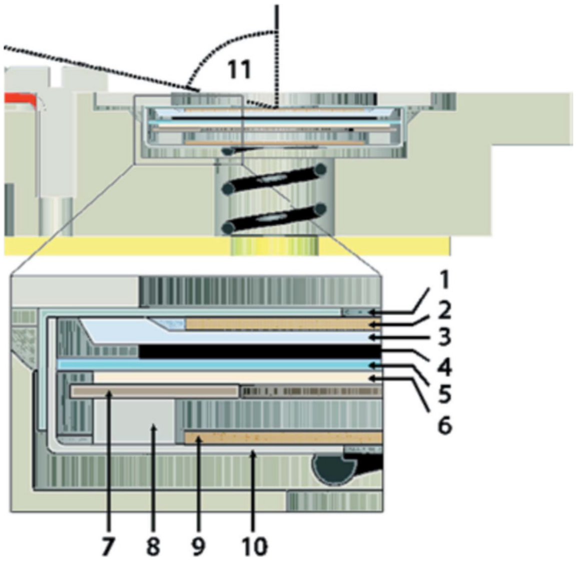

Figure 2.3 Schematic cross section of the holder with a detailed view of an *in operando* coin cell: (1) and (10) stainless steel coin cell housing with 4-5 mm hole; (2) and (9) Kapton foil/glass window (Ø: 8 mm); (3) and (4) current collector and active electrode (Ø: 12 mm); (5) separator with electrolyte (Ø: 17 mm); (6) lithium/sodium/potassium foil (Ø: 16 mm); (7) stainless steel spacer with 6 mm hole; (8) stainless steel wave spring; (11) maximum 2θ at 70°.

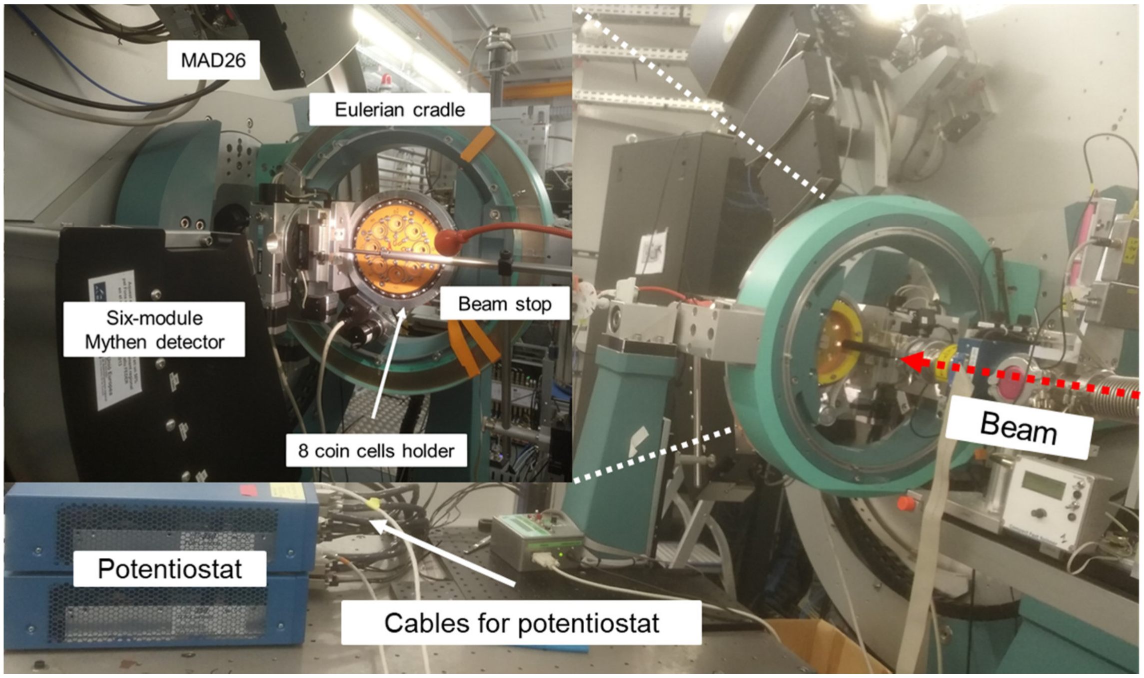

Figure 2.4 *In operando* coin cells holder installed at the MSPD beamline of the synchrotron light source ALBA-CELLS for transmission diffraction experiments.

PETRA III is the third generation synchrotron radiation in Deutsches Elektronen-Synchrotron (DESY), Hamburg, Germany. The storage ring was operated with a current of 100 mA and energy of 6 GeV. The expected photon beam performance is 10^{21} ph/(s mm^2 mrad^2 0.1% BW).[53] P65 is an X-ray Absorption Fine Structure (XAFS) spectroscopy beamline, which is part of the PETRA III extension project. Fine Structure (XAFS) spectroscopy beamline is part of the PETRA III extension project. It provides a millimeter-sized beam and a monochromatic photon flux of up to 10^{12} s^{-1} at 9 keV.[54] The optic design is based on a double crystal monochromator Si 311 and Si 111. Key parameters are a working range of 4 keV-44 keV, a monochromatic photon flux of up to 10^{12} s^{-1}, an energy resolution (Δ E/E) of 0.6 * 10^{-4} (Si 311), and 1.4*10^{-4} (Si 111).[54] The main fractions of the beamline optics of P65 are a stable water-cooled double-crystal monochromator (DCM) and pair of plane mirrors with several coatings and adjustable incidence angle for higher harmonics suppression.[55] **Figure 2.5** gives an overview of the *in operando* XAS instrument at the 65 beamline at PETRA III in DESY.

The Swiss Light Source (SLS) at the Paul Scherrer Institut (PSI) is the 3rd generation synchrotron light source. With an energy of 2.4 GeV, it provides photon beams of high brightness for research in materials science, biology, and chemistry. The material science beamline was operated since 2001 and, can provide experiments in powder diffraction, surface diffraction, and computed tomography with hard X-rays in the energy range 5-40 keV.[56] The material science is powered by a short-period (14 mm) in-vacuum, cryogenically cooled, permanent-magnet undulator, (CPMU, U14), while the front end and optics are designed to optimally exploit the characteristics of the U14 source.

The MSPD beamline is one of the ALBA-CELLS synchrotron facilities. This beamline is focused on powder diffraction techniques and is composed of two experimental stations positioned in series: a High Pressure/Microdiffraction station and a High Resolution/High Throughput powder diffraction station. The X-ray flux intensity for the MSPD beamline was performed in an energy spectrum range from 8 to 50 keV.[57]

The ALBA-CELLS synchrotron located in Cerdanyola del Vallès, Barcelona is the 3rd generation synchrotron light facility. The first official users started in May 2012. The ALBA-CELLS synchrotron operates 7 beamlines including soft X-ray energies (Microscopy, X-Ray Microscopy, Resonant Absorption Scattering, and Photoemission Spectroscopy) and hard X-

Ray energies (Macromolecular Crystallography, Absorption and Emission, Spectroscopy Non-Crystalline Diffraction, and Powder Diffraction). The machine contains a 268 m circumference storage ring with electrons accelerated to 3 GeV and with small emittance (4.8 nm rad).

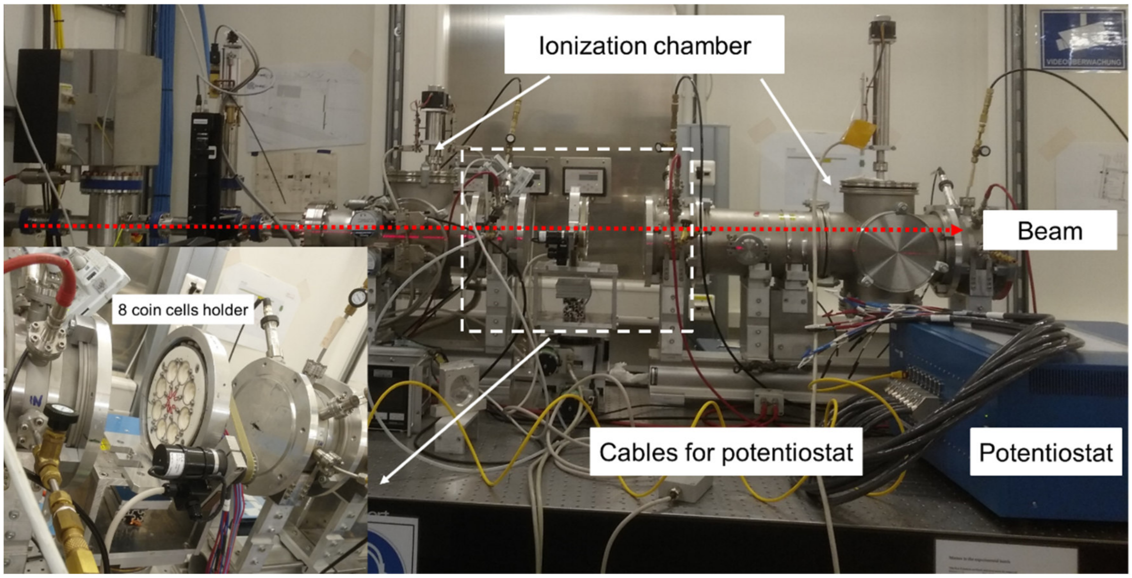

Figure 2.5 Overview of the *in operando* XAS instrument at the 65 beamline at PETRA III in DESY.

3 State-of-The-Art Literature and Aim of This Thesis

As mentioned in the introduction, growing research efforts have been devoted to the development of advanced anode materials with a high output voltage and a high capacity. Many strategies including nanostructured design (e.g. bubble-nanorod-structure,[58,59] bamboo-like structures,[60] nanofibers,[61] and nanowires[62]), the use of a conductive matrix (such as graphene,[63] carbon nanotubes (CNTs),[37] and reduced graphene oxide (rGO)[64]), and heteroatom doping (e.g. by N, B, S, and P) are applied.[65,66] Those strategies play critical roles in many aspects, for example, controlling the interfacial reactions, tolerating volume expansion, maintaining electronic structures, and avoiding excessive side reactions. Furthermore, an in-depth understanding of the underlying relation between Li^+/Na^+/K^+-ion storage mechanisms and the electrochemical behavior is important to improve the performance of rechargeable batteries. However, according to the state-of-the-art-literature,[67–71] the research of understanding of the energy storage mechanism is still lacking or under debate. Therefore, this thesis focuses on the mechanism study of the Fe_2O_3@C, FeS-based electrode material for LIBs, and SnS_2-based electrodes for NIBs and KIBS through *in operando* synchrotron radiation diffraction and XAS. Additionally, the structural design together with strategies to create appropriate carbon matrices are proposed to achieve high-performance rechargeable electrode materials. A detailed and comprehensive understanding of the structure-function-property relationship of these compounds is provided. Furthermore, the influence of the carbon matrix, the electrolyte additive of FEC, electrolytes with different Li-salts, and different carbon additives (Super P and C65) on electrochemical performance are exploited.

Fe_2O_3 is considered as one of the most promising candidates for LIBs due to its high theoretical capacity of 1007 mAh g^{-1}, the relatively low cost, and low toxicity. Many research works were done to overcome the common problem of drastic volume expansion and the large hysteresis in the electrochemical reaction.[72–76] But there is a lack of understanding of the Li-ion storage mechanism in general in Fe_2O_3 materials. Additionally, Dahbi *et al.*[77] demonstrated that 1 M LiTFSI in EC/DMC is higher ionic conductivity than 1 M $LiPF_6$ in the same binary solvent by using Walden rule. The difference of the Li-salts was not investigated in the case of conversion materials. Therefore, this research aims to gain a comprehensive understanding of the lithium-ion storage mechanism in Fe_2O_3@C electrode by using *in operando* synchrotron radiation diffraction and *in operando* XAS. The influence of different Li-salts in EC/DMC solvents is explored.

FeS-based anode materials also attracted the attention of researchers due to enhanced reaction kinetics and decrease the over-potential for lithium storage compared with iron oxides. This is because metal-sulfur bonds in sulfides conversion materials are more easily broken/formed during lithiation/de-lithiation processes. FeS nanosheets and $Fe_{1-x}S/C$ nanocomposites consisting of well-dispersed FeS and Fe_3C nanoparticles and interconnected carbon spheres via a facile hydrothermal method and a subsequent sintering process. According to the state-of-art literature, many efforts have been taken to improve the cycling performance and rate capabilities of the FeS-based electrode. For example, Xu *et al*.[78] prepared carbon-coated FeS nanosheets via surfactant-assisted solution-based synthesis; Su *et al*.[79] presented a core-shell $Fe@Fe_3C/C$ composite and attributed the observed extra capacity beyond the carbon component to reversible redox reactions of some SEI components. However, the mechanism of lithium storage into such FeS-based electrode materials during lithiation and de-lithiation processes is still under debate. McMillan and co-workers claimed that no intermediate Li_2FeS_2 was observed by applying Fe Mössbauer spectroscopy.[68] In contrast, previous research works reported the reduction of $Fe_{1-x}S$ to form the intermediate product of Li_2FeS_2.[69–71] However, there is no evidence for the formation of the intermediate Li_2FeS_2 phase and the conversion reaction of $Li_2FeS_2 + 2Li^+ + 2e^- \rightarrow Fe^0 + 2Li_2S$. Therefore, this study focuses on the fundamental understanding of the crystalline structure changes by observing phase transitions based on *in operando* synchrotron radiation diffraction. Meanwhile, the changes of the local environment and electronic transitions at the Fe K-edge XAS during the first lithiation process are tracked through *in operando* XAS. Moreover, a comprehensive and in-depth investigation into the effect of the interconnected carbon spheres-FeS property relationship is explored. Additionally, *ex-situ* scanning electron microscopy (*ex-situ* SEM) is employed to observe the morphology variation of the cycled electrodes. Furthermore, the charge transfer kinetics and resistive contributions of the $Fe_{1-x}S/C$ electrode at some selected potentials during the 1st cycling and long-term cycling are investigated via electrochemical impedance spectroscopy (EIS).

Currently, although the LIBs have successfully commercialized in the past two decades, they face the hard truth that low abundance and uneven geographical distribution of lithium.[80] For this reason, it is urgent to research and develop alternative battery systems. NIBs and KIBs have been receiving much attention due to the more abundance of sodium and potassium and low cost. NIBs have been well investigated in the latest years with achieving practical progress. However, the research of KIBs is still in the early stage.

According to state-of-the-art literature,[81–84] the assembly between nano-SnS_2 and carbon matrixes is mostly based on poor physical interconnection. The interfacial bonding between active particle and carbon matrixes is not very intimate and effective, which is difficult to keep the electrode integrity. Therefore, it is highly desirable to develop controllable and reliable strategies for the fabrication of novel nanostructured SnS_2/carbon matrix composites.

Herein a composite of porous few-layer SnS_2 nanosheets *in situ* grown on reduced graphene oxide (SnS_2-rGO) is produced to realize both high capacity and excellent cycling operation. This unique SnS_2-rGO will be described in section 6. The novel structure built from SnS_2 nanosheets is closely anchored on the surface of rGO sheets via a strong C-O-Sn bond. Therefore, the unique hybrid material is endowed with high electrochemical activity. A durable SnS_2-rGO electrode with a high specific capacity, superior rate capability, and stable cycling performance for NIBs and KIBs is presented. The structural evolution and phase transformation of the SnS_2-rGO electrode upon cycling are tracked by scanning electron microscopy (SEM). Meanwhile, the effects of different carbon composites (Super P and C65) and the influence of the electrolyte additive FEC on the electrochemical performance in NIBs and KIBs are demonstrated.

4 Understanding the Lithium Storage Mechanism in Core-Shell Fe_2O_3@C Hollow Nanospheres: *in operando* Synchrotron Study

4.1 Introduction

The results in this chapter are published in the following publication: **Chengping Li,** Angelina Sarapulova, Zijian Zhao, Qiang Fu, Vanessa Trouillet, Aleksandr Missiul, Edmund Welter, and Sonia Dsoke, Understanding the Lithium Storage Mechanism in Core-Shell Fe_2O_3@C Hollow Nanospheres Derived from Metal-Organic Frameworks: An *In operando* Synchrotron Radiation Diffraction and *in operando* X-ray Absorption Spectroscopy Study. Reproduced by permission of the American Chemical Society, https://pubs.acs.org/doi/10.1021/acs.chemmater. 9b01504.

Chengping Li prepared the Fe_2O_3@C sample for material characterization and electrochemical performance measurements. A. Sarapulova provided support with the XRD Rietveld refinement and XAS analysis. Z. Zhao, and Q. Fu made the same available and participated in the discussion. V. Trouillet conducted XPS measurement and analysis data. All synchrotron experiments (synchrotron radiation diffraction and XAS) were prepared, carried out, and evaluated by Chengping Li. A. Missiul and E. Welter are beamline scientists, they provided techniques support and instrument adjustments. Prof. H Ehrenberg and S. Dsoke supervised the work and contributed to the completion of the manuscript. Chengping Li wrote the manuscript, all co-authors participated in discussion and manuscript revision. Prof. H Ehrenberg provided fruitful discussion and constructive suggestions.

The continuously increasing use of portable electronic devices such as laptops, mobile phones, and cameras requires the development of cheap, stable, and highly efficient electric energy conversion/storage systems[85,86] Metal-organic frameworks (MOFs) are used as a sacrificial material to fabricate hollow Fe_2O_3 nanospheres as the core, which are coated by a carbon layer as the shell. This research aims to gain a comprehensive understanding of the lithium-ion storage mechanism in the Fe_2O_3@C electrode by using *in operando* synchrotron radiation diffraction and *in operando* XAS. Furthermore, the electrochemical performance in different Li-salt (LP30 and LiTFSI) is investigated.

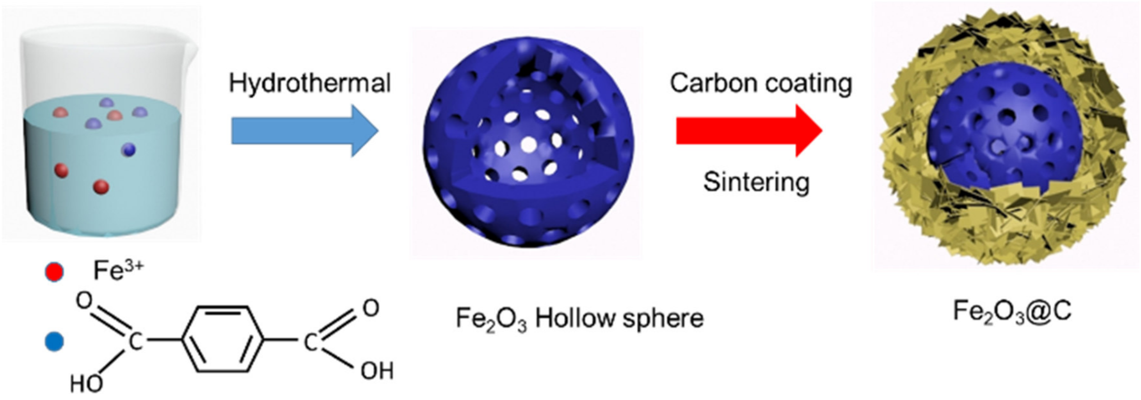

Schematic 4.1 Schematic illustration of the synthesis process of core-shell Fe_2O_3@C composite material derived from metal-organic frameworks (MOFs).

4.2 Experimental

***Synthesis of Fe_2O_3 precursor*:** The Fe_2O_3 precursor was fabricated through hydrothermal reaction.[87] In detail, 0.76 g iron chloride hexahydrate ($FeCl_3·6H_2O$, Alfa Aesar, 99%), 1.51 g sodium citrate dihydrate ($Na_3C_6H_5O_7$, Aldrich, 99%), and 0.275 g urea (CH_4N_2O, Aldrich, 98%), were dissolved in 40 ml deionized water, followed by the addition of 0.4 g polyacrylamide ($(C_3H_5NO)n$, Sigma). The mixture solution turns in a light yellow after 90 minutes of continuous stirring. The obtained solution was then transferred into a 50 ml Teflon-lined autoclave at 180 °C for 12 h. The black Fe_2O_3 product, obtained after cooling down the temperature, was washed with deionized water and ethanol several times and finally dried at 60 °C.

***Synthesis of Fe_2O_3 hollow nanospheres**:* 0.25 g of Fe_2O_3 precursor was dispersed in 30 ml ethanol solution, then $FeCl_3·6H_2O$ ethanol solution (5 ml, 0.1 M) and terephthalic acid ($C_8H_6O_4$, Aldrich, 98%) ethanol solution (5 ml, 0.1 M) was added into the above solution. This mixture was held at 70 °C for 30 mins. Finally, the products were harvested through serval rinse-precipitation cycles with ethanol and dried at 60 °C over-night.

Synthesis of core-shell Fe_2O_3@C nanospheres: 0.2 g of the as-prepared Fe_2O_3 hollow spheres were added into the 40 ml glucose ($C_6H_{12}O_6$, Sigma, 99.5%) solution (0.5 M) with continuous stirring to form a homogenous solution, then transferred to 50 ml Teflon-sealed autoclave and kept 180 °C for 12 h. The product was washed with deionized water and absolute ethanol three times and dried at 60 °C. Finally, the Fe_2O_3@C product was subjected to temperature increase by 10 °C min^{-1} under Argon flow until the temperature reached 450 °C and kept in this condition for 5 h.

Material characterization: X-ray diffraction (XRD) was measured by using synchrotron radiation (λ=0.41311 Å) with Powder Diffraction Beam Line at Barcelona, Spain. The morphology of the product was observed with a thermal field emission scanning electron microscopy (FESEM, Carl Zeiss SMT AG). The element distribution was investigated through energy dispersive spectroscopy (EDS, Quantax 400 SDD, Bruker).[88] Transmission electron microscopy (TEM) and high-resolution transmission electron microscopy (HR-TEM) of the samples were performed with a JEOL JEM-2010 working at 200 kV. The Fourier Transform infrared spectroscopy of the sample was characterized by using Themo Nicolet 670 FT-IR. Thermogravimetric analysis (TGA) was obtained with the thermogravimetric analyzer (Netzsch Gmbh STA 449 C), in which the sample was heated in Argon flow at 10 °C min^{-1} from 35 °C to 800 °C. Raman spectra were tested on LabRam Evolution HR in Via Raman spectroscopy with a laser wavelength of 532 nm (LabRam Evolution HR, HORIBA Jobin Yvon). X-ray photoelectron spectroscopy (XPS) measurements were carried out using a K-Alpha^{+} XPS spectrometer (Thermo-Fisher Scientic, East Grinstead, UK). Data acquisition and processing using the Themo Avantage software is described elsewhere.[89]

Electrochemical characterization: The electrochemical experiments were performed on three-electrode Swagelok-type cells. The working electrode was fabricated by mixing the active material, carbon black (Super P, Timcal Ltd.,) and sodium alginate (3% sodium-alginate in deionized water: isopropanol=9:1 as solvents) with the weight ratio of 7: 2: 1. The slurry was mechanically stirred for 12 h and coated on copper foil. Circular electrodes with the diameter of 12 mm were punched out and dried at 80 °C in a vacuum oven for 24 h. The average thickness and mass loading of active materials were 25 μm and 2.0 mg cm^{-2}, respectively. In three-electrode Swagelok-type cells, the metallic lithium was used as the reference electrode and the counter electrode. LP30 (1 M $LiPF_6$ in EC: DMC=1:1, BASF, Germany) and LiTFSI (1 M Lithium bis (trifluoromethane sulfonyl) imide in EC: DMC=1:1) were used as electrolytes. EIS was performed by using a three-electrode Swagelok-type cell with electrodes having 7 mm of diameter. The position of the reference electrode is located between the working electrode and Li counter electrode. The cells were assembled in an argon-filled glovebox (MBraun) and then placed in a climate chamber (Binder) at 25° C for the electrochemical experiments.

CV, GCPL, and EIS were performed using a multichannel potentiostat (VMP3, Bio-Logic). CV was recorded in the voltage range of 0.01-3.0 V *vs.* Li^+/Li at the scan rates of 0.05, 0.1, 0.2, 0.5, 1, 2, 5, and 10 mV s^{-1}. GCPL measurements were conducted at current densities of 100, 200, 500, 1000, 2000, and 4000 mA g^{-1} between 0.01 and 3.0 V *vs.* Li^+/Li. Long-time cycling performance was performed at 200 mA g^{-1} for 200 cycles. EIS experiments were conducted with frequencies range from 10 mHz to 500 kHz at various selected potentials during the first lithiation/de-lithiation processes. The electrode was equilibrated at the desired potential for 3 h before recording the EIS. The impedance spectra were analyzed using Relaxis 3 software (rhd Instruments, Germany). *In operando* synchrotron radiation diffraction was performed at MSPD at ALBA synchrotron and German Electron Synchrotron in Hamburg (DESY). *In operando* synchrotron radiation diffraction and XAS were measured using CR 2025 *in operando* coin-cell with a glass and Kapton window. The admixture was pressed on the center of Cu mesh with a diameter of 12 mm. Silicon and LaB_6 were used as standard samples for calibration. The Rietveld refinement was applied to analyze the phase composition and purity of samples. The *in operando* XAS measurements were conducted on the P65 beamline of DESY. The XAS spectra were collected in the quick-XAS mode in fluorescence geometry using a PIPS diode. The DEMETER software package was employed to analyze the XAS spectra.[90]

4.3 Results and discussion

4.3.1 Structural, morphological, and chemical characterization of Fe_2O_3@C composite material

The crystallographic structure was characterized by synchrotron radiation diffraction, as shown in **Figure 4.1**. All the XRD patterns in the product can be indexed to the two different phases of Fe_2O_3 with the space group of (maghemite) $Fd\bar{3}m$ and (hematite) $R\bar{3}c$, which partially share the same peak positions, this means the same diffraction angles for the Bragg reflections. The refined phase fractions of (maghemite) $Fd\bar{3}m$ and (hematite) $R\bar{3}c$ are 73 % and 27 %, respectively. The relative lattice parameters are: $a=b=c=8.398 \pm 0.002$ Å (ICSD: 247034) and $a=b=5.032 \pm 0.002$ Å, $c=12.496 \pm 0.002$ Å (ICSD: 15840), respectively. The Fe_2O_3@C material shows two different phase transformation processes during *in operando* synchrotron radiation diffraction experiment (**Figure 4.6**), which reasonably explains that the $Fd\bar{3}m$ and $R\bar{3}c$ phases coexist in Fe_2O_3@C.

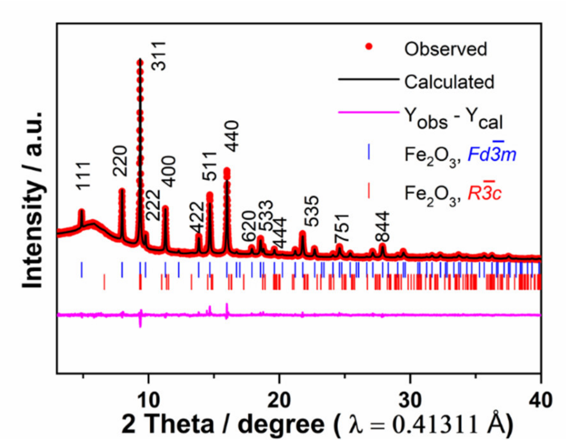

Figure 4.1 Rietveld refinement based on synchrotron diffraction data of Fe_2O_3@C.

The morphology and microstructure of Fe_2O_3 precursor, Fe_2O_3 hollow nanospheres, and Fe_2O_3@C were characterized by SEM and TEM. The SEM images of the Fe_2O_3 precursor (**Figure 4.2a**) and Fe_2O_3 hollow nanospheres (**Figure 4.2b**) show a homogeneous spherical shape with an average size of 200 nm. It is clear that the prepared Fe_2O_3 hollow nanospheres keep the original morphology of Fe_2O_3, while the Fe_2O_3@C final product has a typical core-shell structure (**Figure 4.2c**). The TEM images of Fe_2O_3 hollow nanospheres and Fe_2O_3@C are shown in **Figures 4.2d** and **e**. These images confirm that the Fe_2O_3 nanosphere has a hollow structure with a size of about 200-300 nm. One can observe that in the core-shell structure of Fe_2O_3@C the carbon coating on the surface has a thickness of 30-40 nm. The inset picture in **Figure 4.2e** shows the diffraction rings of 220, 311, and 111. An enlarged high-resolution TEM (HR-TEM) image of the Fe_2O_3@C is presented in **Figure 4.2f**. The measured distance spacing is 0.256 nm, corresponding to the 311 lattice plane of Fe_2O_3.[87] Clearly, Fe_2O_3 nanospheres are wrapped by carbon layers. **Figure 4.2g**, **h**, and **i** present the EDS of Fe_2O_3@C, which show that the elements of Fe, O, and C are homogeneously distributed.

The Raman spectra of the Fe_2O_3 precursor and Fe_2O_3@C are presented in **Figure 4.3a**. The peaks located at 222 cm^{-1}, 280 cm^{-1}, and 393 cm^{-1} are assigned to the A_{1g} and two E_g modes of Fe_2O_3.[91] The Raman spectrum of the Fe_2O_3@C displays typical peaks of the D and G bands at 1311 cm^{-1} and 1581 cm^{-1}, respectively. There is no clear G-band in the Fe_2O_3 precursor. The D-band corresponds to the disordered structure of sp^3 carbon (C-C), while the G-band corresponds to the ordered structure of sp^2 carbon bond stretching.[92] The carbon content and thermal stability of the Fe_2O_3@C were evaluated by TGA performed under Argon and shown in **Figure 4.3b**. The TGA curve shows that a dramatic weight loss takes place from 450 to 650

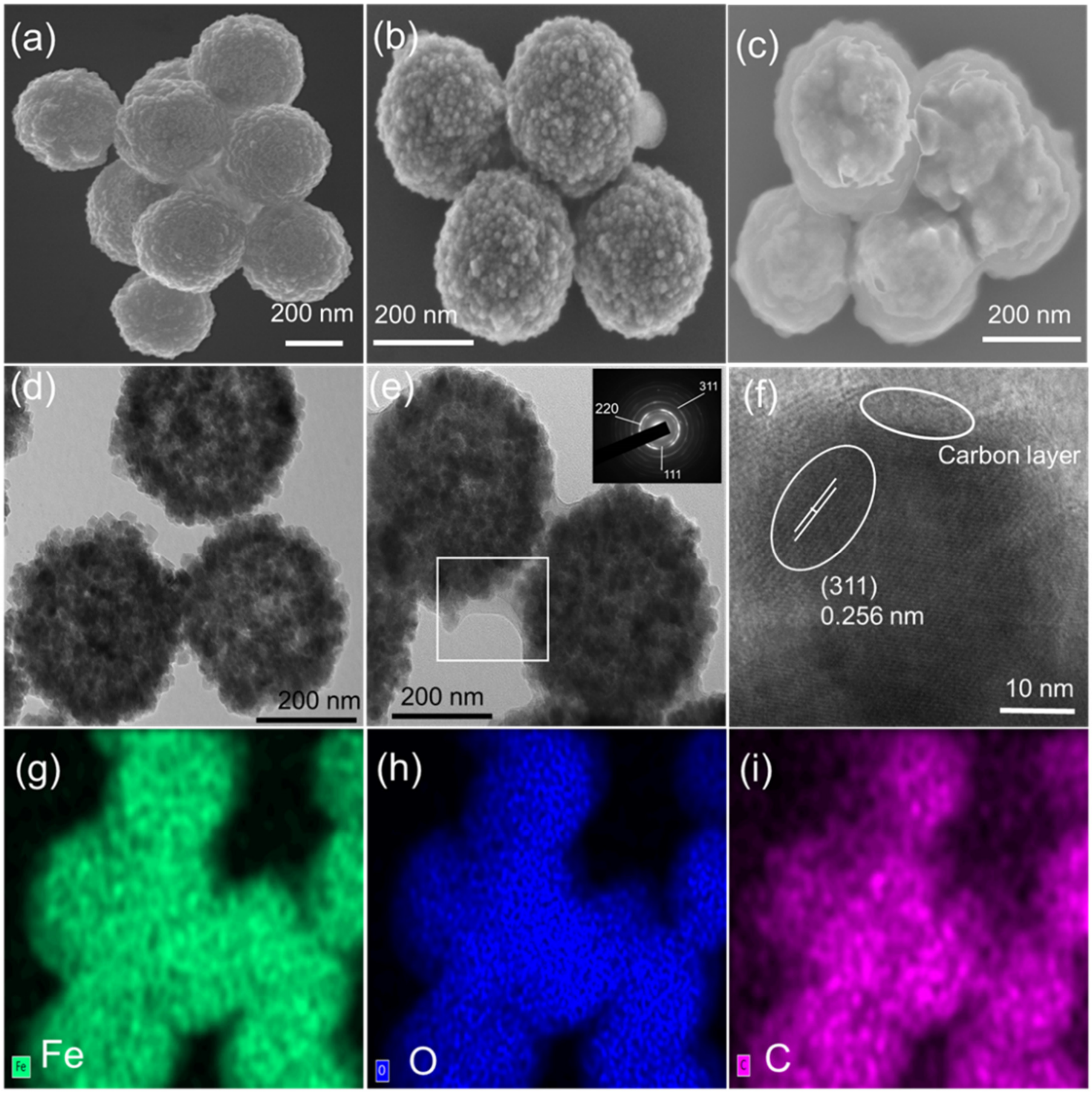

Figure 4.2 The SEM images of Fe_2O_3 precursor (a), Fe_2O_3 hollow nanospheres (b) and Fe_2O_3@C (c), the TEM images of Fe_2O_3 hollow nanospheres (d) and Fe_2O_3@C (e) and the inset picture displays the diffraction rings. The HR-TEM (f) of the Fe_2O_3@C. The EDS (g-i) of Fe, O, and C on Fe_2O_3@C.

°C due to carbon combustion. The TGA reveals that the material is composed of 70 wt% Fe_2O_3 and 30 wt% carbon.

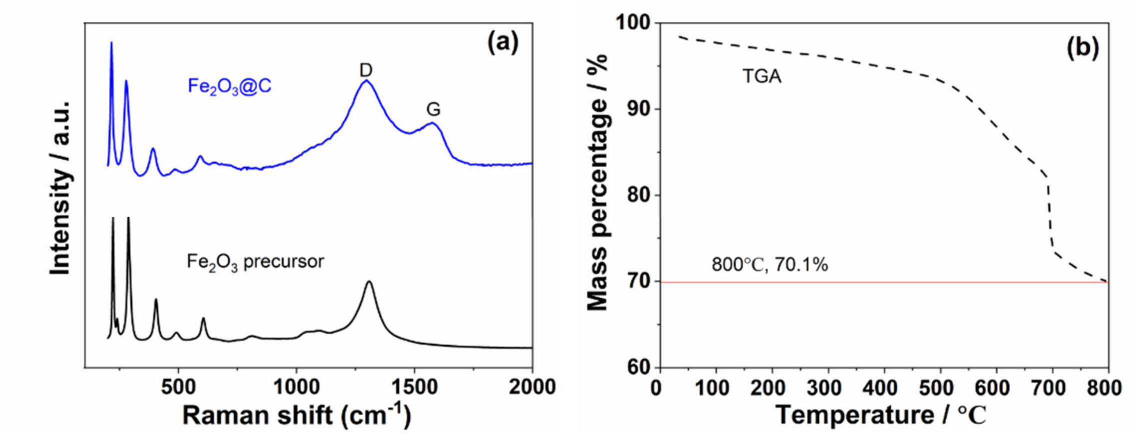

Figure 4.3 (a) The Raman spectra of the Fe_2O_3 precursor and Fe_2O_3@C and (b) TGA curve of the Fe_2O_3@C composite material.

Based on the above results it is possible to conclude the reaction mechanism occurring during the synthesis of Fe_2O_3@C. The reaction mechanism is depicted in **Scheme 4.1** and explained by the following formula:

$$CO(NH_2)_2 + H_2O \rightarrow CO_2 + 2NH_3 \qquad (4.1)$$

$$NH_3 + H_2O \rightarrow NH_3 \cdot H_2O \rightarrow NH_4^+ + OH^- \qquad (4.2)$$

$$2Fe^{3+} + 6OH^- \rightarrow 2Fe(OH)_3 \rightarrow Fe_2O_3 + 3H_2O \qquad (4.3)$$

During the hydrothermal process, when the temperature is higher than 100 °C, urea reacts with water and produces CO_2 and NH_3 (**Equation (4.1)**). Then, NH_3 combines with H_2O forming $NH_3 \cdot H_2O$, which further produces hydroxide ions (OH^-) (**Equation (4.2)**). Ferric-ions (Fe^{3+}) favor to complex with OH^- and precipitates into $Fe(OH)_3$. This compound finally dehydrates forming Fe_2O_3 (**Equation (4.3)**). The Fe_2O_3 precursor combines with terephthalic acid (H_2bdc) and forms the Fe_2O_3 hollow nanospheres. Finally, in the second consecutive hydrothermal and sintering steps, the generated carbon coats on the surface of Fe_2O_3.

To further analyze the composition of Fe_2O_3@C and the oxidation state of the different elements, X-ray photoelectron spectroscopy (XPS) was applied and Fe $2p_{3/2}$, O 1s, and C 1s spectra are shown in **Figure 4.4a-c**. According to Grosvenor *et al.*,[93] the spectrum can be well-fitted with a multiplet, observed in the case of Fe_2O_3. The presence of the typical additional satellite peak at ~719 eV confirms the presence of Fe (+3). The corresponding O 1s peak, stemming from the oxide, is found at 530.0 eV, since further contributions at 531.4 eV and

532.9 eV is attributed to C=O and C-O, respectively.[94] Furthermore, C 1s (**Figure 4.4c**) shows three different components: a main peak at 285.0 eV accompanied by two further ones at 286.3 eV and 288.7 eV, which are attributed to C-C, C-O, and O-C=O,[95] respectively. The presence of carbon, with a predominance of C-C form, confirms the successful hydrothermal reaction of the glucose. The carbon coating on the surface of Fe_2O_3 hollow nanospheres is also confirmed by TEM results (**Figure 4.2e and f**).

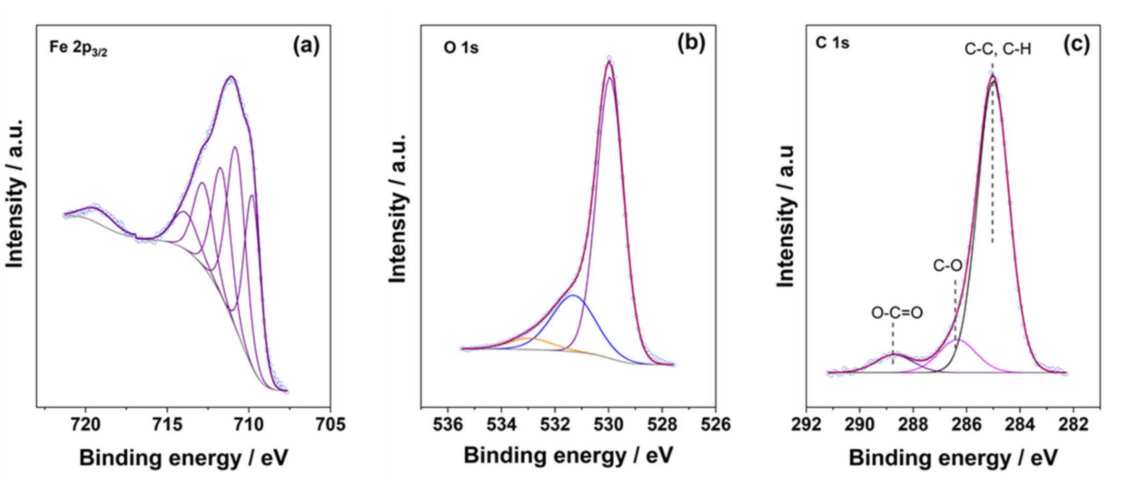

Figure 4.4 The high-resolution XPS spectra of Fe_2O_3@C composite materials in the (a) Fe $2p_{3/2}$, (b) O 1s, and (c) C 1s core-level regions.

4.3.2 *In operando* study: elucidation of the Li-storage mechanism in Fe_2O_3@C

The electrochemical reaction process in LIBs was firstly evaluated by CV. **Figure 4.5a** shows the first five CV plots of Fe_2O_3@C electrode recorded between 0.01 V and 3.0 V *vs.* Li^+/Li at the scan rate of 0.05 mV s^{-1} in LP30. In the first cathodic scan, three peaks centered at 1.68 V, 0.99 V, and 0.80 V can be clearly observed. The small peak at 1.68 V is assigned to the Li insertion into Fe_2O_3 to form $Li_xFe_2O_3$ (**Equation (4.4)** and **(4.5)**, which will be discussed in detail later). The minor shoulder located at 0.99 V corresponds to the phase transition ($Li_xFe_2O_3$, rhombohedral, $0 < x < 1 \rightarrow Li_xFe_2O_3$, cubic, $1 < x < 5$) accompanied by Li^+ insertion into Fe_2O_3 (**Equation (4.6)**). These intermediate products were evidenced and confirmed by *in operando* synchrotron radiation diffraction (**Figure 4.8a** and **b**). The strong reduction peak at 0.80 V is attributed to the reduction of Fe^{3+} to Fe^{2+} and finally to Fe and the simultaneous formation of the solid electrolyte interphase (SEI) layer.[96] At the end of the Li insertion process, 6 Li per formula unit are in total consumed and metallic Fe^0 and Li$_2$O are formed (**Equation (4.8)**). During the anodic scan, two broad peaks appear at 1.61 V and 1.84 V, which are due to the oxidation of Fe to Fe^{2+} and finally to Fe^{3+}, respectively.[97] The detailed electrochemical mechanism will be discussed later on the basis of *in operando* synchrotron radiation diffraction and *in operando* XAS (**Figure 4.6** and **4.7**). During the 2nd cycle, the strong cathodic peak shifts from 0.80 to 0.97 V, while the anodic peaks shift from 1.61 V and 1.84 V to 1.65 V and 1.93 V, respectively. All above mentioned changes in shape and peak positions implicate that the crystalline structure is restored together with the formation of amorphous Fe$_2$O$_3$.[98] What's more, the small cathodic peak located at 0.99 V disappears in the following cycles, which confirms the irreversible phase transformation.[99] From the 3rd to 5th cycle, the well-overlapped CV curves demonstrate the electrochemical stability of this material. In order to evaluate the influence of different lithium salts in the electrolyte, the CVs of the Fe$_2$O$_3$@C were also recorded in LiTFSI by using the same conditions (**Figure 4.5b**). In LiTFSI, the shape of the CV is similar to that observed in LP30. However, the strong reduction peak in the first cathodic scan appears at a lower potential (0.71 V), which could account for the different nature of the SEI formed in this electrolyte.

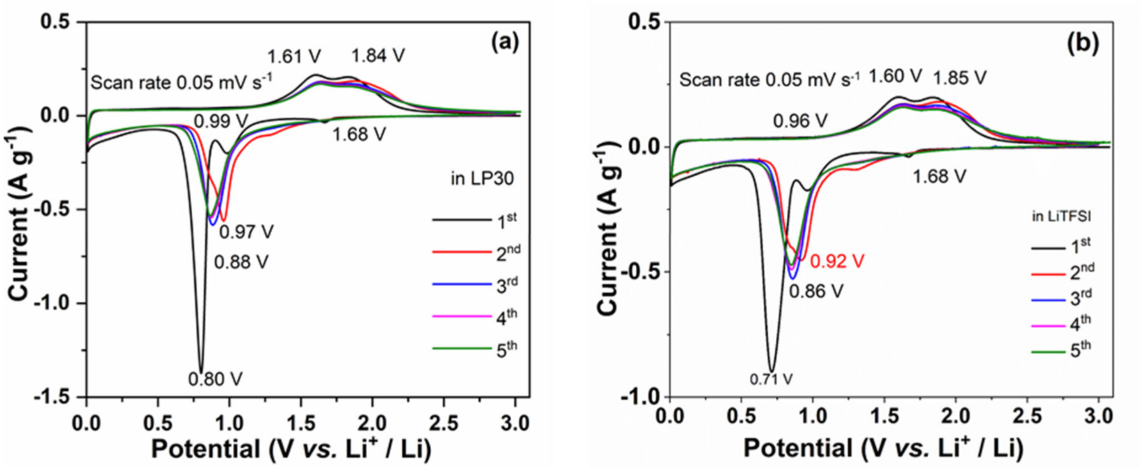

Figure 4.5 CV profiles of the 1st to 5th at 0.05 mV s^{-1} in LP30 (a) and LiTFSI (b).

To further investigate the lithium-ion storage mechanism in the Fe$_2$O$_3$@C electrode and to trace the changes of the crystalline phase, *in operando* synchrotron radiation diffraction was applied during the 1st lithiation/de-lithiation processes. The structural evolution and the corresponding galvanostatic profiles of the Fe$_2$O$_3$@C electrode during the 1st cycle in LP30

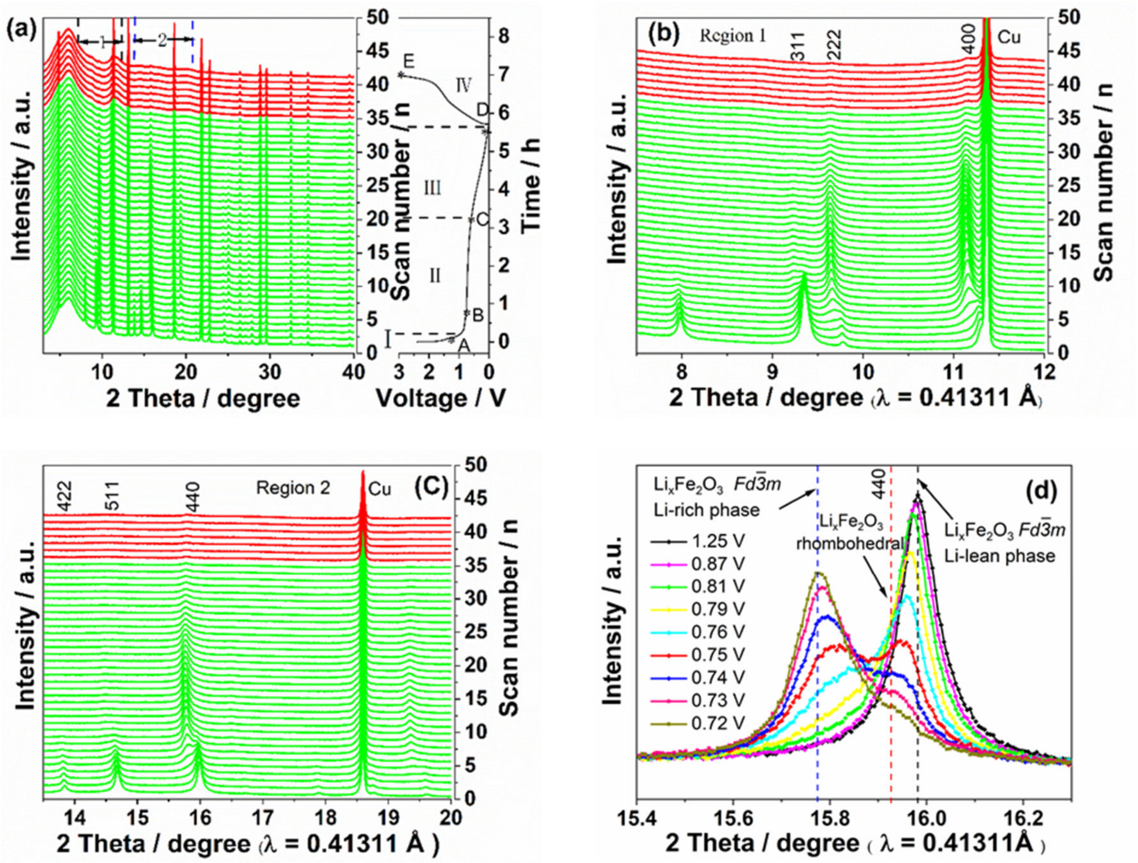

Figure 4.6 *In operando* synchrotron radiation diffraction patterns of Fe_2O_3@C electrode during the 1st lithiation and de-lithiation processes in LP30: (a) the structural evolution during the first lithiation/de-lithiation processes and relative potential profiles. The *in operando* synchrotron radiation diffraction patterns of the selected region 1 (b) and 2(c), (d) is the magnified 440 diffraction peak of the F-centered cubic structure.

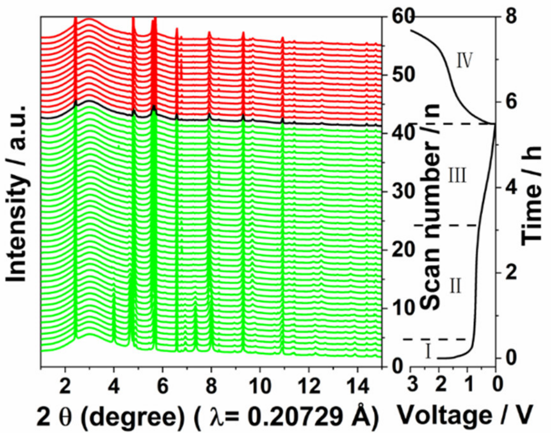

Figure 4.7 *In operando* XRD investigation of the lithium storage mechanism of the Fe_2O_3@C electrode during the 1st lithiation/de-lithiation processes in LiTFSI.

and LiTFSI are shown in **Figure 4.6a** and **Figure 4.7**, respectively. **Figure 4.8a** shows the *in operando* synchrotron radiation diffraction patterns of the Fe_2O_3@C electrode at some selected potentials. The blue and red lines are used to identify the 1st lithiation and de-lithiation processes, respectively. The practical lithiation and de-lithiation capacity in LP30 for *in operando* measurement are 1130 and 363 mAh g^{-1}, respectively. According to the phase composition, the electrochemical processes occurring in the 1st cycle can be divided into four regions (**Figure 4.6a**).

In region I, where the potential quickly drops from ~2.5 to 0.90 V, the first *in operando* synchrotron radiation diffraction is recorded at ~1.25 V. At this potential Fe_2O_3 ($R\bar{3}c$) and Fe_2O_3 ($Fd\bar{3}m$) transform into the intermediate phases $Li_xFe_2O_3$ ($R\bar{3}m$, rhombohedral, $0 < x < 1$) and $Li_xFe_2O_3$ ($Fd\bar{3}m$, Li-lean, $0 < x < 4$), respectively (**Equation (4.4) and (4.5)**). In the Li-lean phase, Li-ion occupies the 8a Wyckoff position of the $Fd\bar{3}m$ structure. The coexistence of $Li_xFe_2O_3$ ($R\bar{3}m$ rhombohedral, $0 < x < 1$) and $Li_xFe_2O_3$ ($Fd\bar{3}m$, Li-lean, $0 < x < 4$) is confirmed by the Rietveld refinement of scan 2 (point A, ~1.25 V), shown in **Figure 4.8b**. In region II (from ~0.90 V to ~0.59 V), the intensity of the 422, 311, and 511 diffraction peaks decreases, while the intensity of the 222, 440, and 400 diffraction peaks increases (see **Figure 4.6b** and **c**). **Figure 4.6d** shows the magnification of the diffraction peak 440 during Li-insertion. By proceeding with the lithiation, the single peak clearly splits into two peaks, accounting for the Li-rich phase and Li-lean phase. These changes of diffraction peaks are attributed to the transformation of $Li_xFe_2O_3$ ($R\bar{3}m$, rhombohedral, $0 < x < 1$) and $Li_xFe_2O_3$ ($Fd\bar{3}m$, Li-lean, $0 < x < 4$) into $Li_xFe_2O_3$ ($Fd\bar{3}m$, Li-rich, $1 < x < 5$) (**Equation (4.6)** and **(4.7)**).

In the Li-rich phase, Li occupies the 8a site and the Fe atom moves from the 8a to 16c Wyckoff position.[100] At scan 6 (point B, ~0.76 V, **Figure 4.8c**) three phases are present together: $Li_xFe_2O_3$ ($R\bar{3}m$, rhombohedral, $0 < x < 1$), $Li_xFe_2O_3$ ($Fd\bar{3}m$, Li-rich, $1 < x < 5$), and $Li_xFe_2O_3$ ($Fd\bar{3}m$, Li-lean, $0 < x < 4$). The Li-rich and Li-lean phases are coexisting during the further Li-ion insertion, while the rhombohedral phase disappears at ~0.75 V (scan pattern 7). By further lithiation (from ~0.72 V to ~0.59V), the Li-rich phase continues to exchange with the Li-lean phase. The cell parameters of both phases do not change during this process, indicating the intercalation mechanism in two phases (**Figure 4.9b**). The $Li_xFe_2O_3$ ($Fd\bar{3}m$, Li-rich, $1 < x < 5$) phase is evidenced by the Rietveld refinement of the scan pattern 20 (point C, ~0.59 V), as shown in **Figure 4.8d**. In region III (from ~0.59 V to ~0.01 V), only the Li-

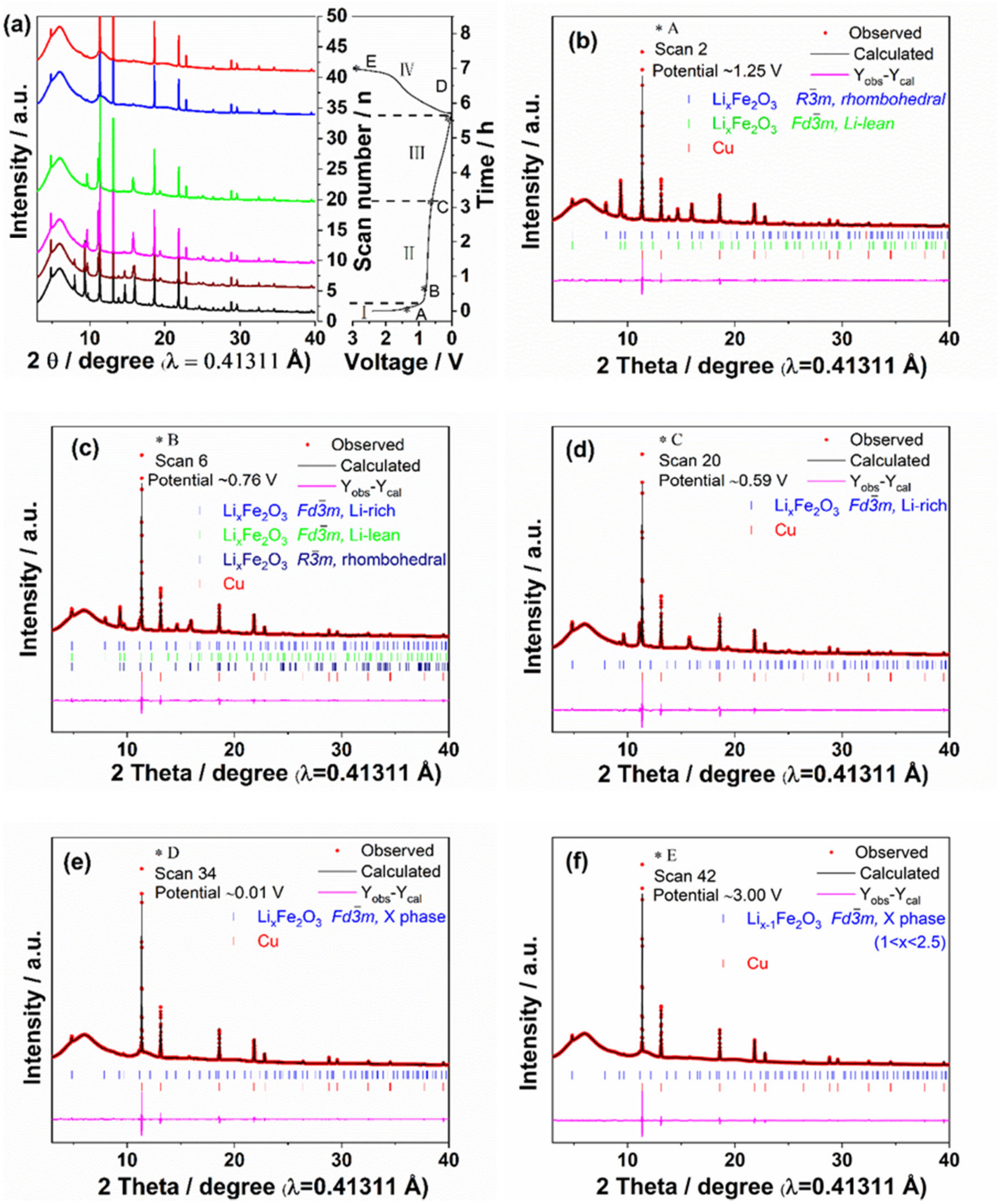

Figure 4.8 (a) *In operando* synchrotron radiation diffraction patterns of the Fe_2O_3@C electrode were collected at various potential states. The Rietveld refinement results of the electrode at some selected potentials (*A - *E): the 1st lithiation to 1.25 V (b), 0.76 V (c), 0.59 V (d), 0.01 V (e), and the1st de-lithiation to 3.00 V (f).

rich phase exists. At the same time, the conversion reaction, which can be recognized from the decreasing intensity of diffraction reflections, starts. At the end of the lithiation process, the Li-rich phase transforms to Fe^0, Li_2O, and $Li_xFe_2O_3$ ($Fd\bar{3}m$, X phase, $0 < x < 2$) (**Equation (4.8)** and **(4.9)**. The marked X phase is distinguished from the Li-rich phase: in the X phase of the $Li_xFe_2O_3$, the Fe atom moves back from 16c to 8a site. The $Li_xFe_2O_3$ ($Fd\bar{3}m$, X phase, $0 < x < 2$) is confirmed by Rietveld refinement of scan 34 (point D, ~0.01 V), as shown in **Figure 4.8e**. Unfortunately, due to the nanoscale and amorphous structure of the material, at the end of the reduction process, it is difficult to observe the reflection of metallic Fe^0 and Li_2O. During the de-lithiation process (region IV, from ~0.01 V to ~3.00 V), the material does not return to the initial Fe_2O_3 structure. Under de-lithiation condition, the partially de-lithiated $Li_{x-1}Fe_2O_3$ ($Fd\bar{3}m$, X phase, $1 < x < 2.5$) with the admixture of amorphous metallic Fe^0 phase are remaining (**Equation (4.10)** and **(4.11)**. The X phase ($Li_{x-1}Fe_2O_3$, $1 < x < 2.5$) in the de-lithiated state is confirmed by the Rietveld fitting of scan 42 (point E, ~3.00 V, **Figure 4.8f**).

Figure 4.9a reports the phase composition of the Fe_2O_3@C electrode during the 1st lithiation processes (pattern 2-20, from ~1.25 V to ~0.59 V). At the beginning of Li insertion (pattern 2 and 3, from ~1.25 V to ~0.87 V), the $Li_xFe_2O_3$ (rhombohedral, $0 < x < 1$) and $Li_xFe_2O_3$ (Li-lean, $0 < x < 4$) phases are coexisting in the electrode. By further Li-ion insertion, the $Li_xFe_2O_3$ (rhombohedral, $0 < x < 1$) and $Li_xFe_2O_3$ (Li-lean, $0 < x < 4$) phases transform to $Li_xFe_2O_3$ (Li-rich, $1 < x < 5$). Three phases are existing during this phase transformation process (pattern 4-7, from ~0.81 V to ~0.75 V). After pattern 7 (~0.75 V), the fraction of the Li-rich phase increases, while the fraction of the Li-lean phase decreases. The percentage of the Li-rich phase is close to 100 % in pattern 20 (~0.59 V). The refined lattice parameters of the rhombohedral phase, Li-rich phase, and Li-lean phase are shown in **Figure 4.9b**. The lattice parameter related to the Li-rich phase is larger respect to the Li-lean phase, indicating that a higher amount of lithium inserts into the Li-rich phase. The lattice parameters of both the Li-rich phase and the Li-lean phase increase with Li insertion. On the same way, also the lattice parameters of the rhombohedral phase increase with Li insertion. On the basis of the aforementioned structure characterization and XRD Rietveld analysis, the lithiation and de-lithiation processes of the Fe_2O_3@C electrode during the 1st electrochemical cycle could be reasonably related to the well-defined three dimensional (3D) architecture, as presented in **Figure 4.9c**. The electrochemical reaction mechanism of Fe_2O_3@C electrode can be summarized as follows:

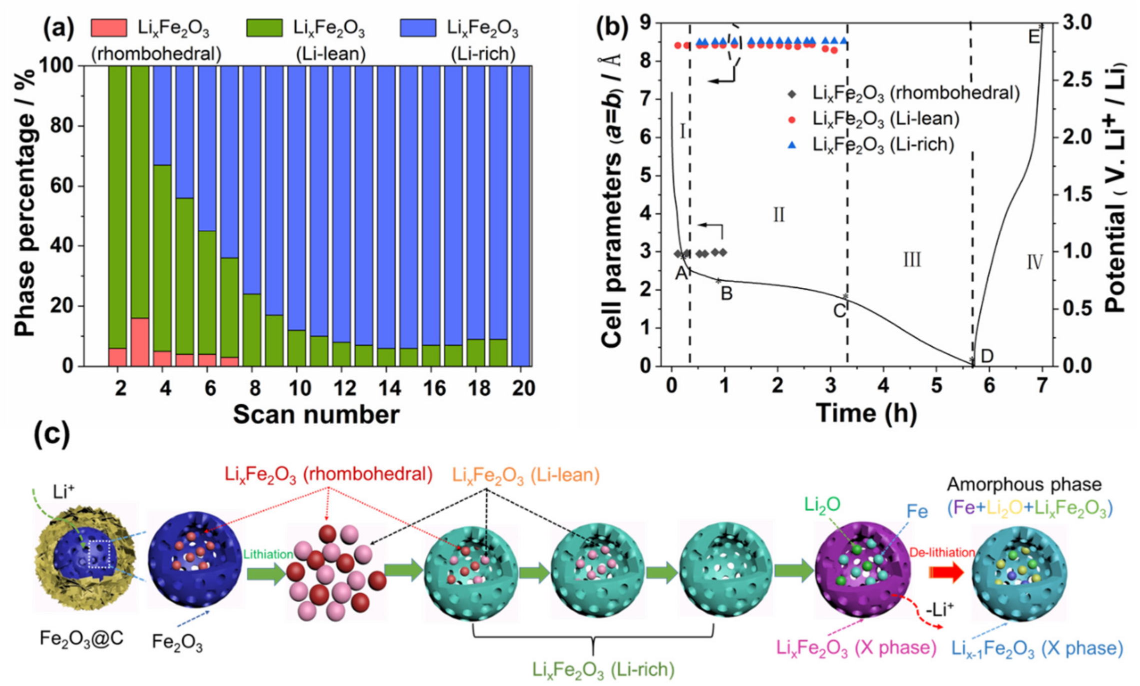

Figure 4.9 The dynamic changes of the phase fraction of the Fe_2O_3@C electrode during the 1st lithiation (a). The changes in cell parameters of Li-rich, Li-lean, and rhombohedral phase during the first lithiation process (b). The schematic illustration of the phase transition process during the first lithiation/de-lithiation processes (c).

Region I (OCV-0.90V, lithium insertion)

$$Fe_2O_3\ (R\overline{3}c) + xLi^+ + xe^- \rightarrow Li_xFe_2O_3\ (R\overline{3}m, \text{rhombohedral}) \tag{4.4}$$

$$Fe_2O_3\ (Fd\overline{3}m) + xLi^+ + xe^- \rightarrow Li_xFe_2O_3\ (Fd\overline{3}m, \text{Li} - \text{lean}) \tag{4.5}$$

Region II (0.90-0.59 V, phase transformation)

$$Li_xFe_2O_3\ (R\overline{3}m, \text{rhombohedral})\ + Li^+ + e^- \rightarrow Li_xFe_2O_3\ (Fd\overline{3}m, \text{Li} - \text{rich}) \tag{4.6}$$

$$Li_xFe_2O_3\ (Fd\overline{3}m, \text{Li} - \text{lean}) + Li^+ + e^- \rightarrow Li_xFe_2O_3\ (Fd\overline{3}m, \text{Li} - \text{rich}) \tag{4.7}$$

Region III (0.59-0.01 V, conversion and intercalation)

$$Li_xFe_2O_3\ (Fd\overline{3}m, \text{Li} - \text{rich}) + (6 - x)Li^+ + (6 - x)e^- \rightarrow 2Fe^0 + 3Li_2O \tag{4.8}$$

$$Li_xFe_2O_3\ (Fd\overline{3}m, \text{Li} - \text{rich}) \rightarrow Li_xFe_2O_3\ (Fd\overline{3}m, \text{X phase}) \tag{4.9}$$

Region IV (0.01-3.00 V, conversion and de-intercalation)

$$Li_xFe_2O_3\ (Fd\bar{3}m, \text{X phase}) \rightarrow Li_{x-1}Fe_2O_3\ (Fd\bar{3}m, \text{X phase}) + Li^+ + e^- \quad (4.10)$$

$$2Fe^0 + 3Li_2O \rightarrow Li_xFe_2O_3\ (Fd\bar{3}m, X\ phase) + (6-x)Li^+ + (6-x)e^- \quad (4.11)$$

To further understand the lithium-ion insertion/de-insertion mechanism, *in operando* XAS was applied to follow the variation of oxidation states and local electronic structure of atoms on a short-range scale.[101] **Figure 4.10a** shows normalized Fe K-edge X-ray absorption near edge structure (XANES) for Fe_2O_3@C at different potentials during the 1st lithiation process. The Fe K-edge shows a continuous shift to lower edge energy (red arrows) when the potential decreases from 0.78 V to 0.22 V during the 1st lithiation process. The maximum of the Fe K-edge white line progressively decreases (blue arrows), as a consequence of the formation of metallic Fe^0 nanoparticles by decreasing the potential. **Figure 4.10b** compares the normalized Fe K-edge of *in operando* XANES spectra during the 1st Li insertion process with standard reference samples of Fe_2O_3 (Fe^{3+}), Fe_3O_4 ($Fe^{8/3+}$), FeO (Fe^{2+}), and Fe. The near-edge energy of pristine Fe_2O_3@C is close to Fe_2O_3 standard reference, which confirms the oxidation state of Fe^{3+} in pristine materials. Clearly, in the potential range from ~0.78 to ~ 0.22 V, the spectra vary between the one of Fe_3O_4 ($Fe^{8/3+}$) and the one of FeO (Fe^{2+}), and finally, at 0.22 V, the spectrum is close to the spectrum of Fe. This phenomenon can be explained with the progressive reduction of Fe^{3+} to Fe^{2+} and with the final formation of metallic Fe^0 nanoparticles at a low potential. **Figure 4.10c** shows the Fourier transforms of Fe K-edge EXAFS of Fe_2O_3@C at selected potentials during the1st lithiation process. The first peak, around 1.5 Å, and the second peak, around 2.7 Å, corresponding to Fe-O shell and Fe-O-Fe shell in the Fe_2O_3 oxide, respectively.[100] Moreover, the Li insertion results in decreased amplitude related to the first Fe-O and second Fe-Fe shells, while the Fe-Fe shell for metallic Fe^0 phase starts to develop (see spectra at 0.6 V) and exhibits an outstanding shell amplitude at the end of the Li insertion process, confirming the conversion to Fe (**Figure 4.10**). The shell position (0.22 V) compared to Fe-Fe shell of Fe foil is slightly different, the reason comes from two sides: (1) the reference spectrum is related to Fe metal foil and this differs from the spectrum at 0.22 V, which is, instead, related to amorphous metallic Fe^0. The structure of Fe foil reference is different from the one of amorphous metallic Fe^0. This leads to the Fourier transform of Fe K-edge EXAFS

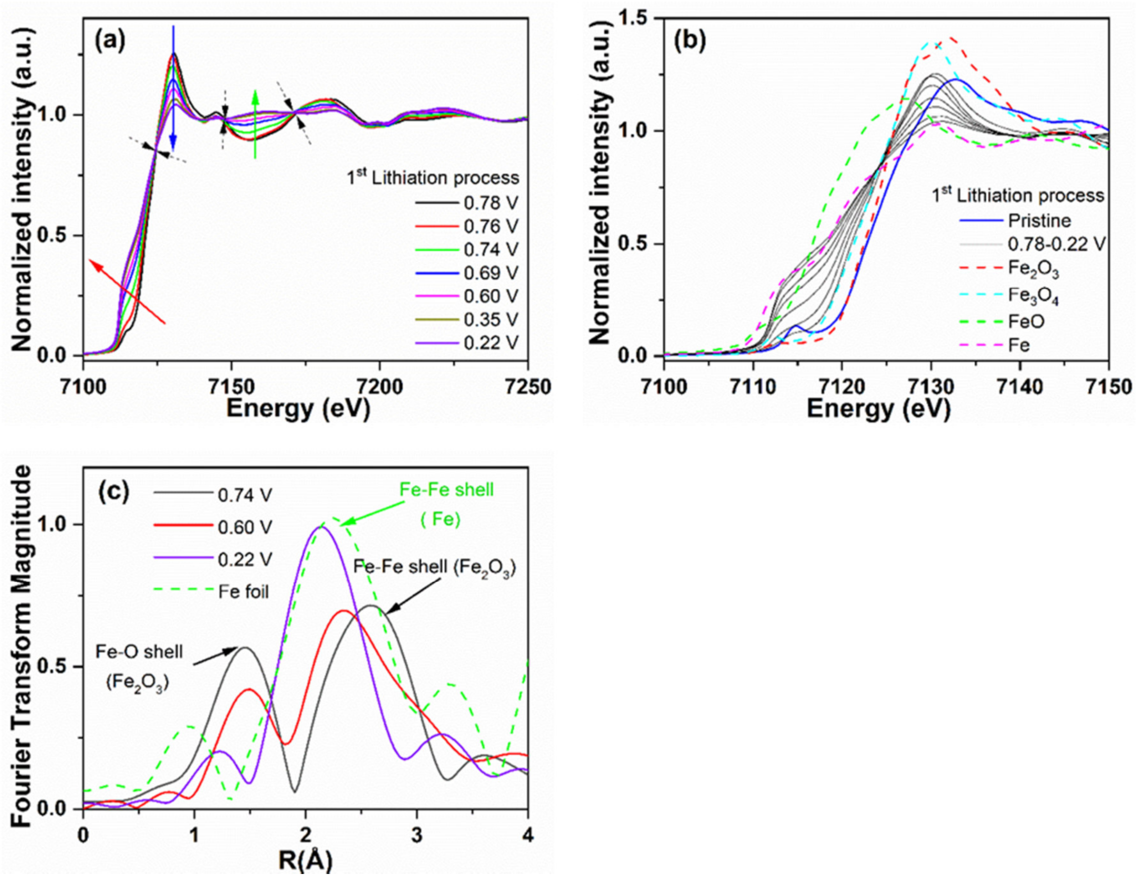

Figure 4.10 Normalized X-ray absorption signals at the Fe K-edge recorded at different potentials (a) and compared with standard references (b) during the 1st lithiation process. The red, blue, and green arrows illustrate the direction of the shift. The Fe_2O_3@C electrode is evaluated at OCV and potential ranging from 0.78 to 0.22 V. The unchanged isosbestic points at 7124 eV, 7148 eV, and 7171 eV. Fourier Transform spectra of Fe K-edge in Fe_2O_3@C during the first lithiation process (c).

of Fe_2O_3@C at 0.22 V (amorphous metallic Fe^0) is not completely close to the Fe-Fe shell of Fe foil reference; (2) the spectrum is recorded at 0.22 V, however, the Fe would be completely reduced at 0.01 V. Unfortunately, we do not have the *in operando* XAS data at 0.01 V due to the beamline time limitation. The last measured point of the Fe-Fe shell is 0.22 V. At this potential the Fe is probably not completely reduced. This is the reason why the Fe-Fe shell at 0.22 V is slightly different compared with the one of Fe reference foil. The second evidence of phase transition during lithiation can be observed from the isosbestic points on the normalized energy of the *in operando* XAS curves (highlighted from the black arrows in **Figure 4.10a**). The presence of the isosbestic point means the absorption coefficients of both species are equal.

Two isosbestic points appear at 7124 eV and 7148 eV, implying a direct electron transfer from Fe^{3+} to Fe^{2+} during the 1st lithiation process.[102,103] Additionally, The first maximum at slightly below 1 Å of the dashed green line is maybe an artifact from pre-processing the data and may indicate a long-wavelength oscillation contribution to the EXAFS in K-space.

Based on the above *in operando* synchrotron radiation diffraction and XAS analysis, the lithium storage mechanism in the Fe_2O_3@C electrode is verified and the phase transition process during the 1st Li-ion insertion/de-insertion process is clear. It is demonstrated that the phase transition during the Li-ion insertion process is composed of two simultaneous processes: one is Fe_2O_3 ($R\overline{3}c$) → $Li_xFe_2O_3$ ($R\overline{3}m$, layered) → $Li_xFe_2O_3$ ($Fd\overline{3}m$, Li-rich), the other is Fe_2O_3 ($Fd\overline{3}m$) → $Li_xFe_2O_3$ ($Fd\overline{3}m$, Li-lean) → $Li_xFe_2O_3$ ($Fd\overline{3}m$, Li-rich). Finally, $Li_xFe_2O_3$ ($Fd\overline{3}m$, Li-rich) transforms into Fe, Li_2O, and $Li_xFe_2O_3$ ($Fd\overline{3}m$, X phase). During the Li-ion de-insertion process, the active material does not return to the initial Fe_2O_3 structure. Instead, the partially de-lithiated $Li_{x-1}Fe_2O_3$ ($Fd\overline{3}m$, X phase, $1 < x < 2.5$) and an amorphous metallic Fe^0 phase remain. In comparison, Adam *et al.*[104] demonstrated that 1.58 mol Li are inserted into Fe_3O_4, leading to the formation of the intermediate phase $(Li_xFe)Fe_2O_4$. The Rietveld refinement confirmed both oxides have the space group of $Fd\overline{3}m$. In Fe_3O_4, Fe^{2+} and Fe^{3+} ions were considered to occupy the Wyckoff positions of 8a and 16d, respectively. In $(Li_xFe)Fe_2O_4$, Fe ions occupy the Wyckoff site of 16d and 16c, respectively. The lithium storage mechanism in the Fe_2O_3@C electrode is different from the insertion in materials like TiO_2 (B),[105] $Li_4Ti_5O_{12}$,[38] and alloy electrode (Sn, Si, P, and Ge).[38] This research work provides fundamental insights on understanding the electrochemical lithiation/de-lithiation mechanism of conversion-type materials.

4.3.3 Electrochemical characterization of Fe_2O_3@C in $LiPF_6$ and LiTFSI-based electrolytes

Figure 4.11a shows the galvanostatic profiles of Fe_2O_3@C electrode at various current densities in the voltage window between 0.01 and 3.00 V *vs.* Li^+/Li in LP30. In agreement with the CV, a small plateau at ~1.2 V is observed during the first cathodic scan, followed by a long plateau at ~0.9 V, corresponding to phase transition and conversion reaction. During the anodic process, the voltage profile shows a relatively rapid increase to around 1.5 V, then a sloped voltage plateau until 2.0 V, followed by a rapid increase up to 3.0 V, features that are in good agreement with the CV profiles. At 0.1 A g^{-1}, the first lithiation and de-lithiation capacities are

1488 and 1130 mAh g^{-1}, respectively, corresponding to a Coulombic efficiency of 76 %. It is important to notice that the obtained Coulombic efficiency at the first cycle is higher than other reports (below 60 %).[106,107] The irreversible capacity at the first cycle is 358 mAh g^{-1}. This can be attributed to the irreversible phase changes and the inevitable consequence of SEI film formation.[72,108] However, the Coulombic efficiency improves during the subsequent cycles. The specific Li insertion and de-insertion capacities at 0.2 A g^{-1} are 873 and 860 mAh g^{-1}, respectively, with a Coulombic efficiency of 99 %. At the highest specific current of 4 A g^{-1}, the specific capacity still remains at 322 mAh g^{-1}, indicating that this material is promising for high power applications. The GCPL curves recorded in LiTFSI are shown in **Figure 4.11b**. In this electrolyte, the same trend as for LP30 can be observed. At 0.1 A g^{-1} the first lithiation and de-lithiation capacities are 1533 and 1142 mAh g^{-1}, corresponding to a Coulombic efficiency of 75 %. At 4 A g^{-1} the capacities are 352 and 346 mAh g^{-1}, for insertion and de-insertion, respectively, corresponding to an improved Coulombic efficiency of 98 %.

Figure 4.11c presents the long-term cycling performance of the Fe_2O_3@C electrode at a specific current of 200 mA g^{-1} in LP30 and in LiTFSI-based electrolytes. The cycling stability in LP30 is different from that in LiTFSI: in LP30, the capacity slowly declines during the first 20 cycles and after that, a gradual increase (up to 928 mAh g^{-1}) can be observed. The capacity decay during the first 20 cycles is attributed to the irreversible phase changes and the formation of the SEI layer on the electrode surface. The increase of capacity after 20 cycles can be assigned to the reversible formation/decomposition of the polymeric gel-like film (PGF) on the Fe_2O_3-based anode material.[109] A similar phenomenon was reported for other metal oxide anode materials like Co_3O_4,[110] NiO,[111] MnO,[112] and $ZnMn_2O_4$.[88] On the other side, the lithiation capacity in LiTFSI continuously decreases from 977 at the 1st cycle to 622 mAh g^{-1} at the 200th cycle. The reason for this difference can be attributed to the nature of the different SEI film, which is forming in the presence of $LiPF_6$ or LiTFSI salt. As expected, the electrolyte does not affect the structural changes of the Fe_2O_3@C composite electrode during the first lithiation/de-lithiation processes. This is proved by the *in operando* synchrotron radiation diffraction measured in LP30 and LiTFSI (**Figure 4.6** and **Figure 4.7**). The rate capability of the material is similar in the two electrolytes (**Figure 4.11d**), with only a slight difference which can be observed during the first 10 cycles. The slightly higher lithiation capacity in LP30 can be related to the decomposition of the electrolyte and SEI formation. Indeed, the

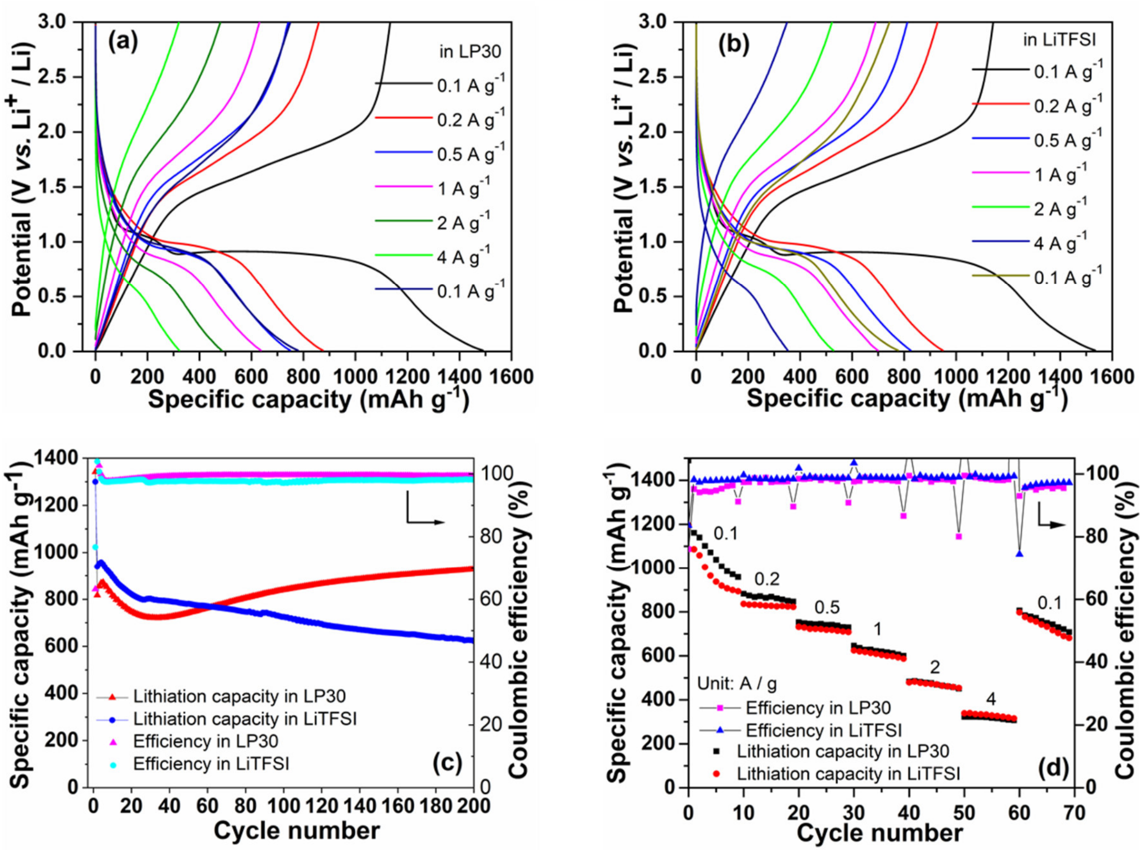

Figure 4.11 The galvanostatic profiles at various current densities in LP30 (a) and LiTFSI (b). (c) Long-term cycling performances and Coulombic efficiencies at a specific current of 0.2 A g^{-1} in LP30 and LiTFSI, respectively. (d) Rate performances and Coulombic efficiencies at current densities ranging from 0.1 to 4 A g^{-1}. All measurements are conducted in the potential range from 0.01 to 3.0 V *vs.* Li^+/Li.

Coulombic efficiency during the first cycles in LP30 is lower with respect to the one in LiTFSI. This is a clear indication of side reactions during reduction (i.e. lithiation) in the first cycles. When the current returns back to 0.1 A g^{-1}, the capacity of Fe_2O_3@C in the two electrolytes is identical. The reversible capacity slowly decreases with the increase of the specific current. When the specific current returns to the initial value of 0.1 A g^{-1}, the capacity of the Fe_2O_3@C electrode recovers back to around 800 mAh g^{-1} in both electrolytes. Fe_2O_3@C composite electrode exhibits a high specific capacity if compared to the electrochemical performance previously reported in other scientific works. For example, Fe_2O_3-MC (Fe_2O_3 *in situ* on the surface of mesoporous carbon) electrode shows a reversible capacity of 703 mAh g^{-1} after 50 cycles at 100 mA g^{-1}; α-Fe_2O_3/graphene nanocomposites exhibit a stable capacity of 771 mAh

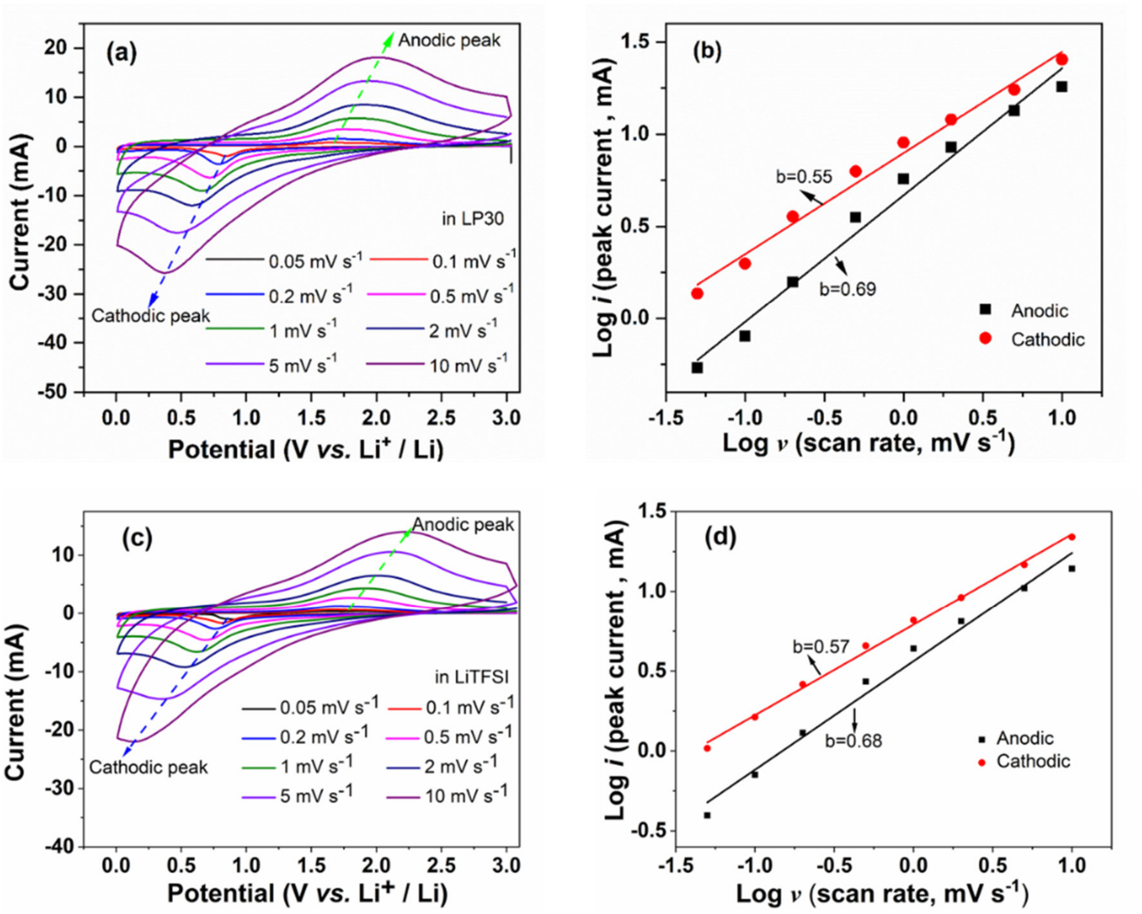

Figure 4.12 Kinetics characterization of the Fe_2O_3@C electrode: CV profiles with scan rates between 0.05 to 10 mV s^{-1} in LP30 (a); the linear relationship of log *i* (peak current) *vs.* log *v* (scan rate) at anodic and cathodic peaks in LP30 (b); CV profiles with scan rates between 0.05 to 10 mV s^{-1} in LiTFSI (c); the linear relationship of log *i* (peak current) *vs.* log *v* (scan rate) at anodic and cathodic peaks in LiTFSI (d).

g^{-1} after 30 cycles at C/10 rate.[113,114] The excellent rate performance and stability of Fe_2O_3@C can be ascribed to its unique core-shell structure and coated carbon layers.

To further investigate the kinetic process and capacitive behavior of the Fe_2O_3@C composite electrode, CV was conducted at various scan rates from 0.05 to 10 mV s^{-1} in LP30, as shown in **Figure 4.12a**. The relationship between the peak current (i, mA) and the scan rate (v, mV s^{-1}) can be used to differentiate a diffusion-controlled mechanism from a surface controlled one. The kinetic parameters can be evaluated based on the following equations (**section 1.4.6**, **Equation (1.11)** and **(1.12)**).[32,115] **Figure 4.12b** shows the linear relationship between log (*i*) and log (*v*) at anodic and cathodic peaks potentials. The *b* values related to anodic and cathodic peaks are 0.69 and 0.55, respectively, demonstrating that the kinetic is controlled by predominant ionic diffusion processes. However, even if the processes are under diffusion control the material displays an excellent rate capability. The CVs and relationship of log (*i*) versus log (*v*) in LiTFSI are shown in **Figure 4.12c** and **d**. In LiTFSI, the *b* values related to anodic and cathodic peaks are 0.68 and 0.57, respectively, suggesting that the electrochemical reaction mechanism is not dependent on the Li-salt used.

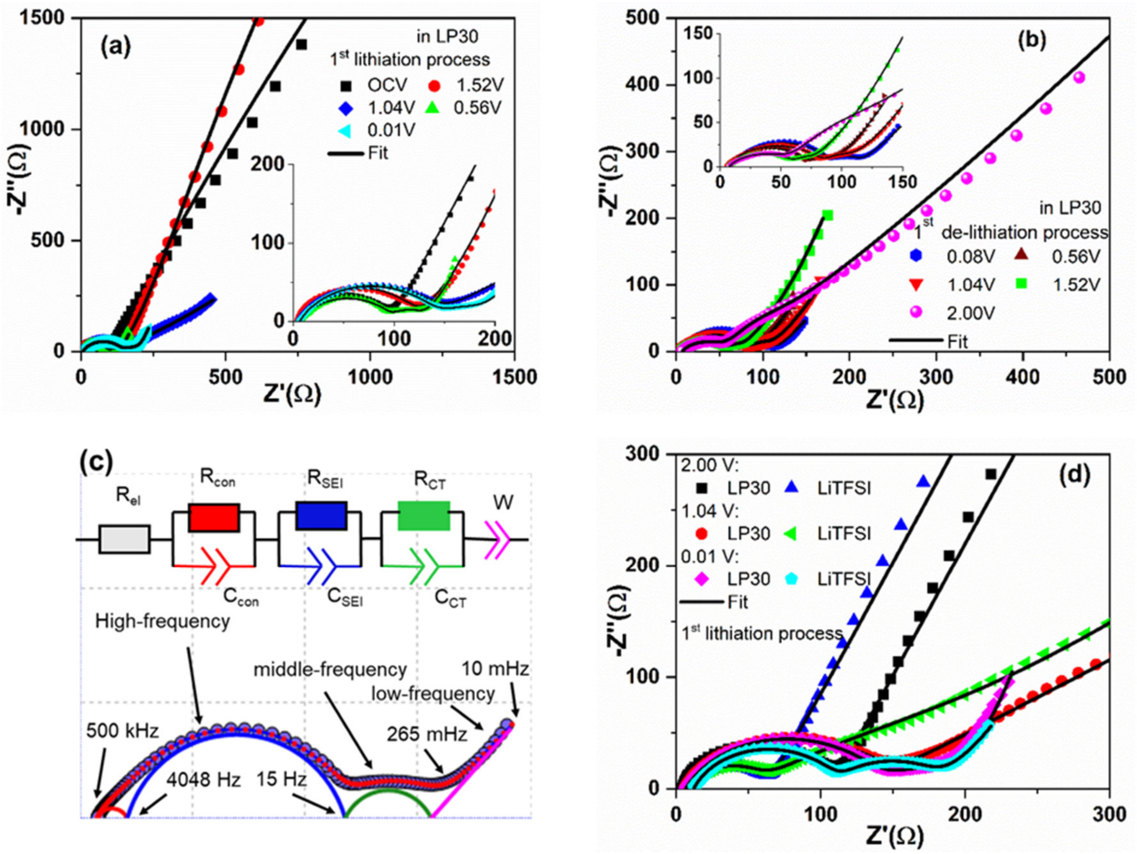

Figure 4.13 Nyquist plots of the Fe_2O_3@C electrode were measured on the freshly assembled cell (OCV) and at some selected potentials during the first lithiation (a) and de-lithiation (b) processes. (c)The equivalent circuit was used for Nyquist plots. (d) Comparison of the Nyquist plots of Fe_2O_3@C electrode measured in LP30 and LiTFSI at potentials of 2.0, 1.04, and 0.01 V during the 1st lithiation process.

Further understanding of the kinetics phenomena and resistive contributions can be achieved by performing EIS. To monitor the resistance evolution during the 1st cycle, EIS measurements were conducted at various potentials between 2.0 and 0.01 V. **Figure 4.13a** and

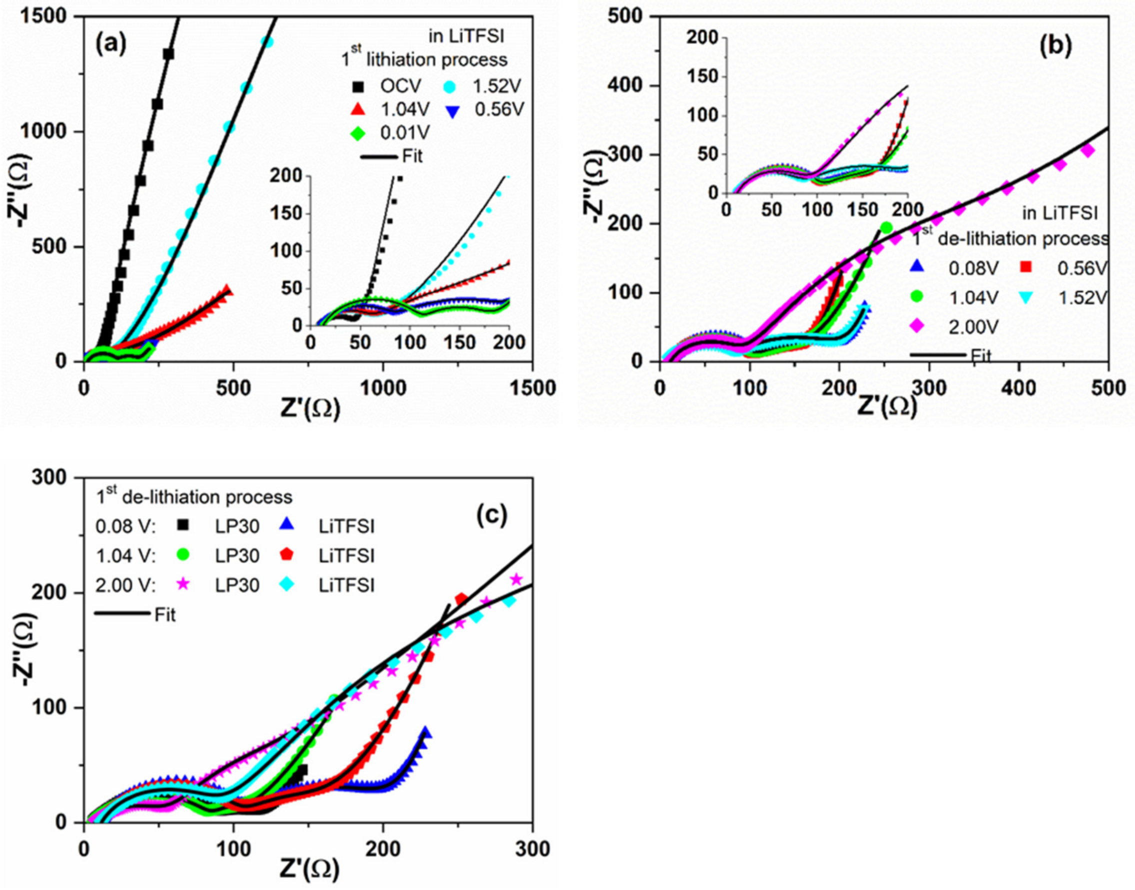

Figure 4.14 Nyquist plots of the Fe_2O_3@C electrode measured on the freshly assembled cell (OCV) and at selected potentials during the first lithiation (a) and de-lithiation (b) processes in LiTFSI. Comparison of the Nyquist plots of the Fe_2O_3@C electrode was evaluated at 2.0, 1.04, and 0.01 V vs. Li^+/Li during the de-lithiation process in LP30 and LiTFSI (c).

b show the experimental and fitted spectra obtained in LP30 at selected potentials during the first lithiation/de-lithiation processes, respectively. **Figure 4.13c** presents the equivalent circuit used for fitting the spectra at the various potentials. Each signal explanation is in **section 1.4.7**. Correspondingly, the Nyquist plot in LiTFSI is displayed in **Figure 4.14a** and **b**, respectively. **Figure 4.13d** compares the Nyquist plots of the electrode in LP30 and LiTFSI at the selected potentials of 2.0, 1.04, and 0.01 V during the first lithiation process. At 2.0 and 1.04 V, the diameter of the high-frequency semicircle in LiTFSI is smaller than the one in LP30, standing for a lower R_{SEI}. At 0.01 V, the R_{SEI} is almost equivalent in the two electrolytes. The Nyquist plots recorded during the first de-insertion process are shown in **Figure 4.14c**. It is noted that the Nyquist profile shows a different trend during the Li de-insertion process in the two electrolytes. The R_{SEI} in LiTFSI is higher than that in LP30 during the Li de-insertion process (from 0.01 to 2.0 V, **Figure 4.14c**).

The R_{el} in LiTFSI is higher than that in LP30, which is due to the different conductivity of the two electrolytes (LP30: $\sigma = 97.3$ mS cm^{-1} and LiTFSI: $\sigma = 51.0$ mS cm^{-1} at room temperature).[77] The R_{el} in two electrolyte systems is stable during the electrochemical processes, which indicates that the conductivity of the electrolyte is independent on the SEI formation and the lithiation/de-lithiation processes (**Figure 4.15a**). The variations of the R_{SEI} at different polarization potentials are shown in **Figure 4.15b**. Interestingly, the R_{SEI} shows a different trend during the first lithiation/de-lithiation processes in the two electrolytes. During Li insertion, the R_{SEI} in LP30 slowly increases from 102 Ω (~2.0 V) to 121 Ω (~1.04 V), followed by a decline to 77 Ω (~0.01 V). In LiTFSI, the R_{SEI} first decreases from 57 Ω (~2.0 V) to 42 Ω (~1.04 V), then sharply increases to 103 Ω (~0.01 V). The R_{SEI} increase is due to the Li insertion ($Fe_2O_3 \rightarrow Li_xFe_2O_3$, from ~2.5 to ~1.0 V) and conversion reaction ($Li_xFe_2O_3 \rightarrow Li_2O + Fe$, from ~0.8 to ~0.01 V), which result in the volume expansion of electrode and lead to the cracking of the SEI film. The decreases of R_{SEI} along Li-insertion can be explained with the fact that the surface of the SEI layer becomes more homogenous or smooth by progressively decreasing the potential. This explanation is reasonable for LP30, however, the R_{SEI} in LiTFSI increases at the end of lithiation. During the Li de-insertion, the R_{SEI} in LP30 continuously decreases from 92 Ω (~0.08 V) to 45 Ω (~2.0 V), while the R_{SEI} in LiTFSI firstly keeps constant at 95 Ω (~0.08-~1.56 V) and finally increases to 110 Ω (~2.0 V). It can be clearly seen that the R_{SEI} in LP30 is lower than that in LiTFSI at the end of the first de-lithiation process, which could be the reason for better stability in LP30 respect to LiTFSI (**Figure 4.11c**). The R_{CT} shows a sharp decline in the two electrolyte systems during the first lithiation process, corresponding to the point where the intermediate phase $Li_xFe_2O_3$ (Li-lean and rhombohedral) is formed. It is noted that R_{CT} in LP30 is lower than that in LiTFSI during the de-lithiation process, implying the different electrochemical reaction kinetics (**Figure 4.15c**). Since the different salt used, as confirmed from the *in operando* synchrotron radiation diffraction, does not influence the structure of the Fe_2O_3@C electrode, the difference in cycling stability can be attributed to the nature of a different SEI film, which consequently influences also the charge transfer kinetics.

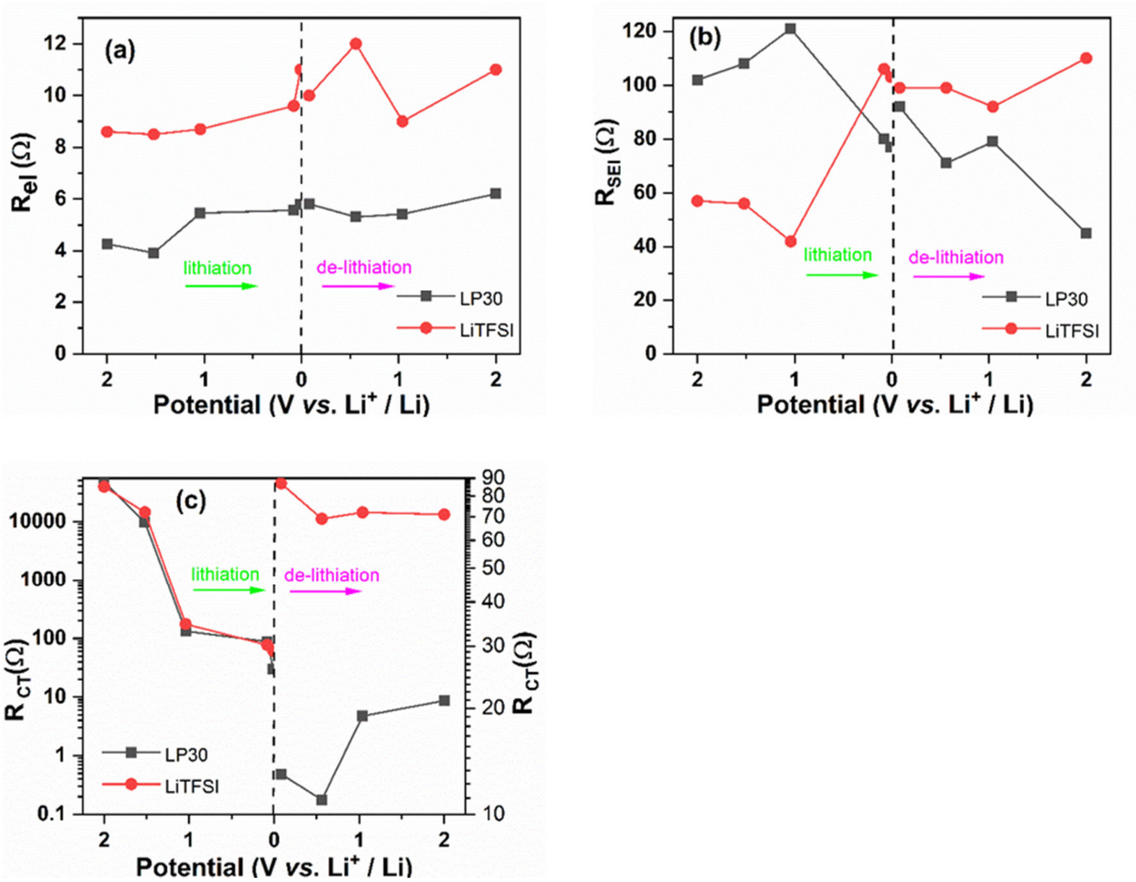

Figure 4.15 Variation changes of the R_{el} (a), R_{SEI} (b), and R_{CT} (c) with electrode polarization in LP30 and LiTFSI during the first lithiation and de-lithiation processes.

4.4 Conclusions

In summary, a core-shell Fe_2O_3@C material derived from MOFs is synthesized via hydrothermal and sintering processes and employed as an anode electrode for Li-ion batteries. The Rietveld refinement shows that the material has two phases of Fe_2O_3 corresponding to spaces group of $Fd\bar{3}m$ (maghemite) and $R\bar{3}c$ (hematite) with a phase fraction of 73 % and 27 %, respectively. The electrode delivers a reversible capacity of 928 mAh g^{-1} at 0.2 A g^{-1} in LP30, while it delivers only 644 mAh g^{-1} at 0.2 A g^{-1} in LiTFSI after 200 cycles. *In operando* synchrotron radiation diffraction demonstrates that $Li_xFe_2O_3$ ($R\bar{3}m$, rhombohedral, $0 < x < 1$) and $Li_xFe_2O_3$ ($Fd\bar{3}m$, Li-lean, $0 < x < 4$) are formed and then these two phases transform into $Li_xFe_2O_3$ ($Fd\bar{3}m$, Li-rich, $1 < x < 5$), which finally converts to metallic Fe^0, Li_2O and $Li_xFe_2O_3$ ($Fd\bar{3}m$, X phase, $0 < x < 2$) at the end of the lithiation process. The *in operando* XAS also confirms the Fe K-edge transformation process and the formation of metallic Fe^0. During the de-lithiation process, the electrode does not return to Fe_2O_3, instead, the $Li_{x-1}Fe_2O_3$ ($Fd\bar{3}m$, X phase, $1 < x < 2.5$) and an amorphous metallic Fe^0 phase remain. The CVs demonstrate that the kinetic is controlled by predominantly ionic diffusion processes, nevertheless, the material shows good capacity retention at high currents). Furthermore, understanding of the kinetics phenomena and resistive contributions in the two types of Li-salt has been achieved by performing electrochemical impedance spectroscopy (EIS). The SEI resistance (R_{SEI}) and Li^+ charge transfer resistance (R_{CT}) in LP30 are lower than those in LiTFSI. The difference in cycling stability in the two electrolytes is attributed to the different SEI film, which also influences the electrochemical reaction kinetics. Future work in our laboratories will address a comprehensive understanding of the SEI nature and evolution in this material through XPS analysis.

5 Effect of Continuous Capacity Rising Performed by $Fe_{1-x}S/C$ Composite Electrodes for Lithium-Ion Batteries

5.1 Introduction

The results in this chapter are extracted from the following two publications: a) **Chengping Li,** Angelina Sarapulova, Kristina Pfeifer, and Sonia Dsoke, Effect of Continuous Capacity Rising Performed by $FeS/Fe_3C/C$ Composite Electrodes for Lithium-Ion Batteries. *ChemSusChem* **2020**, *13*, 986-995; b) **Chengping Li**, Angelina Sarapulova, Kristina Pfeifer, Xianlin Luo, Nicola Pietro Maria Casati, Edmund Welter, Georgian Melinte, Qiang Fu, and Sonia Dsoke, Elucidating the Mechanism of Li Insertion into $Fe_{1-x}S$/Carbon via *in operando* synchrotron Studies. *ACS Applied Materials & Interfaces* (Major revision, under review).

All pristine $FeS/Fe_3C/C$ material for XRD, SEM, EDX, and Raman measurements, and all the working electrodes for electrochemical measurements (CV, GCPL, and EIS) were prepared, carried out, and evaluated by Chengping Li. K. Pfeifer performed SEM and EDX measurements, analysis measurement results. A. Sarapulova provided support with the X-ray diffraction (XRD) Rietveld refinement. G. Melinte performed TEM measurement. X. Luo conducted XPS measurement, analysis data. All synchrotron experiments (synchrotron radiation diffraction and XAS) were prepared, carried out, and evaluated by Chengping Li. N. Casati and E. Welter are beamline scientists, they provided techniques support and instrument adjustments. Prof. H Ehrenberg and S. Dsoke supervised the work and contributed to the completion of the manuscript. Chengping Li wrote the manuscript, all co-authors participated in discussion and manuscript revision. Prof. H Ehrenberg agreed on this project and provided fruitful discussion and constructive suggestions.

In this study, FeS nanosheets and $Fe_{1-x}S/C$ were synthesized via a facile hydrothermal method and a subsequent sintering process.[116–118] The Fe_3C nanoparticles were formed as a by-product but demonstrate a positive influence on the electrochemical performance. Unfortunately, the mechanism of lithium storage into FeS-based electrode material during lithiation and de-lithiation processes is still under debate. McMillan *et al.*[68] proved the intermediate Li_2FeS_2 was not exist by using Fe Mössbauer spectroscopy. Some previous research works reported that the reduction of $Fe_{1-x}S$ to form the intermediate product of Li_2FeS_2.[69–71] However, the intermediate Li_2FeS_2 phase was not evidenced. Therefore, fundamental questions remain: what is the product of the conversion of FeS-based material during the first lithiation and de-lithiation processes? Furthermore, to the best of our knowledge, there is no report about the structural evolution and track of the local environment at the Fe K-edge in the FeS-based electrode.

The purpose of this work is to answer these unsolved questions. This study focuses on the fundamental understanding of the crystalline structure changes by observing phase transitions based on *in operando* synchrotron radiation diffraction. Meanwhile, this work aims to track the changes of the local environment and electronic transitions at the Fe K-edge XAS through *in operando* XAS during the 1st lithiation process. The surface morphology variation of the cycled electrodes is observed by *ex-situ* scanning electron microscopy (*ex-situ* SEM). Electrochemical impedance spectroscopy (EIS) is used to investigate the charge transfer resistance and solid electrochemical interphase resistance of the $Fe_{1-x}S/C$ electrode during the 1st lithiation/de-lithiation processes

5.2 Experimental

Synthesis of FeS nanosheets: 1.35 g iron chloride hexahydrate ($FeCl_3 \cdot 6H_2O$, Alfa Aesar, 99 %), 0.2 g polyacrylamide ($(C_3H_5NO)n$, Sigma-Aldrich), and 0.9 g thiourea (CH_4N_2S, Sigma-Aldrich, 99 %) were dissolved in 80 ml of deionized (DI) water. The mixture solution was kept under continuous stirring for 60 minutes at room temperature. Then, the solution was transferred into a 100 ml Teflon-lined autoclave and heated at 180 °C for 12 h. After washing with DI water several times, the collected black power was finally annealed in Ar/H_2 (Ar/H_2 =95:5) at 600 °C for 5 h with a heating rate of 10 °C min^{-1}.

***Synthesis of $Fe_{1-x}S/C$ composite material*:** 630 mg D-glucose ($C_6H_{12}O_6$, Sigma-Aldrich, 99.5 wt%) was dissolved in 40 ml DI water. The above harvested FeS nanosheets (75 mg) were dispersed into the D-glucose solution. Subsequently, the solution was transferred into a 50 ml Teflon-lined autoclave and heated at 180 °C for 12 h. After cooling down to room temperature, the product was poured out and washed by using rinse-precipitation cycles with DI water. The product was dried at 80 °C. Finally, the harvested black powder was kept in Ar/H_2 (Ar/H_2 =95:5) at 600 °C for 5 h with a heating rate of 10 °C min^{-1}.

Materials characterization: The pristine material was measured at the Materials Science (MS) beamline, Swiss Light Source (λ=0.49310 Å, 25 KeV).[56] The crystallographic information and phase fraction of the FeS and $Fe_{1-x}S/C$-LP30-1h were obtained from an STOE

STADI P COMBI diffractometer (Mo-$K_{\alpha 1}$, λ=0.70930 Å) in Debye-Scherrer geometry. To further visualize the crystalline structure, scanning transmission electron microscopy (STEM) and high-resolution transmission electron microscopy (HR-TEM) of the samples were carried out on an aberration (image) corrected transmission electron microscopy (FEI Company, Titan 80-300) via a Gatan US1000 slow-scan CCD camera. The carbon percentage in the composite was analyzed by using Organic Elemental Analysis (OEA, Vario Micro Cube, Elementar). For SEM/EDX, XPS measurements are described in **section 4.2**.

Electrochemical characterization: Electrochemical measurements were conducted using three-electrode Swagelok-type half cells assembled in an argon-filled glovebox (MBraun, O_2 and $H_2O \leq 0.5$ ppm). The working electrodes were prepared by mixing the active material, carbon black (Super P, Timcal Ltd.), and polyvinylidene fluoride binder (PVDF) with a mass ratio of 7: 2: 1 in N-methyl-2-pyrrolidone solvent (NMP) to form a homogeneous slurry. The slurry was stirred overnight at room temperature and then coated on a copper foil and dried at 80 °C. The circular working electrodes with a diameter of 12 mm were punched out and dried in vacuum at 120 °C for 24 h. The mass loading of active materials is 1.8 mg cm^{-2} for FeS. For $Fe_{1-x}S/C$, the working electrode with low mass loading (0.7 mg cm^{-2}, a diameter of 7 mm) is used for electrochemical impedance study. The working electrodes for Cyclic Voltammetry (CV), rate performance, galvanostatic cycling with potential limitation (GCPL) have an average mass loading of 1.5-2.0 mg cm^{-2} and a thickness of 75 μm. The $Fe_{1-x}S/C$ electrodes are normalized to the entire mass of the composite ($Fe_{1-x}S/C$) as the active material. GCPL, rate performance, CVs, and EIS measurements are described in **section 4.2.** GCPL was conducted at different specific currents between 0.1-5 A g^{-1}. Long-term cycling was performed at 1 A g^{-1} for 500 cycles. *Ex-situ* X-ray diffraction (XRD) and *ex-situ* SEM measurements were performed on cycled electrodes (i.e. cycled with 1 A g^{-1}, after the 9th, 140th, and 500th cycles) in de-lithiated states. The cycled electrodes were disassembled and washed with dimethyl carbonate (DMC, Sigma-Aldrich, 99 %) in an argon-filled glovebox. The *ex-situ* XRD was measured with a STOE STADI P diffractometer (Cu-$K_{\alpha 1}$, λ=1.5406 Å) in flat-sample transmission mode.

***In operando* synchrotron radiation diffraction and *in operando* X-ray absorption spectroscopy:**

For *in operando* measurements, the working electrodes were mixed with the pristine $Fe_{1-x}S/C$ material (70 wt%), carbon black (Super P, Timcal Ltd. 20 wt%), and polytetrafluoroethylene (PTFE beads, Aldrich, 10 wt%). The above mixture (mass loading of 2.5-3.6 mg cm^{-2}) was pressed on the center of copper mesh.[27] A CR2025 coin cell with glass windows was used for synchrotron radiation diffraction and A CR2025 coin cell with Kapton windows was performed XAS measurements, respectively.

The cell was charged/discharged at 80 mA g^{-1} (synchrotron radiation diffraction) and 100 mA g^{-1} (XAS) at 0.01-3.0 V vs. Li^+/Li. *In operando* synchrotron radiation diffraction was performed at the MS beamline, Swiss Light Source.[56] LaB_6 and Si are two standard references used for calibration. *In operando* XAS was carried on the P65 beamline, PETRA III, German Electron Synchrotron (DESY, Hamburg). Fe_2O_3, FeO, Fe_3O_4, and Fe foil were employed as standard material. The XAS spectra were analyzed by the DEMETER software package.[90]

5.3 Results and Discussion

5.3.1 Structural and morphological characterization

The phase fraction and crystal structure of FeS and $Fe_{1-x}S/C$ are evaluated by X-ray diffraction (XRD) and analyzed by the Rietveld refinement using the FullProf software package, as shown in **Figure 5.1a** and **b**. The Rietveld refinement confirms that the XRD reflections of FeS are all indexed to the hexagonal FeS structure model with the space group of *P-62c*. The cell parameters are $a=b=$ 5.966 Å*,* $c=$11.738 Å for stoichiometric domains of FeS (52 %) and $a=b=$ 5.978 Å*,* $c=$11.535 Å for non-stoichiometric domains of Fe_xS (48 %, ($0.875 \leqslant x \leqslant 1$). The Rietveld refinement demonstrates that the pristine $Fe_{1-x}S/C$ ($0 \leqslant x \leqslant 0.125$) material consists of a FeS phase, two phases of Fe_7S_8, and a Fe_3C phase. In detail, the FeS phase (29 %) has the space group of *P-62c*; the Fe_7S_8 has the space group of *C2/c*, partially stoichiometric (40 %) and non-stoichiometric (28 %); and the Fe_3C phase (3 %) has the space group of *Pnma*. The pristine material is labelled $Fe_{1-x}S/C$ for simplicity. The x in $Fe_{1-x}S/C$ ($0 \leqslant x \leqslant 0.125$) varies from 0 (the FeS phase, 29 %, space group of *P-62c*) to 0.125 (the Fe_7S_8 phase, stoichiometric (40 %) and non-stoichiometric (28 %), space group of *C2/c*). The composition of $Fe_{1-x}S/C$ is non-stoichiometric because of ordered vacancies inside the Fe lattice.[119–121] The presence of the Fe_3C phase is beneficial for the capacity increase, as already highlighted in our previous work.[122] Many strategies have been used to prepare single-phase iron sulfide material for exploring the lithium storage mechanism.[119–121] But unfortunately, the obtained sample always contains multi-phases. There are some challenges to prepare single-phase iron sulfide compared with Fe_2O_3, which are summarized as follows: 1) Iron sulfides have a complicated stoichiometry due to the unstable of ferric ion and sulfide ion; 2) Ferric ions are easily combining with oxygen, the obtained products could contain iron oxide or iron hydroxide impurities; 3) The phase diagram of iron sulfides is very complicated. FeS is formed at high reaction temperature (320 °C), Fe_7S_8 appears at low reaction temperature (260 °C).[121]

The pristine material was immersed in the LP30 commercial electrolyte for 1h to observe the effect of the pristine $Fe_{1-x}S$/C contact with the LP30 commercial electrolyte. No optical changes in the material or the electrolyte were observed. Nevertheless, for the investigation of non-visible spontaneous processes, the resulting structural changes of $Fe_{1-x}S$/C are analyzed (**Figure 5.1c**) and compared to the pristine material (**Figure 5.1b**). The phase fraction of $Fe_{1-x}S$/C changes after immersion in LP30. The Fe_9S_{10} (*P2₁*, 63 %) and FeS (*P-62c*, 34 %) phase are confirmed from the Rietveld refinement. The iron sulfides group consists of troilite (FeS) and pyrrhotites with continuously variable compositions. In detail, Fe_7S_8 (4C) has a monoclinic structure with the magnetic property; other pyrrhotites (Fe_9S_{10} (5C) and $Fe_{11}S_{12}$ (6C)) have a hexagonal structure with the non-magnetic property.[123–125] Fe_7S_8 (4C) is recognized as charge-neutral when written as $Fe_2^{3+}Fe_5^{2+}S_8$, which has 29 % of Fe^{3+}. In comparison, Fe_9S_{10} (5C) is written as $Fe_2^{3+}Fe_7^{2+}S_{10}$, which contains 22 % of Fe^{3+}. Additionally, according to literature reports,[123,126] Fe_7S_8 (4C) has 12.5 % of vacancies and Fe_9S_{10} (5C) has less vacancies (10 %). The different amounts of Fe^{3+} and vacancies of pyrrhotites coexist in the pristine $Fe_{1-x}S$/C. The electrolyte (LP30) could stimulate the phase transition from Fe_7S_8 (4C) to Fe_9S_{10} (5C).

The composition of $Fe_{1-x}S$ material strongly depends on the synthesis conditions. The high-temperature treatment initiates the phase transition into pyrrhotite. It is not excluded that part of the material can also be present in the amorphous state. In our synthesized material, most of the mass belongs to the Fe_7S_8 composition. The electrolyte (LP30) could stimulate the phase reaction from the phase Fe_7S_8 ($Fe_{63}S_{72}$, 4C) to the Fe_9S_{10} ($Fe_{63}S_{70}$, 5C) with lost S. For a more detailed phase transition mechanism, more advanced characterization techniques (XPS, TEM, and SEM/EDX) are required. The group of Haines *et al.* investigated the structural instability between troilite (FeS) and pyrrhotite ($Fe_{1-x}S$). Theoretically, they found that Fe_7S_8 (4C) and Fe_9S_{10} (5C) phase coexist at room temperature and could transform into each other.[127] In the following electrochemical characterization part of this paper, the

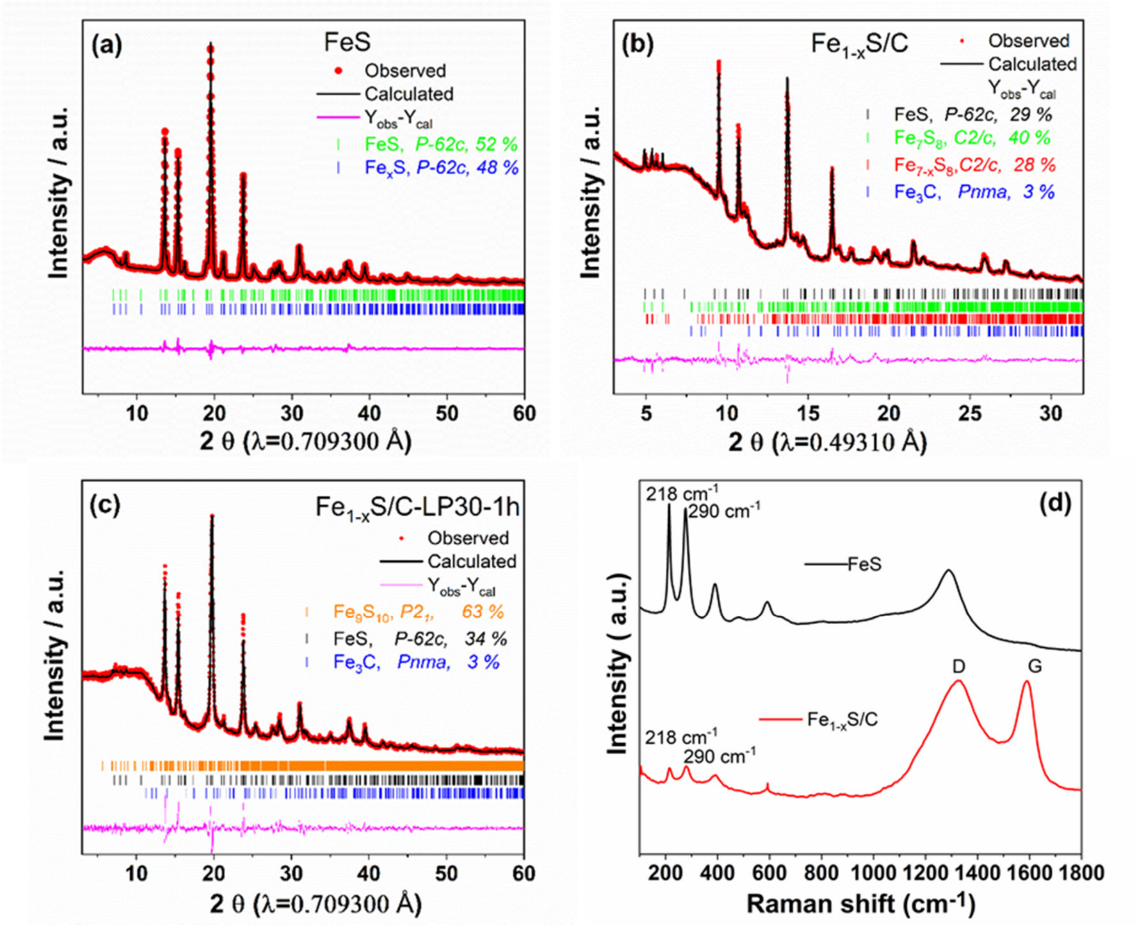

Figure 5.1 Rietveld refinement based on X-ray radiation diffraction data of FeS (a) and $Fe_{1-x}S/C$ (b). The $Fe_{1-x}S/C$ material in LP30 electrolyte for 1h (c) and the Raman spectra of the pristine FeS material and the pristine $Fe_{1-x}S/C$ material (d).

active material is labeled as $Fe_{1-x}S/C$-LP30-1h (which contains Fe_9S_{10} and FeS phases, $0 \leqslant x \leqslant 0.1$). **Table 5.1** displays the detailed information about the cell parameters of each phase.

To better understand the structure of FeS nanosheets and $Fe_{1-x}S/C$ composites, Raman spectroscopy of FeS and $Fe_{1-x}S/C$ were conducted and are shown in **Figure 5.1d**. Both FeS nanosheets and $Fe_{1-x}S/C$ composites have two peaks located at 218 and 290 cm^{-1} that are attributed to the asymmetric and symmetric stretching modes of FeS.[128] In the $Fe_{1-x}S/C$ composites, two distinct peaks presented at 1315 and 1600 cm^{-1}, which are related to the D band and G band of amorphous carbon with the intensity ration of $I_D/I_G=1.0$, implying that the interconnected carbon spheres have a highly disordered carbon structure.[129] The D band is linked to disordered carbon atoms and defects, whereas the G band is due to the relative motion of *sp*^{2} carbon atoms.[130,131]

Table 5.1 The phase fraction, space group, and cell parameters of the $Fe_{1-x}S/C$ and $Fe_{1-x}S/C$-LP30-1h.

		$Fe_{1-x}S/C$			$Fe_{1-x}S/C$-LP30-1h		
Phase fraction	Space group	*a* (Å)	*b* (Å)	*c* (Å)	*a* (Å)	*b* (Å)	*c* (Å)
FeS	*P-62c*	5.951	5.951	11.451	5.958	5.958	11.434
Fe_7S_8	*C2/c*	11.915	6.888	12.917	--	--	--
$Fe_{7-x}S_8$ $(-1 \leqslant x \leqslant 0)$	*C2/c*	11.735	6.679	12.372	--	--	--
Fe_9S_{10}	*P2₁*	--	--	--	6.863	28.930	6.887
Fe_3C	*Pnma*	4.988	6.743	4.304	4.945	6.773	4.306

Scanning electron microscopy (SEM) images of FeS and $Fe_{1-x}S/C$ are given in **Figure 5.2a**, **b** and **c**, **d**, respectively. The low and high magnification SEM images of FeS (**Figure 5.2a** and **b**) reveal that this material has a shape of nanosheets with an average size of 10 μm. These thin nanosheets stack together forming three-dimensional nanoflowers. The energy-dispersive spectroscopy (EDS) elemental maps of FeS nanosheets are displayed in **Figure 5.3a-c**. The corresponding elemental mapping of Fe and S shows a similar intensity distribution, implying that FeS is uniformly dispersed. The $Fe_{1-x}S/C$ composite is composed of FeS and Fe_3C nanoparticles with a size of 50-60 nm and interconnected carbon spheres with 1-2 μm (**Figure 5.2c** and **d**). Herein, FeS nanoparticles are surrounded by interconnected carbon spheres, which are expected to provide the paths for electron movement and effectively buffer the volume expansion upon repeated cycling. The corresponding elemental mapping of $Fe_{1-x}S/C$ (**Figure 5.3d-g**) shows that the nanosized FeS nanoparticles are randomly scattered in the interconnected carbon spheres matrix. The carbon percentage in $Fe_{1-x}S/C$ is 55 wt%, which is

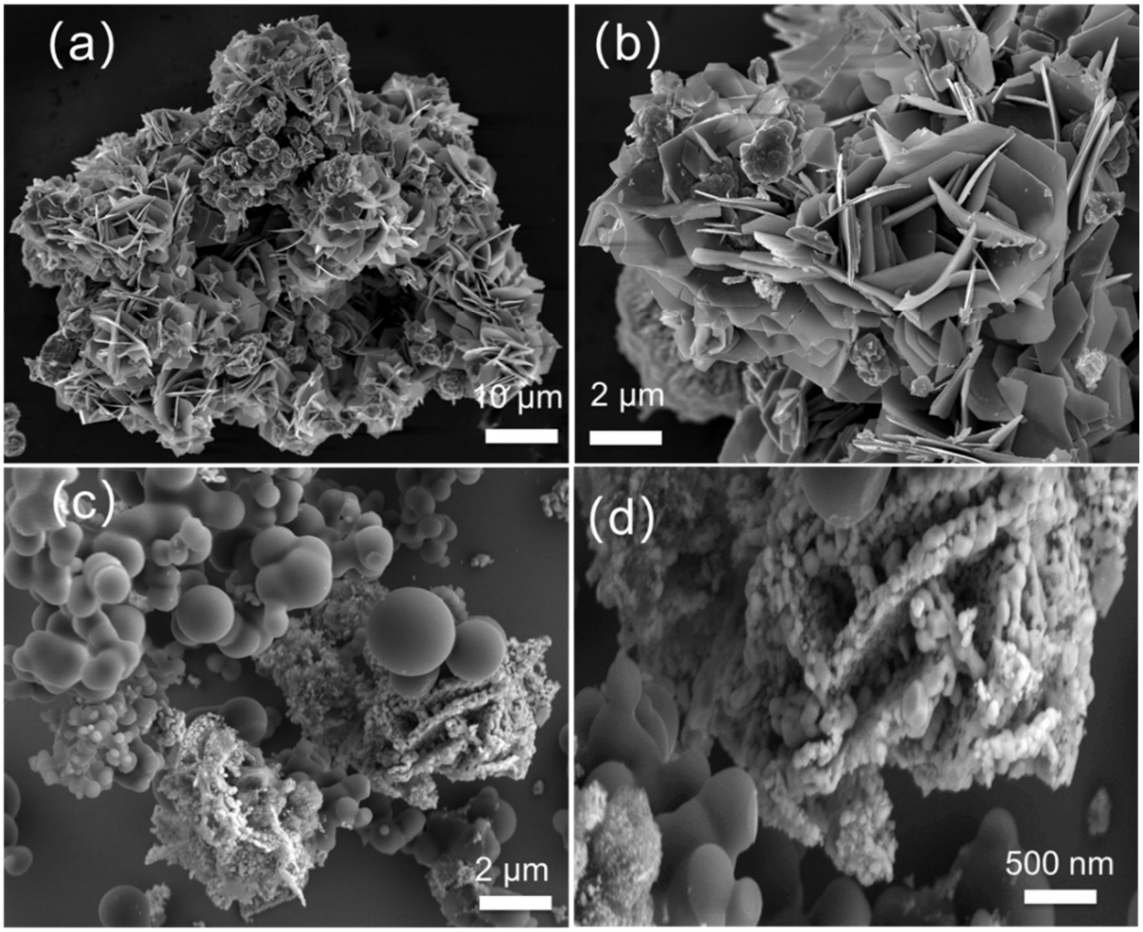

Figure 5.2 SEM images of the FeS nanosheets (a and b) and $Fe_{1-x}S/C$ composites (c and d).

calculated from the Organic Elemental Analysis (OEA) measurements and shown in **Table 5.2**. These results reveal that the introduction of interconnected carbon spheres in FeS drastically affects the phase fraction, the morphology, and the particle size.

Table 5.2 Organic Elemental Analysis (OEA) of the pristine FeS and $Fe_{1-x}S/C$ material.

	N (%)	C (%)	H (%)	S (%)
FeS	0.07	0.32	0.61	40.84
$Fe_{1-x}S/C$	0.36	57.76	1.26	16.51

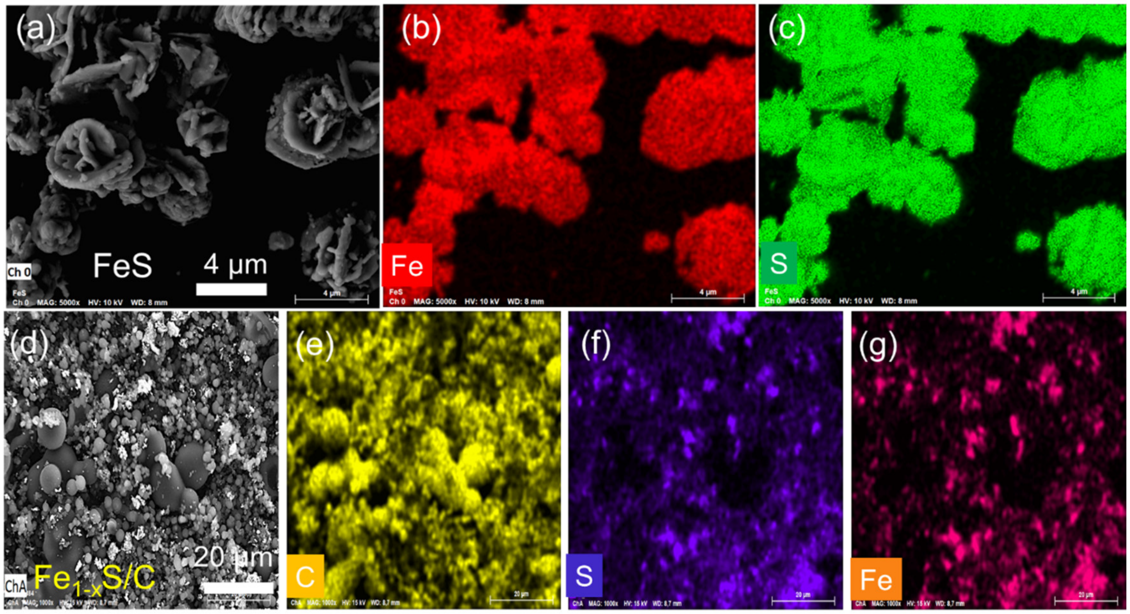

Figure 5.3 The EDS elemental maps of the pristine FeS material (a, b, and c); the EDS of the pristine $Fe_{1-x}S/C$ material (d, e, f, and g).

Furthermore, the scanning transmission electron microscopy (STEM) imaging demonstrates that $Fe_{1-x}S$ nanoparticles have an irregular shape (1-2 μm) composed of nanocomposites (50 nm) in **Figure 5.4a**. The high-resolution transmission electron microscopy (HR-TEM) imaging (**Figure 5.4b**) reveals a polycrystalline sample composed of interconnected nanograins with different crystalline orientations. **Figure 5.4b** shows the lattice spacing of 0.56 nm, which is related to (110) plane of Fe_7S_8.[132] The lattice spacing of 0.26 nm corresponds to the (101) and the lattice spacing of 0.30 nm matches with and (110) crystalline planes of FeS.[133–135] The amorphous carbon layer is also observed by TEM. According to state-of-the-art literature, this unique carbon layer can protect the polysulfide from dissolving into the organic electrolyte.[136,137] STEM-EDS elemental mappings (**Figure 5.4c**) support the finding that $Fe_{1-x}S$ nanoparticles are surrounded by the carbon layer.

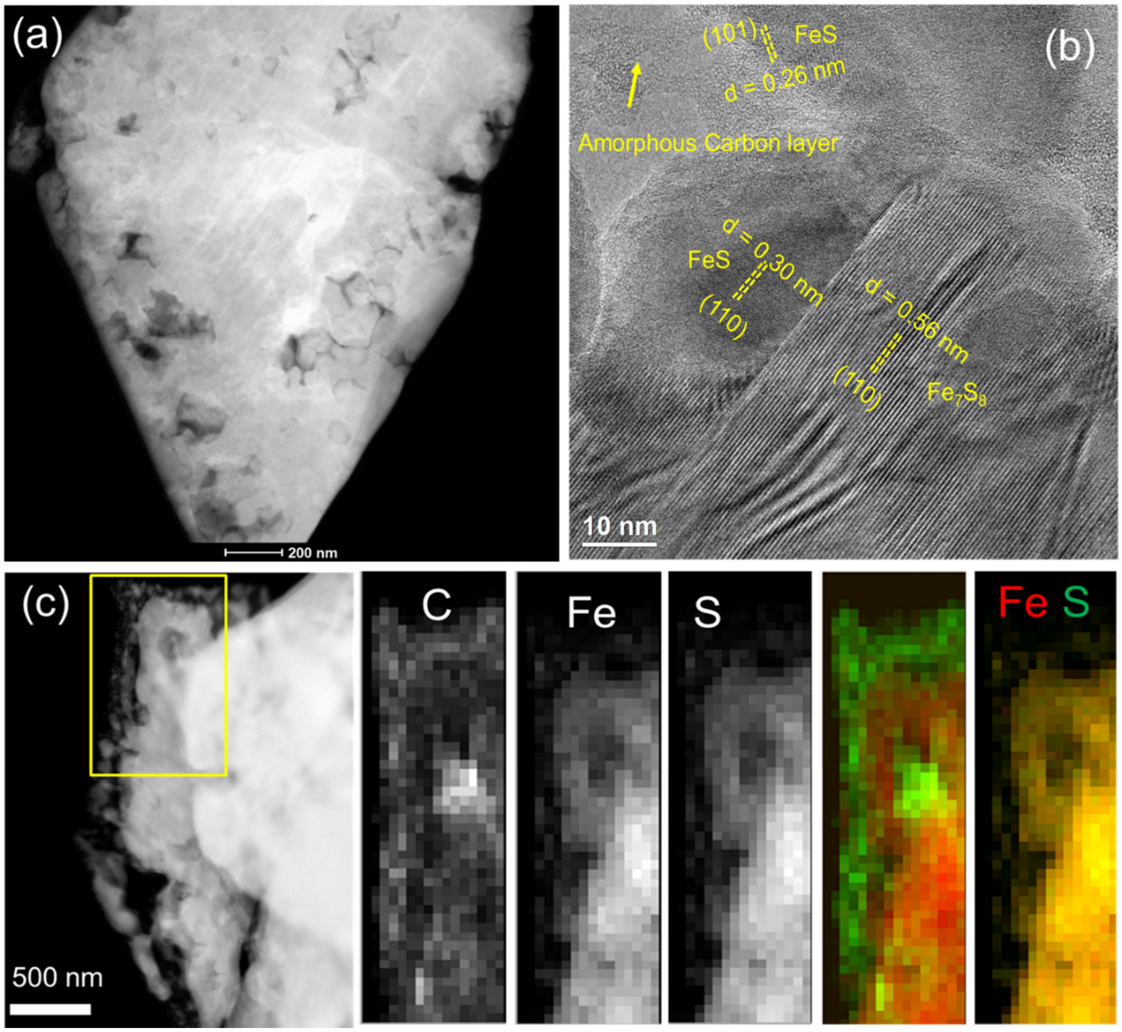

Figure 5.4 STEM (a) and HR-TEM image (b) and STEM-EDS elemental mappings (c) of the $Fe_{1-x}S/C$ composite.

The surface changes of the pristine $Fe_{1-x}S/C$, which was in contact with the LP30 electrolyte are examined by X-ray photoelectron spectroscopy (XPS). The fitting of Fe $2p_{3/2}$ spectrum (**Figure 5.5a**) indicates that the surfaces of both the $Fe_{1-x}S/C$ and the $Fe_{1-x}S/C$-LP30-1h materials contain mainly Fe(2+)-S, Fe(3+)-S, and Fe(3+)-O,[138,139] which correspond to photoelectron peaks at 708.4 eV, 710.5 eV, and 711.6 eV (main peak).[140,141] The presence of Fe(3+)-O on the surface of $Fe_{1-x}S/C$ results from the reaction between Fe(3+)-S/Fe(2+)-S and oxygen/water.[142] Comparing with the satellite peak of the pristine $Fe_{1-x}S/C$ at 715.4 eV, there is a broader photoelectron peak located at 716.6 eV for the $Fe_{1-x}S/C$-LP30-1h composite. This unclear photoelectron peak could be attributed to the satellites of Fe(2+)/Fe(3+) and the influence of Li^+-ions on the surface of the pristine $Fe_{1-x}S/C$ material. Regarding the S 2p spectrum in **Figure 5.5b**, the photoelectron peaks with the binding energy of 168.1 eV, 162.0 eV, and 164.1 eV, are assigned to SO_x^{2-}, S^{2-} of FeS, and S_n^{2-} of FeS_n respectively.[143] In comparison, the intensity of S^{2-} 2p for the pristine $Fe_{1-x}S/C$ slightly decreases the photoelectron peaks slightly shift to higher binding energy after mixing with LP30. The C 1s spectrum displays the C component for both samples: a main peak at 285.0 eV (C-C), other small peaks at and 289.6 eV (O-C=O), 286.4 eV (C-O-C), and 288.0 eV (C=O) in **Figure 5.5c**. After the pristine $Fe_{1-x}S/C$ material contact with LP30 for 1h, the intensities of the peaks at 286.4 eV (C-O-C), 288.0 eV (C=O) increase because of the reaction of the $Fe_{1-x}S/C$ towards to oxygen.

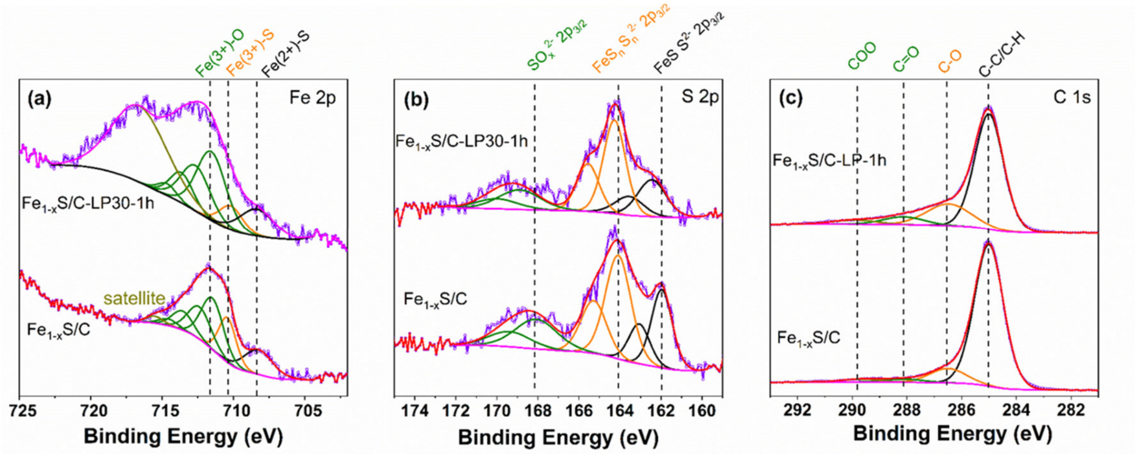

Figure 5.5 XPS spectra of the Fe 2p (a), S 2p (b), and C 1s (c) of the $Fe_{1-x}S/C$-LP30-1h (top) and the pristine $Fe_{1-x}S/C$ (down).

5.3.2 *In operando* synchrotron radiation diffraction and XAS study: elucidation of the Li-storage mechanism in $Fe_{1-x}S/C$

The detailed understanding of the conversion reactions occurring during Li-insertion/de-insertion into and from the $Fe_{1-x}S/C$ electrode is critical for its further improvement. The structural changes of the $Fe_{1-x}S/C$ electrode are studied by using *in operando* synchrotron radiation diffraction during the 1st lithiation/de-lithiation processes. **Figure 5.6a** shows all XRD patterns and the discharge/charge curves of the $Fe_{1-x}S/C$ electrode during the 1st electrochemical process. **Figure 5.6b** presents the 1st cyclic voltammetry (CV) curve, three cathodic peaks (1.29 V, 0.79 V, and 0.39 V) and two oxidation peaks (1.23 V and 1.85 V) are observed. Normally, the plateau occurring in galvanostatic cycling with potential limitation (GCPL) is consistent with cathodic/anodic peaks in CV curve. One can observe that one plateau

(1.22 V) in GCPL and the peaks (1.29 V) in CV curve are not at the identical potential. This small shift is due to the different electrochemical measurement modes: the GCPL (charge/discharge) is performed at a specific current of 0.08 A g^{-1}, while the CV measurements are conducted on 0.05 mV s^{-1}. According to the diffraction peaks trend, the potential profile is divided into four regions:

(I) Region I (~2.60 V → ~1.22 V): Li^+ insertion process;

(II) Region II (~1.22 V → ~0.79 V): conversion step 1;

(III) Region III (~0.79 V → ~0.01 V): conversion step 2;

(IV) Region IV (~0.01 V → ~3.00 V): de-lithiation process.

During the 1st lithiation process, in region I, a fast drop of the potential from ~2.60 V to ~1.22 V occurs. One of the reflections (9.4-9.6 °) slightly shifts to a lower 2θ angle (**Figure 5.7a**), which is ascribed to Li^+ insertion into $Fe_{1-x}S$/C. In region II, the amorphization process (small plateau at ~1.22 V) leads to the intensities of some reflection patterns (5.7, 9.4, 10.6, 13.6, and 16.4 °) gradually decrease, which is attributed to the conversion step 1: $2Fe_{1-x}S + 2Li^+ + 2e^- \rightarrow Li_2Fe_{1-x}S_2 + (1-x)Fe^0$ with the formation of metallic Fe^0 (**Equation (5.1)**). The intensity of the reflection at 13.2-14.0 ° decreases during the 1st lithiation process (~1.22 V→~1.02 V), as it is shown in **Figure 5.7b** (supporting information). In region III, upon further electrochemical reduction, the intensities of the above-mentioned fade out, which is due to the fact that $Fe_{1-x}S$/C material is completely consumed and because synchrotron radiation diffraction doesn't detect such small size products.[67,88,144] More importantly, two new reflections (8.5 and 13.9 °) appear and continuously broaden, which is ascribed to the conversion step 2 with the formation of Li_2S (JCPDS card no. 26-1188) and metallic Fe^0 (**Equation (5.2)**). However, the very broad reflections related to metallic Fe^0 cannot be detected by synchrotron radiation diffraction due to the high background signal. The conversion step 2: $Li_2Fe_{1-x}S_2 + 2Li^+ + 2e^- \rightarrow 2Li_2S + (1-x)\ Fe^0$ is correlated to the small CV peak located at ~0.79 V. One broad cathodic peak at 0.39 V, indicates that the solid electrolyte interphase (SEI) is formed.[145] **Figure 5.6c** depicts *in operando* synchrotron radiation diffraction at different potentials during the 1st discharge/charge processes. The changes of reflection intensities, which correspond to phase-transition processes, can be observed. In region IV, the reflection intensity (5.7 °) continuously decreases, while two broad diffraction peaks shift: 8.5→8.7 ° and 13.9→14.1 °. Both shifts correspond to the Li^+ extraction from Li_2S to form $Li_{2-y}S$ (**Equation (5.3)**). This phase transition process ($Li_2S \rightarrow Li_{2-y}S$) corresponds to the broad anodic peak (~1.23 V) in **Figure 5.6b**. The intensities of the reflection peaks decrease and shift to a higher 2θ angle during the 1st de-lithiation process (1.23→3.00 V, **Figure 5.6e**), which is due to the Li^+-ions extraction Li_2S resulting in a decrease the unit cell of Li_2S. The pronounced oxidation peak (~1.85 V) is consistent with the conversion of Fe^0 and Li_2S to $Li_{2-y}Fe_{1-x}S_2$ ($0.5 < x < 0.8$, $0 < y < 2$, **Equation (5.4)**).[146] This peak is consistent with the small plateau (~1.85 V) observed in the discharging/charging processes (**Figure 5.6a**). The oxidation of Fe^0 and Li_2S does not form the initial $Fe_{1-x}S$ material, which is concluded from the absence of the corresponding reflections at the ~3.00 V (1st de-lithiation state). The interconnected carbon microspheres, which surround the $Fe_{1-x}S$ structure, reduce the contact between $Fe_{1-x}S$ material and the electrolyte, and therefore prevent that products, such as Li_2S and $Li_{2-y}Fe_{1-x}S_2$ ($0.5 < x < 0.8$), dissolve in the electrolyte. The phase transition from Li_2S to $Li_{2-y}S$ was not detected in previous findings. After the 1st de-lithiation process, amorphous lithiated iron sulfide nanoparticles are embedded within the remaining Li_2S matrix.[147,148] The reflection peaks located at 19°~20° are attributed to copper mesh (current collector and holder $Fe_{1-x}S$/C active material). The Cu mesh consists of rather large grains, so that the orientation of only few grains fulfill the diffraction conditions due to the high brilliance of the synchrotron radiation. Therefore, the intensities of the Cu reflections scatter strongly between the patterns. Because of Cu mesh is not polycrystalline material, the poor statistics cause random errors in the observed diffraction peak intensities. A broad reflection shift (8.5→8.7 °) can be observed in **Figure 5.6d** (inset zoom Figure). **Figure 5.6e** shows the magnification of the reflection shift (13.9→14.1 °) at some chosen potentials. During the conversion reaction (from ~0.79 to ~0.01 V), the reflection becomes broader, the intensity increases and the peak shifts to a higher 2θ angle. When the potential changes from ~0.01 to ~3.00 V, the intensities of the broad reflection patterns decline and the peak continuously moves to a higher 2θ angle. Based on the above-described analysis, the electrochemical reaction during the 1st cycle can be proposed as:

Conversion step 1: (from ~1.22 V to ~0.79 V):

$$2Fe_{1-x}S + 2Li^+ + 2e^- \rightarrow Li_2Fe_{1-x}S_2 + (1-x)Fe^0 \tag{5.1}$$

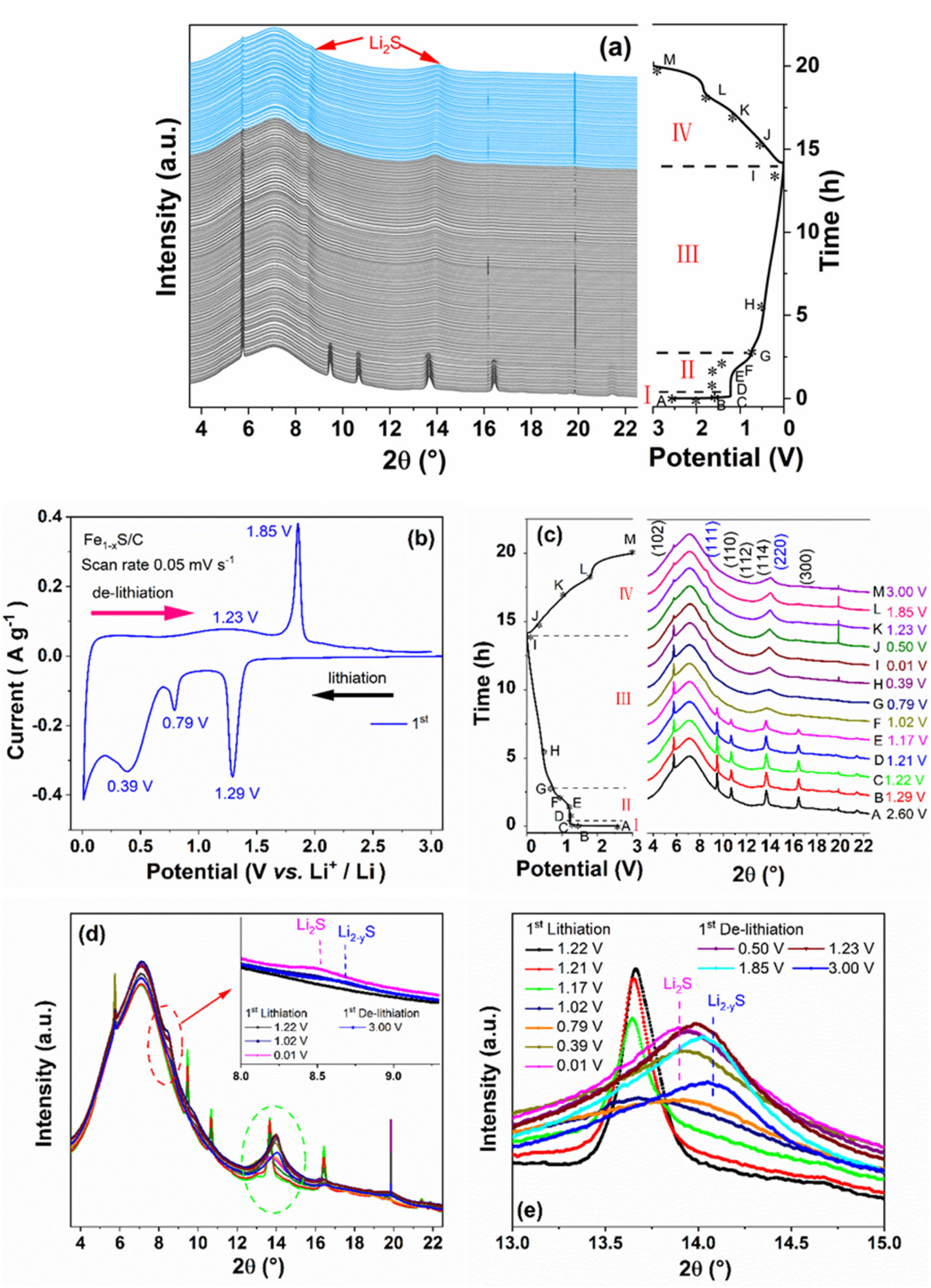

Figure 5.6 *In operando* synchrotron radiation diffraction patterns of the $Fe_{1-x}S$/C electrode during the 1st cycle: the XRD reflection patterns and the relative discharging/charging curves

(a); relative electrochemical potential profiles; the 1st CV curve of the $Fe_{1-x}S$/C electrode (b); XRD reflection patterns at the specific potentials (c); (d) the magnification of the reflection (8.5→8.7 °); the magnification of the reflection shift (13.9→14.1 °) during the 1st electrochemical cycling (e).

Conversion step 2: (from ~0.79 V to ~0.01 V):

$$Li_2Fe_{1-x}S_2 + 2Li^+ + 2e^- \rightarrow 2Li_2S + (1-x)\ Fe^0 \tag{5.2}$$

De-lithiation process: (from ~0.01 V to ~3.00 V):

$$Li_2S \rightarrow Li_{2-y}S + yLi^+ + ye^- \tag{5.3}$$

$$2Li_2S + (1-x)Fe^0 \rightarrow Li_{2-y}Fe_{1-x}S_2 + (2+y)Li^+ + (2+y)e^- \quad (0.5 < x < 0.8) \tag{5.4}$$

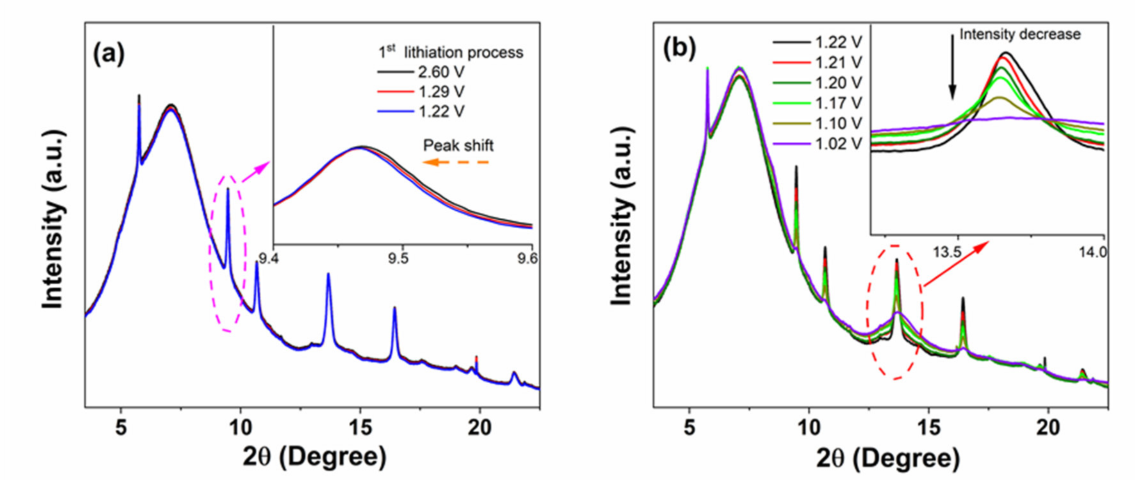

Figure 5.7 (a) The magnification of the reflection shift (9.4-9.6 °) during the 1st lithiation process (2.60→1.22 V); (b) The reflection intensity (13.2-14.0 °) decreases during the 1st lithiation process (1.22→1.02 V).

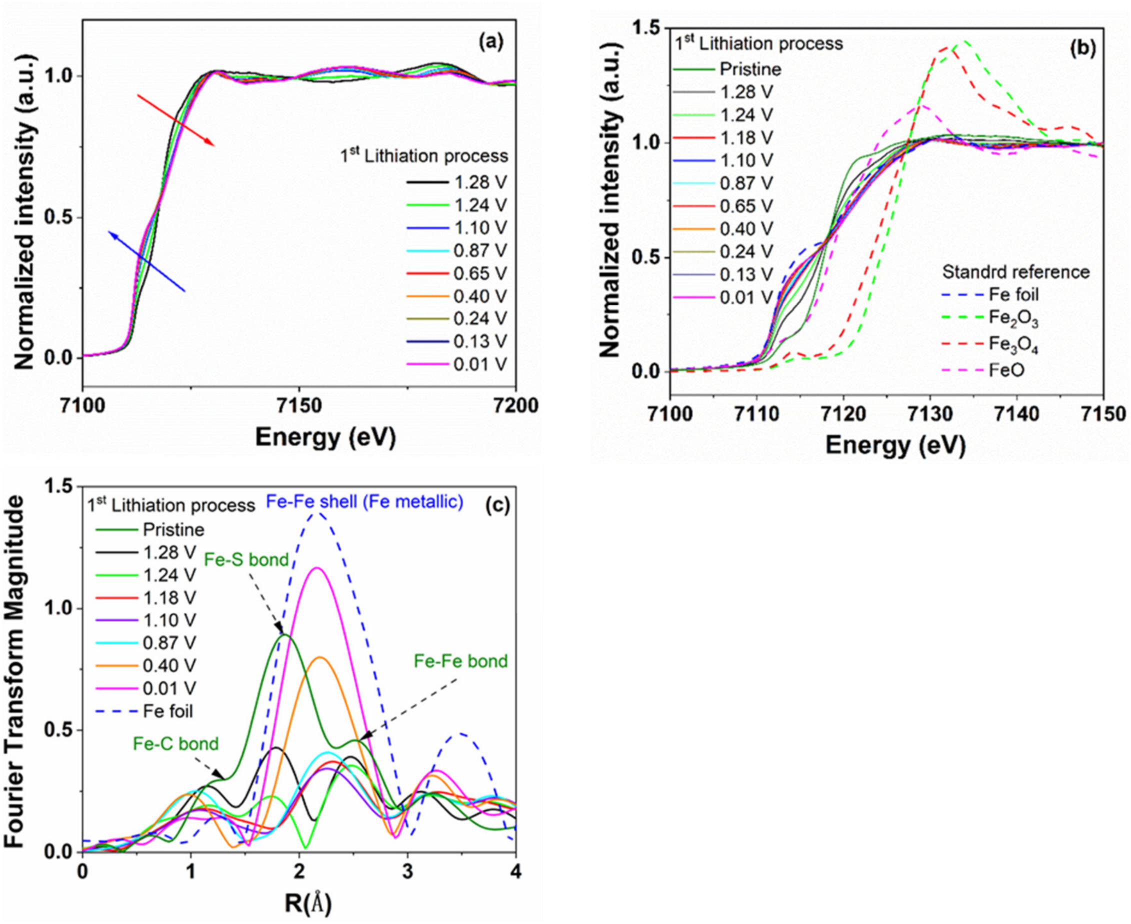

Figure 5.8 The Fe K-edge XANES of the $Fe_{1-x}S/C$ electrode at different potentials (a) and compared with some iron oxides standard references (b). The Fe K-edge FT-EXAFS spectra of the $Fe_{1-x}S/C$ electrode during the 1st lithiation process (c).

To further study the local environment and electronic transitions of the $Fe_{1-x}S/C$ electrode during the first lithiation/de-lithiation processes, *in operando* XAS was applied. The Fe K-edge X-ray absorption near-edge structure (XANES) of the $Fe_{1-x}S/C$ electrode (**Figure 5.8a**) presents a continuous move to lower edge energy (blue arrow) together with the changing edge slope (red arrow), corresponding to the decreasing of the oxidation state of Fe and dramatically structural changes (~1.28 V→~0.01 V). The conversion reaction of the $Fe_{1-x}S$ material can also be proved by the appearance of several isosbestic points in all regions of the spectra. In comparison with some standard reference samples in **Figure 5.8b**. The oxidation state of the pristine $Fe_{1-x}S/C$ is Fe^{2+}, confirmed by the spectrum is very near to the one of the FeO standard reference. Clearly, in the potential region between OCV and ~ 0.01 V, the spectrum shifts from FeO to the Fe foil reference. This phenomenon is due to the progressive reduction of $Fe_{1-x}S$

upon lithium insertion. During the 1st lithiation process, the magnitude of Fourier transforms (FT) of Fe K-edge Extended X-ray absorption fine structure (EXAFS) spectra of $Fe_{1-x}S/C$ is presented in **Figure 5.8c**. The FT-EXAFS peak of the pristine material (OCV) at 1.86 Å can be assigned to a Fe-S bond. The FT-EXAFS peak at 2.55 Å could be attributed to the Fe-Fe bond in $Fe_{1-x}S$ material. Additionally, the FT-EXAFS peak at 1.38 Å can be fitted as Fe-C bond.[149,150] During the reduction process (OCV →~1.28 V→ ~1.24 V), the abovementioned three FT-EXAFS peaks become weaker and weaker, which is because $Fe_{1-x}S/C$ structure gradually deforms as more Li^+-ions insert. The newly appeared peaks (after ~1.18 V) at 2.2 Å [67] are attributed to the Fe-Fe coordination shell of the metallic Fe^0. The amplitude of the peaks related to metallic Fe^0 at ~0.01 V is smaller than the one of Fe foil reference. This small discrepancy is because of the Fe foil reference has a body-centered cubic (bcc) structure, in comparison, the formed nanometer-sized metallic Fe^0 is amorphous.[151,152]

5.3.3 Electrochemical impedance spectroscopy evolution and morphological characteristics during the 1st lithiation and de-lithiation processes

To further investigate the charge transfer kinetics and resistive contributions during the 1st cycle, EIS measurements are performed and presented in **Figure 5.9**. **Figure 5.9a** and **b** display the experimental and fitted spectra obtained at various potentials. The zoom in the high-to-middle frequency region (from 190 kHz to 218 mHz) is displayed in **Figure 5.9a** and **b**. **Figure 5.9c** depicts the equivalent circuit used for fitting the spectra at the specific potentials. The equivalent circuit is described in **section 1.4.7**. One of the Nyquist plot fitting examples at the lithiation state (0.48 V) is shown in **Figure 5.10**. **Figure 5.9d** displays the variations of R_{el} during the 1st reduction process. The average R_{el} value during the 1st de-lithiation process is higher than that during the 1st lithiation process. R_{el} slightly increases from 3.8 Ω to 4.3 Ω during the 1st lithiation process, and R_{el} decreases from 4.4 Ω to 4.2 Ω during the 1st de-lithiation process. The changes of R_{el} is due to the SEI formation process consuming Li^+-ion and organic compounds from the electrolyte.[153] The changes of R_{SEI} at various potentials are shown in **Figure 5.9e**. During the 1st lithiation process (~1.04 V→~0.01V), R_{SEI} increases from 30 Ω to 45 Ω, which is due to the formation of SEI at lower potential upon Li^+ insertion. During the 1st de-lithiation process (~0.10 V→~2.00 V), R_{SEI} declines from 47 Ω to 26 Ω. The above-mentioned variation of the R_{SEI} indicates that the SEI film is formed during Li^+-ions insertion process and it is decomposed during Li^+-ions extraction.[154,155] Additionally, at the beginning of the 1st lithiation process (~2.00 and ~1.05 V), the Nyquist plots display one semicircle in the

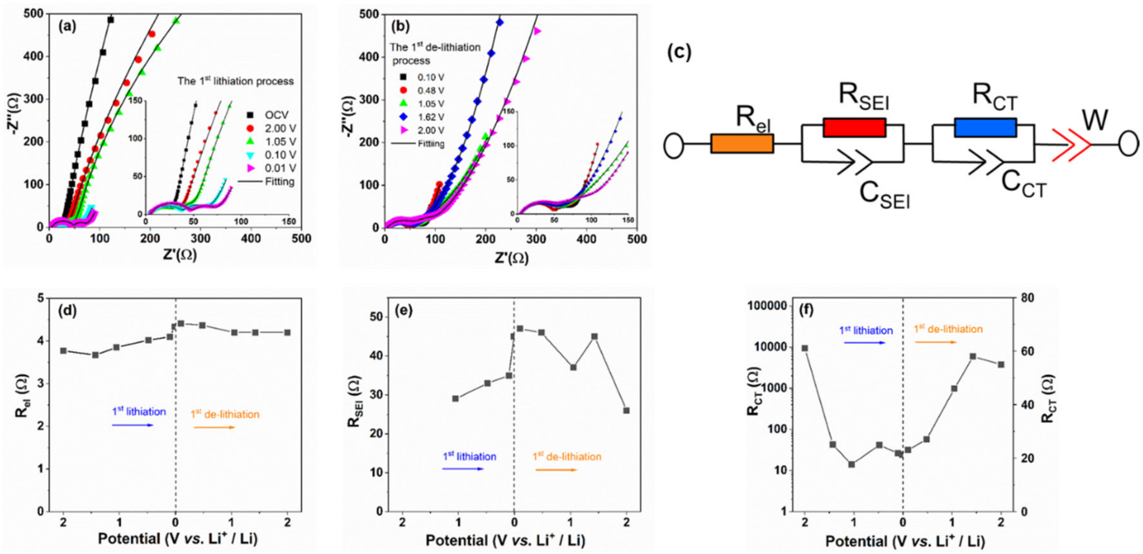

Figure 5.9 Nyquist plots of the $Fe_{1-x}S$/C electrode were obtained from EIS measurements (the zoom figures show the Nyquist plots in the high-middle frequency region): (a) lithiation process OCV-~0.01 V; (b) de-lithiation process ~0.01-~2.00 V; (c) The equivalent circuit used for fitting the EIS experiment data; (d) electrolyte resistance R_{el}; (e) SEI resistance R_{SEI}; (f) charge transfer resistance R_{CT}.

high-frequency region (from 190 kHz to 27 Hz). On the other side, when the potential is ~0.10 and ~0.01 V, the Nyquist plots are composed of two semicircles (the one at higher frequencies corresponding to R_{SEI}), which further confirms that the SEI is formed at low potentials. Additionally, the slope of the $Fe_{1-x}S$/C electrode declines with the decrease of the potential (from ~2.00 to ~0.01 V) in the low-frequency region (from 18 mHz to 218 mHz), which implies fast Li^+ mobility as more Li^+-ions insert. During the 1st lithiation process (~2.00 V→~1.05 V), the R_{CT} sharply declines from 9359 Ω to 14 Ω (**Figure 5.9f**), then the R_{CT} increases again from 14 Ω to 42 Ω with the potential decreases (~1.05 V→ ~0.48 V). The much lower R_{CT} values at the potential of ~1.43-1.05 V is because of the initial Li^+-ions insertion process ($Fe_{1-x}S \rightarrow Li_2Fe_{1-x}S_2$), accompanied by fast charge transfer kinetics. The charge transfer kinetics becomes slow during the subsequent conversion reaction ($Li_2Fe_{1-x}S_2 \rightarrow Li_2S + Fe^0$) which also includes the formation of the SEI layer, as observed by the increase of R_{CT} at ~1.05-0.48 V. During the 1st de-lithiation process, R_{CT} increases to 58 Ω (~1.43 V). The increases of R_{CT} is caused by Li^+-ions extraction from a less conductive SEI. By increasing the potential to ~2 V the R_{CT} decreases to 55 Ω, indicating that the SEI decomposes at high potential. Zhao *et al.*[88] demonstrated similar findings in another type of conversion materials.

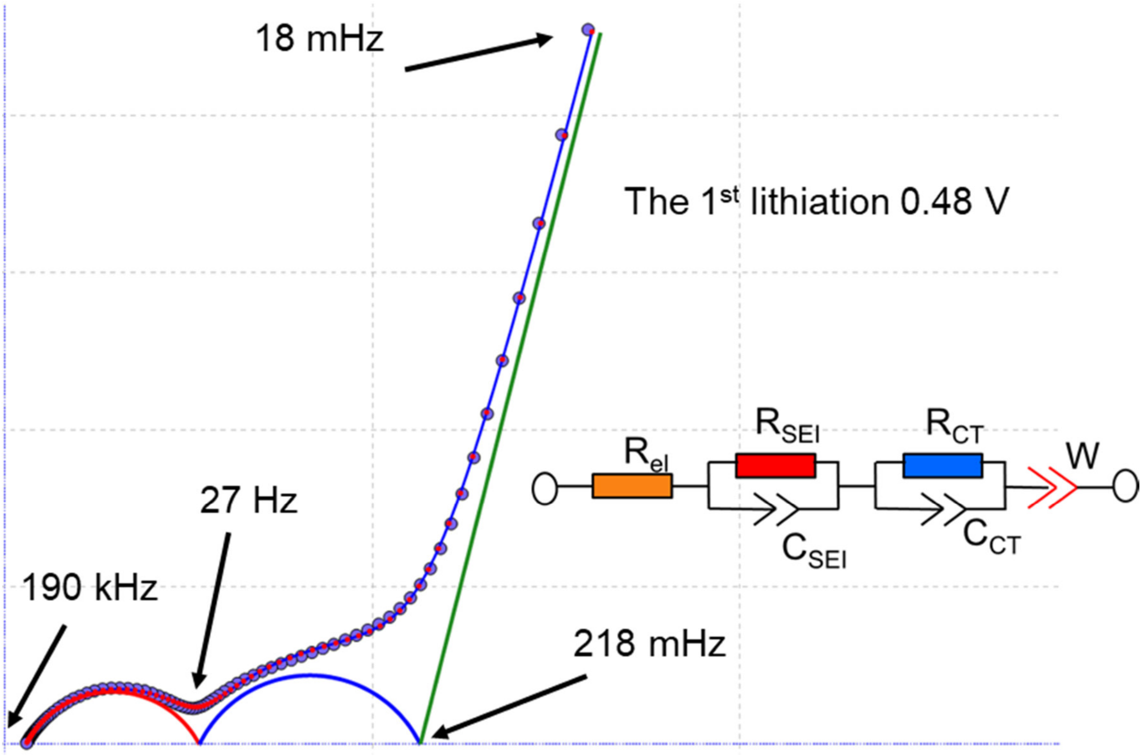

Figure 5.10 Nyquist plot obtained at the 1st lithiation 0.48 V of the $Fe_{1-x}S$/C electrode.

Figure 5.11 presents the surface morphology changes of the fresh $Fe_{1-x}S$/C electrode and electrodes at the 1st lithiation and de-lithiation states. The fresh electrode (**Figure 5.11a** and **d**) is composed of homogeneously distributed $Fe_{1-x}S$ (50～60 nm) interconnected with carbon spheres (1-2 μm). The surface morphology of the electrodes after the 1st lithiation (**Figure 5.11b** and **e**) and de-lithiation (**Figure 5.11c** and **f**) has an irreversible alteration of bigger particle size due to active material pulverization. This is assigned to the Li^+ insertion/extraction into/from the active material, resulting in notable roughness increase and amplification of the converted grains.[156,157] As it can be observed, in the 1st de-lithiated electrode, more cavities are present in comparison with the 1st lithiated electrode, indicating that the $Fe_{1-x}S$ pulverizes already after the first cycle. These microstructural alternations provide new reaction sites in the $Fe_{1-x}S$/C electrodes, facilitating the electrochemical reaction process in the following cycles and SEI film forms.[157]

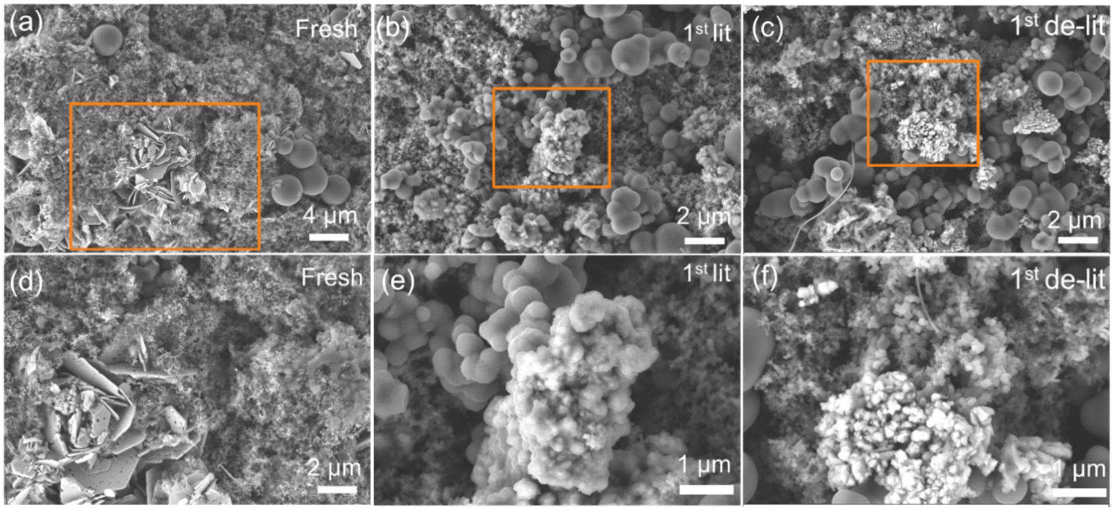

Figure 5.11 Surface morphology changes of $Fe_{1-x}S/C$ electrodes at different states: fresh electrode (a, d); the 1st lithiation electrode (b, e); the 1st de-lithiation electrode (c, f).

5.3.4 Electrochemical performance and kinetic process of FeS and $Fe_{1-x}S/C$

Since huge disparities of FeS nanosheets and $Fe_{1-x}S/C$ composites were observed by the previously described analytics, a decisively different electrochemical behavior is expected for the respective electrodes. To better understand the lithium-storage mechanism taking place in the electrodes cyclic voltammetry (CV) measurements were conducted at a scan rate of 0.05 mV s^{-1} in the voltage range from 0.01 to 3.0 V *vs.* Li^+/Li for the FeS and $Fe_{1-x}S/C$ electrodes, respectively. **Figure 5.12a** and **b** show CV profiles of the first five cycles.

The related equations from state-of-the-art literature[134,145,158–160] related to lithium insertion in FeS and Fe_3C are shown below:

$$2FeS + 2Li^+ + 2e^- \rightarrow Li_2FeS_2 + Fe^0 \quad (5.5)$$

$$FeS + 2Li^+ + 2e^- \rightarrow Li_2S + Fe^0 \quad (5.6)$$

$$2Li_2S + Fe^0 - (x+2)Li^+ - (x+2)e^- \rightarrow Li_{2-x}FeS_2 \quad (5.7)$$

$$Li_{2-x}FeS_2 + xLi^+ + xe^- \rightleftharpoons Li_2FeS_2 \quad (5.8)$$

$$Li_2FeS_2 + 2Li^+ + 2e^- \rightarrow 2Li_2S + Fe^0 \quad (5.9)$$

$$Fe_3C + 1/6Li \rightleftharpoons Li_{1/6}C + 3Fe^0 \quad (5.10)$$

The lithium storage mechanism for Fe_3C is based on conversion mechanism, it is reported that only 1/6 Li per unit can insert Fe_3C material (around 26 mAh g^{-1}),[160] and the phase fraction of Fe_3C in $Fe_{1-x}S/C$ is 3 %. It is expected that the capacity contribution from Fe_3C for $Fe_{1-x}S/C$ electrode is negligible. Considering the CV of the FeS electrode, three reduction peaks appear at 1.7 V, 1.26 V, and 0.76 V, while only one oxidation peak appears at 1.88 V during the first scan. According to previous literature reports,[134,145,159] the small peak at 1.7 V corresponds to the formation of the intermediate phase Li_2FeS_2 during the Li^+ insertion into the FeS bulk (**Equation (5.5)**). The sharp peak at around 1.26 V is related to the conversion reaction belonging to the formation of metallic Fe nanocrystals and Li_2S matrices (**Equation (5.6)**).[78] The broad peak at 0.76 V is assigned to the formation of solid electrolyte interphase (SEI) on the electrode surface.[161] In the first anodic process, the oxidation peak at 1.88 V corresponds to the oxidation of metallic Fe^0 to form $Li_{2-x}FeS_2$ (**Equation (5.7)**).[162] In the subsequent cycles, the reduction peaks at 0.76 and 1.26 V shift to 0.79 and 1.42 V, respectively, and the oxidation peak at 1.88 V shifts to 1.91 V. Those changes indicate that some irreversible reactions occur during the first electrochemical process. During the second to fifth cathodic scans, a new broad reduction peak appears at 2.0 V and can be related to the phase transformation from $Li_{2-x}FeS_2$ to Li_2FeS_2 (**Equation (5.8)**).[146] The sharp peak at 1.42 V corresponds to the lithiation process (**Equation (5.9)**). Correspondingly, the oxidation peak at 1.91 V in the second cycle accounts for the reversible de-lithiation process from Li_2FeS_2 to $Li_{2-x}FeS_2$ (**Equation (5.8)**).[78,145] Upon the first five CV scans, the intensity of the redox peaks gradually decreases indicating that the capacity decreases. This might result from the unstable formation of the SEI layer and the sluggish reaction kinetics of pure FeS nanosheets.[133,158] The CV curves of the $Fe_{1-x}S/C$ electrode are similar to those of FeS except for the additional broad cathodic peak at 0.39 V, which is attributed to side reactions between the $Fe_{1-x}S/C$ material and the electrolyte and SEI formation.[163] The conversion reaction between Fe_3C and Li can be described as **Equation (5.10)** with less capacity contribution. Moreover, the intensity of the reduction/oxidation peaks are much weaker due to the interconnected carbon spheres. Comparing the CV curves of FeS and $Fe_{1-x}S/C$ electrodes the peak current densities and the peak potentials of the $Fe_{1-x}S/C$ electrode barely change after the first cycle. This points out that better structural stability and good reversibility is accomplished for the $Fe_{1-x}S/C$ electrode. In addition, the polarization voltage of the $Fe_{1-x}S/C$ electrode is 0.46 V which is lower than that of the FeS electrode (0.50 V). This demonstrates that the interconnected carbon spheres morphology improves the conductivity of the $Fe_{1-x}S/C$ electrode leading to a reduced electrode polarization.

Figure 5.12c and **d** display the lithiation/de-lithiation profiles of FeS and $Fe_{1-x}S/C$ electrodes at the 1st, 2nd, 5th, 35th, 80th, 140th, 225th, and 500th cycle at a specific current of 1 A g^{-1}. During the first lithiation of the FeS electrode, a long potential plateau at around 1.3 V and a short potential plateau at 0.8 V are observed, which corresponds to the lithiation process forming Li_2S, Fe, and the SEI layer formation, respectively. During the de-lithiation process, the long potential plateau at 1.8 V is related to the formation of $Li_{2-x}FeS_2$. All these potential plateaus are in agreement with the peaks observed in the CV curves. The FeS electrode delivers a first lithiation capacity of 900 mAh g^{-1} and a de-lithiation capacity of 782 mAh g^{-1} with a Coulombic efficiency of 87 %. An irreversible capacity of 118 mAh g^{-1} at the first cycle results from the inevitable formation of the SEI film on the surface of the active material and electrolyte decomposition.[133] In the second and fifth cycle, the reduction and oxidation plateaus shift to 1.4 and 1.9 V, respectively. The reason is an increased electrode polarization. In the second cycle, The FeS electrode delivers a de-lithiation capacity of 763 mAh g^{-1} while the Coulombic efficiency increases to 97 %. After the 5th cycle, it still delivers a lithiation capacity of 760 mAh g^{-1} and a de-lithiation capacity of 738 mAh g^{-1} with the Coulombic efficiency of 97 %. Examining the subsequent cycles of the FeS sample (the 35th, 80th, and 140th) a drop of the reduction plateau to lower potentials accompanied by a gradual decrease in de-lithiation capacity can be observed. This behavior is attributed to an enhancement of the electrode polarization during cycling. Furthermore, in the 225th and 500th cycles no pronounced potential plateau is observed implying structural changes or pulverization. After the 500th cycle, the voltage plateau disappears and the electrode delivers a very low de-lithiation capacity of 150 mAh g^{-1}. This fact confirms that the structure of FeS nanosheets is destroyed. When comparing the FeS sample to the $Fe_{1-x}S/C$ sample, the potential plateau of the $Fe_{1-x}S/C$ electrode is much shorter. During the first lithiation process, two plateaus are located at 1.3 and 0.8 V corresponding to the formation of Li_2S, Fe, and SEI layers, respectively. A broad peak at 1.20 V corresponds to the oxidation of Fe^0 and a very short potential plateau at 1.8 V related to $Li_{2-x}FeS_2$ formation is observed in the first de-lithiation process. In the first cycle, the $Fe_{1-x}S/C$ electrode shows lithiation and de-lithiation capacities of 946 and 530 mAh g^{-1}, respectively and a Coulombic efficiency of 56 %. The huge irreversible capacity of 416 mAh g^{-1} is attributed to the SEI layer formation, electrolyte decomposition and side reactions. In the subsequent cycles, the reduction plateau shifts from 1.3 to 1.4 V and the long slope disappears implying that an irreversible reaction occurred. In the second cycle, it delivers a de-lithiation capacity of 490 mAh g^{-1} and the Coulombic efficiency increases to 93 % while the 5th cycle

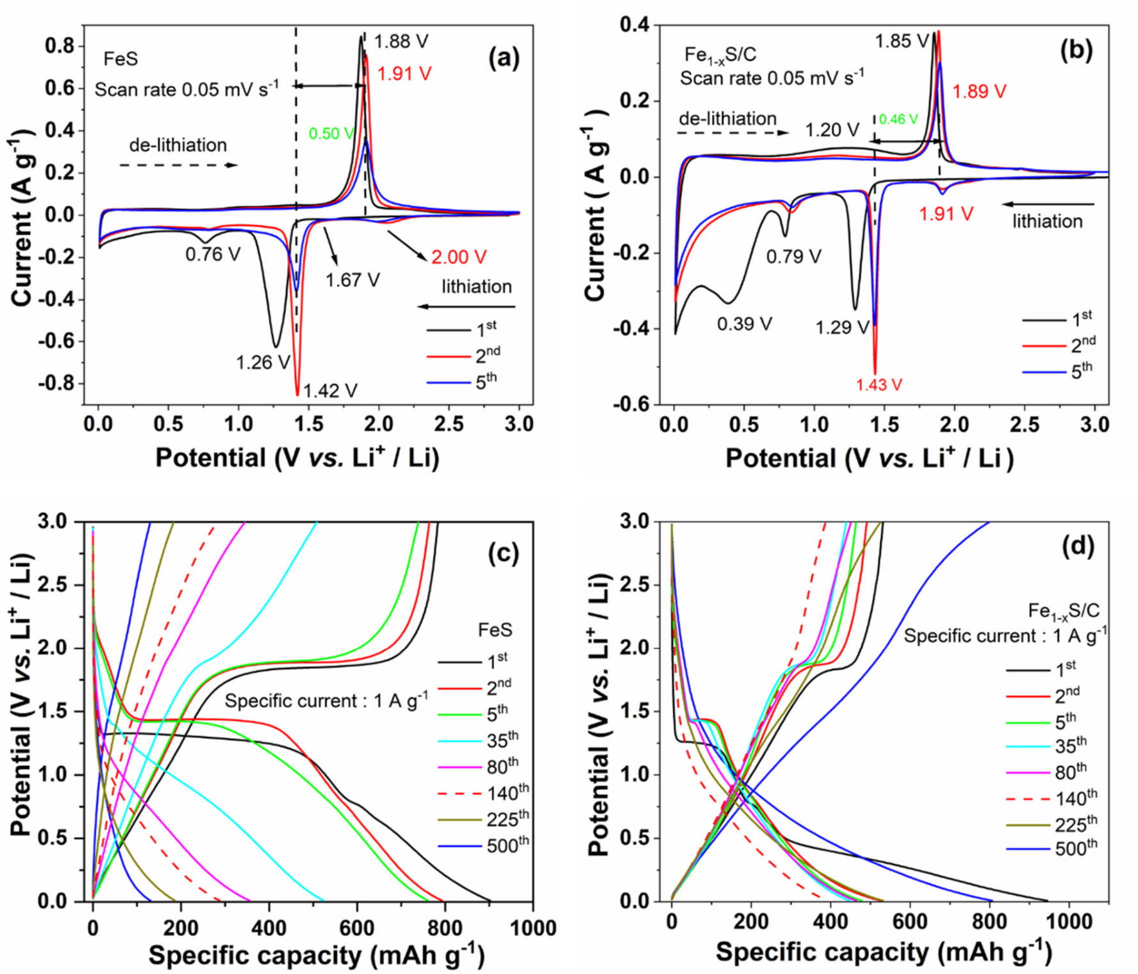

Figure 5.12 CV curves of FeS (a) and $Fe_{1-x}S/C$ (b) electrodes at a scan rate of 0.05 mV s^{-1}; galvanostatic lithiation/de-lithiation capacity profiles at different cycles for FeS (c) and $Fe_{1-x}S/C$ (d) electrodes at the specific current of 1 A g^{-1}.

shows a lithiation capacity of 476 mAh g^{-1} and a de-lithiation capacity of 463 mAh g^{-1} with a CE of 97 %. It becomes apparent that the length of potential plateau decreases upon cycling (the 5th, 35th, 80th, and 140th). At the 140th cycle, the potential plateau disappears and the electrode shows the lowest capacity of 395 mAh g^{-1}at this state. Interestingly, a capacity increase of the $Fe_{1-x}S/C$ electrode is observed upon further cycling. It is important to note that the lithiation/de-lithiation profiles after the 140th cycle with no clear plateau is strongly different from that at the first five cycles. Moreover, the specific capacity increases to 800 mAh g^{-1}. According to the conversion mechanism for lithium storage, Fe_3C can insert only 1/6 Li per unit (26 mAh g^{-1}), which is negligible compared to the high capacity of 800 mAh g^{-1}.[160]

This novel phenomenon has been observed for the first time and will be discussed hereafter in detail.

To evaluate the new effect of interconnected carbon spheres on FeS-based electrodes, rate performances were applied at different specific currents in the voltage range from 0.01 to 3.0 V *vs.* Li^+/Li for the FeS and $Fe_{1-x}S/C$ electrodes and are shown in **Figure 5.13a** and **b**, respectively. On the one hand, the FeS electrode delivers 874, 819, 748, 674, 624, and 460 mAh g^{-1} at specific currents of 0.1, 0.2, 0.5, 1, 2, and 5 A g^{-1}, respectively. When the specific current is set back to 0.1 A g^{-1} the specific capacity reaches 788 mAh g^{-1}. On the other hand, the $Fe_{1-x}S/C$ electrode delivers 815, 676, 610, 572, 532, and 457 mAh g^{-1} at specific currents of 0.1, 0.2, 0.5, 1, 2, and 5 A g^{-1}, respectively. As the specific current returns to 0.1 A g^{-1} the specific capacity can be rebound to 724 mAh g^{-1}. **Figure 5.13c** directly compares the capacity values of FeS and $Fe_{1-x}S/C$ electrodes at the various specific currents. Between 0.1 and 2 A g^{-1}, the FeS electrode displays higher capacities with respect to the $Fe_{1-x}S/C$ electrode. However, at the highest specific current (5 A g^{-1}) both electrodes deliver the same specific capacity of 460 mAh g^{-1}. Furthermore, long-term cycling performance of FeS and $Fe_{1-x}S/C$ electrodes were investigated at a specific current of 1 A g^{-1} for the potential range of 0.01-3.0 V *vs.* Li^+/Li (**Figure 5.13d**). Both electrodes display a different behavior upon cycling. Despite the FeS electrode initially shows a much higher capacity compared to the $Fe_{1-x}S/C$ electrode, its capacity rapidly fades to 130 mAh g^{-1}. Apart from that, the $Fe_{1-x}S/C$ electrode shows a capacity fluctuation during the first 140 cycles. After that, the capacity increases to 800 mAh g^{-1} after 500 cycles. A possible reason for such extra-capacity could be the catalytic activation of Fe_3C. It is reported that Fe_3C plays the role of catalyst to decrease the concentration of SEI components and boost the reversible formation/decomposition of the SEI layer upon cycling.[79,160] Besides that, the $Fe_{1-x}S/C$ particles are shrinking due to pulverization, leading to higher electrochemical efficiency. Additionally, smaller particles can lead to higher capacities due to less inactive material parts. Most plausible, the abovementioned trends result from surface-capacitive behavior of the material and therefore improve the electrochemical kinetics.

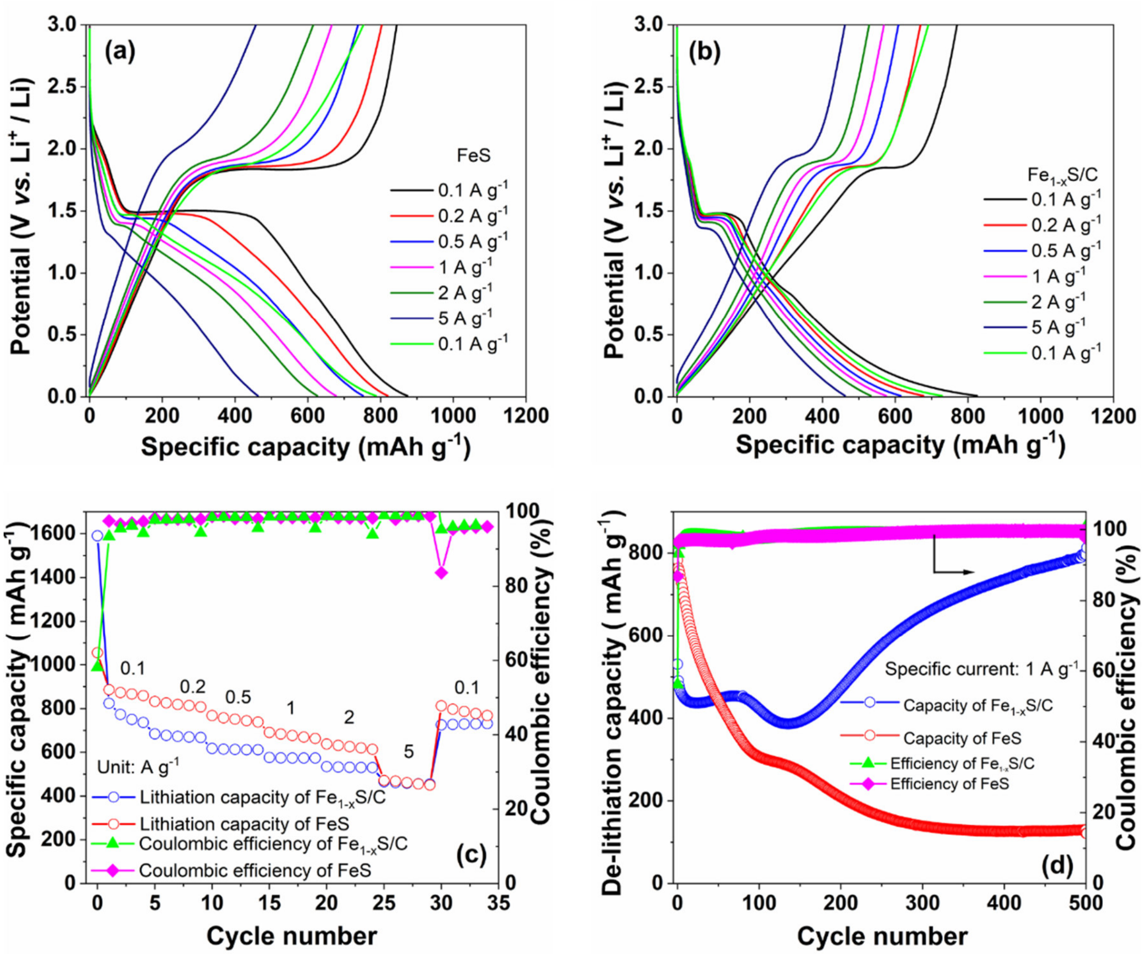

Figure 5.13 Lithiation and de-lithiation capacity profiles of FeS (a) and $Fe_{1-x}S/C$ (b) electrodes at different specific currents; rate performance of FeS and $Fe_{1-x}S/C$ electrodes (c); long-term cycling and CE of FeS and $Fe_{1-x}S/C$ electrodes at a specific current of 1 A g^{-1}.

To prove the transformation of diffusion-controlled behavior to surface-capacitive energy storage process after 140 cycles, CVs measurements were conducted at various scan rates. This experiment should allow insights into the storage mechanism during initial cycling. **Figure 5.14a** and **b** show CV profiles of FeS and $Fe_{1-x}S/C$ electrodes at scan rates between 0.05 and 10 mV s^{-1}. **Figure 5.14c** and **d** present the linear relationship between the log (*i*) and log (*v*) at cathodic and anodic peaks for FeS and $Fe_{1-x}S/C$ electrodes, respectively. According to **Equation 1.11-1.12 (section 1.4.6)**, after linear fitting, the calculated b value of cathodic and anodic peaks for the FeS electrode are 0.40 and 0.46, respectively; while that for the $Fe_{1-x}S/C$ electrode are 0.53 and 0.64, respectively. As expected, this analysis confirms that the ion-diffusion behavior controls the electrochemical process in both FeS and $Fe_{1-x}S/C$ electrodes for the initial cycles. The diffusion-controlled mechanism can explain the initial capacity fading.

An enhanced stress is applied to the FeS active material by diffusion as compared to a surface controlled process. Therefore, an initial pulverization and phase amorphization of both samples is expected leading to a contact loss between the particles which results in an inferior percolation an increased resistance. We expect that the interconnected carbon spheres matrix of the $Fe_{1-x}S/C$ sample buffers the pulverization and allows a stable change to a surface-capacitive mechanism during cycling. In this case, the interconnected carbon spheres undertake the role of a conductive matrix with pulverized FeS nanoparticles distributed on it. Those particles exhibit surface-capacitive behavior which is indicated by the loss of the plateaus and the simultaneous capacity increase. To prove this interpretation, further cycling experiments and *ex*-situ measurements were conducted and are presented in the following chapter.

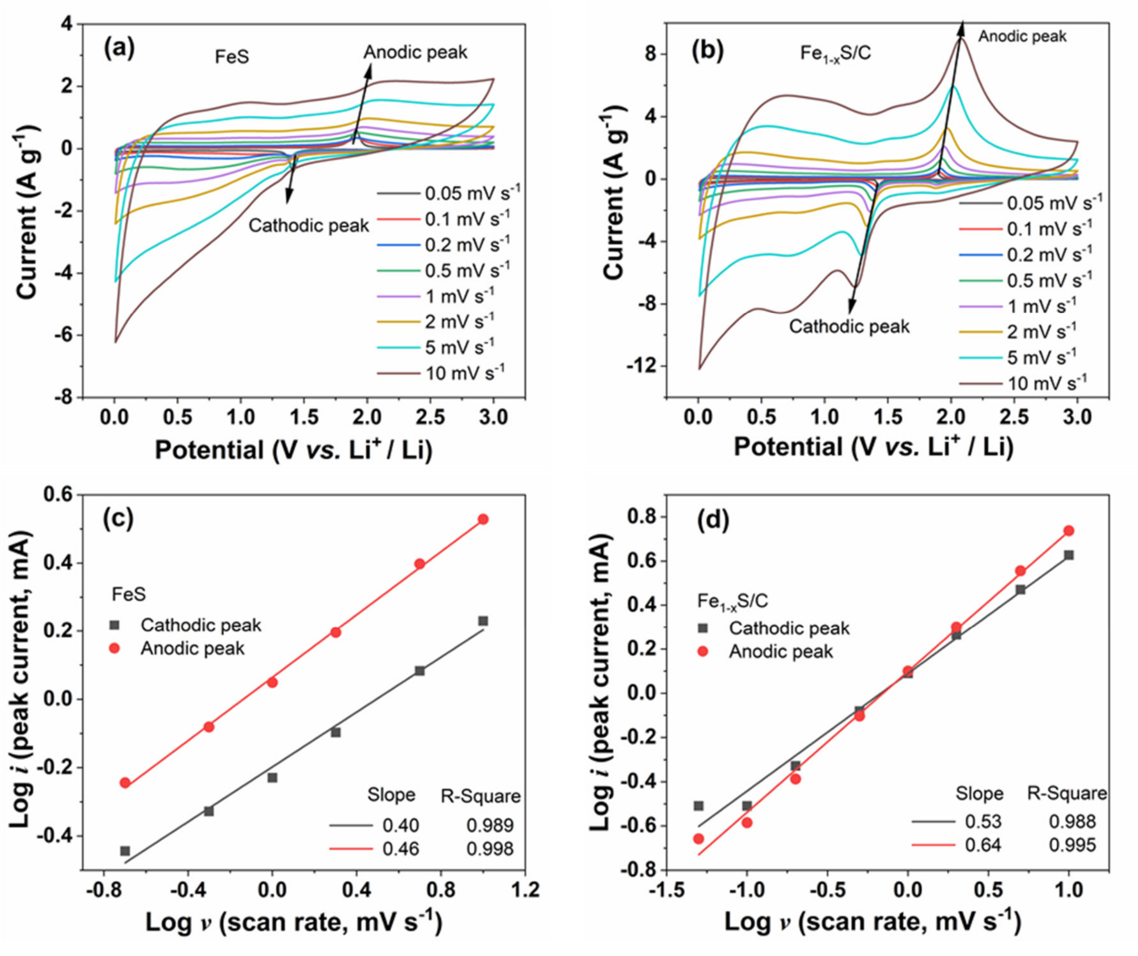

Figure 5.14 CV profiles at various scan rates ranging from 0.05 to 10 mV s^{-1} for FeS (a) and $Fe_{1-x}S/C$ (b) electrodes; the linear relationship between the log (*i*) and log (*v*) at cathodic and anodic peaks for FeS (c) and $Fe_{1-x}S/C$ (d) electrodes.

5.3.5 Phase fraction, morphology and electrochemical performance of the cycled electrode

The above-shown results highlight that the lithium storage mechanism strongly changes during cycling. In order to understand this mechanism, FeS and $Fe_{1-x}S/C$ electrodes have been analyzed after the 140th galvanostatic cycle by complementary techniques such as CV, *ex-situ* XRD, and SEM. To understand the differences between fresh and cycled electrodes, CV measurements were performed after different cycle numbers and shown in **Figure 5.15a** and **c**. It can be observed that after the 140th cycle at 1 A g^{-1} the redox peaks become weaker for both the FeS (**Figure 5.15a**) and the $Fe_{1-x}S/C$ electrode (**Figure 5.15c**). This demonstrates an unstable cycling feature resulting from irreversible phase transitions and pulverization. It is noted that in the $Fe_{1-x}S/C$ electrode, the oxidation peak becomes broader and shifts (from 1.89 to 2.05 V) after 140 cycles, which indicates that the $Fe_{1-x}S/C$ electrode has higher resistance upon cycling. This result is deeply analyzed by electrochemical impedance spectroscopy (EIS) measurements and will be shown later. The oxidation/reduction peaks are nearly disappearing for the FeS electrode, implying that the faradaic reaction does not exist anymore. More interestingly, the cathodic peak (located at 0.84 V) of the $Fe_{1-x}S/C$ electrode appears at the 5th CV cycle of the fresh electrode due to the formation of SEI. However, there is a very broad cathodic peak in the 5th CV recorded after 140 cycles, which is related to some irreversible reactions. **Figure 5.15b** and **d** present CVs of FeS and $Fe_{1-x}S/C$ electrodes at different sweep rates after the 140th cycles. Cycled electrodes show no clear peaks compared with that of fresh ones (**Figure 5.14a** and **b**). This confirms that the amorphous phases exist in the cycled electrode.

To further investigate the phase fraction and phase transition during the repeated lithiation/de-lithiation processes, *ex-situ* XRD of $Fe_{1-x}S/C$ and FeS electrodes at the 9th, 140th, and 500th cycle are performed and shown in **Figure 5.16a** and **b**, respectively. The FeS and $Fe_{1-x}S/C$ show sharp and clear XRD reflection patterns (**Figure 5.1a** and **b**), while XRD reflection patterns of the cycled $Fe_{1-x}S/C$ electrode shows broad reflections, corresponding to Li_2S and $Li_{2-x}FeS_2$. The reason behind this is that during repeated lithiation and de-lithiation processes, the material becomes amorphous. In contrast, the XRD reflection of the FeS electrode becomes sharper (such as 30°, 32°, and 37°), indicating that the particle size increases upon cycling.

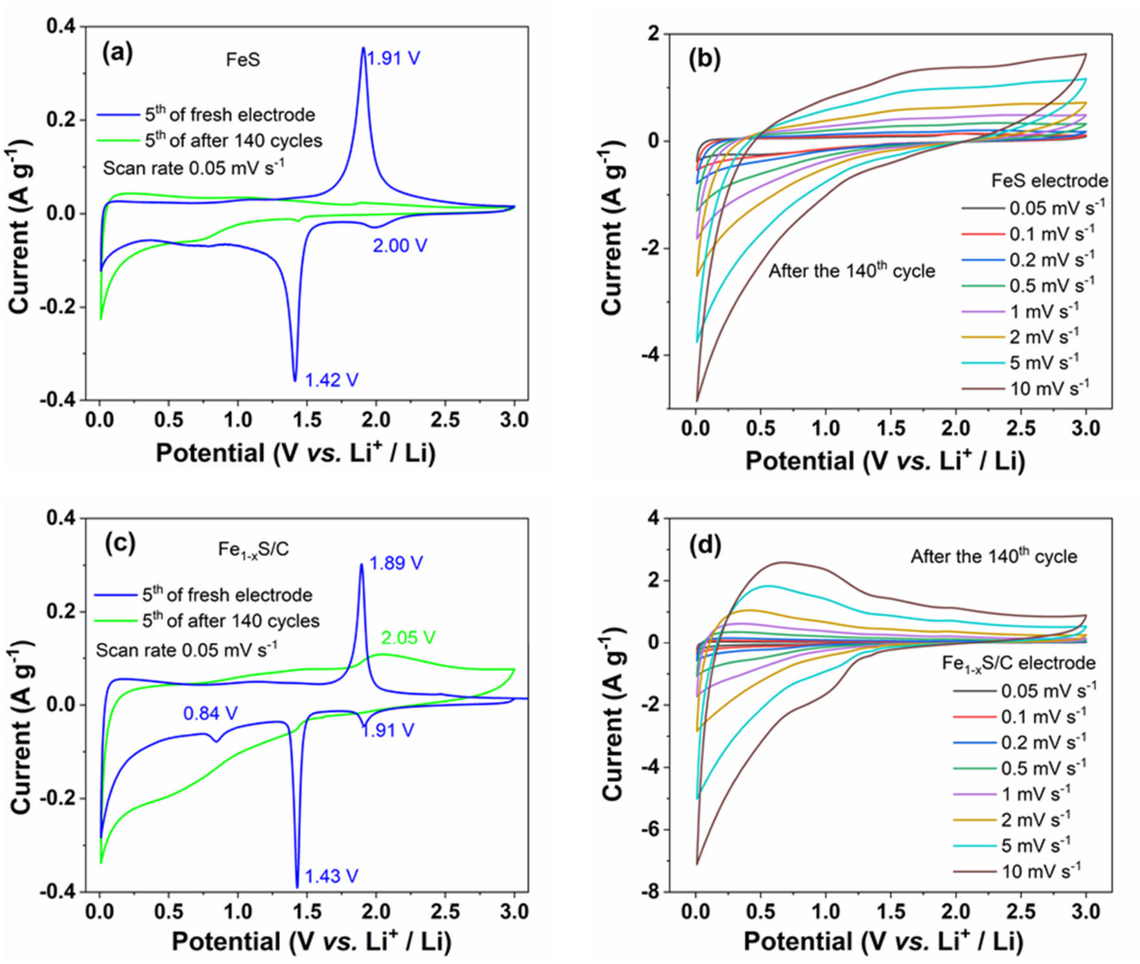

Figure 5.15 The 5th CV curves of the fresh electrode and after the 140th cycle for FeS (a) and $Fe_{1-x}S/C$ (c) electrodes; CV profiles at different sweep rates between 0.05 and 10 mV s^{-1} for FeS (b) and $Fe_{1-x}S/C$ (d) electrodes.

Figure 5.17a-c show the *ex-situ* SEM of the FeS electrode at the 9th, 140th, and 500th cycle. Compared with the fresh FeS pristine material, the morphology of the cycled FeS particle has an irreversible change. Comparing the *ex-situ* SEM images of FeS electrode at different cycles, it is interesting that some small clusters of FeS particles tend to agglomerate and form a large bulk, especially in the regions I, II, and III. The *ex-situ* SEM image of the 9th cycle is composed of nanoparticles and many holes (region I, **Figure 5.17a**), while the FeS particles crowd together and the holes disappear after the 140th cycle (region II, **Figure 5.17b**). Finally, the particles further agglomerate forming a large bulk at the 500th cycle (region III, **Figure 5.17c**). The nanoparticle agglomeration is not beneficial for the reaction between active material and electrolyte during cycling, this can explain the specific capacity decreases of the FeS electrode

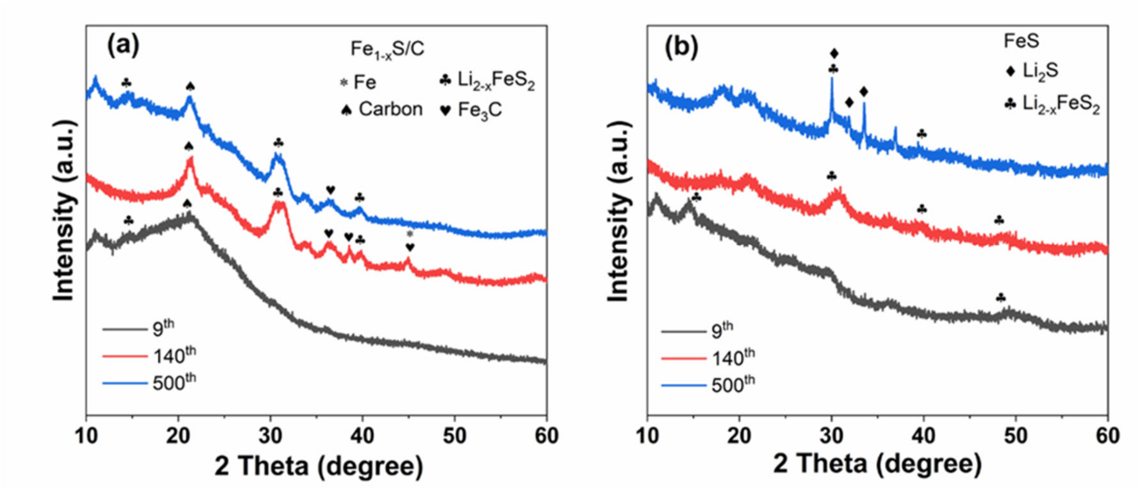

Figure 5.16 *Ex-situ* XRD reflection patterns of $Fe_{1-x}S/C$ (a) and FeS electrodes (b) at the 9th, 140th, and 500th cycle (λ=1.5406 Å). Note: fluorescence radiation contributed the observed high background.

upon cycling. Moreover, the *ex-situ* SEM of the $Fe_{1-x}S/C$ particles at the 9th (**Figure 5.17d**) cycle shows large agglomerated clusters which are wrapped by SEI films similar to the FeS electrode. The particle transforms into smaller ones (**Figure 5.17e** and **f**, at the 140th and 500th cycle) and tends to interconnect with each other upon cycling. This kind of smaller particles equally distributed with the interconnected carbon spheres can enlarge the contact between the active material and electrolyte thus resulting in high efficiency of electrochemical reaction, which is the most probable reason for the capacity increase upon cycling.

EIS has been performed to examine the kinetics of Li^+ insertion/de-insertion processes upon cycling. **Figure 5.18a** and **b** show the Nyquist plots of the FeS electrode at different cycles (1st, 50th, 100th, 150th, and 200th) at the bias potential of 0.86 V vs. Li^+/Li during lithiation and de-lithiation processes, respectively; correspondingly, the Nyquist plots of the $Fe_{1-x}S/C$ electrode are shown in **Figure 5.18c** and **d**. The inset pictures in **Figure 5.18** display the zoom in the high-frequency area. The Nyquist plots of FeS and $Fe_{1-x}S/C$ electrodes were fitted using an equivalent circuit described in **Figure 5.9c**. each sign is explained in **section 1.4.7**.

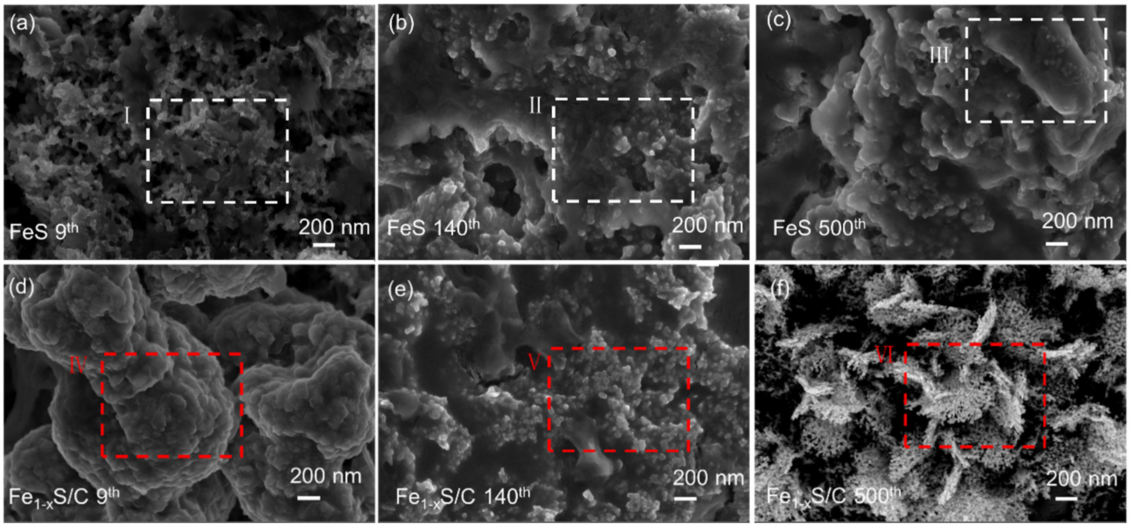

Figure 5.17 Morphological and structural changes of the FeS electrode at the 9th (a), 140th (b), and 500th (c) cycle; the corresponding *ex-situ* SEM of the $Fe_{1-x}S/C$ electrode at the 9th (d), 140th (e), and 500th (f) cycle.

It is worth to note that the overall impedance of the FeS and $Fe_{1-x}S/C$ electrode shows a resistance increase in both lithiation and de-lithiation conditions upon cycling. Comparing the Nyquist plots of FeS and $Fe_{1-x}S/C$ electrodes at some selected cycles (i.e. the 1st, 100th, and 200th) in lithiation and de-lithiation conditions (**Figure 5.19a** and **b**), it is observed that the diameter of the semicircle for the $Fe_{1-x}S/C$ electrode is smaller than that for the FeS electrode. This demonstrates that the $Fe_{1-x}S/C$ electrode has rapid electrochemical reaction kinetics that benefits from the addition of interconnected carbon spheres. Moreover, the slope in the low-frequency region for the $Fe_{1-x}S/C$ electrode is larger than that for the FeS electrode which implies faster Li^+ mobility in the $Fe_{1-x}S/C$ electrode.[67,88]

Figure 5.20 displays resistivity values as calculated by Relaxis 3 software in lithiation and de-lithiation conditions, respectively. The electrolyte resistance R_{el} for the $Fe_{1-x}S/C$ electrode (11 Ω) is almost unchanged upon cycling, while the R_{el} for the FeS electrode first increases until the 100th cycle, then it remains quite stable at 8 Ω (**Figure 5.20a** and **d**). The small difference of R_{el} value among the $Fe_{1-x}S/C$ and FeS electrode is probably due to inside cell connections. The calculated value of the R_{SEI} is shown in **Figure 5.20b** and **e**. For the $Fe_{1-x}S/C$ electrode R_{SEI} slightly increases in both lithiation and de-lithiation conditions upon cycling. Furthermore, R_{SEI} in lithiation condition is higher than that in the de-lithiation state, indicating

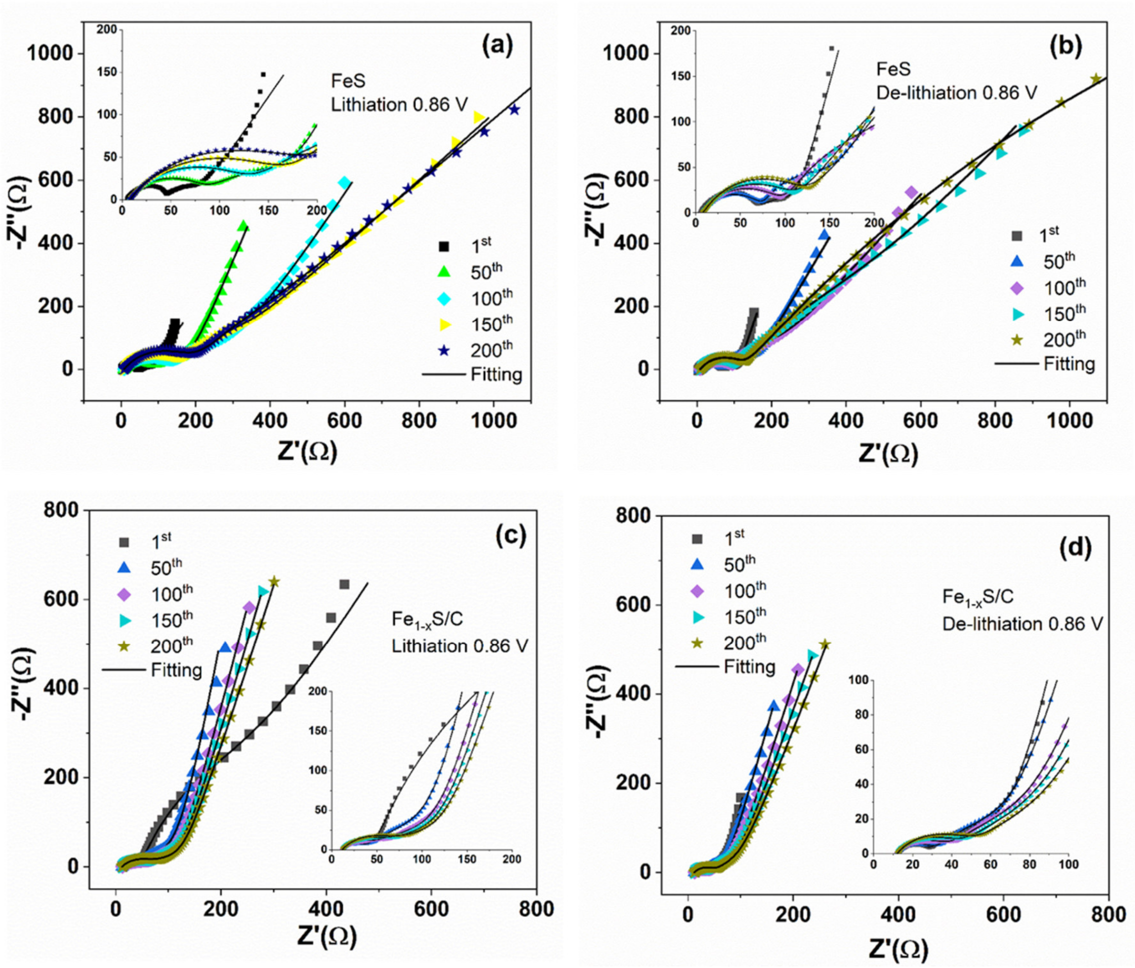

Figure 5.18 Nyquist plots of the FeS electrode at different cycles in lithiation (a) and de-lithiation (b) conditions (0.86 V); Nyquist plots of the $Fe_{1-x}S/C$ electrode at selected cycles in lithiation (c) and de-lithiation (d) states (0.86V), the inset shows the zoom of Nyquist plots in the high-frequency region.

the dynamic nature of the SEI layer which grows in the lithiation process and partially decomposes in the de-lithiation process.[154,155] R_{SEI} of the FeS electrode drastically increases during the first 100 cycles, then it decreases but remains still higher than that of $Fe_{1-x}S/C$ electrode. It is demonstrated that Fe_3C exhibits great activity in promoting the partially reversible formation/decomposition of the SEI layer.[164] R_{CT} of the $Fe_{1-x}S/C$ electrode (**Figure 5.20c**) slightly decreases in lithiation condition upon cycling, and R_{CT} value remains almost stable in the de-lithiation condition. The rapid charge-transfer kinetics of $Fe_{1-x}S/C$ may benefit from partial nanoparticles reaggregation mostly occurring during the initial cycles while the

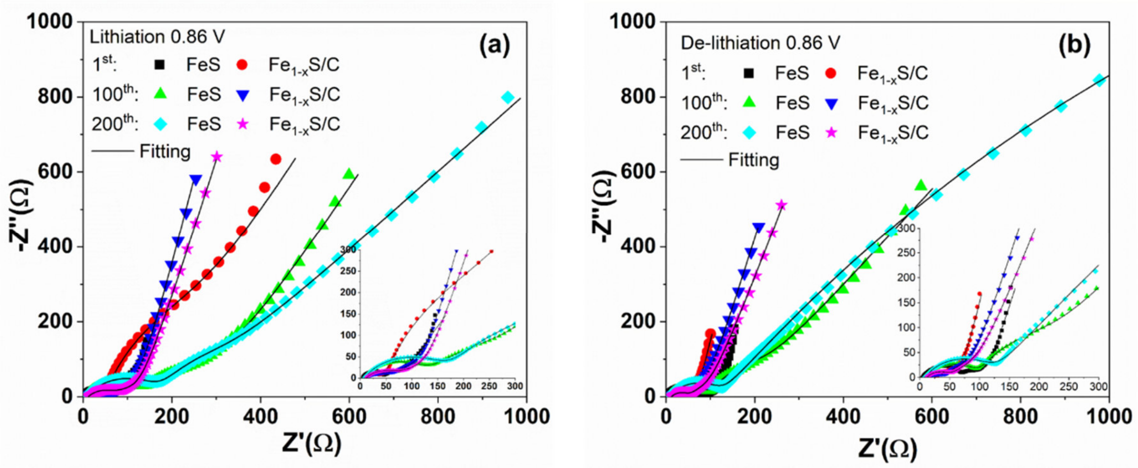

Figure 5.19 The Nyquist plots of FeS and $Fe_{1-x}S/C$ electrodes at some selected cycles (the 1st, 100th, and 200th) in lithiation (a) and de-lithiation conditions (b).

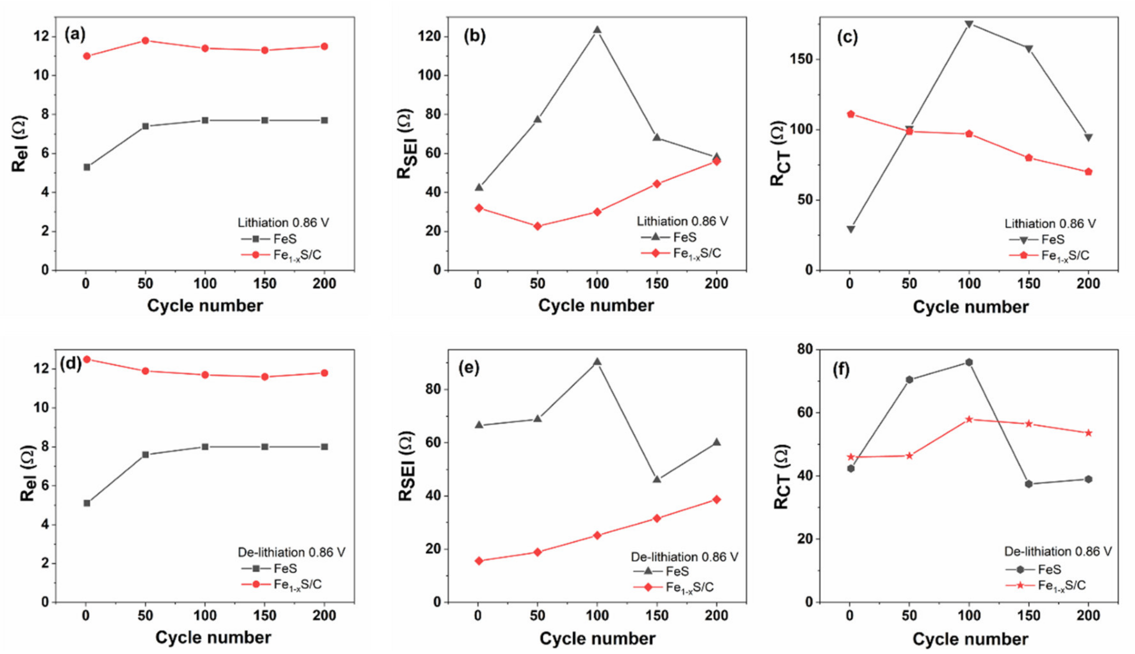

Figure 5.20 Calculated resistance values for FeS and $Fe_{1-x}S/C$ electrodes in the lithiation condition: R_{el} (a), R_{SEI} (b), R_{CT} (c); in the de-lithiation condition: R_{el} (d), R_{SEI} (e), and R_{CT} (f).

morphology appears more stabilized upon further cycling.[165] In contrast, R_{CT} of the FeS electrode sharply increases until the 100th cycle corresponding to the huge capacity decay; in subsequent cycles, R_{CT} of the FeS electrode continuously declines but is still higher than that of the $Fe_{1-x}S/C$ electrode in lithiation condition (**Figure 5.20f**). In summary, the interconnected carbon spheres morphology can improve Li^+/electron mobility and form a better protective SEI layer thus promoting the redox reaction.[27]

5.4 Conclusions

In summary, FeS nanosheets and $Fe_{1-x}S$/C nanocomposites consisting of well-dispersed FeS and Fe_3C nanoparticles and interconnected carbon spheres were synthesized via a facile hydrothermal method and a subsequent sintering process. It is observed that the interconnected carbon spheres have significant impacts on the electrochemical performance of FeS-based electrodes. The catalytic activity of Fe_3C is highlighted, which was formed as a beneficial by-product during the conducted synthesis. Due to the unique formulation of the composite, electrochemical cycling performance is significantly enhanced. This is accompanied by a continuous increase in capacity. To understand the different lithium storage mechanisms and evaluate the effect of interconnected carbon spheres on FeS-based electrodes some techniques such as CV, *ex-situ* XRD, and SEM were applied. The introduction of interconnected carbon spheres in FeS drastically affects the phase fraction, morphology, and particle size. More importantly, the interconnected carbon spheres have a profound influence on the kinetic process and crystal structure during cycling. Furthermore, such carbon spheres change the transformation of diffusion-controlled behavior to a surface-capacitive energy storage process. Indeed, interconnected carbon spheres improve the electron conductivity, reduce the crystallite sizes, and maintain structural integrity. Especially for long cycling procedures, the well-distributed FeS nanoparticles with small average diameters provide sufficient electrode-electrolyte contact areas for high lithium-ion flux across the interface. A reduction of the lithium-ion diffusion length during cycling significantly promotes the electrochemical processes, especially at high specific currents.

For the first time, the lithium storage mechanism related to $Fe_{1-x}S$/C anode was tracked in real-time during the 1st lithiation/de-lithiation processes. Electronic changes and structural alterations are investigated by combining *in operando* analytic techniques such as synchrotron radiation diffraction and XAS. The analysis of these data reveals the occurring of a phase transition $2Fe_{1-x}S + 2Li^+ + 2e^- \rightarrow Li_2Fe_{1-x}S_2 + (1-x)Fe^0$ and $Li_2Fe_{1-x}S_2 + 2Li^+ + 2e^- \rightarrow 2Li_2S + (1-x)\ Fe^0$ dring the 1st lithiation process. *In operando* XAS confirms the redox reaction of $Fe^{2+} + 2e^- \rightleftharpoons Fe^0$ and the Fe K-edge XAS transformation process. During the 1st de-lithiation process, Fe^0 and Li_2S convert to $Li_{2-y}Fe_{1-x}S_2$ and Li^+ is extracted from Li_2S

to form $Li_{2-y}S$. Here is the first time that the phase transition from Li_2S to $Li_{2-y}S$ $(0 < y < 2)$ is detected. After the 1st de-lithiation process, amorphous lithiated iron sulfide nanoparticles are embedded within the remaining Li_2S matrix. HR-TEM proves the presence of Fe_7S_8 and FeS in $Fe_{1-x}S$/C nanocomposites. The amorphous carbon layer is also observed by TEM. XPS also confirms the presence of carbon, which provides the electronic pathway for fast charge transfer and buffers the lithiation/de-lithiation-induced volume variation. The kinetic process demonstrates that SEI film is formed during Li^+-ions insertion process and then it is decomposed during Li^+-ions extraction. Furthermore, *ex-situ* SEM shows that the surface morphology has an irreversible alteration due to $Fe_{1-x}S$ pulverization. These results can shed light on the lithium storage mechanism for conversion-type material, especially for the iron-deficient sulfides.

6 Investigation of SnS_2-rGO Sandwich Structure as Anodes for Sodium-ion and Potassium-ion Batteries

6.1 Introduction

NIBs and KIBs have been receiving much attention due to the more abundance sodium and potassium and low cost.[166–170] NIBs have been well investigated in the latest years with achieving practical progress. However, the research of KIBs is still in the early stage.[171,172] Currently, carbon-based anode materials cannot fulfill the increasing demands for NIBs and KIBs, which have high energy storage density and power density. Hence, developing alternative anode materials with stable cycling performance, high reversible capacity, and superior rate capability is critical for both NIBs and KIBs.

Among the reported NIBs and KIBs anodes, many metal oxides have been investigated. Especially transition metal oxides suffer from several problems when employed as anode materials which limit their use. The swelling and shrinking of active materials particles lead to electrodes pulverization during Na^+/K^+-ions insertion/extraction processes.[173,174] This behavior is quite challenging and needs to be addressed. Therefore, the Fe_2O_3@C material is not selected as a research target. Compared with metal oxides, metal sulfides have captured tremendous interest due to their low cost and environmental friendliness. The crystallographic van der Waals gaps of metal sulfides are beneficial for Na^+/K^+-ions insertion/extraction, which generates a large capacity. Moreover, metal-sulfur bonds are less ionic than metal-oxide bonds, which is kinetically favorable for the conversion reaction, leading to good reversibility redox kinetics and reversibility.[8,175,176] These advantages are the major motivations that drive the research of metal sulfides as NIBs and KIBs anodes to date.

Among them, Sn-based compounds such as Sn_4P_3,[177,178] and SnS_2[80,179] undergoing conversion and alloying reactions are expected to be promising anode candidates owing to their high theoretical capacities. Therefore, FeS-based materials capable of only conversion reactions are also not chosen as a research target. SnS_2, with a layered CdI_2 crystalline-like structure ($a = b = 3.65$ Å, $c = 5.90$ Å, space group *P-3m1*) consists of tin atoms sandwiched between two hexagonal layers of sulfur atoms. Many research on SnS_2 in LIBs and NIBs is already published: For example, Li *et al.*[180] reported the SnS_2@C electrode (80 wt% of the whole electrode mass) delivered a reversible capacity of 629 mAh g^{-1} at 0.2 A g^{-1} after 200 cycles in SIBs. Zhang *et al.*[181] prepared 3D honeycomb-like rGO anchored with SnS_2 quantum dots (3D SnS_2 QDs/rGO) composite electrode (70 wt% of the whole electrode mass) with 862 mAh g^{-1} for LIB at 0.1 A g^{-1} after 200 cycles, 233 mAh g^{-1} for SIB at 0.5 A g^{-1} after 200 cycles. However, there is a lack of a systematic research of SnS_2-based materials in NIBs and KIBs.

The layered structure SnS_2, in which the CdI2-type layers are loosely bounded by weak van der Waals forces and hence easily susceptible to the intercalation of Na^+/K^+-ions.[182–184] Additionally, a large interlayer spacing (0.59 nm) makes SnS_2 suitable to host Na^+/K^+-ions through the intercalation process. However, the poor electronic conductivity and the huge volume expansion during repeated electrochemical reaction resulting in the pulverization of active materials and the rapid capacity decay, impede its practical applications. Previous studies reported that combining nanostructured SnS_2-based material with a conducting matrix is an effective way to improve the electrochemical properties of electrodes. For example, Li *et al*. reported SnS_2 cross-linked by carbon nanotubes (CNTs) anode electrode (80 wt% of total electrode mass) for SIBs which achieved a high reversible specific capacity of 758 mAh g^{-1} at 100 mA g^{-1} and a superior rate capability.[185] Lakshmi *et al.* prepared SnS_2 nanoparticles anchored onto reduced graphene oxide (rGO) (80 wt% of total electrode mass) through a chemical route, which displays an impressive capacity of 350 mAh g^{-1} at 25 mA g^{-1}.[80] Especially, rGO with large surface area, excellent conductivity, and good flexibility, was considered as an outstanding matrix for loading layered materials. However, in the reported research works,[81–84] the assembly between nano-SnS_2 and carbon matrixes is mostly based on poor physical interconnection. The interfacial bonding between active particle and carbon matrixes is not very intimate and effective, which makes it difficult to keep the electrode integrity. Therefore, it is highly desirable to develop controllable and reliable strategies for the fabrication of novel nanostructured SnS_2/carbon-matrixe composites.

Herein a composite of porous few-layer SnS_2 nanosheets *in situ* grown on reduced graphene oxide (SnS_2-rGO) is produced via hydrotherameral reaction. The novel structure built from SnS_2 nanosheets is closely anchored on the surface of rGO sheets via a strong C-O-Sn bond. The designed structure is featured with: 1) porous few-layer SnS_2 nanosheets providing a shortened diffusion route for sodium/potassium-ions movement and mass transport. The porous structure can alleviate mechanical strain, which is caused by repeated sodium/potassium-ion insertion/extraction resulting in huge volume expansion; 2) rGO layers work as high-speed electronic pathways and a flexible cushion layer to buffer the anisotropic volumetric expansion. Therefore, the unique hybrid material is endowed with high electrochemical activity. A durable SnS_2-rGO electrode with a high specific capacity, superior rate capability, and stable cycling performance for NIBs and KIBs is presented. The structural evolution and phase transformation of the SnS_2-rGO electrode upon cycling are tracked by *ex-situ* SEM. Meanwhile, the effects of different carbon composites (Super P and C65) and the influence of the electrolyte additive fluoroethylene carbonate (FEC) on the electrochemical performance in NIBs and KIBs are evaluated. Furthermore, the kinetics of underlying processes is investigated by electrochemical impedance spectroscopy.

6.2 Experiment

Synthesis of $MnCO_3$ microcubes template: $MnCO_3$ microcubes were synthesized by a simple mixing method.[186] Typically, $MnSO_4 \bullet H_2O$ (1 mmol, 0.17 g) and $(NH_4)_2SO_4$ (10 mmol, 1.32 g) were dissolved in 70 ml of water, then 7 ml of ethanol was added with stirring. NH_4HCO_3 (10 mmol, 0.79 g) was dissolved in water (70 ml) with stirring. After all solutions complete dispersion, the NH_4HCO_3 solution was added to the mixture mentioned above at room temperature. After around 2 min the final solution turned milky white, which indicated the initial formation of $MnCO_3$ microcubes. The mixture solution was maintained at 50 °C aged for 9 h in an oven. $MnCO_3$ microcubes were separated from the reaction mixture by centrifugation and washed several times with deionized water and ethanol to remove impurities. Finally, $MnCO_3$ microcubes were dried at 50 °C in an oven.

Synthesis $MnCO_3$@SnS_2-rGO: 210 mg Tin (IV) chloride pentahydrate ($SnCl_4 \cdot 5H_2O$, Sigma-Aldrich, 98 %) and 300 mg thioacetamide acid (TAA, C_2H_5NS, Sigma-Aldrich, 99 %) were dissolved in 50 ml of ethanol solution. Subsequently, 140 mg as-prepared $MnCO_3$ microcubes template was dispersed in the above solution. Then, 10 ml graphene oxide solution (4 mg/ml, dispersion in H_2O, Sigma-Aldrich) was added into the mixture solution. The mixture solution was stirred for 60 min at room temperature. Finally, the solution was transferred into a 100 ml Teflon-lined autoclave and heated at 120 °C for 12 h. After cooling down to room temperature, the product was centrifuged and washed serval times with deionized water. The product was dried at 80 °C.

Synthesis porous SnS_2-rGO: The above-harvested $MnCO_3$@SnS_2-rGO (75 mg) was dispersed into the hydrochloric acid solution (0.1 M, 10 ml) to selectively remove the $MnCO_3$

microcubes template at room temperature for 24 h. After washing with deionized water several times, the final product SnS_2-rGO was dried at 60 °C.

Materials characterization: The crystal structure and phase purity of the sample was characterized at PETRA-III (DESY, Hamburg) by using powder diffraction beamline P02.1 (λ=0.20723 Å). XPS, SEM/EDX, TEM, OEA, and Raman measurements are performed and described in **section 4.2**.

Electrochemical characterization: The working electrode was fabricated by mixing 70 mass % SnS_2-rGO powder, 20 mass % carbon black (C65, Timcal Ltd.), and 10 mass % carboxymethyl cellulose (Sigma-Aldrich) dissolved in deionized water (3 wt %) in a speed-mixer (DAC150.1 FVZ) from Hauschild. SnS_2-rGO and carbon black were first mixed at 800 rpm for 2 min without solvent. Then, ethanol was added and mixed (1000 rpm for 10 min and 2500 rpm for 10 min, respectively) to harvest a viscous paste. Finally, the binder solution was added and mixed at 800 rpm for 10 min. the slurry was coated on aluminium foil and dried at 80 °C for one day. Then, the electrodes were cut into discs (12 mm in diameter) and dried at 120 °C overnight under vacuum condition. The mass loading of SnS_2-rGO is 1.5-2.0 mg cm^{-2} with a thickness of 65 μm. For comparison, another carbon (Super P, Timcal Ltd.) was also used as electronic conducting additive, the working electrode was made in the same way.

Electrochemical measurements were performed by using three-electrode Swagelok-type half cells, the cells were assembled inside an argon-filled glovebox (MBraun, O_2 and $H_2O \leq$ 0.5 ppm). For NIBs cells, a sodium metal foil was used as a counter electrode and reference electrode. 1 M sodium perchlorate ($NaClO_4$) dissolved into ethylene carbonate/dimethyl carbonate (EC: DMC=1:1 in mass) was used as sodium-based electrolyte. For KIBs cells, a potassium metal foil was used as a counter electrode and reference electrode. 1 M potassium bis(fluorosulfonyl) (KFSI) dissolved into EC: DMC=1:1 in mass was used as potassium-based electrolyte. A glass-fiber disc (Whatman GF/D) was used as a separator. Since Fluoroethylene carbonate (FEC) was confirmed for improving cycling stability in LIBs, therefore, to check the effects of FEC on the SnS_2-rGO electrode in NIBs and KIBs. 5 wt% FEC additive was added into $NaClO_4$ and KFSI electrolytes, respectively. All electrochemical measurements were conducted on multichannel potentiostat (VMP3, Bio-Logic), and the cells were put in a climate chamber (Binder) at room temperature. Galvanostatic discharge/charge with potential limitation (GCPL) and Cyclic Voltammetry (CV) were measured in the potential range of a

0.01-3.0 V *vs.* Na^+/Na and 0.01-3.0 V *vs.* K^+/K, respectively. Electrochemical impedance spectroscopy (EIS) experiments was performed scanning from 10 mHz to 500 kHz at different selected potentials. The EIS data were collected every 10 cycles and impedance spectra were analyzed utilizing Relaxis 3 software (rhd Instruments, Germany).

6.3 Results and Discussion

6.3.1 Structure and morphology

The crystal structure and phase fraction of the product is investigated by X-ray diffraction (XRD) as shown in **Figure 6.1a**. The Rietveld refinement reveals that the SnS_2-rGO composite is composed of SnS_2 and rGO. The SnS_2 phase (63 %) has space group of *P-3m1*, the lattice parameters are: $a=b=3.621 \pm 0.002$ Å, $c=6.443 \pm 0.002$ Å. The lattice constant along c-direction increases a little bit from 5.9 Å to 6.4 Å, which probably due to the effect of water and ethanol during the synthesis process. Wang *et al.*[187] obtained the SnS_2 nanosheets with much higher c-direction (9.7 Å), which caused by solvent molecules intercalation interlayer or the cysteine decomposition. The rGO phase (37 %) has space group of *Fmmm*, and the lattice parameters are: $a= 2.464 \pm 0.002$ Å, $b=4.154 \pm 0.002$ Å, $c=6.271 \pm 0.002$ Å. The XPS measurements are employed to further investigate the chemical composition and elemental oxidation states of the as-prepared SnS_2-rGO. Two peaks at 487.2 and 495.6 eV correspond to the Sn $3d_{5/2}$ and Sn $3d_{3/2}$, which confirms the presence of Sn^{4+} in SnS_2.[84,179] The additional two small peaks at 488.0 and 496.4 eV are related to the Sn $3d_{5/2}$ and Sn $3d_{3/2}$ of Sn^{4+} in SnO_2 (**Figure 6.1b**). This is caused by a conversion of SnS_2 to SnO_2 on the surface. The S 2p spectrum (**Figure 6.1c**) can be divided into two kinds of doublets. The first doublet is composed of the peaks located at 162.1 eV (S $2p_{3/2}$) and 163.3 eV (S $2p_{1/2}$) corresponding to binding energies of SnS_2.[188] The second doublet consists of the peaks at 164.0 eV (S $2p_{3/2}$) and 165.1 eV (S $2p_{1/2}$), which are attributed to the formation of C-S-C, implying that S is possibly covalently bonded with carbon.[179,189,190] The C 1s spectra (**Figure 6.1d**) can be assigned to four signals: 285.0 eV for C-C/C=C, 286.0 eV for C-O-C, 287.0 eV for C-S, and 289.1 eV for O-C=O.[191,192] These results further support that SnS_2-rGO composites have been successfully obtained.

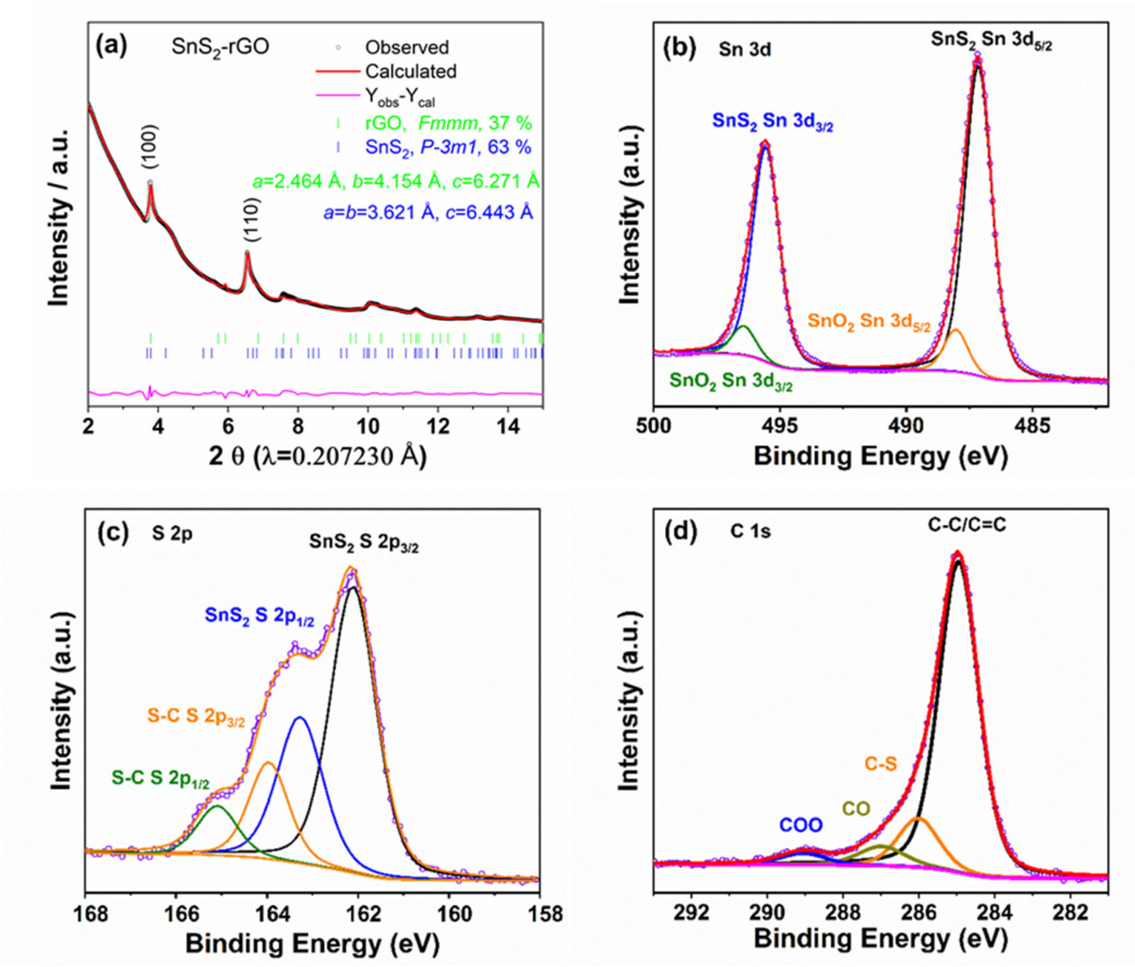

Figure 6.1 Rietveld refinement from X-ray radiation diffraction data of SnS$_2$-rGO (a), high-resolution XPS spectra Sn 3d (b), S 2p (c), and C 1s (d) of SnS$_2$-rGO.

The Rietveld refinement reveals the MnCO$_3$ template with the space group of *R-3c* and the cell parameters are *a*=*b*= 4.795 Å*, c*=15.692 Å (**Figure 6.2a**). The controlled self-assembly of MnCO$_3$ shows a microcube structure with an average size of 2-3 μm (**Figure 6.2c**). The intermediate product MnCO$_3$@SnS$_2$-rGO (**Figure 6.2d**) sample shows a typical nanosheet structure. MnCO$_3$ microcubes in the MnCO$_3$@SnS$_2$-rGO product are observed (**Figure 6.2d**). The MnCO$_3$ template was removed by hydrochloric acid treatment to obtain a porous structure. The developed vacancies surrounding the SnS$_2$ nanosheets are beneficial for facilitating the electrolyte impregnation and counteract volume variations during repeated electrochemical cycling measurements. Additionally, the Raman spectra of the porous SnS$_2$-rGO is given in **Figure 6.2b**. The peak at 311.7 cm^{-1} is related to the A$_{1g}$ Raman-active vibration mode. The rGO is characterized by the disordered D band and graphitic G band located at 1330 and 1590 cm^{-1}, which are assigned to the defects in the hexagonal graphitic layer and the vibration of carbon atoms in a 2D hexagonal lattice, respectively.[193–195] The intensity ratio of I_D/I_G is 1.17, which indicates that the rGO has a highly disordered carbon structure compared with the well-ordered graphite ($I_D/I_G < 0.5$).

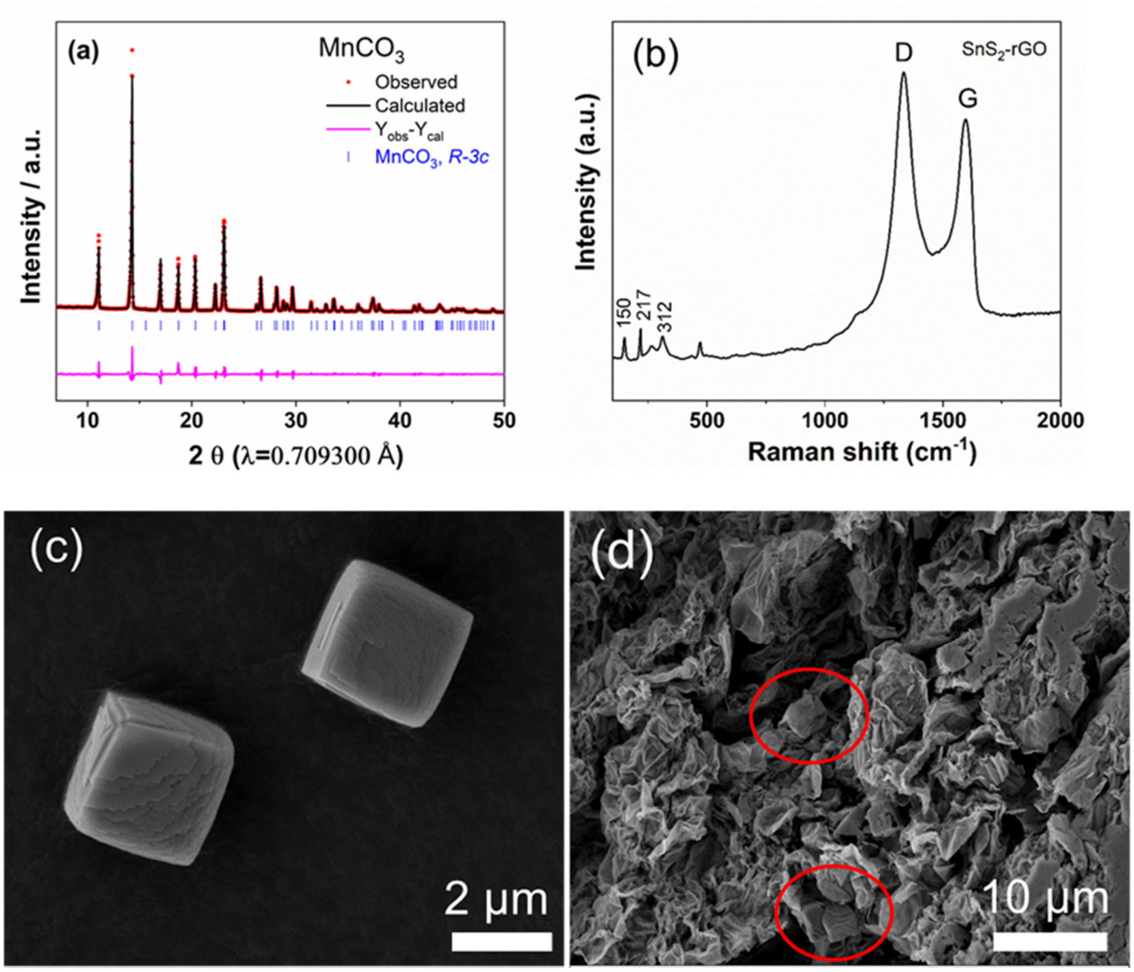

Figure 6.2 XRD patterns of the $MnCO_3$ microcubes template (a); Raman spectra of the SnS_2-rGO (b); SEM images of the $MnCO_3$ microcubes template (c) and $MnCO_3$@SnS_2-rGO (d).

The SnS_2-rGO (**Figure 6.3a**) displays a rippled sheet-like morphology. The high magnification SEM image (**Figure 6.3b**) shows that SnS_2 nanocrystals are ranging from 2 to 4 nm in size and reveals few-layered features. The EDX mappings demonstrate that the SnS_2-rGO (**Figure 6.4a**) is composed of Sn (**Figure 6.4b**), S (**Figure 6.4c**), and C (**Figure 6.4d**). The signals are homogeneous, which indicates a uniform distribution of the chemical

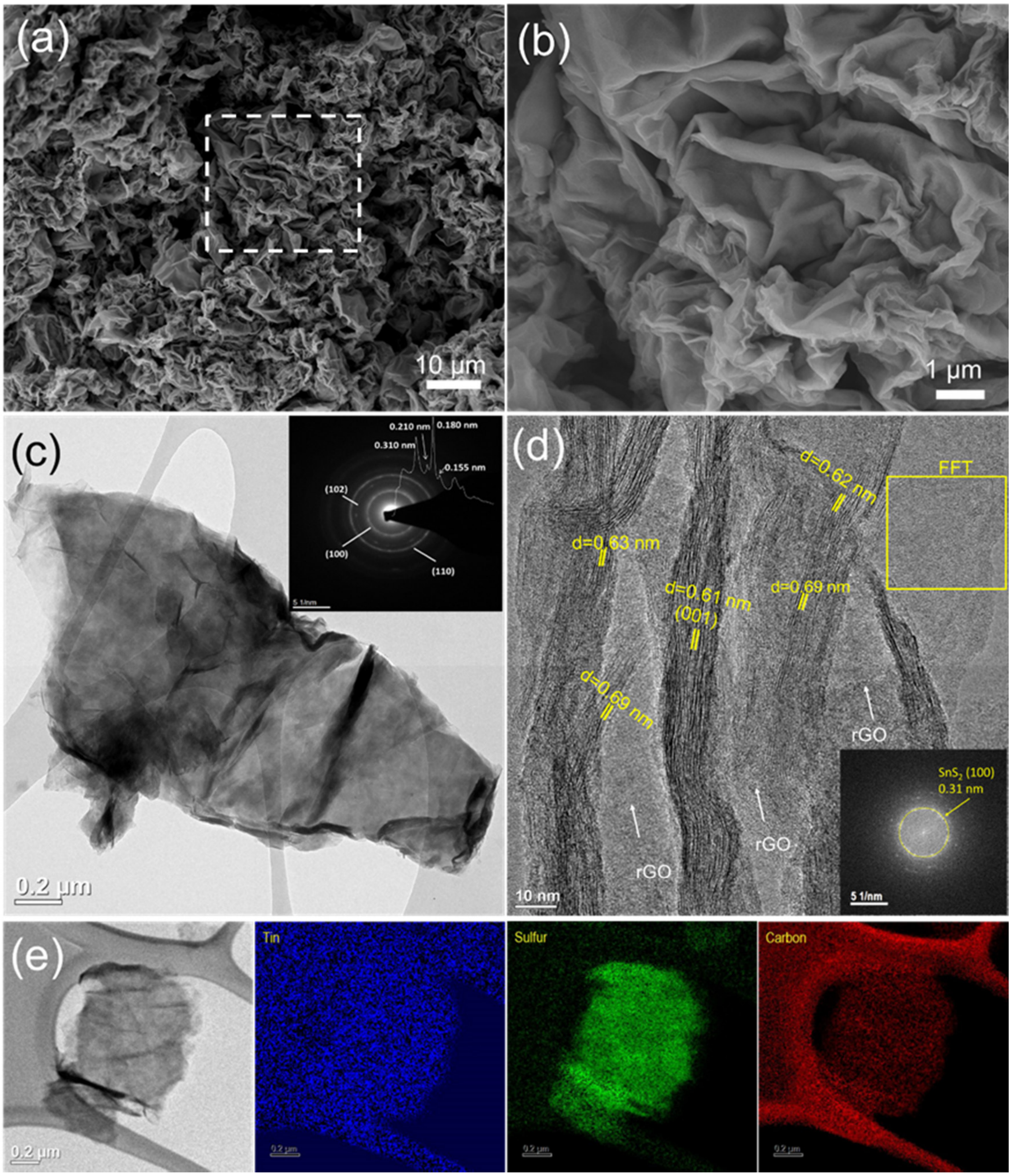

Figure 6.3 SEM image (a), high-magnification SEM image (b), TEM image (c), the inset of c is the diffraction rings of SAED pattern, HR-TEM image (d), EFTEM image (e), and Sn, S, and C elemental mapping images of the SnS_2-rGO.

composition and high structure affinity between the rGO sheets and the SnS_2 nanosheets. The carbon percentage of the SnS_2-rGO composite is 15.60 %, which was obtained from Organic Elemental Analysis (OEA, **Table 6.1**). The TEM image reveals the ultrafine SnS_2 nanocrystals (**Figure 6.3c**). The selected area electron diffraction (SAED) in the inset of **Figure 6.3c** displays a series of diffraction rings with an interlayer distance of 0.310, 0.210, and 0.180 nm, corresponding to the (100), (102), and (110) planes of crystalline SnS_2.[179,184] The HR-TEM image of the edge (**Figure 6.3d**) shows SnS_2 nanosheets lying between rGO nanosheets, confirming that SnS_2 nanosheets are *in situ* grown on the rGO nanosheets. The lattice spacing of 0.61 nm is consistent with the (001) crystalline plane of SnS_2.[196] The diffraction ring of (100) with an interlayer distance of 0.310 nm is obtained from the fast Fourier transform (FFT) of HR-TEM. The amorphous rGO is indicated by the arrow. The energy-filtered transmission electron microscopy (EFTEM) and EDX elemental mapping images (**Figure 6.3e**), and high resolution elemental and chemical maps using electron energy loss spectroscopy (EELS) (**Figure 6.5**) further demonstrate that SnS_2 nanosheets are homogeneously distributed in rGO. Based on the above-mentioned surface morphology analysis, it's concluded that SnS_2 nanosheets are not only *in situ* grown on the rGO nanosheets but also surrounded by carbon. This unique structure is composed of ultrasmall SnS_2 nanosheets and a highly conductive rGO nanosheets network, which can shorten sodium/potassium-ions diffusion routes and tolerate volume expansion.

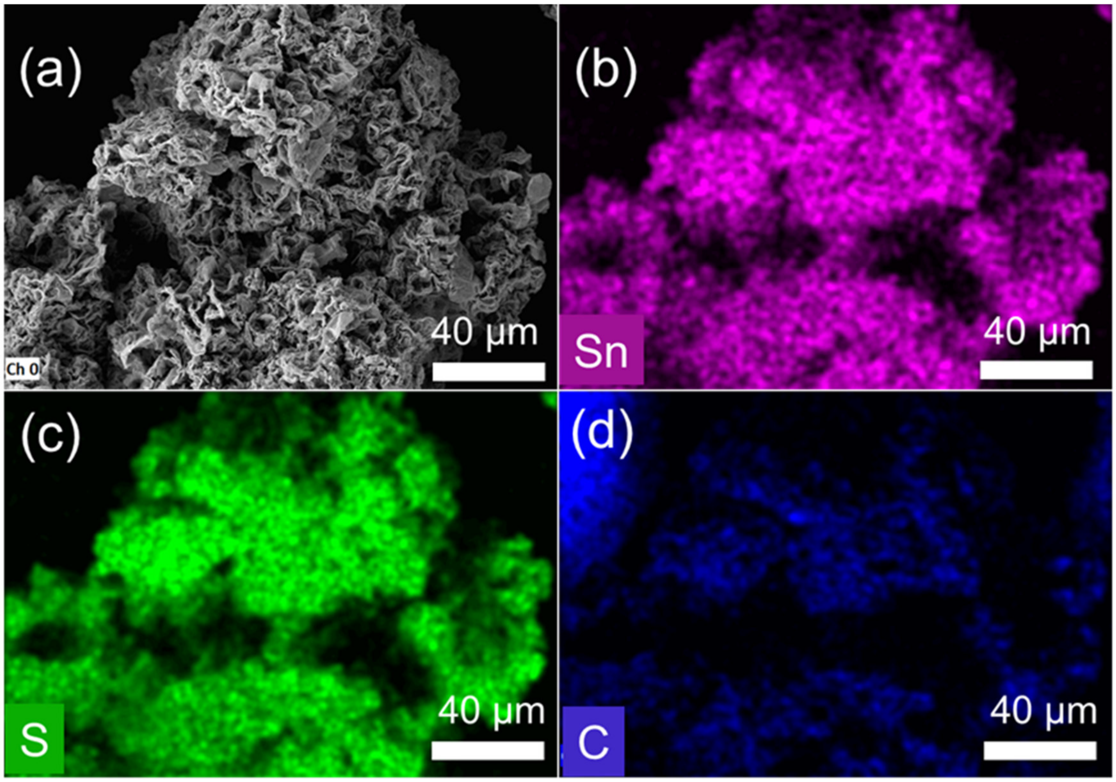

Figure 6.4 SEM image (a) and EDX elemental mapping of elemental (b) Sn, (c) S, and (d) C.

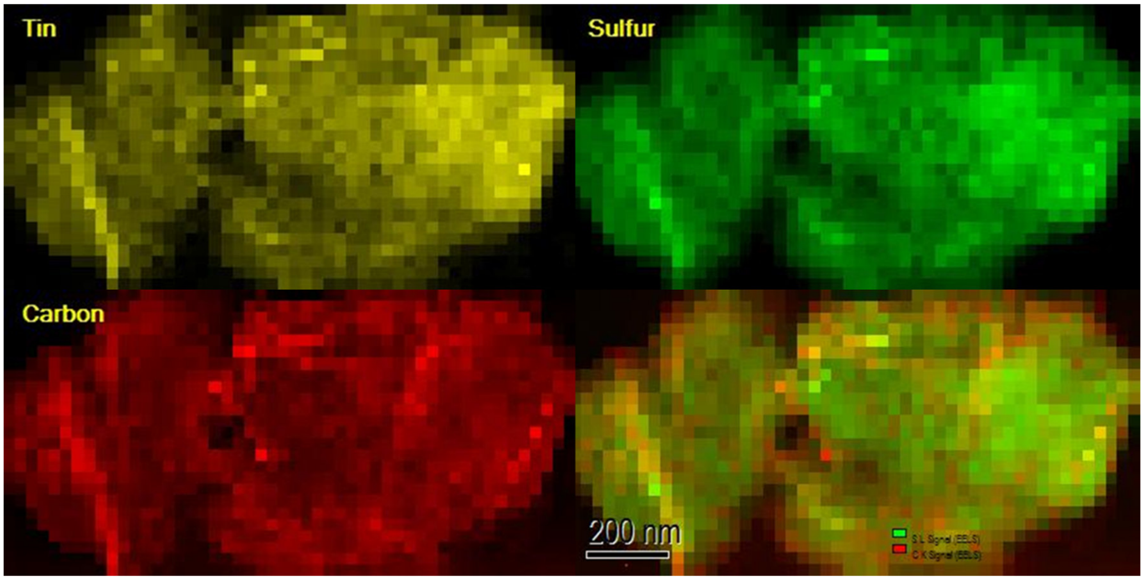

Figure 6.5 Electron energy loss spectroscopy (EELS) mapping of the SnS_2-rGO.

Table 6.1 Organic Elemental Analysis (OEA) of the pristine SnS_2-rGO material.

	N (%)	C (%)	H (%)	S (%)
SnS_2-rGO	0.18	15.60	0.82	28.14

6.3.2 Influence of FEC electrolyte additive on the SnS_2-rGO electrode for NIBs

Since FEC additive is an effective electrolyte additive for improving SEI films and cycling stability that is frequently used in LIBs,[197–199] it could also affect the electrochemical of the SnS_2-rGO electrode for NIBs. Therefore, the effect of FEC on the long-term cycling stability of the SnS_2-rGO electrode was investigated. The Na/SnS_2-rGO half cells were cycled with and without the addition of 5 wt% FEC. The presence of FEC can improve the cycle performance of the material, similar to reports in the literature for phosphorus/carbon (a-P/C), Sb/C, rGO/Sb_2S_3, and $NaNi_{1/2}Mn_{1/2}O_2$.[200–203] As shown in **Figure 6.6**, the SnS_2-rGO electrode in the FEC-free electrolyte can deliver a capacity of 270 mAh g^{-1} after 300 cycles, whereas the SnS_2-rGO electrode in the 5 wt% FEC-containing electrolyte can maintain an almost constant capacity of 417 mAh g^{-1} over 300 cycles, exhibiting superior cycling stability. This enhanced capacity with FEC additive could be owing to FEC modify the surface passivation layer, including SEI films. 1 M $NaClO_4$ in EC: DMC=1:1 with 5 wt% FEC was therefore selected as the main electrolyte for further experiments. Additionally, the reversible capacity of the SnS_2-rGO electrode in the FEC-free electrolyte and 5 wt% FEC-containing electrolyte is 192 and 300 mAh g^{-1} during the 1st cycle. This could be due to the different SEI film properties (chemical composition and thickness); more experiments (XPS, SEM, and EDX) are planned to investigate the influence of FEC electrolyte additive on the SnS_2-rGO electrode.

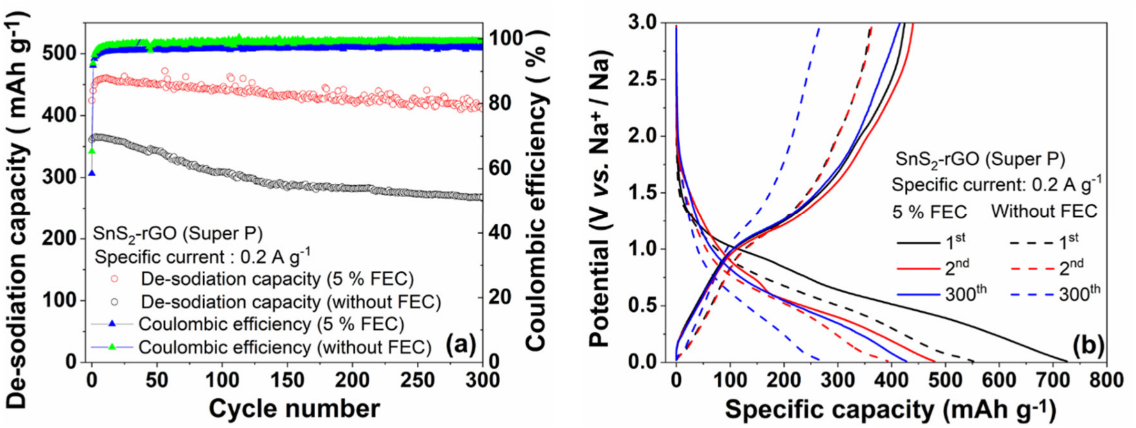

Figure 6.6 Effect of FEC on electrochemical performances**:** long-term cycling and CE of the SnS_2-rGO electrode with Super P carbon additive at a specific current of 0.2 A g^{-1} (a); galvanostatic sodiation/de-sodiation capacity profiles at some selective cycles (b).

6.3.3 Influence of carbon additives on the SnS_2-rGO electrode for NIBs

The influence of the carbon additives on the performance of the SnS_2-rGO electrode was evaluated. CV is carried out with a scan rate of 0.05 mV s^{-1} in 1 M $NaClO_4$ in EC: DMC=1:1 with 5 wt% FEC in a voltage range of 0.01-3.0 V *vs.* Na^+/Na. The CV curves of the SnS_2-rGO electrode with Super P and C65 are displayed in **Figure 6.7a** and **b**, respectively. During the first sodiation process, three clear cathodic peaks appear at 1.88, 1.04, and 0.47 V. The small peak at 1.88 V could be associated with Na^+-ions insertion into SnS_2 layers forming Na_xSnS_2 (**Equation 6.1**).[184,204] The peak at 1.04 V is attributed to the conversion of Na_xSnS_2 into metallic Sn and the formation of Na_2S (**Equation 6.2**). The other cathodic peak at 0.47 V can be ascribed to the Na-Sn alloying process (**Equation 6.3**) and the formation of solid electrolyte interphase (SEI).[182,196] Correspondingly, in the following anodic scan, there are some oxidation peaks. The oxidation peaks at 0.36 V is due to the de-alloying reaction of $Na_{3.75}Sn$.[205]

The peak at 0.76 V can be assigned to the formation of Na_xSnS_2. The distinct oxidation signal at 1.20 V can be associated with the de-sodiation reaction of Na_xSnS_2.[182] Furthermore, the CV curves are nearly congruent for the 2nd and 3rd cycles, indicating good electrochemical reversibility of the SnS_2-rGO composite for the sodiation and de-sodiation reactions. The electrode prepared with Super P displays more redox peaks as compared with C65. This is related to the Na storage ability of Super P and will be discussed later in detail.

$$xNa + SnS_2 + xe^- \rightarrow Na_xSnS_2 \tag{6.1}$$

$$Na_xSnS_2 + (4-x)\ Na^+ + (4-x)e^- \rightarrow Sn + 2Na_2S \tag{6.2}$$

$$Sn + 3.75\ Na^+ + 3.75\ e^- \rightarrow Na_{3.75}Sn \tag{6.3}$$

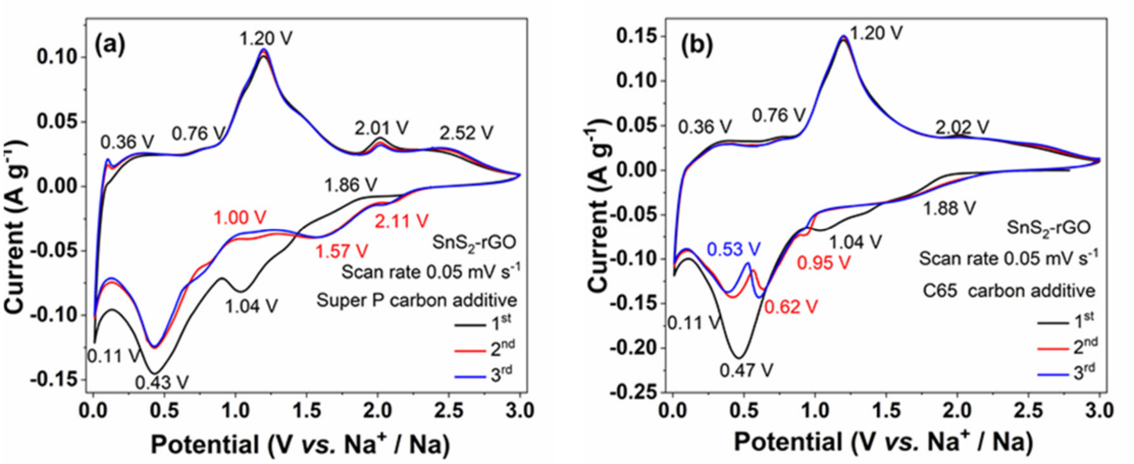

Figure 6.7 CV curves of SnS_2-rGO electrode at a scan rate of 0.05 mV s^{-1} in 1 M $NaClO_4$ in EC: DMC=1:1 with 5 wt% FEC in the voltage range of 0.01–3.0 V *vs.* Na^+/Na with different carbon additive: Super P (a) and C65 (b), both are 20 wt% of the total electrode mass.

Figure 6.8a depicts the long-term cycling performance of the SnS_2-rGO electrode (70 wt% mass) with Super P and C65 conductive additives. The long-term electrochemical behaviour was investigated at the specific current of 0.2 A g^{-1} in the potential window of 0.01-3.0 V *vs.* Na^+/Na. The SnS_2-rGO electrode with C65 exhibits excellent capacity retention during cycling. A reversible de-sodiation capacity of 635 mAh g^{-1} is obtained after 250 cycles. In contrast, the SnS_2-rGO electrode with Super P only delivers a reversible de-sodiation capacity of 420 mAh g^{-1} after 250 cycles at the same specific current. Rate capability tests were performed at different specific currents from 0.05 to 5 A g^{-1} in the voltage range from 0.01 to 3.0 V *vs.*

Na^+/Na for the SnS_2-rGO electrode and are shown in **Figure 6.8b**. The rate performance of the SnS_2-rGO electrode again proves the advantages of C65. At the initially lower specific current of 0.05 A g^{-1}, a high reversible capacity of 706 mAh g^{-1} is reached by the SnS_2-rGO electrode with C65. Upon increasing the specific current to 0.1, 0.2, 0.5, 1, 2, and 5 A g^{-1}, the specific capacity slightly decreases to 712, 675, 592, 522, 424, and 210 mAh g^{-1}, respectively. When the specific current is set back to 0.05 A g^{-1}, the specific capacity recovers to 745 mAh g^{-1}, which is higher than the initial capacity of 706 mAh g^{-1}. In contrast, the specific capacity of the SnS_2-rGO electrode with Super P is much lower than that with C65 at all tested current densities. The Super P containing electrode delivers 513, 481, 442, 390, 339, 207, and 523 mAh g^{-1} at specific currents of 0.05, 0.1, 0.2, 0.5, 1, 2, and 5 A g^{-1}, respectively. It is previously reported that Super P and C65 are widely used as conductive additives for LIBs and SIBs.[206–208] Both carbons have chain-like networks of round shaped particles (20-30 nm).They display similar Brunauer–Emmett–Teller (BET) surface areas and pore volumes: Super P (62 m^2 g^{-1}, 0.11 cm^3 g^{-1}), C65 (64 m^2 g^{-1}, 0.12 cm^3 g^{-1}). Theoretically, the very similar chemical properties of Super P and C65 should not cause the very different long-term cycling performance and rate performance. Pfeifer *et al.*[206] reported that the de-sodiation capacity of Super P and C65 is 170 mAh g^{-1} and 70 mAh g^{-1} at 0.2 A g^{-1}, respectively. This means that a component Super P, which should be an inactive additive, is active. This could detrimentally influence the active material, lead to a loss of buffering features and causes the SnS_2-rGO electrode cracking. Also, the conductive paths can be interrupted or destroyed if Super P itself expands. Therefore, the capacity of the Super P containing electrode can be lower.

Figure 6.8c and **d** present the sodiation/de-sodiation profiles of the SnS_2-rGO electrode with Super P and C65 conductive carbons of the 1st, 2nd, 3rd, 150th, and 250th cycle at the specific current of 0.2 A g^{-1}. In consistence with the CV curves, three plateaus and a sloping curve can be observed in the first sodiation process, associated with the formation of Na_xSnS_2 (1.88 V),[182] the conversion reaction (1.04 V), and alloying reaction (0.01−0.47 V), respectively.[204] Moreover, the first de-sodiation potential plateau at 1.22 V may appear due to the de-sodiation reaction of Na_xSnS_2.[183] The SnS_2-rGO electrode with Super P delivers a first sodiation capacity of 726 mAh g^{-1} and a de-sodiation capacity of 424 mAh g^{-1} with a CE of 59 %. The irreversible capacity of 302 mAh g^{-1} at the first cycle is attributed to the inevitable formation of the SEI film on the surface of the active material and electrolyte decomposition.[209] In contrast, the SnS_2-rGO electrode with C65 presents a first sodiation capacity of 1094 mAh g^{-1}

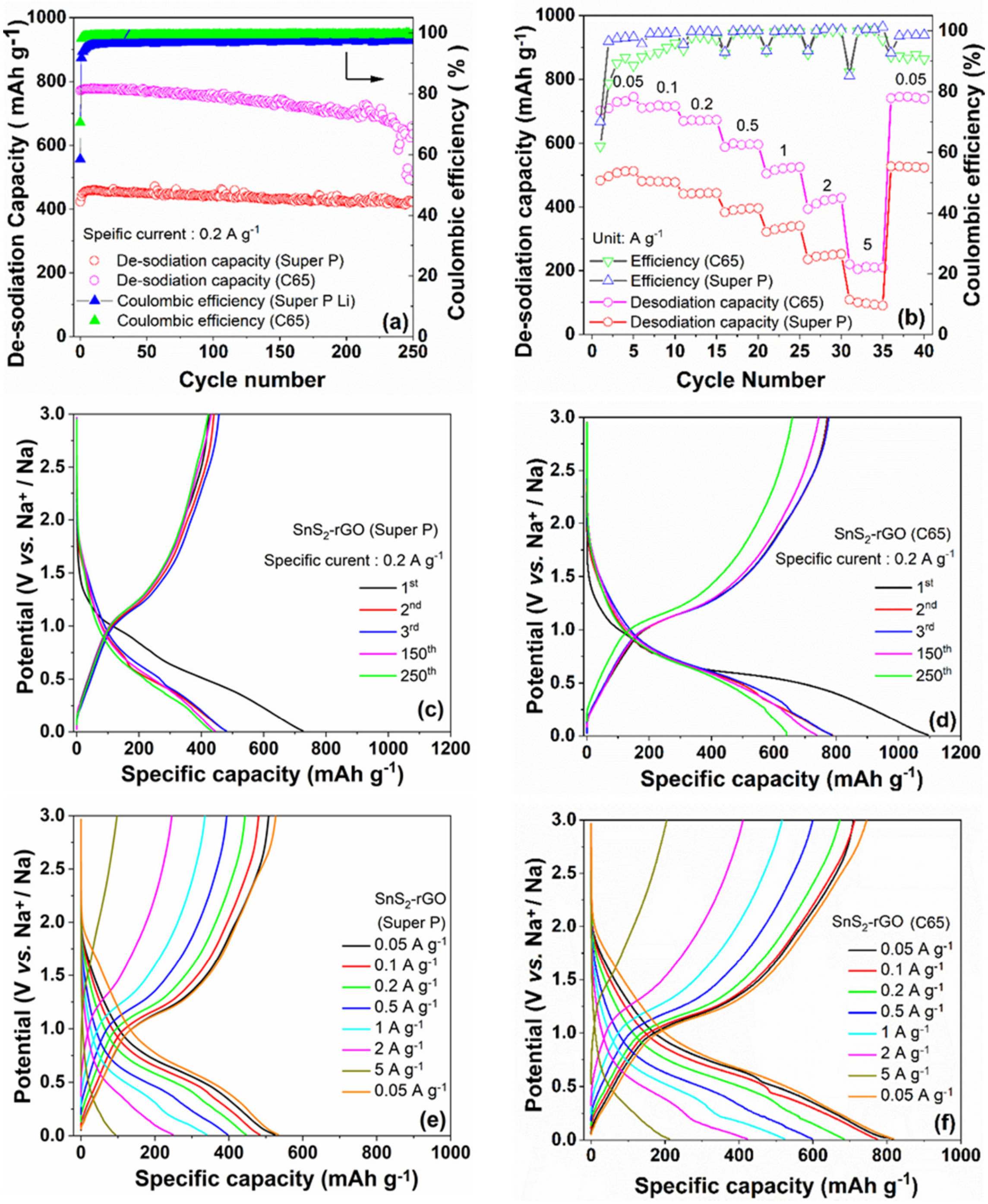

Figure 6.8 Electrochemical performances of SnS_2-rGO electrode in 1 M $NaClO_4$ in EC: DMC=1:1 with 5 wt% FEC**:** The long-term cycling and CE with Super P and C65 conductive carbons at a specific current of 0.2 A g^{-1} (a); rate performance (b); galvanostatic sodiation/de-sodiation capacity profiles at some selective cycles with Super P (c) and C65 (d); sodiation and de-sodiation capacity curves with Super P (e) and C65 conductive additive (f) at different specific currents.

and a de-sodiation capacity of 772 mAh g^{-1} with a CE of 71 %. Similarly, the irreversible capacity of 322 mAh g^{-1} at the first cycle takes place due to the formation of the SEI and electrolyte decomposition. The CE increases to be 99 % after the second cycle and is maintained in the subsequent cycles, indicating the high reversibility of the electrochemical reactions. **Figure 6.8e** and **f** compare the specific capacity values of the SnS_2-rGO electrode with Super P and C65 conductive additives at various specific currents, respectively. The different long-term cycling and rate performance were inspiring to further investigate the kinetics and resistance parameters.

To further distinguish between surface-controlled and diffusion-controlled reactions of the SnS_2-rGO, CV curves of the as-prepared SnS_2-rGO electrode at various scan rates ranging from 0.05 to 2 mV s^{-1} 1 M $NaClO_4$ in EC: DMC=1:1 with 5 wt% FEC were investigated and shown in **Figure 6.9**. The CV curves exhibit the redox peaks in each curve, which matches well with the sodiation/de-sodiation profiles (**Figure 6.6**). Additionally, both current intensities of the SnS_2-rGO electrode with Super P (**Figure 6.9a**) and C65 (**Figure 6.9b**) increase with the increase of the scan rates. The CV curves maintain a similar shape even at a high scan rate of 2 mV s^{-1}. The current obeys a power-law with the scan rate (**section 1.4.6**, **Equation 1.11-1.12**). **Figure 6.9c** shows the linear fitting of log (i) and log (v). The values of b of the SnS_2-rGO electrode with Super P are 0.795 and 0.804 for the cathodic and anodic peaks, respectively. For the SnS_2-rGO electrode with C65, the b value for the cathodic and anodic peaks is both times 0.795. The above-described analysis confirms that the surface-capacitive behavior controls the electrochemical process in the SnS_2-rGO electrode for the initial cycles,[122] thus leading to a high rate performance.

Furthermore, to quantify the surface-capacitive contribution in the SnS_2-rGO electrode by using **Equation 1.13-1.14** in **section 1.4.6**. **Figure 6.9d** presents the relationship of $|i(v)|v^{-1/2}$ versus $v^{1/2}$, and the derived coefficients k_1 and k_2. The surface-capacitive contribution (Q_p) of the SnS_2-rGO electrode with Super P (**Figure 6.10a**) and C65 additive (**Figure 6.10b**) increases for higher sweep rates, demonstrating that surface-capacitive behavior holds competitive advantages in the whole electrochemical process, especially at high scan rates. **Figure 6.10c** and **d** display the detailed surface-capacitive contributions at 1 mV s^{-1}.

To further investigate the kinetics phenomena and resistive contributions, EIS measurements were performed. **Figure 6.11** depicts the Nyquist plot of the SnS_2-rGO electrode with Super P (**Figure 6.11a** and **b**) and C65 (**Figure 6.11c** and **d)** obtained at some potentials (from 2.0 to 0.01 V) in 1 M $NaClO_4$ in EC: DMC=1:1 with 5 wt% FEC during the first sodiation and de-sodiation processes. The inset figures in **Figure 6.11** show the zoom in the high to middle-frequency area. **Figure 6.11e** shows the equivalent circuit, which is used to fit the experimental data. Each signal explanation is given in **section 1.4.7**.

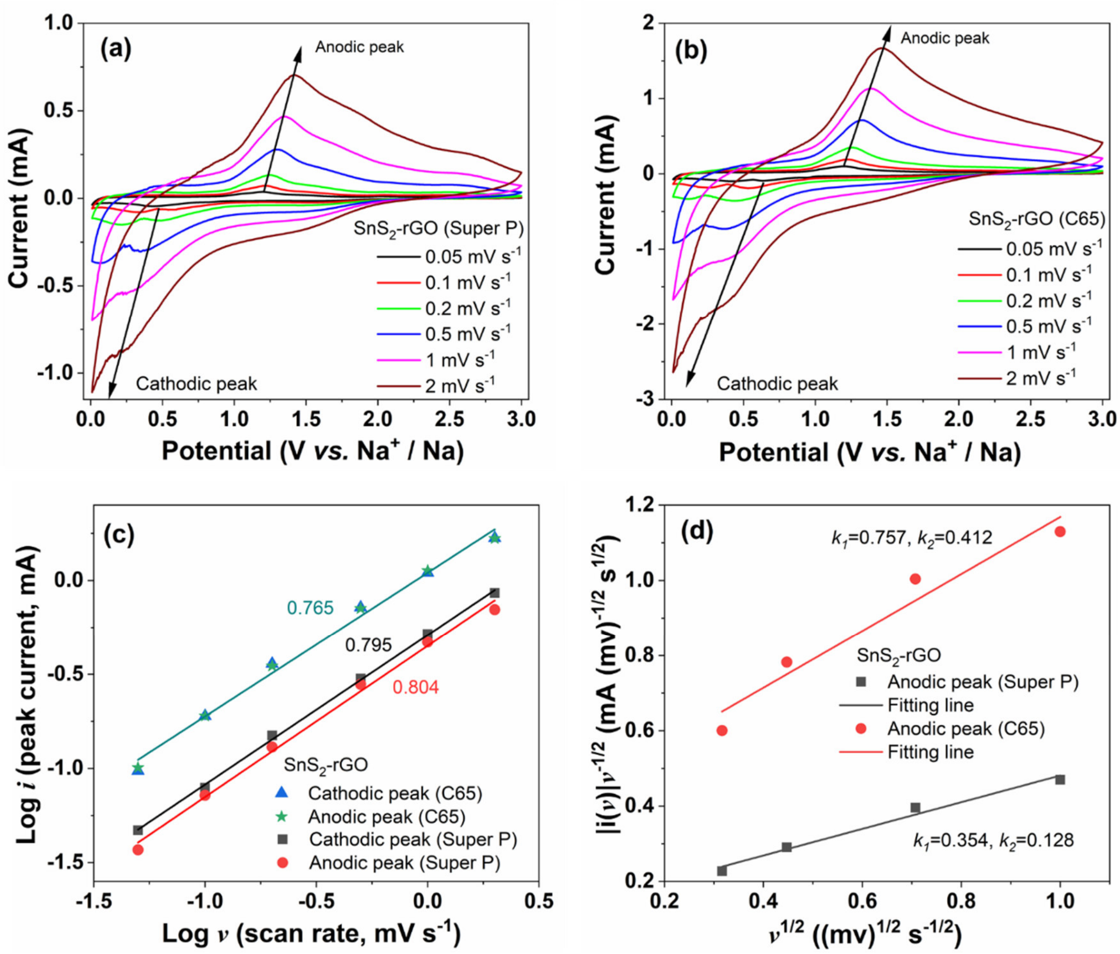

Figure 6.9 CV curves at various scan rates ranging from 0.05 to 2 mV s^{-1} of the SnS_2-rGO with Super P (a) and C65 (b) in 1 M $NaClO_4$ in EC: DMC=1:1 with 5 wt% FEC; the relationship of log *i* vs. log *v* plots at each redox peak (c); the linear fitting of $|i(v)|v^{-1/2}$ versus $v^{1/2}$ at the selected potentials (d).

The resistivity values can be obtained after fitting the Nyquist plots, the R_{el} does not change much during the 1st electrochemical processes, which illustrates that the conductivity of the electrolyte is stable. The changes of R_{CT} at various polarization potentials are shown in **Table**

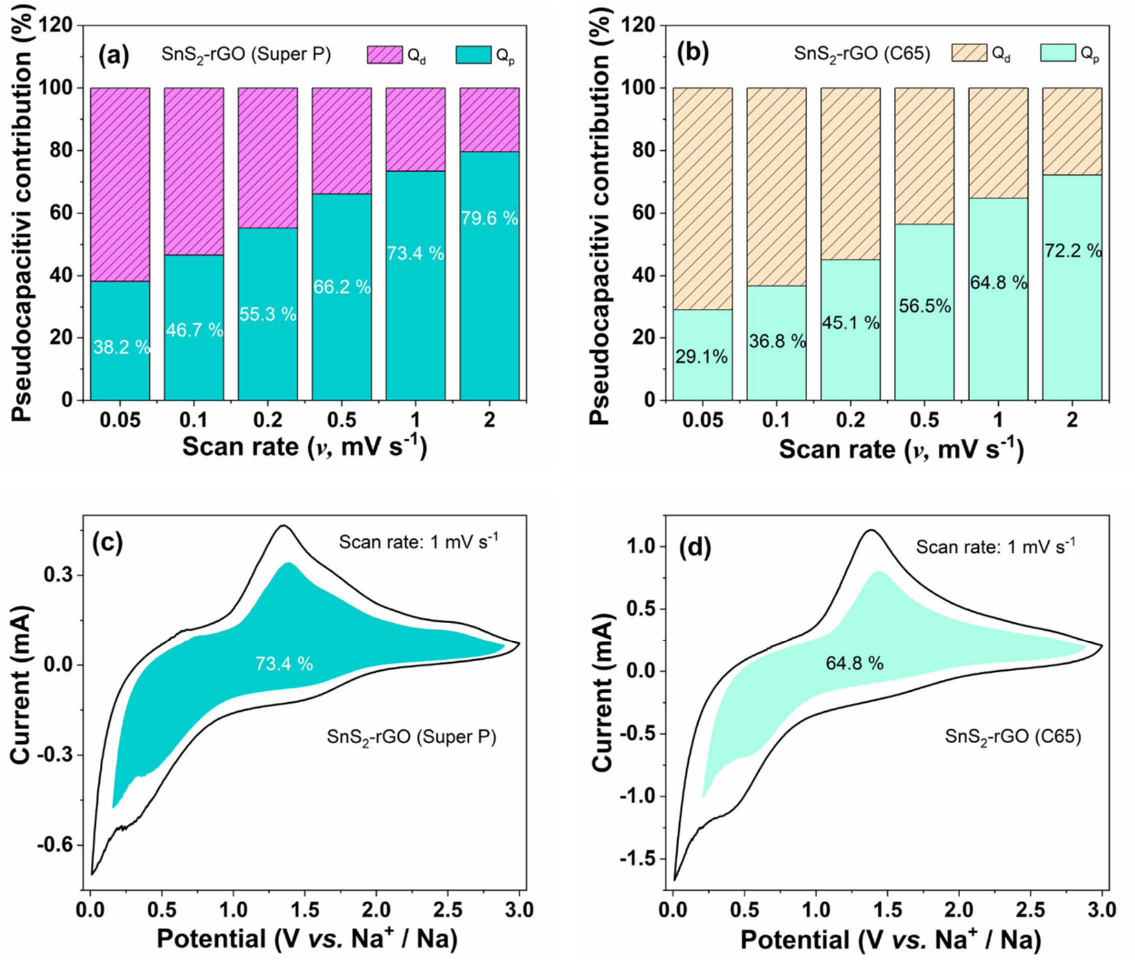

Figure 6.10 Bar chart exhibiting the contribution ratio of surface-capacitive contribution at different scan rates of the SnS$_2$-rGO with Super P (a) and C65 (b); CV plots with the surface-capacitive contribution shown by the coloured regions at a scan rate of 1 mV s^{-1} of the SnS$_2$-rGO with Super P (c) and C65 (d).

6.2. As can be observed, during the 1st sodiation process, R$_{CT}$ of the SnS$_2$-rGO electrode with Super P first decreases from ~18 kΩ (~2.0 V) to ~200 Ω (~0.01V), which is owing to the sodium-ion insertion ($xNa + SnS_2 + xe^- \rightarrow Na_xSnS_2$, from ~2.0 to ~1.0 V) followed by the conversion and alloying reaction ($Na_xSnS_2 + (4-x)\,Na^+ + (4-x)e^- \rightarrow Sn + 2Na_2S$, $Sn + 3.75\,Na^+ + 3.75\,e^- \rightarrow Na_{3.75}Sn$, from ~0.4 to ~0.1 V). During the 1st de- sodiation process, R$_{CT}$ continuously increases from ~180 Ω (~0.1 V) to ~700 Ω (~2.0 V) due to Na$^+$-ions extraction from the active material. The SnS$_2$-rGO electrode with C65 also shows the same tendency. Furthermore, for both conductive additives, the diffusion resistance in the low-frequency region first decreases (2.0-1.05 V) then increases (0.1-0.01 V) during the sodiation and de-sodiation processes.

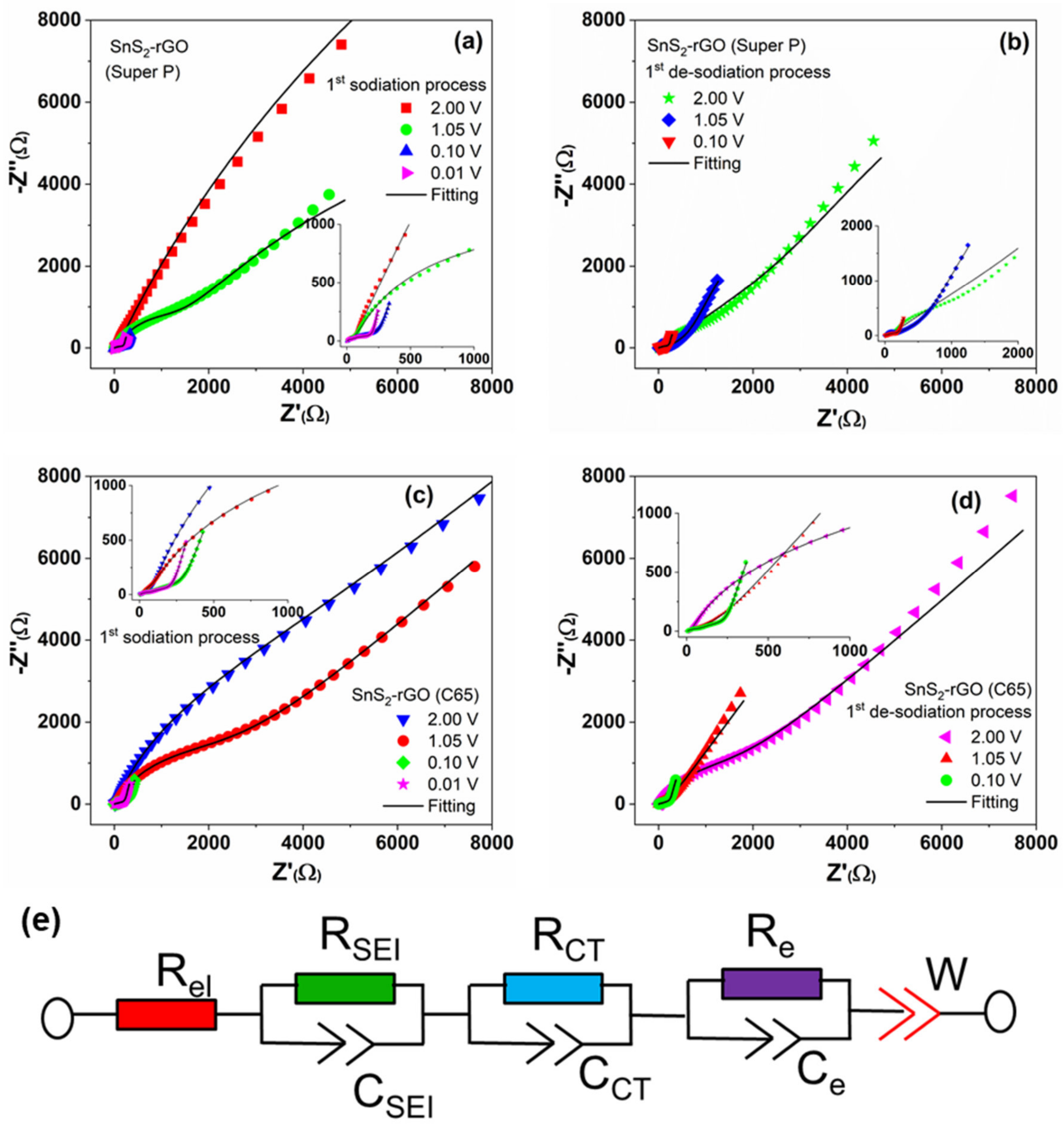

Figure 6.11 Nyquist plots of the SnS$_2$-rGO electrode with Super P at different potentials during the 1st sodiation (a) and de-sodiation (b) conditions in 1 M NaClO$_4$ in EC: DMC=1:1 with 5 wt% FEC; Nyquist plots of the SnS$_2$-rGO electrode with C65 at various potentials during the 1st sodiation (c) and de-sodiation (d) states. The inset figures show the zoom of Nyquist plots in the high-frequency region (e). This equivalent circuit is used to fit the EIS experiment data.

To further track the kinetics of sodiation/de-sodiation processes upon cycling, EIS was performed at chosen cycles as shown in **Figure 6.12**. The Nyquist plots of the SnS$_2$-rGO electrode with Super P at various cycles (1st, 10th, 20th, 30th, and 40th) at the bias potential of

1.05 V vs. Na$^+$/Na during sodiation and de-sodiation processes are presented in **Figure 6.12a** and **b**, respectively. Correspondingly, the Nyquist plots of the SnS$_2$-rGO electrode with C65 are shown in **Figure 6.12c** and **d**. The inset in **Figure 6.12** shows the zoom in the high-frequency area. The diameter values for the semicircle on the spectra in the middle frequency region correspond to charge transfer resistance R$_{CT}$ of the electrochemical reaction.[210,211] Note that the diameter of the semicircle for SnS$_2$-rGO with Super P and C65 decreases upon cycling. In addition, the slope in the low-frequency region for the SnS$_2$-rGO electrode with Super P increases upon cycling (**Figure 6.12a** and **b**). The slope of the SnS$_2$-rGO electrode with C65 also shows the same phenomenon. This implies that the diffusion resistance increases with the number of cycles for both carbon additives.

Table 6.2 The charge transfer resistance (R$_{CT}$) of the SnS$_2$-rGO electrode at some selected potentials during the 1st sodiation and de-sidiation processes.

Potential		SnS$_2$-rGO (Super P)	SnS$_2$-rGO (C65)
		R$_{CT}$	R$_{CT}$
1st sodiation process	2.00 V	18 kΩ	17 kΩ
	1.05 V	1 kΩ	1 kΩ
	0.10 V	200 Ω	170 Ω
0.01 V	--	--	--
1st de-sodiation process	0.10 V	180 Ω	240 Ω
	1.05 V	400 Ω	280 Ω
	2.00 V	700 Ω	800 Ω

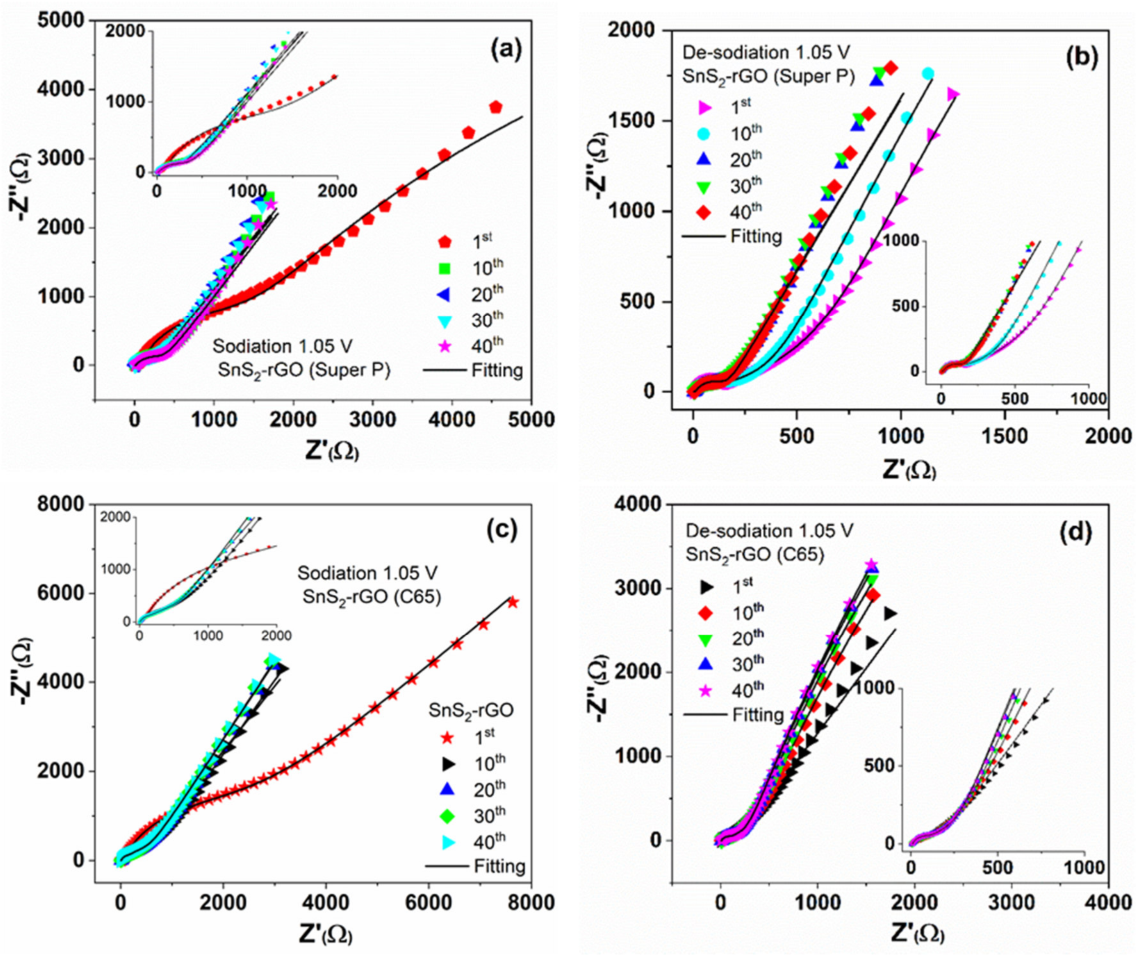

Figure 6.12 Nyquist plots of the SnS$_2$-rGO electrode with Super P at various cycles in sodiation (a) and de-sodiation (b) conditions (1.05 V) in 1 M NaClO$_4$ in EC: DMC=1:1 with 5 wt% FEC; Nyquist plots of the SnS$_2$-rGO electrode with C65 at different cycles in sodiation (c) and de-sodiation (d) conditions (1.05 V), the inset displays the zoom of Nyquist plots in the high-frequency region.

Figure 6.13 presents resistivity values as obtained by fitting the spectra with Relaxis 3 software in sodiation and de-sodiation conditions, respectively. The electrolyte resistance R_{el} for the SnS$_2$-rGO with Super P and with C65 are almost unchanged upon cycling (**Figure 6.13a** and **d**). The obtained value of the R_{SEI} is shown in **Figure 6.13b** and **e**. During the sodiation process, the values of R_{SEI} for SnS$_2$-rGO with Super P and with C65 are sharply decreasing from 450 Ω to around 100 Ω upon cycling. However, the value of R_{SEI} for SnS$_2$-rGO displays different tendencies in de-sodiation states depending on the respective carbon. As can be observed, R_{SEI} for SnS$_2$-rGO with Super P decreases from 100 Ω to 40 Ω, while R_{SEI} for SnS$_2$-rGO with C65 first decreases (60 to 40 Ω) then increases to 80 Ω then keep stable. This could be due to the electrode with Super P decomposition leading to SEI layer cracked. That's the reason for much lower specific capacity with Super P carbon additive. Furthermore, R_{SEI} in sodiation condition is higher than that in the de-sodiation state for both carbon additive, suggesting the dynamic nature of the SEI layer, which forms during the sodiation process and partially decomposes in de-sodiation process.[154,155] R_{CT} of SnS_2-rGO with Super P and with C65 drastically decrease from 1 kΩ to 400 Ω after the first 10 cycles and remain stable upon cycling (**Figure 6.13c** and **f**). In de-sodiated states, the R_{CT} value decreases upon cycling. The R_{CT} increase indicates that the particle size increases and the active material aggregates during cycling, as also confirmed from post-mortem SEM analysis.

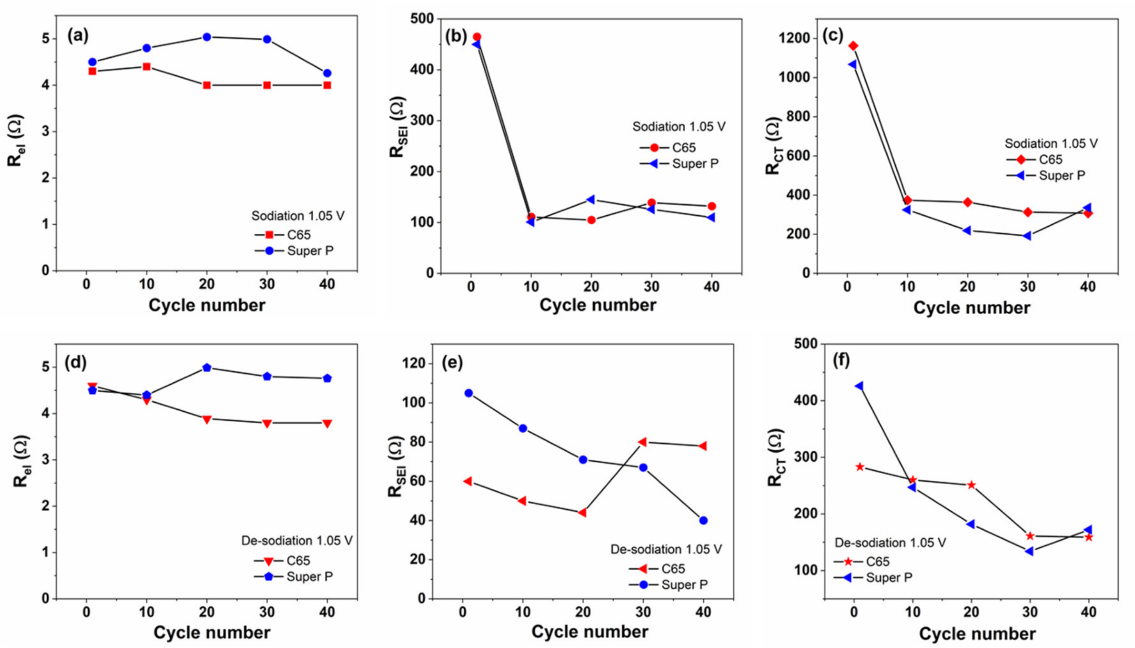

Figure 6.13 Resistance values for the SnS_2-rGO electrode with Super P and C65 in sodiation condition in 1 M $NaClO_4$ in EC: DMC=1:1 with 5 wt% FEC: R_{el} (a), R_{SEI} (b), R_{CT} (c); in de-sodiation condition: R_{el} (d), R_{SEI} (e), and R_{CT} (f).

Investigation of morphological changes of the SnS_2-rGO electrodes with Super P carbon additive before cycling and after the 1st sodiation/de-sodiation are conducted and shown in **Figure 6.14**. The morphology of the pristine electrode (**Figure 6.14a** and **d**) is composed of SnS_2-rGO nanosheets interconnected with conductive carbon. The EDS elemental mapping (**Figure 6.15**a) also confirms that the active material SnS_2-rGO is surrounded by carbon. The surface of the electrode after the 1st sodiation (**Figure 6.14b** and **e**) shows that distinct cracks

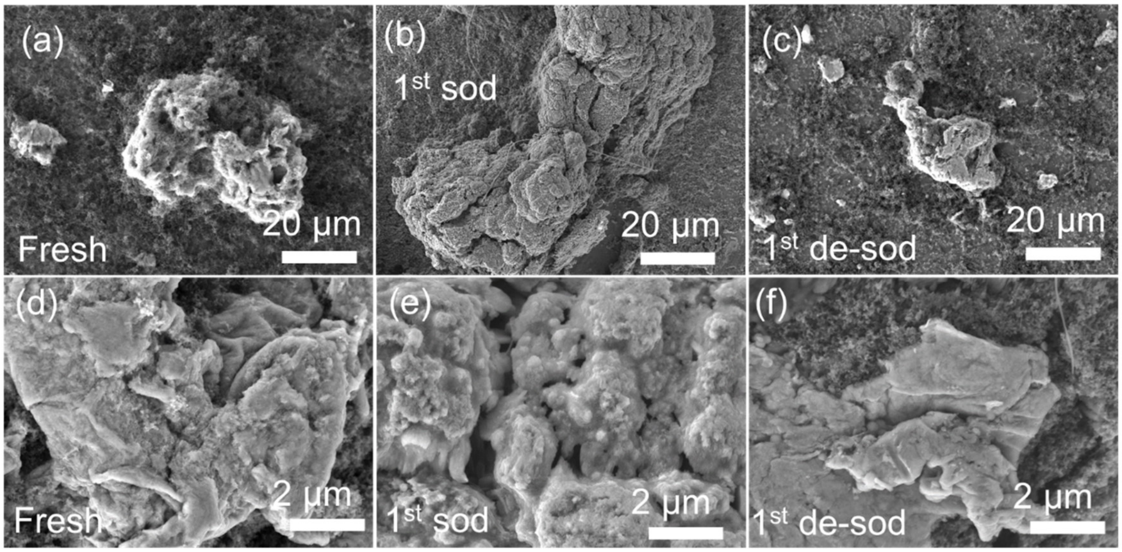

Figure 6.14 SEM images of the fresh SnS$_2$-rGO electrode with Super P carbon additive (a and d); the 1st sodiation state (b and e); and the 1st de-sodiation state (c and f).

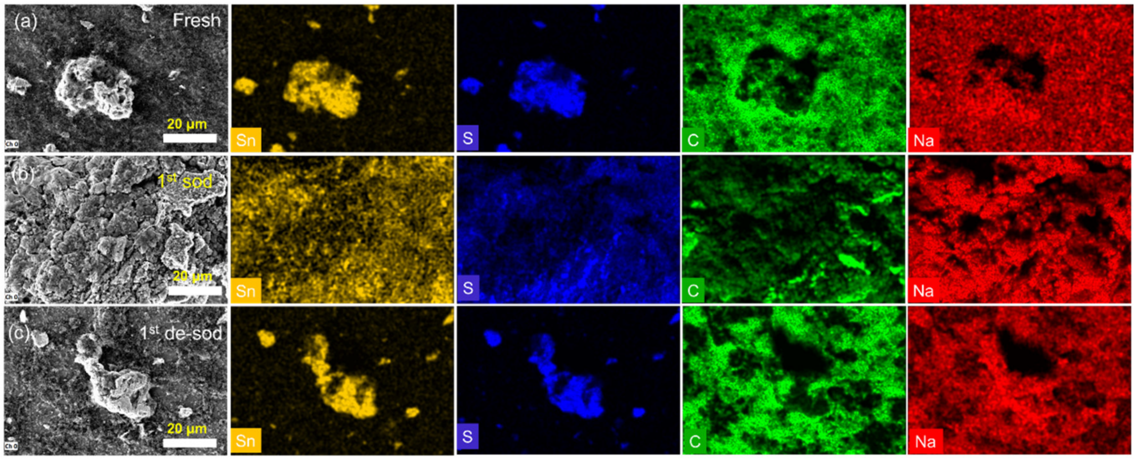

Figure 6.15 EDS elemental mapping of the fresh SnS$_2$-rGO electrode with Super P carbon additive (a); the 1st sodiation state (b); and the 1st de-sodiation states (c).

and large agglomeration appeared. This is due to Na$^+$-ion insertion, which causes large volume expansion. The electrode after the 1st de-sodiation (**Figure 6.14c** and **f**) shows a micro-sized bulk material, which is significantly aggregated and pulverized. The EDS analysis confirms that Sn, S, Na, and C are homogenously distributed in sodiated products and Sn, S are homogeneously distributed in the de-sodiatiated samples (**Figure 6.15b** and **c**).

6.3.4 Influence of FEC electrolyte additive on the SnS_2-rGO electrode for KIBs

As reported above, FEC is an efficient electrolyte additive in NIBs, therefore to further check the influence of the FEC additive in potassium-ion cells, long-term cycling stability measurements of the SnS_2-rGO electrode with Super P and C65 were performed and are shown in **Figure 6.16a** and **b**, respectively. The effect of 1 M KFSI/EC:DMC (1:1 by mass) without FEC and with 5 wt% FEC additive on electrochemical performance was compared. Surprisingly, the cycling behavior of the cell without FEC additive is superior to that of with 5 wt% FEC additive, in contrast to the results from NIBs. FEC may behave different in potassium-ion batteries.[203] Indeed, Komaba *et al.*[212] also reported that the FEC additive has a bad influence on the cycling stability of graphitic anodes in potassium cells. It could be concluded that the role of the FEC additive is different in sodium and potassium cells. The KFSI-based electrolyte containing FEC could increase the content of carbonyl groups and the number of K-F bonds. This behavior can accelerate the decomposition of electrolyte and side reactions during the cycling process. Additionally, the solvation energy of K^+ in the electrolyte with FEC (1.281 eV) is larger than that without FEC (0.305 eV), indicating that the K^+-ion diffusion and the desolvation in the electrolyte was hindered by the addition of FEC.[213] Therefore, 1 M KFSI/EC:DMC (1:1 by mass) without FEC additive was used in further electrochemical measurements.

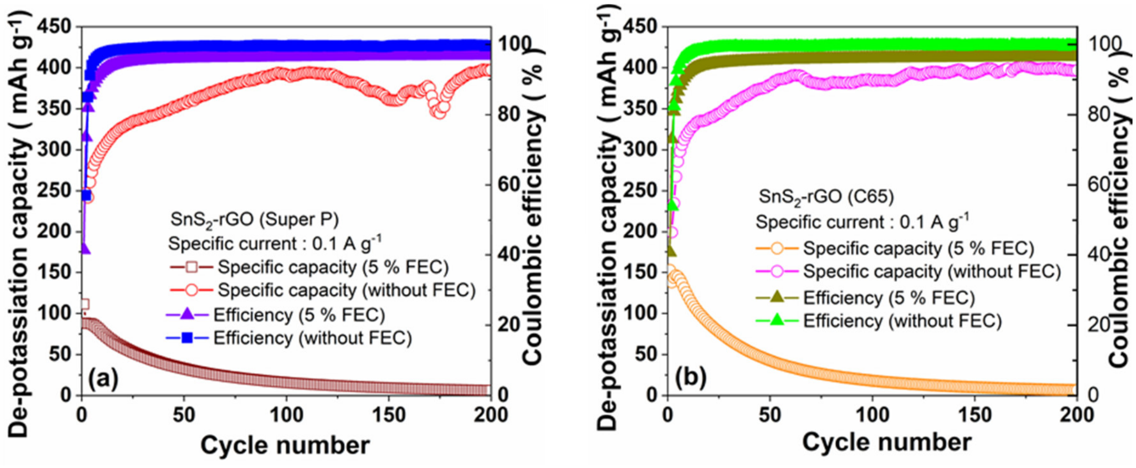

Figure 6.16 Effect of FEC on electrochemical performances in 1 M KFSI/EC:DMC-based electrolyte**:** long-term cycling and Coulombic efficiency of the SnS_2-rGO electrode with Super P (a) and C65 (b) at a specific current of 0.1 A g^{-1}.

6.3.5 Influence of carbon additives on the SnS_2-rGO electrode for KIBs

The effects of different carbon additives (Super P and C65) on the SnS_2-rGO electrode are evaluated, **Figure 6.17a** and **b** display the corresponding CV curves at a scan rate of 0.05 mV s^{-1} in a voltage ranging from 0.01 to 3.0 V *vs.* K^+/K in 1 M KFSI/EC:DMC, respectively. According to previous reports,[214–217] in the first cathodic scan, the small peak located at 2.40 V can be assigned to the K^+-ions insertion into the SnS_2 material (**Equation 6.8**). The peaks at 0.86 and 0.62 V for the SnS_2-rGO electrode with Super P and at 0.73 V for that with C65 are assigned to the conversion of SnS into metallic Sn and K_2S and the formation of an SEI film (**Equation 6.9**). The peak emerged at 0.14 V is attributed to an alloying reaction (**Equation 6.10**). The reduction peaks (0.86, 0.62, and 0.73 V) become weaker in the subsequent scan, indicating amorphization processes after the first cycle. Correspondingly, in the first anodic scan, the oxidation peaks at 0.50 V is related to the de-alloying of KSn, and the signal at 1.05 V to the formation of K_xSnS_2. The distinct oxidation peak at 1.61 V is related to the de-potassiation of K_xSnS_2. The 2nd and 3rd CV cycles are well overlapped, implying good electrochemical reversibility of the SnS_2-rGO composite during the potassiation and de-potassiation reactions. In analogy to what was observed in Na-based electrolyte, the SnS_2-rGO electrode with Super P has more redox peaks than that with C65 carbon additive. Moreover, the CV area with Super P is larger than that with C65, indicating a higher capacity. The higher K-ion storage ability with Super P carbon additive will be discussed later.

$$SnS_2 + 2K^+ + 2e^- \rightarrow SnS + K_2S \tag{6.8}$$

$$SnS + 2K^+ + 2e^- \rightarrow Sn + K_2S \tag{6.9}$$

$$23Sn + 4K^+ + 4e^- \rightarrow K_4Sn_{23} \tag{6.10}$$

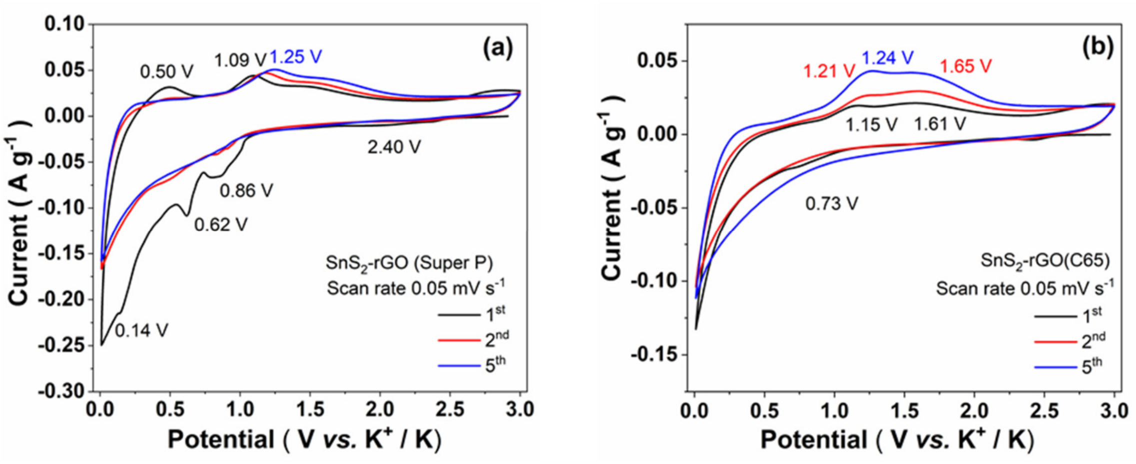

Figure 6.17 CV curves of the SnS$_2$-rGO electrode at a scan rate of 0.05 mV s^{-1} in the potential ranging from 0.01 to 3.0 V *vs.* K$^+$/K in 1 M KFSI/EC:DMC with Super P (a) and C65 (b), respectively.

Figure 6.18a shows the long-term cycling performance of the SnS$_2$-rGO electrode with Super P and C65 at a specific current of 0.1 A g^{-1} in 1 M KFSI/EC:DMC in a potential range of 0.01 to 3.0 V *vs.* K$^+$/K. Both electrodes display specific capacity increases upon cycling. The specific capacity of the SnS$_2$-rGO electrode with Super P increases from 247 to 398 mAh g^{-1} from the 1st to 200th cycle. Similarly, the specific capacity of the SnS$_2$-rGO electrode with C65 increases from 199 to 398 mAh g^{-1}. The SnS$_2$-rGO electrodes with Super P and C65 both reach high Coulombic efficiencies (99 %) expect in the first few cycles. **Figure 6.18b** depicts the rate performance of the SnS$_2$-rGO electrode at various specific currents from 0.05 to 5 A g^{-1} in the voltage range between 0.01 and 3.0 V *vs.* K$^+$/K. The SnS$_2$-rGO electrode containing Super P shows higher rate performance than the electrode containing C65. At a low specific current of 0.05 A g^{-1}, the SnS$_2$-rGO electrode with Super P presents a high reversible capacity of 446 mAh g^{-1}. With the increase of specific currents to 0.1, 0.2, 0.5, 1, 2, and 5 A g^{-1}, the specific capacity slightly decreases to 439, 402, 310, 225, 142, and 63 mAh g^{-1}, respectively. When the specific current returns to 0.05 A g^{-1}, the cell delivers 499 mAh g^{-1}, which is even higher than the initial capacity of 446 mAh g^{-1}. In contrast, the specific capacity of the SnS$_2$-rGO electrode with C65 is much lower than that with Super P under all tested specific currents. The specific capacity of the SnS$_2$-rGO electrode with C65 delivers 420, 400, 320, 194, 112, 52, and 11 mAh g^{-1} at specific currents of 0.05, 0.1, 0.2, 0.5, 1, 2, and 5 A g^{-1}, respectively. **Figure 6.18c** and **d** present the potassiation/de-potassiation profiles of the SnS$_2$-rGO electrode with Super P and C65 at the 1st, 2nd, 50th, 100th, and 200th cycle at a specific current of 0.1 A g^{-1}, respectively. In consistence with the CV curves, the plateaus and slopes appear in the first potassiation process, which is attributed to the formation of K_xSnS_2 (2.40 V), the conversion reaction (0.83-0.70 V), and alloying reaction (0.60-0.01 V), respectively. Moreover, the first de-potassiation potential plateau at 0.50 V is due to the de-alloying reaction. The pronounced plateau located at 1.09 V is assigned to K^+-ion extraction from the material. The SnS_2-rGO electrode with Super P delivers a first potassiation capacity of 433 mAh g^{-1} and a de-potassiation capacity of 247 mAh g^{-1} with a CE of 57 %. The irreversible capacity of 186 mAh g^{-1} at the first cycle is related to the inevitable formation of the SEI layer on the surface of the active material and electrolyte decomposition.[209] In the following cycles, the SnS_2-rGO electrode with Super P shows an increase of de-potassiation capacity. The de-potassiation capacity has a value of 398 mAh g^{-1} after the 200th cycle. In comparison, the SnS_2-rGO electrode with C65 presents a first potassiation capacity of 369 mAh g^{-1} and a de-potassiation capacity of 199 mAh g^{-1} with a CE of 54 %. The irreversible capacity of the first cycle is 170 mAh g^{-1}. The CE increases to 99 % from the second cycle and is stable in the subsequent cycles, implying high reversibility of the electrochemical reactions. **Figure 6.18e** and **f** compare the specific capacity values of the SnS_2-rGO electrode with Super P and C65 at the various specific currents, respectively. The rate performance of the electrode with C65 in KIBs poorer compared with that in NIBs, which could be due to the different interaction of K^+-ions with the conductive carbons than of the Na^+-ions. Furthermore, the size and mass of the ion also plays an important role and can highly influence the rate capability.

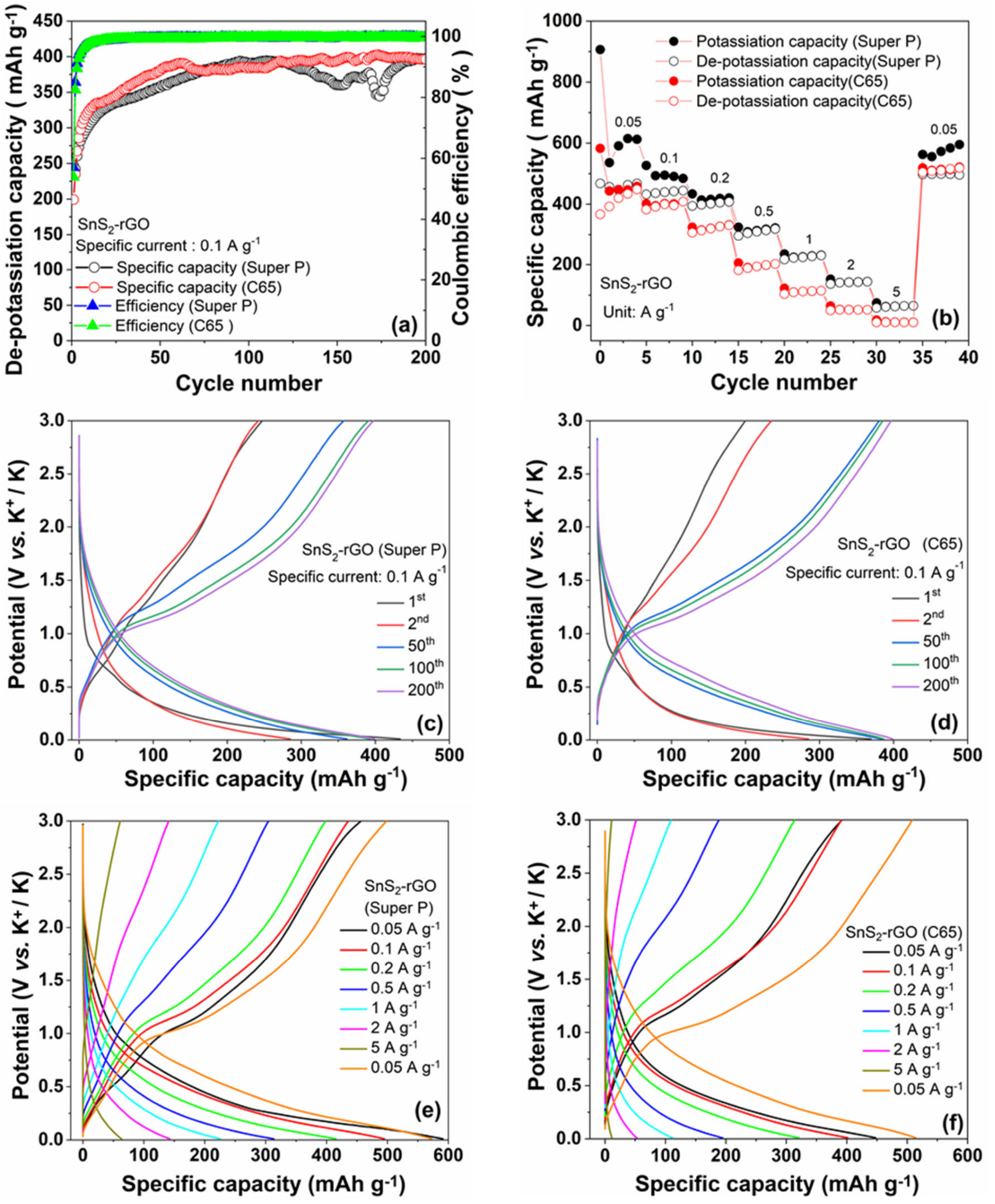

Figure 6.18 Electrochemical performances of the SnS$_2$-rGO electrode with Super P and C65 in 1 M KFSI/EC:DMC at the specific current of 0.1 A g^{-1} (a); rate performance (b); galvanostatic potassiation/de-potassiation capacity curves at some chosen cycles with Super P (c) and C65 (d); potassiation and de-potassiation capacity curves with Super P (e) and C65 (f) at various specific currents.

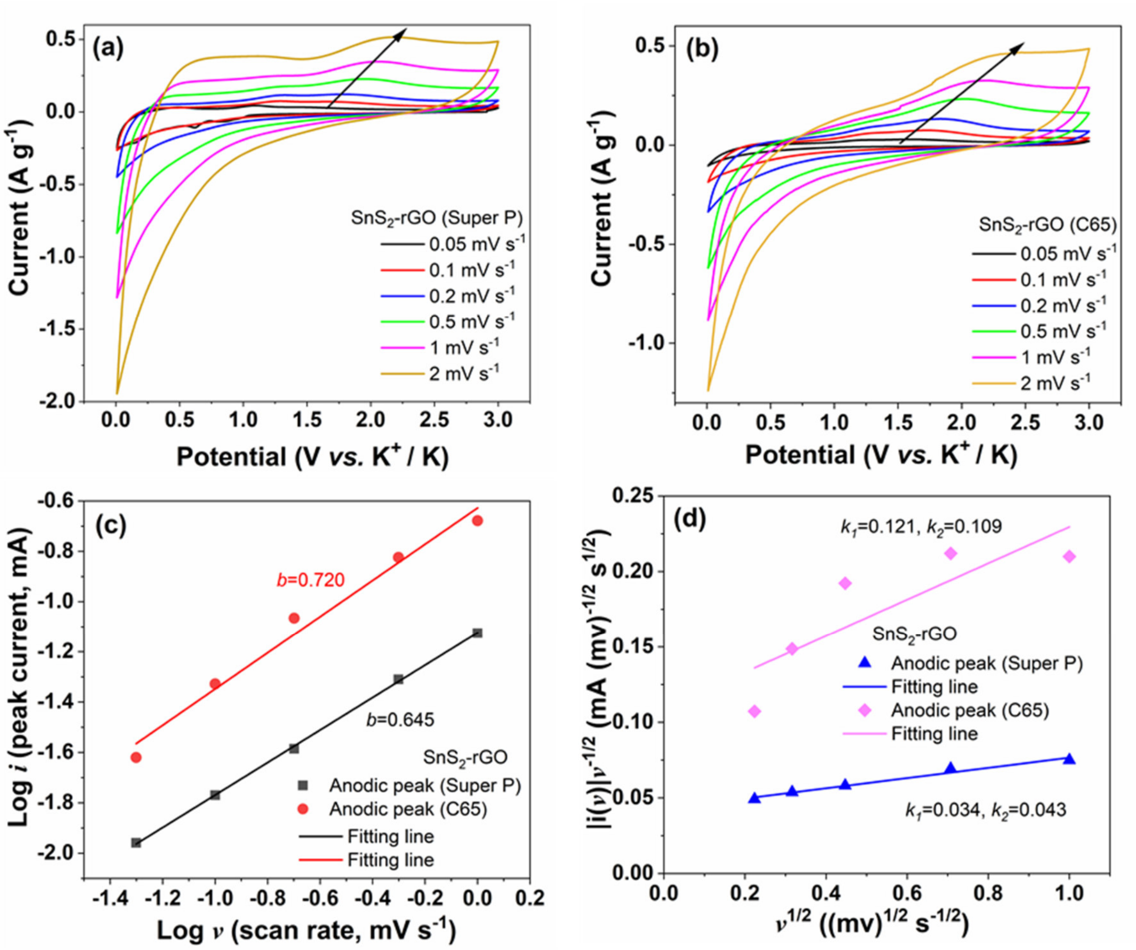

Figure 6.19 CV curves at different scan rates ranging from 0.05 to 2 mV s^{-1} of the SnS$_2$-rGO with Super P (a) and C65 (b) in 1 M KFSI/EC:DMC; the linear fitting of log *i vs*. log *v* plots at each redox peak (c); the relationship of linear fitting of $|i(v)|v^{-1/2}$ and $v^{1/2}$ at the selected potentials (d).

To further investigate the surface-controlled behavior and diffusion-controlled behavior in KIBs, the CV measurements at different scan rates are conducted. **Figure 6.19 a** and **b** show CV curves of the SnS$_2$-rGO electrode with Super P and C65 in 1 M KFSI/EC:DMC at different scan rates ranging from 0.05 to 2 mV s^{-1}, respectively. As presented in **Figure 6.19c**, the *b* value can be determined from the linear fitting the log (*i*) and log (*v*) (**section 1.4.6**, **Equation 1.11-1.12**).[29–31] The value of *b* for the SnS$_2$-rGO electrode with Super P is 0.645 for the anodic peaks. In the case of the SnS$_2$-rGO electrode with C65, the *b* value for the anodic peaks is 0.720, which indicates that the electrochemical behavior of the SnS$_2$-rGO electrode is composed of both diffusion processes and surface-capacitive processes.

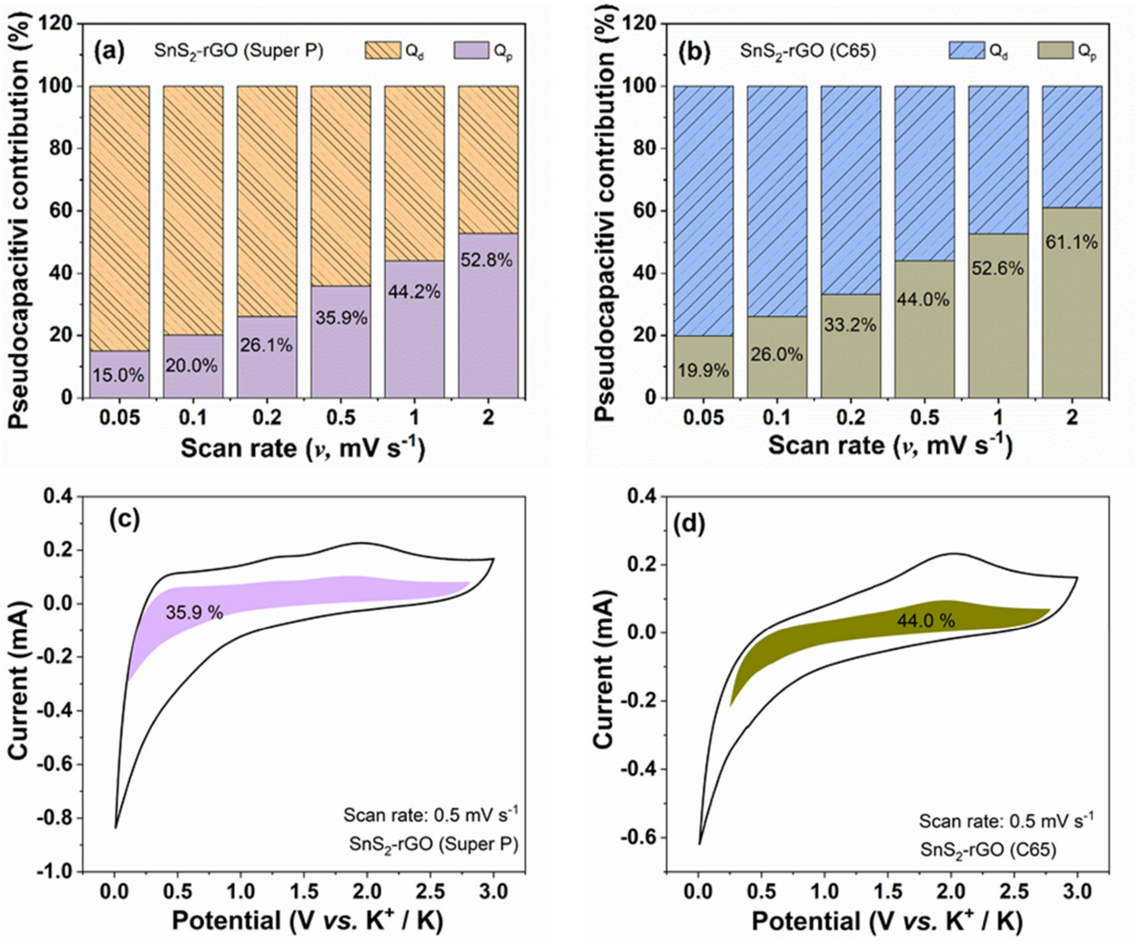

Figure 6.20 Bar chart exhibiting the contribution ratio of surface-capacitive contribution at different scan rates of the SnS$_2$-rGO with Super P (a) and C65 (b); CV plots with the surface-capacitive contribution shown by the coloured regions at a scan rate of 1 mV s^{-1} of SnS$_2$-rGO with Super P (c) and C65 (d).

According to Dunn *et al.*[29] a quantitative analysis was conducted to determine the fraction of pseudo-capacitance contribution in the CV curve (**section 1.4.6**, **Equation 1.13-1.14**). **Figure 6.19d** displays the relationship of $|i(v)|v^{-1/2}$ and $v^{1/2}$, and the derived coefficients k_1 and k_2. For the SnS$_2$-rGO electrode with Super P (**Figure 6.20a**), the percentage of the surface-controlled process increases from 15.0, 20.0, 26.1, 35.9, 44.2, to 52.8 % with a scan rate increase of 0.05, 0.1, 0.2, 0.5, 1, and 2 mV s^{-1}. Similarly, the proportion of the surface-controlled processes for the SnS$_2$-rGO electrode with C65 (**Figure 6.20b**) increases from 19.9, 26.0, 33.2, 44.0, 52.6, to 61.1 %, which indicates that surface-capacitive behavior holds competitive advantages in the whole electrochemical process especially at high scan rates. From **Figure 6.20c** and **d**, it can be seen that the surface-capacitive contribution (Q_p) is 35.9 %

and 44.0 % of the total charge storage at a scan rate of 0.5 mV s^{-1} for SnS$_2$-rGO with Super P and C65, respectively.

EIS measurements were carried out to further evaluate the kinetic parameters and resistive contributions. **Figure 6.21** presents the Nyquist plot of the SnS$_2$-rGO electrode with Super P (**Figure 6.21a** and **b**) and C65 (**Figure 6.21c** and **d)** recorded at various potentials in 1 M KFSI/EC:DMC during the first potassiation and de-potassiation processes. The inset pictures in **Figure 6.21** present the high to middle-frequency region. **Figure 6.21e** describes the equivalent circuit employed to fit the experimental data.

Table 6.3 The charge transfer resistance (R_{CT}) of the SnS$_2$-rGO electrode at some selected potentials during the 1st potassiation and de-potassiation processes.

		SnS$_2$-rGO (Super P)	SnS$_2$-rGO (C65)
Potential		R_{CT}	R_{CT}
1st potassiation process	2.00 V	300 kΩ	163 kΩ
	1.05 V	52 kΩ	41 kΩ
	0.10 V	1 kΩ	1 kΩ
0.01 V	--	--	--
1st de-potassiation process	0.10 V	1 kΩ	1 kΩ
	1.05 V	4 kΩ	2.5 kΩ
	2.00 V	41 kΩ	35 kΩ

Table 6.3 shows the change of the R_{CT} at various polarization potentials during the 1st potassiation and de-potassiation processes. During the 1st potassiation process, the R_{CT} of the SnS$_2$-rGO electrode with Super P decreases from ~300 kΩ (~2.0 V) to ~1 kΩ (~0.01V). The R_{CT} decrease is due to the potassium-ions insertion ($SnS_2 + 2K^+ + 2e^- \rightarrow SnS + K_2S$, from ~2.0 to ~1.0 V) followed by conversion and alloying reactions ($SnS + 2K^+ + 2e^- \rightarrow Sn +$

K_2S, $23Sn + 4K^+ + 4e^- \rightarrow K_4Sn_{23}$ from ~0.5 to ~0.1 V). For the SnS_2-rGO electrode with C65, R_{CT} also decreases from ~160 kΩ (~2.0 V) to ~1 kΩ (~0.01V) during the 1st potassiation process. During the 1st de-potassiation process of the SnS_2-rGO electrode with Super P, R_{CT} continuously increases from ~1 kΩ (~0.1 V) to ~42 kΩ (~2.0 V) due to K^+ extraction from the active material. In comparison, the R_{CT} value of the SnS_2-rGO electrode with C65 increases from ~1 kΩ (~0.1 V) to ~35 kΩ (~2.0 V). The R_{CT} of Super P higher than that of C65 electrode during the 1st de-potassiation (1.05 and 2.00 V). The changes of R_{CT} with cycling are discussed later.

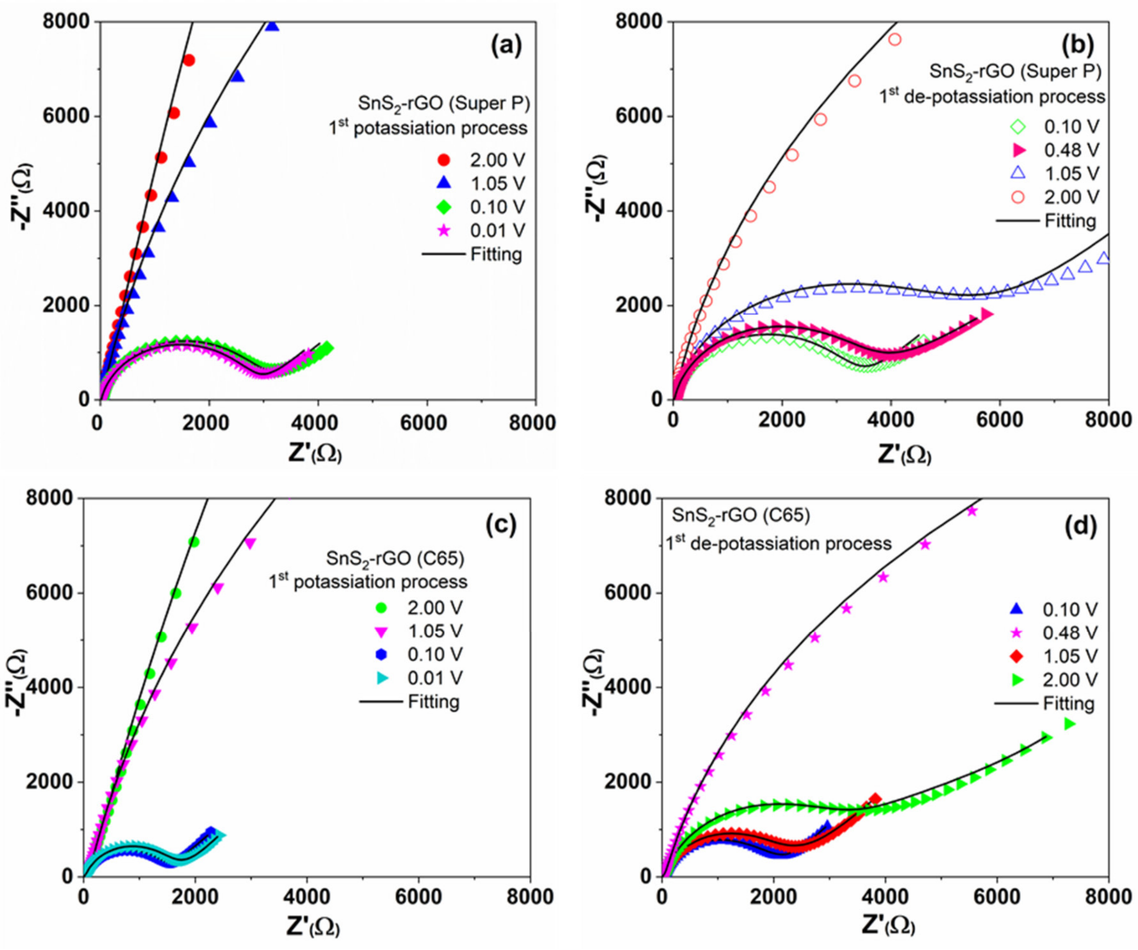

Figure 6.21 Nyquist plots of the SnS_2-rGO electrode with Super P at different potentials during the 1st potassiation and de-potassiation processes (b) conditions; Nyquist plots of the SnS_2-rGO electrode with C65 at various potentials during the 1st sodiation (c) and de-sodiation (d) states. (e) This equivalent circuit is used to fit the EIS experiment data.

To further investigate the kinetics of potassiation/de-potassiation processes upon cycling, EIS was performed after different cycles, as shown in **Figure 6.22**. The Nyquist plots of the SnS$_2$-rGO electrode with Super P and with C65 at various cycles (1st, 10th, 20th, 30th, and 40th) at the fixed potential of 0.48 V *vs*. K$^+$/K during potassiation/de-potassiation processes are presented in **Figure 6.22a-b** and **c-d**, respectively. The values of the diameter values of the semicircle on the spectra in the middle-frequency region are related to the charge transfer resistance (R$_{CT}$) of the electrochemical reaction.[210,211] The diameter of the semicircle for SnS$_2$-rGO with Super P and C65 increases upon cycling. This could be due to the SnS$_2$-rGO electrode polarization with cycling, which will be discussed later.

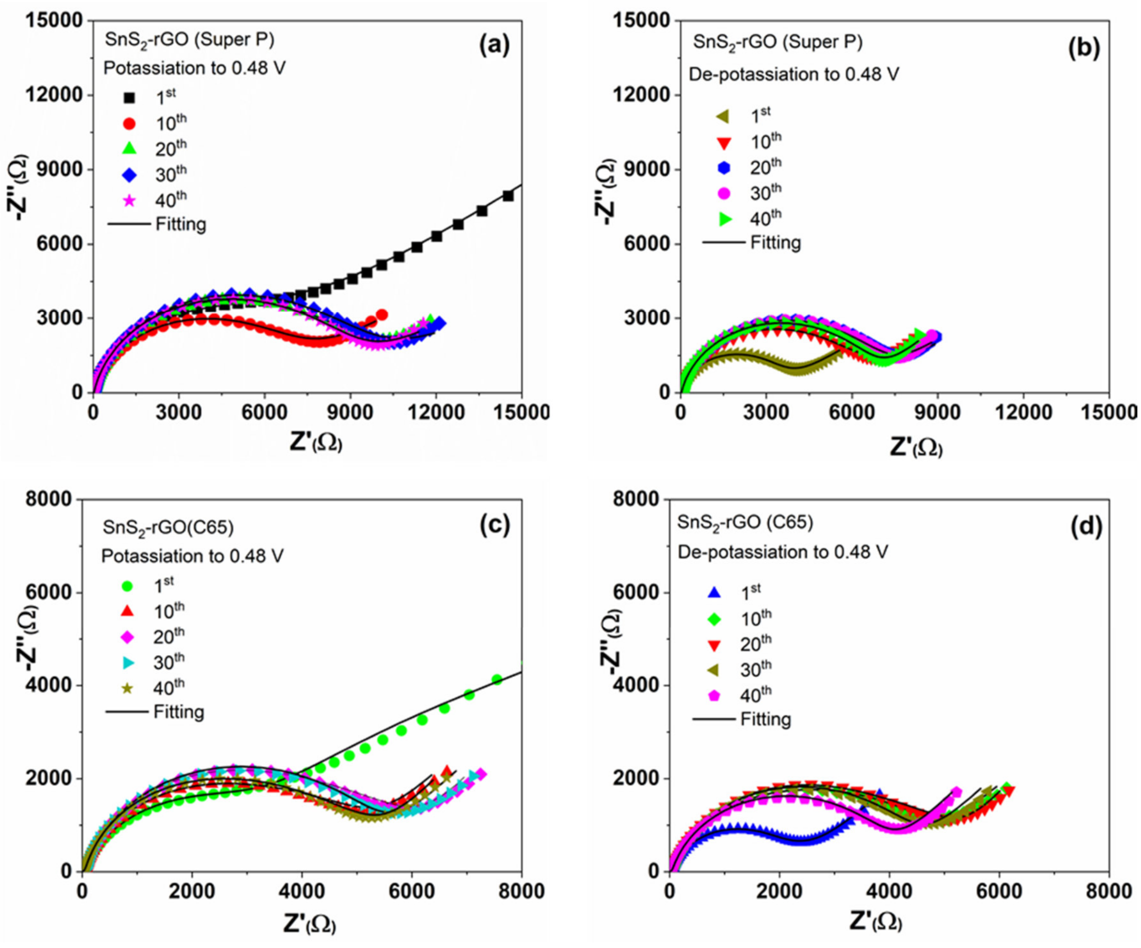

Figure 6.22 Nyquist plots of the SnS$_2$-rGO electrode with Super P at different cycles in potassiation (a) and de-potassiation (b) states (0.48 V); Nyquist plots of the SnS$_2$-rGO electrode with C65 at various cycles in in potassiation (c) and de-potassiation (d) conditions (~0.48 V).

The resistance values obtained from the Relaxis 3 software during further potassiation and de-potassiation processes are shown in **Figure 6.23**. The electronic resistance R_e for the SnS_2-rGO with Super P electrode is lower than that of the electrode with C65 carbon additive (**Figure 6.23a** and **d**). The R_{SEI} value of the SnS_2-rGO with Super P increases from ~6 kΩ to ~7 kΩ during the potassiation process and from ~3 kΩ to ~5 kΩ during the de-potassiation process upon cycling. On the other side, the R_{SEI} value of the SnS_2-rGO with C65 decreases from ~3 kΩ to ~1 kΩ during the potassiation process and from ~2 kΩ to ~1 kΩ during the de-potassiation process upon cycling (**Figure 6.23b** and **e**). This could be due to a different formation of the SEI layer. The homogeneity and thickness can be affected differently when changing conductive carbon. Most probably, as R_e is lower for SuperP more electrons can reach the interface and contribute to the reduction of the electrolyte, which promotes SEI formation. Super P forms a more homogenous and thicker SEI layer which can protect the active material and lead to a superior rate capability (**Figure 6.18b**). Furthermore, the changes of R_{CT} with cycling are investigated (**Figure 6.23c** and **f**). During the potassiation process, R_{CT} first decreases and increases smoothly for both carbon additives. While in de-potassiation process, R_{CT} of the SnS_2-rGO with Super P is almost stable (~1 kΩ) after 40 cycles. Different from that, the R_{CT} value of the SnS_2-rGO with C65 sharply increases to ~4 kΩ and slightly decreases upon cycling. The R_{CT} of the SnS_2-rGO with C65 increases could be due to the electrode broken and SEI cracked. The big differences of the R_{CT} resistance values depending on the different carbon additives (Super P and C65) lead to different cycling performances and especially rate performances (**Figure 6.18b**).

To correlate the morphology changes with the EIS and electrochemical performance, *ex-situ* SEM measurements of the SnS_2-rGO electrode with Super P were performed. There are visible cracks and large aggregation after the 1st potassiation (**Figure 6.24a** and **b**) compared with the fresh electrode (**Figure 6.14a** and **d**). The morphology of the electrode after the 1st de-potassiation (**Figure 6.24c** and **d**) exhibits smaller particles in size of 20-30 nm and a number of cavities, which indicated electrode polarization aggregated with cycling. The observed fibers are residues from the separator. The EDS elemental mapping of the 1st potassiation and de-potassiation are presented in **Figure 6.25a** and **b**, respectively. The images indicate uniform distributions of Sn, S, C, and K in the potassiated product, and a homogenous distribution of Sn and S in the de-potassiated product. There is a significant amount of residual K in SnS_2

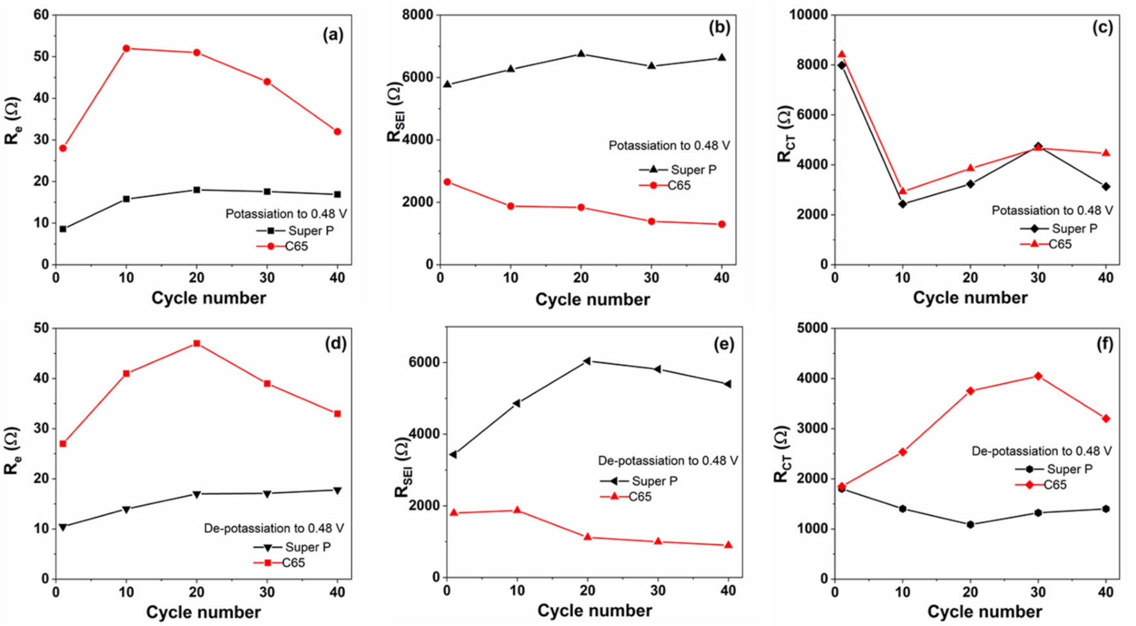

Figure 6.23 Resistance values for the SnS_2-rGO electrode with Super P and C65 in potassiation condition: R_e (a), R_{SEI} (b), R_{CT} (c); in de-potassiation states: R_e (d), R_{SEI} (e), and R_{CT} (f).

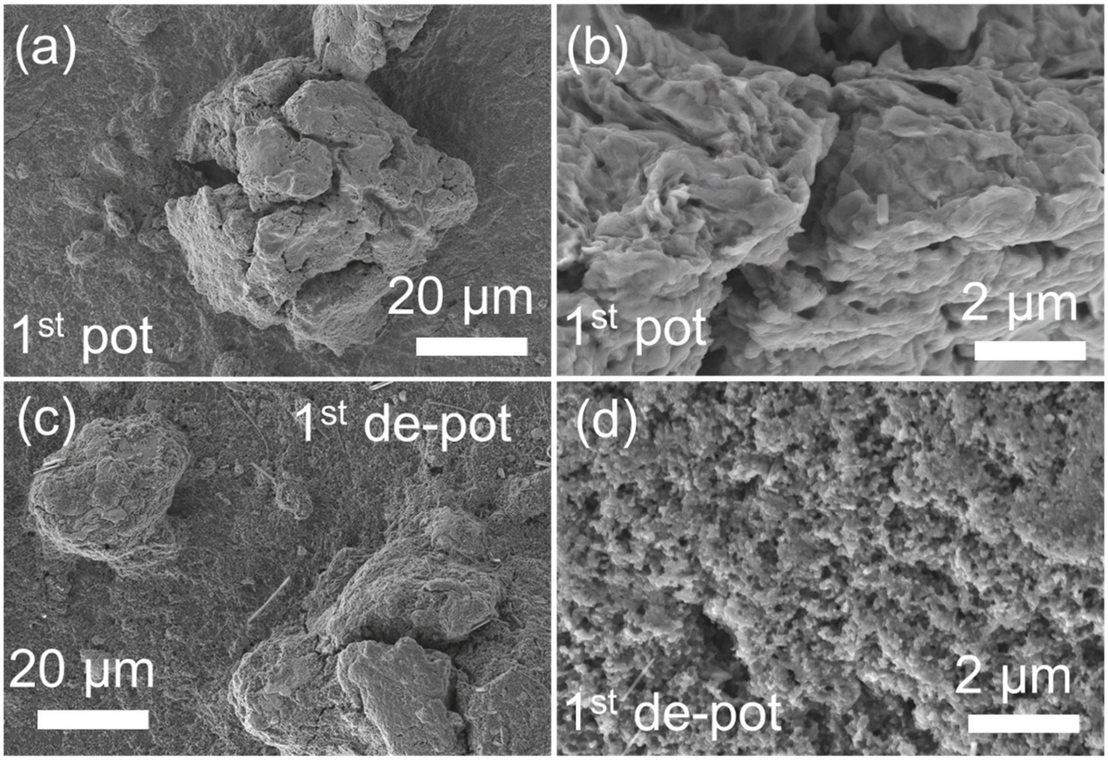

Figure 6.24 SEM images of the SnS_2-rGO electrode with Super P carbon additive in the 1st potassiation state (a and b) and the 1st de-potassiation states (c and d).

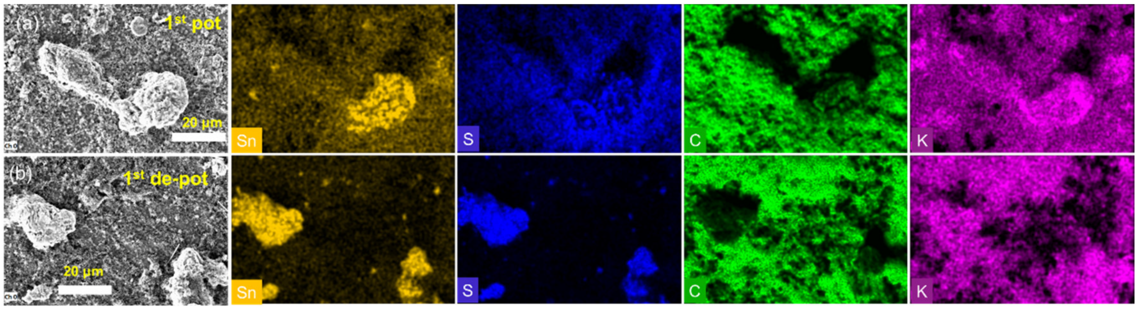

Figure 6.25 EDS elemental mapping of the SnS_2-rGO electrode with Super P carbon additive in the 1st potassiation state (a) and the 1st de-potassiation states (b).

particles at the de-potassiated state (**Figure 6.25b**), which indicates the incomplete reaction. There is no new formation of regions, which consist solely of carbon or the Sn-based phases.

6.4 Conclusions

In summary, porous few-layer SnS_2 nanosheets were grown *in situ* on reduced graphene oxide (rGO) and successfully fabricated by template assistance and subsequent hydrothermal reaction. When applied as an anode for NIBs and KIBs, the SnS_2-rGO anode delivers high reversible de-sodiation capacities (C65: 635 mAh g^{-1}, Super P: 420 mAh g^{-1}; at 0.2 A g^{-1} after 250 cycles) and de-potassiation capacities (C65 and Super P: 398 mAh g^{-1} at 0.1 A g^{-1} after 200 cycles). This unique structure ensures not only rapid Na^+-ion/K^+-ion diffusion and electron transport through the bulk material but also provides strong structure stability to buffer the large volume changes during repeated cycling processes. It is demonstrated that the electrolyte additive (FEC) can improve the specific capacity and stability of the SnS_2-rGO electrode in NIBs, while negatively affecting the performance in KIBs. Two different carbon conductive additives (Super P and C65) are evaluated in NIBs and KIBs.

It is found that the SnS_2-rGO electrode with C65 has superior long-term cycling and rate performance than that with Super P in NIBs. This is due to the higher de-sodiation capability of Super P, which should be inactive. This could detrimentally influence the active material, lead to a loss of buffering features and cause the SnS_2-rGO electrode cracking. EIS shows that the variation of R_{SEI} can be correlated to the cracks on the electrode based on the SnS_2-rGO electrode with Super P. Also, the conductive paths can be interrupted or destroyed if Super P itself expands due to the higher de-sodiation capacity. This leads to an inferior capacity of the Super P containing electrode

In contrast, the SnS_2-rGO electrode with Super P shows a better rate performance than that with C65 in KIBs, which could be due to the insertion of K^+-ions with the conductive carbons. This insertion behaviour for K^+-ions is different from Na^+-ions. Most probably, Super P forms a more homogenous and thicker SEI layer which can protect the active material and lead to a superior rate capability.

7 Conclusions and outlooks

7.1 Conclusions

In this thesis, the strategy of nanostructural design and the application of a conductive matrix is successfully adopted to develop advanced anode materials with a low-lying redox potential and a high capacity. Furthermore, an in-depth understanding of the underlying relation between Li^+/Na^+/K^+-ions storage mechanisms is elaborated. These new insights are important to improve the performance of rechargeable batteries. Fe_2O_3@C and FeS-based electrode materials for LIBs and SnS_2-based for NIBs and KIBs are comprehensively studied in this work.

The core-shell Fe_2O_3@C material derived from MOFs is synthesized via hydrothermal treatment and subsequent sintering processes and employed as an electrode for Li-ion batteries. The Rietveld refinement shows that the material has two phases of Fe_2O_3 corresponding to the space groups of (maghemite) $Fd\overline{3}m$ and (hematite) $R\overline{3}c$ with a phase fraction of 73 % and 27 %, respectively. The electrode delivers a reversible capacity of 928 mAh g^{-1} at 0.2 A g^{-1} in LP30, while it delivers only 644 mAh g^{-1} at 0.2 A g^{-1} in LiTFSI after 200 cycles. *In operando* synchrotron radiation diffraction demonstrates that $Li_xFe_2O_3$ ($R\overline{3}m$, layered and rhombohedral) and $Li_xFe_2O_3$ ($Fd\overline{3}m$, Li-lean) are formed and then these two phases transform into $Li_xFe_2O_3$ ($Fd\overline{3}m$, Li-rich), which finally converts to metallic Fe^0, Li_2O and $Li_xFe_2O_3$ ($Fd\overline{3}m$, X phase) at the end of the lithiation process. The *in operando* XAS also confirms the Fe K-edge XAS transformation process and the formation of metallic Fe^0. During the de-lithiation process, the electrode does not return to Fe_2O_3. Instead, the $Li_{x-1}Fe_2O_3$ ($Fd\overline{3}m$, X phase, $1 < x < 2.5$) and an amorphous metallic Fe^0 phase remain. In comparison, Adam *et al.*[104] found that the intermediate phase $(Li_xFe)Fe_2O_4$ was formed with 1.58 mol Li inserted into Fe_3O_4. The Rietveld refinement confirmed both oxides have the space group of $Fd\overline{3}m$. In Fe_3O_4, Fe^{2+} and Fe^{3+} ions are considered to occupy the Wyckoff positions of 8a and 16d, respectively. In $(Li_xFe)Fe_2O_4$, Fe ions occupy the Wyckoff site of 16d and 16c, respectively.

The CVs demonstrate that kinetic processes are controlled by predominantly ionic diffusion. Nevertheless, the material shows good capacity retention at high currents (at 4 A g^{-1}, 347 mAh g^{-1} and 311 mAh g^{-1} in LP30 and LiTFSI, respectively). Furthermore, understanding of the kinetics phenomena and resistive contributions in the two types of Li-salt-based electrolytes has been achieved by performing electrochemical impedance spectroscopy.

The SEI resistance (R_{SEI}) and Li^+ charge transfer resistance (R_{CT}) in LP30 are lower than those in LiTFSI. The different cycling stabilities in the two electrolytes are attributed to the different features of the SEI films, which also influences the electrochemical reaction kinetics.

Metal-sulfur bonds in sulfide conversion materials are more easily broken/formed during Li-ion repeated insertion/extraction processes compared with metal-oxygen bonds. FeS nanosheets and $Fe_{1-x}S$/C nanocomposites consisting of well-dispersed FeS and Fe_3C nanoparticles and interconnected carbon spheres were synthesized via a facile hydrothermal method and a subsequent sintering process. It is observed that the interconnected carbon spheres have a significant impact on the electrochemical performance of FeS-based electrodes. The catalytic activity of Fe_3C, which was formed as a beneficial by-product during the conducted synthesis, is highlighted in this study. Due to the unique formulation of the composite electrochemical cycling performance is significantly enhanced. This is accompanied by a continuous increase of the capacity. It is further discovered that the introduction of interconnected carbon spheres in FeS drastically affects the phase fraction, morphology, and particle size. More importantly, the interconnected carbon spheres have a profound influence on the kinetic process and crystal structure during cycling. Furthermore, such carbon spheres change the transformation of diffusion-controlled behavior to a surface-capacitive energy storage process. Indeed, interconnected carbon spheres improve the electron conductivity, reduce the crystal size, and maintain structural integrity. Especially for long-term cycling procedures, the well-distributed FeS nanoparticles with small average diameters provide sufficient electrode-electrolyte contact areas for high lithium-ion flux across the interface. A reduction of the lithium-ion diffusion length during cycling significantly promotes the electrochemical processes, especially at high specific current.

NIBs and KIBs have been receiving much attention due to the higher abundance of sodium and potassium and low cost compared with the limited Li resources. Porous SnS_2-rGO nanosheets were *in situ* grown on reduced graphene oxide (rGO). The SnS_2-rGO electrode shows promising properties when applied as anode material for NIBs and KIBs. The SnS_2-rGO anode delivers high reversible de-sodiation capacities (C65: 635 mAh g^{-1}, Super P: 420 mAh g^{-1}; at 0.2 A g^{-1} after 250 cycles) and de-potassiation capacities (C65 and Super P: 398 mAh g^{-1} at 0.1 A g^{-1} after 200 cycles). Such excellent electrochemical performances are attributed to the unique sandwich structure of SnS_2-rGO-SnS_2. This unique structure ensures not only rapid Na-ion/K-ion diffusion and electron transport throughout the bulk material, but also provides good structural stability to buffer the large volume changes during cycling processes. It is demonstrated that the electrolyte additive (FEC) can improve the specific capacity and stability of the SnS_2-rGO electrode in NIBs, while the FEC additive is negatively impairing the performance of KIBs. The KFSI-based electrolyte containing FEC could increase the content of carbonyl group and the number of K-F bonds. This behavior accelerated the decomposition of electrolyte and side reactions during the cycling process in addition to the also higher solvation energy of in the electrolyte with FEC. It is found that the SnS_2-rGO electrode with C65 has superior long-term cycling and rate performance than that with Super P in NIBs. The variation of R_{SEI} from EIS results can confirm a cracking of the SnS_2-rGO electrode with Super P. The SnS_2-rGO electrode with Super P shows a better rate performance than that with C65 in KIBs, which could be due to a different insertion of K^+-ions in the conductive carbons as compared to Na^+-ions.

7.2 Outlooks

The strategy of combining metal oxides/sulfides with carbonaceous materials as anodes material is useful for researchers in the field of rechargeable batteries. Additionally, the SEI film plays a vital role in the conversion/alloying-type anode materials, especially in the aspect of long-term cycling. Future work will address a comprehensive understanding of the SEI nature and evolution in the Fe_2O_3@C material through XPS, *ex-situ* SEM and XRD, EDX analysis.

For FeS-based material, the structural transformation of $Fe_{1-x}S$/C after immersion in LP30 1h is very interesting. XRD Rietveld refinement proved detailed information on this phase transformation process. However, the reason why the transformation happened is still not clear. The iron sulfides group consists of troilite (FeS) and pyrrhotites with continuously variable compositions. For a more detailed phase transition mechanism, more advanced characterization techniques (XPS, TEM, and SEM/EDX) are required.

Since the effects of FEC on the long-term cycling stability of the SnS_2-rGO electrode for NIBs and KIBs have been investigated, it is also interesting to study the influence of FEC on surface morphology by SEM/EDX and SEI composition by XPS. Additionally, further research work could address the side reactions and the role of the individual solvent in NIBs and KIBs by *in operando* techniques (Raman spectroscopy, XPS, and Fourier transform infrared microscopy). This could guide researchers toward strategies for more effective electrolyte optimization. Furthermore, the potassium-ion storage capacity of two different carbon additives (Super P and C65) is needed to be investigated. It is planned to investigate C65 carbon additive distribution and its connection pathways in the SnS_2-rGO electrode.

8 References

[1] D. Larcher, J.-M. Tarascon, *Nat. Chem.* **2015**, *7*, 19.

[2] C. Liu, F. Li, L.-P. Ma, H.-M. Cheng, *Adv. Mater.* **2010**, *22*, E28.

[3] Z. Yang, J. Zhang, M. C. W. Kintner-Meyer, X. Lu, D. Choi, J. P. Lemmon, J. Liu, *Chem. Rev.* **2011**, *111*, 3577.

[4] G. L. Soloveichik, *Annu. Rev. Chem. Biomol. Eng.* **2011**, *2*, 503.

[5] B. Dunn, H. Kamath, J.-M. Tarascon, *Science* **2011**, *334*, 928.

[6] Y. Wang, J. Yi, Y. Xia, *Adv. Energy Mater.* **2012**, *2*, 830.

[7] M. Armand, J.-M. Tarascon, *Nature* **2008**, *451*, 652.

[8] J.-Y. Hwang, S.-T. Myung, Y.-K. Sun, *Chem. Soc. Rev.* **2017**, *46*, 3529.

[9] K. Kubota, M. Dahbi, T. Hosaka, S. Kumakura, S. Komaba, *Chem. Rec.* **2018**, *18*, 459.

[10] J. Liu, C. Xu, Z. Chen, S. Ni, Z. X. Shen, *Green Energy Environ.* **2018**, *3*, 20.

[11] J. O. Gil Posada, P. J. Hall, *J. Power Sources* **2014**, *262*, 263.

[12] K. Young, S. Yasuoka, *Batteries* **2016**, *2*, 3.

[13] J.-Y. Luo, Y.-Y. Xia, *Adv. Funct. Mater.* **2007**, *17*, 3877.

[14] W. Wang, W. Li, S. Wang, Z. Miao, H. K. Liu, S. Chou, *J. Mater. Chem. A* **2018**, *6*, 6183.

[15] B. L. Ellis, L. F. Nazar, *Curr. Opin. Solid State Mater. Sci.* **2012**, *16*, 168.

[16] J. C. Pramudita, D. Sehrawat, D. Goonetilleke, N. Sharma, *Adv. Energy Mater.* **2017**, *7*, 1602911.

[17] H. Kim, J. C. Kim, M. Bianchini, D.-H. Seo, J. Rodriguez-Garcia, G. Ceder, *Adv. Energy Mater.* **2018**, *8*, 1702384.

[18] W. Zhang, Y. Liu, Z. Guo, *Sci. Adv.* **2019**, *5*, eaav7412.

[19] X. Wu, Y. Chen, Z. Xing, C. W. K. Lam, S. Pang, W. Zhang, Z. Ju, *Adv. Energy Mater.* **2019**, *9*, 1900343.

[20] G.-L. Xu, Q. Wang, J.-C. Fang, Y.-F. Xu, J.-T. Li, L. Huang, S.-G. Sun, *J. Mater. Chem. A* **2014**, *2*, 19941.

[21] C. Vaalma, D. Buchholz, M. Weil, S. Passerini, *Nat. Rev. Mater.* **2018**, *3*, 18013.

[22] J.-Y. Hwang, S.-T. Myung, Y.-K. Sun, *Adv. Funct. Mater.* **2018**, *28*, 1802938.

[23] P. K. Nayak, L. Yang, W. Brehm, P. Adelhelm, *Angew. Chemie Int. Ed.* **2018**, *57*, 102.

[24] C. E. Holland, J. W. Weidner, R. A. Dougal, R. E. White, *J. Power Sources* **2002**, *109*, 32.

[25] W.-B. Hua, X.-D. Guo, Z. Zheng, Y.-J. Wang, B.-H. Zhong, B. Fang, J.-Z. Wang, S.-L. Chou, H. Liu, *J. Power Sources* **2015**, *275*, 200.

[26] G. A. Muller, J. B. Cook, H.-S. Kim, S. H. Tolbert, B. Dunn, *Nano Lett.* **2015**, *15*, 1911.

[27] G. Tian, Z. Zhao, A. Sarapulova, C. Das, L. Zhu, S. Liu, A. Missiul, E. Welter, J. Maibach, S. Dsoke, *J. Mater. Chem. A* **2019**, *7*, 15640.

[28] V. Augustyn, J. Come, M. A. Lowe, J. W. Kim, P.-L. Taberna, S. H. Tolbert, H. D. Abruña, P. Simon, B. Dunn, *Nat. Mater.* **2013**, *12*, 518.

[29] T. Brezesinski, J. Wang, S. H. Tolbert, B. Dunn, *Nat. Mater.* **2010**, *9*, 146.

[30] L. Li, S. Peng, N. Bucher, H.-Y. Chen, N. Shen, A. Nagasubramanian, E. Eldho, S. Hartung, S. Ramakrishna, M. Srinivasan, *Nano Energy* **2017**, *37*, 81.

[31] H. Lindström, S. Södergren, A. Solbrand, H. Rensmo, J. Hjelm, A. Hagfeldt, S.-E. Lindquist, *J. Phys. Chem. B* **1997**, *101*, 7717.

[32] V. Augustyn, P. Simon, B. Dunn, *Energy Environ. Sci.* **2014**, *7*, 1597.

[33] P. Yu, C. Li, X. Guo, *J. Phys. Chem. C* **2014**, *118*, 10616.

[34] C. Zhao, C. Yu, M. Zhang, H. Huang, S. Li, X. Han, Z. Liu, J. Yang, W. Xiao, J. Liang, X. Sun, J. Qiu, *Adv. Energy Mater.* **2017**, *7*, 1602880.

[35] M. Abdollahifar, S.-S. Huang, Y.-H. Lin, Y.-C. Lin, B.-Y. Shih, H.-S. Sheu, Y.-F. Liao, N.-L. Wu, *J. Power Sources* **2018**, *378*, 90.

[36] B. BOUKAMP, *Solid State Ionics* **1986**, *20*, 31.

[37] S. Goriparti, E. Miele, F. De Angelis, E. Di Fabrizio, R. Proietti Zaccaria, C. Capiglia, *J. Power Sources* **2014**, *257*, 421.

[38] J. Lu, Z. Chen, F. Pan, Y. Cui, K. Amine, *Electrochem. Energy Rev.* **2018**, *1*, 35.

[39] M. Yoshio, H. Wang, K. Fukuda, T. Umeno, T. Abe, Z. Ogumi, *J. Mater. Chem.* **2004**, *14*, 1754.

[40] C. Bommier, X. Ji, *Isr. J. Chem.* **2015**, *55*, 486.

[41] W. Luo, Z. Jian, Z. Xing, W. Wang, C. Bommier, M. M. Lerner, X. Ji, *ACS Cent. Sci.* **2015**, *1*, 516.

[42] S. Guo, J. Yi, Y. Sun, H. Zhou, *Energy Environ. Sci.* **2016**, *9*, 2978.

[43] P. Senguttuvan, G. Rousse, V. Seznec, J.-M. Tarascon, M. R. Palacín, *Chem. Mater.* **2011**, *23*, 4109.

[44] I. T. Kim, A. Magasinski, K. Jacob, G. Yushin, R. Tannenbaum, *Carbon N. Y.* **2013**, *52*, 56.

[45] F. Lin, Y. Liu, X. Yu, L. Cheng, A. Singer, O. G. Shpyrko, H. L. Xin, N. Tamura, C. Tian, T.-C. Weng, X.-Q. Yang, Y. S. Meng, D. Nordlund, W. Yang, M. M. Doeff, *Chem. Rev.* **2017**, *117*, 13123.

[46] A. Ulvestad, A. Singer, J. N. Clark, H. M. Cho, J. W. Kim, R. Harder, J. Maser, Y. S. Meng, O. G. Shpyrko, *Science (80-.).* **2015**, *348*, 1344.

[47] H. Liu, F. C. Strobridge, O. J. Borkiewicz, K. M. Wiaderek, K. W. Chapman, P. J. Chupas, C. P. Grey, *Science (80-.).* **2014**, *344*, 1252817.

[48] J. J. Rehr, R. C. Albers, *Rev. Mod. Phys.* **2000**, *72*, 621.

[49] M. Giorgetti, *ISRN Mater. Sci.* **2013**, *2013*, 1.

[50] P. P. R. M. L. Harks, F. M. Mulder, P. H. L. Notten, *J. Power Sources* **2015**, *288*, 92.

[51] J. McBreen, W. E. O'Grady, K. I. Pandya, *J. Power Sources* **1988**, *22*, 323.

[52] M. Herklotz, J. Weiß, E. Ahrens, M. Yavuz, L. Mereacre, N. Kiziltas-Yavuz, C. Dräger, H. Ehrenberg, J. Eckert, F. Fauth, L. Giebeler, M. Knapp, *J. Appl. Crystallogr.* **2016**, *49*, 340.

[53] E. Weckert, in *AIP Conf. Proc.*, AIP, **2004**, pp. 73–76.

[54] E. Welter, R. Chernikov, M. Herrmann, R. Nemausat, in *AIP Conf. Proc.*, **2019**, p. 040002.

[55] E. Welter, *J. Synchrotron Radiat.* **2012**, *19*, 905.

[56] P. R. Willmott, D. Meister, S. J. Leake, M. Lange, A. Bergamaschi, M. Böge, M. Calvi, C. Cancellieri, N. Casati, A. Cervellino, Q. Chen, C. David, U. Flechsig, F. Gozzo, B. Henrich, S. Jäggi-Spielmann, B. Jakob, I. Kalichava, P. Karvinen, J. Krempasky, A. Lüdeke, R. Lüscher, S. Maag, C. Quitmann, M. L. Reinle-Schmitt, T. Schmidt, B. Schmitt, A. Streun, I. Vartiainen, M. Vitins, X. Wang, R. Wullschleger, *J. Synchrotron Radiat.* **2013**, *20*, 667.

[57] F. Fauth, I. Peral, C. Popescu, M. Knapp, *Powder Diffr.* **2013**, *28*, S360.

[58] J. S. Cho, Y. J. Hong, Y. C. Kang, *ACS Nano* **2015**, *9*, 4026.

[59] Y. Chen, Z. Lu, L. Zhou, Y.-W. Mai, H. Huang, *Energy Environ. Sci.* **2012**, *5*, 7898.

[60] Y. Sun, R. B. Sills, X. Hu, Z. W. Seh, X. Xiao, H. Xu, W. Luo, H. Jin, Y. Xin, T. Li, Z. Zhang, J. Zhou, W. Cai, Y. Huang, Y. Cui, *Nano Lett.* **2015**, *15*, 3899.

[61] L. Qiao, X. Wang, L. Qiao, X. Sun, X. Li, Y. Zheng, D. He, *Nanoscale* **2013**, *5*, 3037.

[62] V. Schmidt, J. V. Wittemann, U. Gösele, *Chem. Rev.* **2010**, *110*, 361.

[63] D. A. C. Brownson, D. K. Kampouris, C. E. Banks, *J. Power Sources* **2011**, *196*, 4873.

[64] Y.-X. Wang, S.-L. Chou, H.-K. Liu, S.-X. Dou, *Carbon N. Y.* **2013**, *57*, 202.

[65] J. Xu, M. Wang, N. P. Wickramaratne, M. Jaroniec, S. Dou, L. Dai, *Adv. Mater.* **2015**, *27*, 2042.

[66] S. Wang, L. Xia, L. Yu, L. Zhang, H. Wang, X. W. D. Lou, *Adv. Energy Mater.* **2016**, *6*, 1502217.

[67] C. Li, A. Sarapulova, Z. Zhao, Q. Fu, V. Trouillet, A. Missiul, E. Welter, S. Dsoke,

Chem. Mater. **2019**, *31*, 5633.

[68] C. H. W. Jones, P. E. Kovacs, R. D. Sharma, R. S. McMillan, *J. Phys. Chem.* **1990**.

[69] C. Wang, M. Lan, Y. Zhang, H. Bian, M.-F. Yuen, K. (Ken) Ostrikov, J. Jiang, W. Zhang, Y. Y. Li, J. Lu, *Green Chem.* **2016**, *18*, 3029.

[70] Y. Liu, M. Zhong, L. Kong, A. Li, X. Sun, D. Wang, X.-H. Bu, *Inorg. Chem. Front.* **2019**, *6*, 50.

[71] Y. Xiao, J.-Y. Hwang, I. Belharouak, Y.-K. Sun, *ACS Energy Lett.* **2017**, *2*, 364.

[72] A. Clauset, C. R. Shalizi, M. E. J. Newman, *ACS Nano* **2007**, *11*, 5140.

[73] Y.-M. Lin, P. R. Abel, A. Heller, C. B. Mullins, *J. Phys. Chem. Lett.* **2011**, *2*, 2885.

[74] X. Lv, J. Deng, B. Wang, J. Zhong, T.-K. Sham, X. Sun, X. Sun, *Chem. Mater.* **2017**, *29*, 3499.

[75] Z.-W. Zhao, T. Wen, K. Liang, Y.-F. Jiang, X. Zhou, C.-C. Shen, A.-W. Xu, *ACS Appl. Mater. Interfaces* **2017**, *9*, 3757.

[76] J. Hu, J. Zheng, L. Tian, Y. Duan, L. Lin, S. Cui, H. Peng, T. Liu, H. Guo, X. Wang, F. Pan, *Chem. Commun.* **2015**, *51*, 7855.

[77] M. Dahbi, F. Ghamouss, F. Tran-Van, D. Lemordant, M. Anouti, *J. Power Sources* **2011**, *196*, 9743.

[78] C. Xu, Y. Zeng, X. Rui, N. Xiao, J. Zhu, W. Zhang, J. Chen, W. Liu, H. Tan, H. H. Hng, Q. Yan, *ACS Nano* **2012**, *6*, 4713.

[79] X. Zhao, D. Xia, J. Yue, S. Liu, *Electrochim. Acta* **2014**, *116*, 292.

[80] V. Lakshmi, Y. Chen, A. A. Mikhaylov, A. G. Medvedev, I. Sultana, M. M. Rahman, O. Lev, P. V. Prikhodchenko, A. M. Glushenkov, *Chem. Commun.* **2017**, *53*, 8272.

[81] Y. Zhang, C. Zhao, Z. Zeng, J. M. Ang, B. Che, Z. Wang, X. Lu, *Electrochim. Acta* **2018**, *278*, 156.

[82] D. Kong, H. He, Q. Song, B. Wang, Q.-H. Yang, L. Zhi, *RSC Adv.* **2014**, *4*, 23372.

[83] M. Sathish, S. Mitani, T. Tomai, I. Honma, *J. Phys. Chem. C* **2012**, *116*, 12475.

[84] Y. Zhang, P. Zhu, L. Huang, J. Xie, S. Zhang, G. Cao, X. Zhao, *Adv. Funct. Mater.* **2015**, *25*, 481.

[85] M. Pasta, C. D. Wessells, R. A. Huggins, Y. Cui, *Nat. Commun.* **2012**, *3*, 1149.

[86] H. Pan, Y.-S. Hu, L. Chen, *Energy Environ. Sci.* **2013**, *6*, 2338.

[87] C. Li, Q. Hu, Y. Li, H. Zhou, Z. Lv, X. Yang, L. Liu, H. Guo, *Sci. Rep.* **2016**, *6*, 25556.

[88] Z. Zhao, G. Tian, A. Sarapulova, V. Trouillet, Q. Fu, U. Geckle, H. Ehrenberg, S. Dsoke, *J. Mater. Chem. A* **2018**, *6*, 19381.

[89] K. L. Parry, A. G. Shard, R. D. Short, R. G. White, J. D. Whittle, A. Wright, *Surf.*

Interface Anal. **2006**, *38*, 1497.

[90] D. Wang, X. Bie, Q. Fu, D. Dixon, N. Bramnik, Y.-S. Hu, F. Fauth, Y. Wei, H. Ehrenberg, G. Chen, F. Du, *Nat. Commun.* **2017**, *8*, 15888.

[91] P. Bhattacharya, M. Kota, D. H. Suh, K. C. Roh, H. S. Park, *Adv. Energy Mater.* **2017**, *7*, 1700331.

[92] Q. Guan, J. Cheng, B. Wang, W. Ni, G. Gu, X. Li, L. Huang, G. Yang, F. Nie, *ACS Appl. Mater. Interfaces* **2014**, *6*, 7626.

[93] A. P. Grosvenor, B. A. Kobe, M. C. Biesinger, N. S. McIntyre, *Surf. Interface Anal.* **2004**, *36*, 1564.

[94] T. Fujii, F. M. F. de Groot, G. A. Sawatzky, F. C. Voogt, T. Hibma, K. Okada, *Phys. Rev. B* **1999**, *59*, 3195.

[95] G. P. López, D. G. Castner, B. D. Ratner, *Surf. Interface Anal.* **1991**, *17*, 267.

[96] Y. Liu, J. Xu, X. Qin, H. Xin, X. Yuan, J. Zhang, D. Li, C. Song, *J. Mater. Chem. A* **2015**, *3*, 9682.

[97] X. Xu, Y. Wan, J. Liu, Y. Chen, L. Li, X. Wang, G. Xue, D. Zhou, *Electrochim. Acta* **2017**, *246*, 766.

[98] Y. Jiang, D. Zhang, Y. Li, T. Yuan, N. Bahlawane, C. Liang, W. Sun, Y. Lu, M. Yan, *Nano Energy* **2014**, *4*, 23.

[99] Z. Wang, D. Luan, S. Madhavi, Y. Hu, X. W. (David) Lou, *Energy Environ. Sci.* **2012**, *5*, 5252.

[100] S. Park, T. Matsui, S. Takai, T. Yao, *Solid State Ionics* **2014**, *255*, 50.

[101] S. Permien, S. Indris, U. Schürmann, L. Kienle, S. Zander, S. Doyle, W. Bensch, *Chem. Mater.* **2016**, *28*, 434.

[102] K. Cheaib, B. Maurice, T. Mateo, Z. Halime, B. Lassalle-Kaiser, *J. Synchrotron Radiat.* **2019**, *26*, 1980.

[103] I. A. Vinokurov, J. Kankare, *J. Phys. Chem. B* **1998**, *102*, 1136.

[104] R. Adam, M. Lepple, N. A. Mayer, D. M. Cupid, Y. Qian, P. Niehoff, F. M. Schappacher, D. Wadewitz, G. Balachandran, A. Bhaskar, N. Bramnik, V. Klemm, E. Ahrens, L. Giebeler, F. Fauth, C. A. Popescu, H. J. Seifert, M. Winter, H. Ehrenberg, D. Rafaja, *Int. J. Mater. Res.* **2017**, 146.111509.

[105] Y. Tang, Y. Zhang, O. I. Malyi, N. Bucher, H. Xia, S. Xi, Z. Zhu, Z. Lv, W. Li, J. Wei, M. Srinivasan, A. Borgna, M. Antonietti, Y. Du, X. Chen, *Adv. Mater.* **2018**, *30*, 1802200.

[106] G. Zhou, D.-W. Wang, P.-X. Hou, W. Li, N. Li, C. Liu, F. Li, H.-M. Cheng, *J. Mater. Chem.* **2012**, *22*, 17942.

[107] J. Zhu, T. Zhu, X. Zhou, Y. Zhang, X. W. Lou, X. Chen, H. Zhang, H. H. Hng, Q. Yan, *Nanoscale* **2011**, *3*, 1084.

[108] Y. Jin, L. Dang, H. Zhang, C. Song, Q. Lu, F. Gao, *Chem. Eng. J.* **2017**, *326*, 292.

[109] W. Wei, S. Yang, H. Zhou, I. Lieberwirth, X. Feng, K. Müllen, *Adv. Mater.* **2013**, *25*, 2909.

[110] F. Zheng, Z. Yin, H. Xia, Y. Zhang, *Mater. Lett.* **2017**, *197*, 188.

[111] G. Li, Y. Li, J. Chen, P. Zhao, D. Li, Y. Dong, L. Zhang, *Electrochim. Acta* **2017**, *245*, 941.

[112] F. Zheng, Z. Yin, H. Xia, G. Bai, Y. Zhang, *Chem. Eng. J.* **2017**, *327*, 474.

[113] T. Zhang, C. Zhu, Y. Shi, Y. Li, S. Zhu, D. Zhang, *Mater. Lett.* **2017**, *205*, 10.

[114] Y. Zhao, X. Zhai, D. Yan, C. Ding, N. Wu, D. Su, Y. Zhao, H. Zhou, X. Zhao, J. Li, H. Jin, *Electrochim. Acta* **2017**, *243*, 18.

[115] K. Zhang, M. Park, L. Zhou, G.-H. Lee, J. Shin, Z. Hu, S.-L. Chou, J. Chen, Y.-M. Kang, *Angew. Chemie Int. Ed.* **2016**, *55*, 12822.

[116] L. Zhang, H. Bin Wu, X. W. D. Lou, *Adv. Energy Mater.* **2014**, *4*, 1300958.

[117] J. Liu, Y. Wen, Y. Wang, P. A. van Aken, J. Maier, Y. Yu, *Adv. Mater.* **2014**, *26*, 6025.

[118] X. Xu, J. Liu, Z. Liu, J. Shen, R. Hu, J. Liu, L. Ouyang, L. Zhang, M. Zhu, *ACS Nano* **2017**, *11*, 9033.

[119] N. Belzile, Y.-W. Chen, M.-F. Cai, Y. Li, *J. Geochemical Explor.* **2004**, *84*, 65.

[120] J. P. R. de Villiers, D. C. Liles, M. Becker, *Am. Mineral.* **2009**, *94*, 1405.

[121] W. Han, M. Gao, *Cryst. Growth Des.* **2008**, *8*, 1023.

[122] C. Li, A. Sarapulova, K. Pfeifer, S. Dsoke, *ChemSusChem* **2020**, *13*, 986.

[123] R. S. Multani, K. E. Waters, *Can. J. Chem. Eng.* **2018**, *96*, 1185.

[124] N. Belzile, Y. W. Chen, M. F. Cai, Y. Li, *J. Geochemical Explor.* **2004**, *84*, 65.

[125] C. Burda, X. Chen, R. Narayanan, M. A. El-Sayed, *Chem. Rev.* **2005**, *105*, 1025.

[126] M. Becker, J. De Villiers, D. Bradshaw, *Miner. Eng.* **2010**, *23*, 1045.

[127] C. R. S. Haines, C. J. Howard, R. J. Harrison, M. A. Carpenter, *Acta Crystallogr. Sect. B Struct. Sci. Cryst. Eng. Mater.* **2019**, *75*, 1208.

[128] E. B. Hansson, M. S. Odziemkowski, R. W. Gillham, *Corros. Sci.* **2006**, *48*, 3767.

[129] F. Cheng, K. Huang, S. Liu, J. Liu, R. Deng, *Electrochim. Acta* **2011**, *56*, 5593.

[130] A. C. Ferrari, J. Robertson, *Phys. Rev. B* **2000**, *61*, 14095.

[131] C. Gómez-Navarro, R. T. Weitz, A. M. Bittner, M. Scolari, A. Mews, M. Burghard, K. Kern, *Nano Lett.* **2007**, *7*, 3499.

[132] Y.-X. Wang, J. Yang, S.-L. Chou, H. K. Liu, W. Zhang, D. Zhao, S. X. Dou, *Nat. Commun.* **2015**, *6*, 8689.

[133] C. Zhu, Y. Wen, P. A. van Aken, J. Maier, Y. Yu, *Adv. Funct. Mater.* **2015**, *25*, 2335.

[134] Y. Xu, W. Li, F. Zhang, X. Zhang, W. Zhang, C.-S. Lee, Y. Tang, *J. Mater. Chem. A* **2016**, *4*, 3697.

[135] W. Yang, H. Zhao, L. Chen, C. Fang, Z. Rui, L. Yang, H. Wan, J. Liu, Y. Zhou, P. Wang, Z. Zou, *Chem. Eng. J.* **2017**, *326*, 1040.

[136] L. Fei, Q. Lin, B. Yuan, G. Chen, P. Xie, Y. Li, Y. Xu, S. Deng, S. Smirnov, H. Luo, *ACS Appl. Mater. Interfaces* **2013**, *5*, 5330.

[137] Y. Ma, H. D. Asfaw, K. Edström, *Chem. Mater.* **2015**, *27*, 3957.

[138] S. Boursiquot, M. Mullet, J.-J. Ehrhardt, *Surf. Interface Anal.* **2002**, *34*, 293.

[139] M. Mullet, S. Boursiquot, M. Abdelmoula, J.-M. Génin, J.-J. Ehrhardt, *Geochim. Cosmochim. Acta* **2002**, *66*, 829.

[140] J. E. Thomas, C. F. Jones, W. M. Skinner, R. S. C. Smart, *Geochim. Cosmochim. Acta* **1998**, *62*, 1555.

[141] Y. Lan, E. C. Butler, *Environ. Sci. Technol.* **2016**, *50*, 5489.

[142] E. J. Kim, J. H. Kim, A. M. Azad, Y. S. Chang, *ACS Appl. Mater. Interfaces* **2011**, *3*, 1457.

[143] Q. Wang, W. Zhang, C. Guo, Y. Liu, C. Wang, Z. Guo, *Adv. Funct. Mater.* **2017**, *27*, 1703390.

[144] S. Permien, S. Indris, A.-L. Hansen, M. Scheuermann, D. Zahn, U. Schürmann, G. Neubüser, L. Kienle, E. Yegudin, W. Bensch, *ACS Appl. Mater. Interfaces* **2016**, *8*, 15320.

[145] C. Xing, D. Zhang, K. Cao, S. Zhao, X. Wang, H. Qin, J. Liu, Y. Jiang, L. Meng, *J. Mater. Chem. A* **2015**, *3*, 8742.

[146] B. Wu, H. Song, J. Zhou, X. Chen, *Chem. Commun.* **2011**, *47*, 8653.

[147] Q. Ma, H. Song, Q. Zhuang, J. Liu, Z. Zhang, C. Mao, H. Peng, G. Li, K. Chen, *Chem. Eng. J.* **2018**, *338*, 726.

[148] S. S. Zhang, *J. Mater. Chem. A* **2015**, *3*, 7689.

[149] F. Kong, X. Fan, A. Kong, Z. Zhou, X. Zhang, Y. Shan, *Adv. Funct. Mater.* **2018**, *28*, 1803973.

[150] K. Strickland, E. Miner, Q. Jia, U. Tylus, N. Ramaswamy, W. Liang, M.-T. Sougrati, F. Jaouen, S. Mukerjee, *Nat. Commun.* **2015**, *6*, 7343.

[151] L. Zhao, X. Yu, J. Yu, Y. Zhou, S. N. Ehrlich, Y.-S. Hu, D. Su, H. Li, X.-Q. Yang, L. Chen, *Adv. Funct. Mater.* **2014**, *24*, 5557.

[152] S. Kostov, M. DenBoer, E. Strauss, D. Golodnitsky, S. . Greenbaum, E. Peled, *J. Power Sources* **1999**, *81–82*, 709.

[153] S. J. An, J. Li, C. Daniel, D. Mohanty, S. Nagpure, D. L. Wood, *Carbon N. Y.* **2016**, *105*,

52.

[154] S. J. Rezvani, F. Nobili, R. Gunnella, M. Ali, R. Tossici, S. Passerini, A. Di Cicco, *J. Phys. Chem. C* **2017**, *121*, 26379.

[155] S. J. Rezvani, R. Gunnella, A. Witkowska, F. Mueller, M. Pasqualini, F. Nobili, S. Passerini, A. Di Cicco, *ACS Appl. Mater. Interfaces* **2017**, *9*, 4570.

[156] F. Liao, J. Światowska, V. Maurice, A. Seyeux, L. H. Klein, S. Zanna, P. Marcus, *Appl. Surf. Sci.* **2013**, *283*, 888.

[157] F. Liao, J. Światowska, V. Maurice, A. Seyeux, L. H. Klein, S. Zanna, P. Marcus, *Phys. Chem. Chem. Phys.* **2015**, *17*, 619.

[158] M. Huang, A. Xu, H. Duan, S. Wu, *J. Mater. Chem. A* **2018**, *6*, 7155.

[159] D. T. Tran, S. S. Zhang, *J. Mater. Chem. A* **2015**, *3*, 12240.

[160] L. Su, Z. Zhou, P. Shen, *Electrochim. Acta* **2013**, *87*, 180.

[161] D. Golodnitsky, E. Peled, *Electrochim. Acta* **1999**, *45*, 335.

[162] J. Seo, Y. Jun, S. Park, H. Nah, T. Moon, B. Park, J.-G. Kim, Y. J. Kim, J. Cheon, *Angew. Chemie Int. Ed.* **2007**, *46*, 8828.

[163] P. Lou, Y. Tan, P. Lu, Z. Cui, X. Guo, *J. Mater. Chem. A* **2016**, *4*, 16849.

[164] H. Lyu, J. Liu, S. Qiu, Y. Cao, C. Hu, S. Guo, Z. Guo, *J. Mater. Chem. A* **2016**, *4*, 9881.

[165] F. Maroni, S. Gabrielli, A. Palmieri, E. Marcantoni, F. Croce, F. Nobili, *J. Power Sources* **2016**, *332*, 79.

[166] M. Zhao, X. Xie, C. E. Ren, T. Makaryan, B. Anasori, G. Wang, Y. Gogotsi, *Adv. Mater.* **2017**, *29*, 1702410.

[167] L. Fan, X. Li, B. Yan, J. Feng, D. Xiong, D. Li, L. Gu, Y. Wen, S. Lawes, X. Sun, *Adv. Energy Mater.* **2016**, *6*, 1502057.

[168] Z. Jian, W. Luo, X. Ji, *J. Am. Chem. Soc.* **2015**, *137*, 11566.

[169] L. Xue, Y. Li, H. Gao, W. Zhou, X. Lü, W. Kaveevivitchai, A. Manthiram, J. B. Goodenough, *J. Am. Chem. Soc.* **2017**, *139*, 2164.

[170] W. Zhang, J. Mao, S. Li, Z. Chen, Z. Guo, *J. Am. Chem. Soc.* **2017**, *139*, 3316.

[171] J. Sun, H.-W. Lee, M. Pasta, H. Yuan, G. Zheng, Y. Sun, Y. Li, Y. Cui, *Nat. Nanotechnol.* **2015**, *10*, 980.

[172] J. Han, M. Xu, Y. Niu, G.-N. Li, M. Wang, Y. Zhang, M. Jia, C. M. Li, *Chem. Commun.* **2016**, *52*, 11274.

[173] I. Sultana, M. M. Rahman, S. Mateti, V. G. Ahmadabadi, A. M. Glushenkov, Y. Chen, *Nanoscale* **2017**, *9*, 3646.

[174] H. Kang, Y. Liu, K. Cao, Y. Zhao, L. Jiao, Y. Wang, H. Yuan, *J. Mater. Chem. A* **2015**, *3*, 17899.

[175] H. Tan, Y. Feng, X. Rui, Y. Yu, S. Huang, *Small Methods* **2020**, *4*, 1900563.

[176] X. Sun, P. Bonnick, V. Duffort, M. Liu, Z. Rong, K. A. Persson, G. Ceder, L. F. Nazar, *Energy Environ. Sci.* **2016**, *9*, 2273.

[177] Y. Kim, Y. Kim, A. Choi, S. Woo, D. Mok, N.-S. Choi, Y. S. Jung, J. H. Ryu, S. M. Oh, K. T. Lee, *Adv. Mater.* **2014**, *26*, 4139.

[178] W. Zhang, W. K. Pang, V. Sencadas, Z. Guo, *Joule* **2018**, *2*, 1534.

[179] L. Fan, X. Li, X. Song, N. Hu, D. Xiong, A. Koo, X. Sun, *ACS Appl. Mater. Interfaces* **2018**, *10*, 2637.

[180] S. Li, Z. Zhao, C. Li, Z. Liu, D. Li, *Nano-Micro Lett.* **2019**, *11*, 14.

[181] Y. Zhang, Y. Guo, Y. Wang, T. Peng, Y. Lu, R. Luo, Y. Wang, X. Liu, J.-K. Kim, Y. Luo, *Nanoscale Res. Lett.* **2018**, *13*, 389.

[182] B. Qu, C. Ma, G. Ji, C. Xu, J. Xu, Y. S. Meng, T. Wang, J. Y. Lee, *Adv. Mater.* **2014**, *26*, 3854.

[183] Y. Ren, J. Wang, X. Huang, J. Ding, *Mater. Lett.* **2017**, *186*, 57.

[184] P. Zhou, X. Wang, W. Guan, D. Zhang, L. Fang, Y. Jiang, *ACS Appl. Mater. Interfaces* **2017**, *9*, 6979.

[185] H. Li, M. Zhou, W. Li, K. Wang, S. Cheng, K. Jiang, *RSC Adv.* **2016**, *6*, 35197.

[186] J. B. Fei, Y. Cui, X. H. Yan, W. Qi, Y. Yang, K. W. Wang, Q. He, J. B. Li, *Adv. Mater.* **2008**, *20*, 452.

[187] Y. Wang, J. Zhou, J. Wu, F. Chen, P. Li, N. Han, W. Huang, Y. Liu, H. Ye, F. Zhao, Y. Li, *J. Mater. Chem. A* **2017**, *5*, 25618.

[188] X. Jiang, X. Yang, Y. Zhu, J. Shen, K. Fan, C. Li, *J. Power Sources* **2013**, *237*, 178.

[189] P. Zheng, Z. Dai, Y. Zhang, K. N. Dinh, Y. Zheng, H. Fan, J. Yang, R. Dangol, B. Li, Y. Zong, Q. Yan, X. Liu, *Nanoscale* **2017**, *9*, 14820.

[190] S. Zhang, F. Yao, L. Yang, F. Zhang, S. Xu, *Carbon N. Y.* **2015**, *93*, 143.

[191] Y. Jiang, Y. Feng, B. Xi, S. Kai, K. Mi, J. Feng, J. Zhang, S. Xiong, *J. Mater. Chem. A* **2016**, *4*, 10719.

[192] Z. Wang, Y. Dong, H. Li, Z. Zhao, H. Bin Wu, C. Hao, S. Liu, J. Qiu, X. W. Lou, *Nat. Commun.* **2014**, *5*, 5002.

[193] B. Luo, Y. Fang, B. Wang, J. Zhou, H. Song, L. Zhi, *Energy Environ. Sci.* **2012**, *5*, 5226.

[194] C. Chae, H.-J. Noh, J. K. Lee, B. Scrosati, Y.-K. Sun, *Adv. Funct. Mater.* **2014**, *24*, 3036.

[195] Y. Liu, H. Kang, L. Jiao, C. Chen, K. Cao, Y. Wang, H. Yuan, *Nanoscale* **2015**, *7*, 1325.

[196] J. Cui, S. Yao, Z. Lu, J.-Q. Huang, W. G. Chong, F. Ciucci, J.-K. Kim, *Adv. Energy Mater.* **2018**, *8*, 1702488.

[197] G. M. Veith, M. Doucet, R. L. Sacci, B. Vacaliuc, J. K. Baldwin, J. F. Browning, *Sci. Rep.* **2017**, *7*, 6326.

[198] A. Schiele, B. Breitung, T. Hatsukade, B. B. Berkes, P. Hartmann, J. Janek, T. Brezesinski, *ACS Energy Lett.* **2017**, *2*, 2228.

[199] T. Hou, G. Yang, N. N. Rajput, J. Self, S.-W. Park, J. Nanda, K. A. Persson, *Nano Energy* **2019**, *64*, 103881.

[200] D. Y. W. Yu, P. V. Prikhodchenko, C. W. Mason, S. K. Batabyal, J. Gun, S. Sladkevich, A. G. Medvedev, O. Lev, *Nat. Commun.* **2013**, *4*, 2922.

[201] J. Qian, X. Wu, Y. Cao, X. Ai, H. Yang, *Angew. Chemie Int. Ed.* **2013**, *52*, 4633.

[202] J. Qian, Y. Chen, L. Wu, Y. Cao, X. Ai, H. Yang, *Chem. Commun.* **2012**, *48*, 7070.

[203] S. Komaba, T. Ishikawa, N. Yabuuchi, W. Murata, A. Ito, Y. Ohsawa, *ACS Appl. Mater. Interfaces* **2011**, *3*, 4165.

[204] J. Wang, C. Luo, J. Mao, Y. Zhu, X. Fan, T. Gao, A. C. Mignerey, C. Wang, *ACS Appl. Mater. Interfaces* **2015**, *7*, 11476.

[205] W. Sun, X. Rui, D. Yang, Z. Sun, B. Li, W. Zhang, Y. Zong, S. Madhavi, S. Dou, Q. Yan, *ACS Nano* **2015**, *9*, 11371.

[206] K. Pfeifer, S. Arnold, Ö. Budak, X. Luo, V. Presser, H. Ehrenberg, S. Dsoke, *J. Mater. Chem. A* **2020**, *8*, 6092.

[207] M. E. Spahr, D. Goers, A. Leone, S. Stallone, E. Grivei, *J. Power Sources* **2011**, *196*, 3404.

[208] M. Widmaier, N. Jäckel, M. Zeiger, M. Abuzarli, C. Engel, L. Bommer, V. Presser, *Electrochim. Acta* **2017**, *247*, 1006.

[209] Z. Zhang, H. Zhao, J. Fang, X. Chang, Z. Li, L. Zhao, *ACS Appl. Mater. Interfaces* **2018**, *10*, 28533.

[210] J.-M. Tarascon, M. Armand, *Nature* **2001**, *414*, 359.

[211] J. Huang, Z. Jiang, *Electrochim. Acta* **2008**, *53*, 7756.

[212] X. Bie, K. Kubota, T. Hosaka, K. Chihara, S. Komaba, *J. Mater. Chem. A* **2017**, *5*, 4325.

[213] J. Xie, J. Li, W. Zhuo, W. Mai, *Mater. Today Adv.* **2020**, *6*, 100035.

[214] J. Xie, Y. Zhu, N. Zhuang, X. Li, X. Yuan, J. Li, G. Hong, W. Mai, *J. Mater. Chem. A* **2019**, *7*, 19332.

[215] L. Cao, B. Zhang, X. Ou, C. Wang, C. Peng, J. Zhang, *ChemElectroChem* **2019**, *6*, 2254.

[216] K. Huang, Z. Xing, L. Wang, X. Wu, W. Zhao, X. Qi, H. Wang, Z. Ju, *J. Mater. Chem. A* **2018**, *6*, 434.

[217] C. Sheng, C. Zhang, X. Shen, S. Zhao, L. Fu, Y. Wu, J. Wang, Y. Chen, *Batter. Supercaps* **2020**, *3*, 56.

9 Other related works during my PhD study

In addition to the study of Fe_2O_3@C in LIBs, FeS-based anode material for LIBs, and SnS_2-rGO as anode materials for NIBs and KIBs, other works have been done, including the microcubic SnS_2 and porous MoS_2 nanosheets as anodes material for NIBs and KIBs.

9.1 Microcubes SnS_2 as Anodes for Sodium-ion Batteries and Potassium-ion Batteries

Microcubes SnS_2 is composed of ultrathin nanosheets, which is grown in a facile $MnCO_3$ template. Uniform $MnCO_3$ microcubes were prepared by a simple co-precipitation method and were removed through HCl solution washing. The final product of microcubes SnS_2 are featured with hollow nanostructures with well-defined interior voids and low density. The microcubes SnS_2 is employed as anode for NIBs and KIBs, the reversibility, rate performance, the kinetic process, and electrochemical impedance are investigated. *In operando* synchrotron radiation diffraction is performed to track the structural variation and phase transformation of the SnS_2. The surface morphology changes of the SnS_2 electrode upon cycling are tracked by *ex-situ* SEM. Furthermore, the effect of different carbon additives (Super P and C65) on electrochemical performance for NIBs and KIBs is investigated.

Detailed information can be found: The First draft of Manuscript

9.2 Porous molybdenum disulfide nanosheet-based spheres for Sodium-ion Batteries and Potassium-ion Batteries

A porous molybdenum disulfide (MoS_2) was prepared via the SiO_2 template assistant method, along with the evaluation of the electrochemical performance in NIBs and KIBs. MoS_2 is a promising anode material for NIBs and KIBs. MoS_2 has a layered structure that is similar to graphene. Additionally, the weak van der Waals forces between the layers allow easy intercalation of alkali metal ions. Furthermore, the high abundance of molybdenum and sulfur, along with the diversity of morphologies. The electrochemical performance of MoS_2 is strongly related to its particle size and morphology. Agglomeration tendencies and low conductivity are the drawbacks that penalize the electrochemical performance.

XRD Rietveld refinement reveals MoS_2 with a mixed phase of 2H-MoS_2 and 3R-MoS_2. SEM shows uniformly sized nanosheet-based structures. The initial de-sodiation capacity of

MoS_2 is 525 mAh g^{-1} at 0.2 A g^{-1} with a Coulombic efficiency of ~ 98 %. In KIBs, the initial potassiation capacity of the MoS_2 electrode is 348 mAh g^{-1} at 0.1 A g^{-1}. The Na/K^+-ion storage mechanism and kinetic process are needed to be investigated.

10 Publications and conferences

Publications during the PhD period

[1] **Chengping Li**, Angelina Sarapulova, Zijian Zhao, Qiang Fu, Vanessa Trouillet, Aleksandr Missiul, Edmund Welter, and Sonia Dsoke, Understanding the Lithium Storage Mechanism in Core−Shell Fe_2O_3@C Hollow Nanospheres Derived from Metal−Organic Frameworks: An *In operando* Synchrotron Radiation Diffraction and *in operando* X-ray Absorption Spectroscopy Study, ***Chem. Mater.*** 2019, 31, 5633−5645

[2] **Chengping Li**, Angelina Sarapulova, Kristina Pfeifer, and Sonia Dsoke, Effect of Continuous Capacity Rising Performed by FeS/Fe_3C/C Composite Electrodes for Lithium-Ion Batteries. ***ChemSusChem*** 2020, 13, 986–995.

[3] **Chengping Li,** Angelina Sarapulova, Kristina Pfeifer, Xianlin Luo, Nicola Pietro Maria Casati, Edmund Welter, Georgian Melinte, Qiang Fu, and Sonia Dsoke, Elucidating the Mechanism of Li Insertion into $Fe_{1-x}S$/Carbon via *in operando* Synchrotron Studies. ***ACS Applied Materials & Interfaces*** (Major revision, under review).

[4] Zijian Zhao, Guiying Tian, Angelina Sarapulova, Georgian Melinte, Juan Luis Gómez-Urbano, **Chengping Li**, Suya Liu, Edmund Welter, Martin Etter, and Sonia Dsoke, Mechanism Study of Carbon Coating Effects on Conversion-Type Anode Materials in Lithium-Ion Batteries: Case Study of $ZnMn_2O_4$ and ZnO−MnO Composites. ***ACS Appl. Mater. Interfaces*** 2019, 11, 29888−29900.

Conferences

[1] **C. Li,** A. Sarapulova, K. Pfeifer, S. Dsoke, H. Ehrenberg. "Effect of carbon on FeS-based electrodes for Lithium-ion Batteries." 10. **2019** Advanced Lithium Batteries for Automobile Applications ABAA-12 in Ulm, Germany. Poster Presentation.

[2] **C. Li**, A. Sarapulova, H. Ehrenberg, S. Dsoke. "Understanding the Lithium Storage Mechanism in Core-Shell Fe_2O_3@C Hollow Nanospheres Derived from Metal-Organic Frameworks: An In situ diffraction using synchrotron radiation and in situ X-ray absorption spectroscopy (XAS)." 08. **2019** the 70th Annual Meeting of the International Society of Electrochemistry in Durban, South Africa. Poster Presentation.

[3] **C. Li**, A. Sarapulova, K. Pfeifer, X. Luo, N. Casati, E. Welter, G, Melinte, Q. Fu, S. Dsoke. "Elucidating the Mechanism of Li Insertion into $Fe_{1-x}S$/Carbon via *in operando* Synchrotron Studies." 09. **2020** the 71st Annual Meeting of the International Society of Electrochemistry, online meeting. Poster Presentation.